



**DEEP LEVEL DEFECTS IN ELECTRON-IRRADIATED ALUMINUM GALLIUM
NITRIDE GROWN BY MOLECULAR BEAM EPITAXY**

DISSERTATION

Michael R. Hogsed, Captain, USAF

AFIT/DS/ENP/05-01

**DEPARTMENT OF THE AIR FORCE
AIR UNIVERSITY**

AIR FORCE INSTITUTE OF TECHNOLOGY

Wright-Patterson Air Force Base, Ohio

APPROVED FOR PUBLIC RELEASE; DISTRIBUTION UNLIMITED

The views expressed in this thesis are those of the author and do not reflect the official policy or position of the United States Air Force, Department of Defense, or the United States Government.

AFIT/DS/ENP/05-01

DEEP LEVEL DEFECTS IN ELECTRON-IRRADIATED ALUMINUM GALLIUM
NITRIDE GROWN BY MOLECULAR BEAM EPITAXY

DISSERTATION

Presented to the Faculty

Graduate School of Engineering and Management

Air Force Institute of Technology

Air University

Air Education and Training Command

in Partial Fulfillment of the Requirements for the

Degree of Doctor of Philosophy

Michael R. Hogsed, BS, MS

Captain, USAF

March 2005



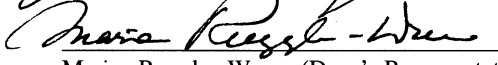
APPROVED FOR PUBLIC RELEASE; DISTRIBUTION UNLIMITED

AFIT/DS/ENP/05-01


DEEP LEVEL DEFECTS IN ELECTRON-IRRADIATED ALUMINUM GALLIUM
NITRIDE GROWN BY MOLECULAR BEAM EPITAXY

Michael R. Hogsed, BS, MS
Captain, USAF

Approved:

	<u>Date</u>
 Yung Kee Yeo (Chairman)	<u>13 Jan 2005</u>
 James A. Lott (Member)	<u>14 JAN '05</u>
 Mohamed Ahoujja (Member)	<u>14 Jan. 2005</u>
 James C. Petrosky (Member)	<u>14 JAN 05</u>
 Marina Ruggles-Wrenn (Dean's Representative)	<u>14 JAN 05</u>

Accepted:

 Robert A. Calico, Jr. Dean, Graduate School of Engineering and Management	<u>15 Feb 05</u> Date
---	--------------------------

Abstract

Electronic and optoelectronic devices having exceptional performance capabilities are being fabricated from wide band gap semiconductor materials such as gallium nitride (GaN) and its ternary alloy aluminum gallium nitride (AlGaN). These devices are also attractive candidates for integration into future Air Force communication and sensor platforms, including those that must operate in the space radiation environment.

However, radiation-induced performance degradation in GaN and AlGaN devices has been observed, and this has been attributed to the creation of microscopic point defects such as vacancies, interstitials, and related defect complexes, which have been associated with energy levels deep in the semiconductor band gap. In recent years, several of these defect energy levels in GaN have been experimentally observed and characterized, but very few studies have been performed on radiation-induced defect energy levels in AlGaN.

In this dissertation research, the electrical and optical properties of high energy electron-irradiated $n\text{-Al}_x\text{Ga}_{1-x}\text{N}$ epitaxial films are characterized for aluminum mole fractions from $x = 0.0$ to 0.3 using deep level transient spectroscopy (DLTS), temperature-dependent Hall, and cathodoluminescence (CL) measurements, and the results are compared with those of the as-grown $n\text{-Al}_x\text{Ga}_{1-x}\text{N}$. The DLTS measurements reveal the presence of electron traps in as-grown GaN that are characteristic of those designated A, B, C, D, and E in the literature. Also, three electron traps, labeled D, P1, and P2 are observed in the as-grown AlGaN. Following 1.0 MeV electron irradiation of

the AlGaIn, it has been found that four additional electron traps labeled R1, R2, R3, and R4 are created and their properties are characterized for the first time, to the best of our knowledge. Three of these traps, R1-R3, correspond to radiation-induced traps reported in GaN. The newly discovered fourth trap, R4, appears to be unique to AlGaIn, and may thus be related to aluminum displacement. Furthermore, this new electron trap R4 is the most prominent radiation-induced defect in the DLTS spectra. Although the other radiation-induced traps begin to anneal under and applied voltage bias at or below 430 K in AlGaIn Schottky barrier diodes, this R4 trap is thermally stable up to 450 K, and could be a contributor to the deleterious radiation effects reported for AlGaIn/GaN high electron mobility transistors (HEMTs). It has also been found that trap levels deepen significantly in the energy band gap with increase in aluminum mole fraction.

The room temperature concentration of electrons in the conduction band, determined by Hall measurement, is found to decrease significantly in both GaN and AlGaIn following 1.0 MeV electron irradiation at a fluence of $1 \times 10^{17} \text{ cm}^{-2}$. The dose-averaged carrier removal rate, η , was found to depend foremost on the initial carrier concentration, n_o , regardless of the aluminum mole fraction. For $6.5 \times 10^{16} \leq n_o \leq 8.2 \times 10^{17} \text{ cm}^{-3}$, the carrier removal rate shows a linear dependence on n_o given by $\eta = (3.96 \times 10^{-18} n_o - 0.15) \text{ cm}^{-1}$. This relationship is attributed, in part, to a process whereby nitrogen interstitials passivate shallow silicon donors by forming Si-N_i complexes.

Following 1.0 MeV electron irradiation at a fluence of $1 \times 10^{17} \text{ cm}^{-2}$, the peak CL intensities of the GaN and AlGaIn samples were reduced, on average, by 50%. This reduction is attributed to the creation of non-radiative recombination centers.

For all of the GaN and AlGa_N samples, the observed radiation effects of carrier removal and luminescence degradation are stable at room temperature. For comparison of radiation tolerance, a sample of a commonly used semiconductor material, gallium arsenide (GaAs), was irradiated and characterized along with the GaN and AlGa_N samples. It is shown that GaAs has a carrier removal rate 2 times higher than the GaN and AlGa_N, and the luminescence intensity degrades to less than 1% of the original value after irradiation with the 1.0 MeV electron dose of $1 \times 10^{17} \text{ cm}^{-2}$.

AFIT/DS/ENP/05-01

Dedicated to the living Word (John 1:1-18), in whom I have life and hope.

Acknowledgments

As might be expected, this dissertation is the culmination of the most comprehensive technical research I have ever conducted. The experience has given me a better understanding of how many people contribute to the success of such an effort, and I wish to briefly acknowledge some of the people who made this particular dissertation work a success.

Prof. Yung Kee Yeo, my advisor, kept me going in the right direction and gave me every resource that I needed to accomplish the experimental work. Throughout the entire program he demonstrated an unwavering commitment to my professional development and successful degree completion.

Dr. Mohammed Ahoujja, from the University of Dayton, gave me laboratory training and worked closely with me during analysis of the Hall-effect and DLTS data. He provided encouragement and guidance during some critical times when experimental difficulties seemed intractable.

Dr. James Petrosky was an outstanding class instructor who gave me a solid background in radiation effects physics. He initiated and maintained the agreement with Wright State University that made it possible for me to use the electron accelerator, and he supplied, among other resources, one of the test materials used in this research. His help was made possible by funding from DTRA/CS.

LtCol James Lott took extra time to give me what proved to be valuable advice at the outset of this research. His thorough review of the dissertation manuscript resulted in many helpful changes that will benefit the reader.

Dr. Mee-Yi Ryu assisted me in many ways throughout the research effort. She spent a great deal of time giving me training in nearly every area of the AFIT clean room and semiconductor characterization laboratories.

The Wright State University researchers Dr. David Look, Dr. Gary Farlow, and Mr. Zhaoqiang Fang were invaluable to the success of this dissertation research. The designs and analyses of my experiments were strongly influenced by their groundbreaking work with gallium nitride. They graciously provided expert advice on many occasions.

Mr. Larry Callaghan, Mr. Bill Siskaninetz and Mr. Tim Cooper from AFRL/MLPS and AFRL/SNDD lent their skills and equipment at various times when equipment became unavailable at AFIT. Also, Dr. Joe Van Nostrand of AFRL/MLPS provided one of the test materials used in this research.

I would not have had the necessary diligence to complete this work were it not for the loving support and encouragement of my dear wife, Lori. Additionally, our parents encouraged us both at so many critical times, and our local church family helped us to maintain perspective and joy throughout the process.

To each person mentioned above, I wish to express my sincere gratitude for what you gave to help me reach this important professional milestone.

Table of Contents

	Page
Abstract.....	iv
Dedication.....	vii
Acknowledgments.....	viii
Table of Contents.....	x
List of Figures.....	xii
List of Tables	xviii
I. Introduction	1
II. Background	6
2.1 Physics of Semiconductor Devices.....	6
2.1.1 Semiconductor Properties	6
2.1.2 Metal-Semiconductor Contacts.....	12
2.2 Properties of $\text{Al}_x\text{Ga}_{1-x}\text{N}$ Material and Devices	19
2.3 Defect Characteristics	26
2.4 Radiation Damage Mechanisms	33
2.4.1 Interactions.....	33
2.4.2 Carrier Removal.....	38
2.4.3 Carrier Trapping, Generation, and Recombination.....	42
2.4.4 Mobility Degradation.....	46
2.4.5 Luminescence Degradation.....	46
2.5 Radiation Effects on $\text{Al}_x\text{Ga}_{1-x}\text{N}$ Devices	48
2.5.1 SBD Response	48
2.5.2 HEMT Response.....	49
III. Experimental Procedures	51
3.1 Sample Selection and Preparation	51
3.2 Irradiation Procedures.....	57
3.3 Deep Level Transient Spectroscopy (DLTS).....	59
3.4 Hall Effect Measurements.....	63

3.4.1 Room Temperature Hall Effect Measurements	63
3.4.2 Temperature Dependent Hall Effect Measurements	67
3.5 Cathodoluminescence	68
IV. Analytical Procedures	71
4.1 Deep Level Transient Spectroscopy (DLTS)	71
4.1.1 Capacitance Transient Analysis	71
4.1.2 Trap Concentration	73
4.1.3 Pulse Width Dependence	74
4.1.4 Field Dependence	78
4.2 Temperature Dependent Hall Effect Measurements	79
V. Experimental Results and Analysis	82
5.1 Deep Level Transient Spectroscopy (DLTS)	82
5.1.1 Unirradiated GaN (wafer A2)	82
5.1.2 Irradiated GaN (Wafer A2)	95
5.1.3 Unirradiated Al _{0.14} Ga _{0.86} N (Wafer B2)	103
5.1.4 Irradiated Al _{0.14} Ga _{0.86} N (Wafer B2)	109
5.1.5 Unirradiated Al _{0.20} Ga _{0.80} N (Wafer C1)	116
5.1.6 Irradiated Al _{0.20} Ga _{0.80} N (Wafer C1)	118
5.1.7 Unirradiated Al _{0.30} Ga _{0.70} N (Wafer D1)	121
5.1.8 Irradiated Al _{0.30} Ga _{0.70} N (Wafer D1)	125
5.1.9 DLTS Analysis	127
5.2 Hall Effect Measurements	135
5.3 Cathodoluminescence	149
VI. Conclusions and Recommendations	162
6.1 Conclusions	162
6.2 Recommendations	164
Appendix: C-V and I-V Measurements	165
Bibliography	177

List of Figures

Figure	Page
II-1. Various radiative transitions observed in semiconductor luminescence spectra.	11
II-2. (a) Energy band diagram of an isolated metal adjacent to an isolated n-type semiconductor. (b) Energy band diagram of a metal-semiconductor contact in thermal equilibrium (after Sze [16]).	13
II-3. Diagram of a Schottky Barrier Diode (SBD).....	17
II-4. Schottky barrier diode under a) no bias; b) forward bias; and c) reverse bias.....	18
II-5. Atomic locations for wurtzite crystal structure of GaN. The graph on the left illustrates the orientation of the (0001) direction, with Ga represented by black and N by white balls. The graph on the right is presented looking down the (000 $\bar{1}$) direction for a Ga face surface [40].	20
II-7. Calculated room temperature band gap energy of $\text{Al}_x\text{Ga}_{1-x}\text{N}$ versus aluminum mole fraction for different bowing parameters.	24
II-8. Calculated band gap energy of $\text{Al}_x\text{Ga}_{1-x}\text{N}$ versus aluminum mole fraction at three different temperatures. A bowing parameter of $b=0.35$ is assumed.	24
II-9. Schematic of an AlGaN/GaN HEMT.	25
II-10. Calculated displacement introduction rates in GaN and $\text{Al}_{0.30}\text{Ga}_{0.70}\text{N}$ for a range of assumed displacement energies (E_d) based on the displacement cross section given by equation II-30.	37
III-1. Measured CL peak energies (black squares) of $\text{Al}_x\text{Ga}_{1-x}\text{N}$ samples versus x. The CL measurements are performed at $T = 6$ K.	55
III-2. Schematic diagram of DLTS system used in this study. The Keithly 237 SMU is used for I-V measurements (after Scofield [72])	60
III-3. Applied voltage pulses and corresponding capacitance transients in the DLTS measurement procedure.	62
III-4. Schematic of Temperature Dependent Hall measurement system.	64
III-5. Illustration of Hall effect in planar sample with Van der Pauw contact geometry [15].	65
III-6. Schematic of cathodoluminescence system [84].	69

IV-1. Illustration of how a rate window peak is obtained from temperature dependent capacitance transients (after Lang [85]).	72
IV-2. Energy band diagram of a Schottky barrier diode and single trap level: a) before; b) during; and c) after forward bias voltage pulse.	75
IV-3. Energy band illustration of trapping at dislocation-related point defects. The situation for small occupation numbers ($N(t) \ll N_T$) resembles that for isolated point defects (after Omling <i>et al.</i> [69]).	77
IV-4. Potential barrier and emission processes a) for a charged (donor-type) electron trap and b) for a neutral (acceptor-type) electron trap (after Ganichev [73]).	79
V-1. DLTS spectrum of unirradiated GaN (sample A2-4b). Trap labels are assigned based on similarity to previously reported traps. The Arrhenius plots of peaks A, B, C, and D are shown in the inset.	83
V-2. DLTS spectrum of unirradiated GaN (sample A2-4b) at different filling pulse widths. The trap C dominates at large pulse width in this temperature scan, but it greatly diminished in a subsequent temperature scan. The inset shows various rate windows for $t_p = 10^{-2}$ s, illustrating that trap C is only dominant for large rate windows.	87
V-3. DLTS spectrum of unirradiated GaN (sample A2-4b) produced by two consecutive temperature scans.	88
V-4. Double correlated DLTS spectra of unirradiated GaN (sample A2-4b). The four pulsing conditions isolate four sections of the $V_r = 0$ to -4 V depletion region. The summation of these four different signals (solid dark gray line) closely matches the signal obtained with the pulsing conditions $V_f = 0$, $V_r = -4$ V (dashed light gray line).	89
V-5. Double correlated DLTS spectra of peak D in unirradiated GaN (sample A2-4b).	90
V-6. Arrhenius plots corresponding to the low temperature peaks shown in figure V-5. Inset are the activation energies plotted against the square root of the mean field strength. The error bars represent the standard errors determined from data variance.	92
V-7. Double correlated DLTS spectrum of peak A in unirradiated GaN (sample A2-4b).	93
V-8. Peak heights of four traps versus filling pulse width in GaN (sample A2-4b). The 47 s^{-1} rate window was used for this comparison.	94
V-9. DLTS spectra of GaN (sample A2-4a) irradiated at two consecutive 1.0 MeV electron doses. Unirradiated GaN (sample A2-4b) is overlaid for comparison.	96
V-10. Capacitance versus temperature for GaN (sample A2-4a) before and after two consecutive 1.0 MeV electron irradiations.	97

V-11. C-V curves at various temperatures for 1.0 MeV electron irradiated GaN (sample A2-4a).	98
V-12. C-V curve of 1.0 MeV electron irradiated GaN (sample A2-4a), showing the effect of carrier freeze-out at this temperature. The normal C-V curve from unirradiated GaN (sample A2-4b) is overlaid for comparison.	99
V-13. Double correlated DLTS spectra of peaks D and E in irradiated GaN (sample A2-5a). The rate window is 610 s^{-1}	100
V-14. Double correlated DLTS spectra of peaks D and E in irradiated GaN (sample A2-5a) showing the effect of field strength in the spatial region defined by forward pulse pair $V_{f1} = 0 \text{ V}$ and $V_{f2} = -1 \text{ V}$. The rate window is 610 s^{-1}	101
V-15. DLTS spectra of peaks D and E in irradiated GaN (sample A2-5a) before and after annealing at $350 \text{ }^{\circ}\text{C}$ for 15 minutes. The rate window is 610 s^{-1}	102
V-16. DLTS spectrum of pre-irradiated $\text{Al}_{0.14}\text{Ga}_{0.86}\text{N}$ (sample B2-21d). The Arrhenius plots of the two peaks are shown in the inset.	104
V-17. Electric field dependence of electron trap P1 activation energy in $\text{Al}_{0.14}\text{Ga}_{0.86}\text{N}$ (sample B2-8b). DDLTS signals are measured in the spatial region defined by the forward voltage pulse pair $V_{f1} = -1$ and $V_{f2} = -2 \text{ V}$, with field increase provided by increasing reverse bias V_r . Error bars apply to random sources of error in these comparative measurements. Inset shows 47s^{-1} peak positions when field strength is raised nearly one order of magnitude. No peak temperature shift is observed.	106
V-18. DLTS spectrum of unirradiated $\text{Al}_{0.14}\text{Ga}_{0.86}\text{N}$ (sample B2-21d) at various pulse widths. The peak heights of P1 and P2 are plotted versus filling pulse width in the inset.	107
V-19. Normalized peak height of electron trap P1 versus reverse bias voltage.	108
V-20. DLTS spectrum of 1.0 MeV electron irradiated $\text{Al}_{0.14}\text{Ga}_{0.86}\text{N}$ (sample B2-21b) at short ($20 \text{ }\mu\text{s}$) and long (0.1 s) pulse width.	110
V-21. DLTS spectrum of 1.0 MeV electron irradiated $\text{Al}_{0.14}\text{Ga}_{0.86}\text{N}$ (sample B2-21b) at $20 \text{ }\mu\text{s}$ pulse width. Inset is the Arrhenius plot constructed from visible peak positions. Open circles are measured data. Dotted lines are the individual peaks modeled using equations IV-4 to IV-6. Dashed line is spectrum from the pre-irradiated data. The solid line is the sum of all the peaks.	111
V-22. DLTS spectrum of 1.0 MeV electron irradiated $\text{Al}_{0.14}\text{Ga}_{0.86}\text{N}$ (sample B2-21b) before and after annealing. The dashed and dotted lines represent the spectrum after cycling up to 430 and 450 K, respectively.	114

V-23. DLTS spectrum of 0.62 MeV electron irradiated $\text{Al}_{0.14}\text{Ga}_{0.86}\text{N}$ (sample B2-21d) before and after 350 °C annealing. The spectrum of unirradiated $\text{Al}_{0.14}\text{Ga}_{0.86}\text{N}$ (sample B2-21d) is overlaid (dotted line).....	115
V-24. DLTS spectrum of unirradiated $\text{Al}_{0.20}\text{Ga}_{0.80}\text{N}$ (sample C1-38c). The Arrhenius plots of the two peaks are shown in the inset.....	117
V-25. DLTS spectrum of 1.0 MeV electron irradiated $\text{Al}_{0.20}\text{Ga}_{0.80}\text{N}$ (sample C1-38a) before and after 350 °C annealing. The spectrum of unirradiated $\text{Al}_{0.20}\text{Ga}_{0.80}\text{N}$ (sample C1-38c) is overlaid (dotted line).	119
V-26. DLTS spectrum of 1.0 MeV electron irradiated $\text{Al}_{0.20}\text{Ga}_{0.80}\text{N}$ (sample C1-40b) before and after 400 °C annealing.	120
V-27. DLTS spectrum of unirradiated sample D1-38c ($\text{Al}_{0.30}\text{Ga}_{0.70}\text{N}$). The Arrhenius plot of peaks P0 and P1 are shown in the inset.....	122
V-28. DLTS spectra of unirradiated $\text{Al}_{0.30}\text{Ga}_{0.70}\text{N}$ (sample D1-38c) at four different reverse bias voltages. Inset is the normalized peak P0 for each of the traces, showing that the peak shape is unchanged with reverse bias voltage.	123
V-29. Normalized peak height of electron trap P0 in $\text{Al}_{0.30}\text{Ga}_{0.70}\text{N}$ versus reverse bias voltage.....	124
V-30. DLTS spectra of $\text{Al}_{0.30}\text{Ga}_{0.70}\text{N}$ (sample D1-38c) before and after 0.62 MeV electron irradiation.	126
V-31. DLTS spectra of unirradiated $\text{Al}_x\text{Ga}_{1-x}\text{N}$ for $x=0$, $x=0.14$, $x=0.20$, and $x=0.30$	128
V-32. DLTS spectra of $\text{Al}_x\text{Ga}_{1-x}\text{N}$ ($x=0.14$ and $x=0.20$) before and after 1.0 MeV electron irradiation.	129
V-33. Measured electron trap energy versus aluminum mole fraction for traps labeled R2, R3, R4, D, P0, and P1 in this study. The dotted lines represents a possible extension to GaN trap D with decrease in aluminum mole fraction.	131
V-34. Measured electron trap energy versus band gap energy for traps labeled R2, R3, R4, D, P0, and P1 in this study. The dotted line represents a possible extension to GaN trap D with decrease in band gap energy.	132
V-35. Arrhenius plots of all $\text{Al}_x\text{Ga}_{1-x}\text{N}$ traps characterized in this study.	134
V-36. Dose-averaged carrier removal versus initial room temperature carrier concentration in $\text{Al}_x\text{Ga}_{1-x}\text{N}$	136
V-37. Temperature dependent Hall data for GaN (sample A2-1) before and after 1.0 MeV electron irradiation. Model (lines) are for a two donor fit with ($N_{D1}=1.9 \times 10^{17}$, $E_{D1}=17$ meV, $N_{D2}=7.5 \times 10^{16}$, $E_{D2}=60$ meV, $N_A=2.3 \times 10^{16}$) and ($N_{D1}=1.64 \times 10^{17}$, $E_{D1}=19$	

meV, $N_{D2}=1.55 \times 10^{17}$, $E_{D2}=59$ meV, $N_A=8.7 \times 10^{16}$) for the unirradiated and irradiated data respectively.	137
V-38. Carrier concentration versus inverse temperature of unirradiated $Al_{0.14}Ga_{0.86}N$ (sample B2-16) before and after correction for a secondary conduction layer. The corresponding mobility plots are shown in the inset.	140
V-39. Carrier concentration versus inverse temperature of unirradiated $Al_{0.30}Ga_{0.70}N$ (sample D2-7) before and after correction for a secondary conduction layer. The corresponding mobility plots are shown in the inset.	141
V-40. Temperature dependent carrier concentration of $Al_{0.20}Ga_{0.80}N$ (sample C1-9) before and after 1.0 MeV electron irradiation at two consecutive doses.	142
V-41. Temperature dependent carrier concentration of $Al_{0.20}Ga_{0.80}N$ (sample C2-2) before and after 1.0 MeV electron irradiation.	143
V-42. Temperature dependent carrier concentration of $Al_{0.30}Ga_{0.70}N$ (sample D2-7) before and after 1.0 MeV electron irradiation.	144
V-43. Sheet carrier concentration versus temperature in $Al_{0.27}Ga_{0.73}N/GaN$ single heterostructure (sample E1-3) before and after 1.0 MeV electron irradiation.	146
V-44. Hall Mobility versus temperature in $Al_{0.27}Ga_{0.73}N/GaN$ single heterostructure (sample E1-3) before and after 1.0 MeV electron irradiation.	147
V-45. Sheet resistivity versus temperature in $Al_{0.27}Ga_{0.73}N/GaN$ single heterostructure (sample E1-3) before and after 1.0 MeV electron irradiation.	148
V-46. Normalized CL spectra of unirradiated $Al_xGa_{1-x}N$ for $x = 0, 0.14, 0.20$, and 0.30	150
V-47. Normalized CL spectra of $Al_xGa_{1-x}N$ ($x=0.0$ and $x=0.2$) before and after 1.0-MeV electron irradiation with a fluence of $1.1 \times 10^{17} \text{ cm}^{-2}$	151
V-48. Normalized luminescence intensity in $Al_xGa_{1-x}N$ irradiated at two consecutive 1.0 MeV electron doses with 2×10^{16} and $1.1 \times 10^{17} \text{ e}^- \text{ cm}^{-2}$	153
V-49. Normalized luminescence intensity in $Al_xGa_{1-x}N$ irradiated at two consecutive 1.0 MeV electron doses with 2×10^{16} and $1.1 \times 10^{17} \text{ e}^- \text{ cm}^{-2}$. Data are produced from the average of four samples ($x=0.0$ to 0.20). The reported degradation of an electron irradiated InGaN LED [53] is overlaid for comparison.	154
V-50. CL spectrum of GaN (sample A1-16) before and after 1.0 MeV electron irradiation with a fluence of $1.1 \times 10^{17} \text{ cm}^{-2}$	155
V-51. CL spectrum of GaN (sample A2-1) before and after 1.0 MeV electron irradiation with a fluence of $1.1 \times 10^{17} \text{ cm}^{-2}$	156

V-52. CL spectrum of $\text{Al}_{0.14}\text{Ga}_{0.86}\text{N}$ (sample B2-39) before and after 1.0 MeV electron irradiation with a fluence of $1.1 \times 10^{17} \text{ cm}^{-2}$.	157
V-53. CL spectrum of $\text{Al}_{0.20}\text{Ga}_{0.80}\text{N}$ (sample C1-9) before and after 1.0 MeV electron irradiation with a fluence of $1.1 \times 10^{17} \text{ cm}^{-2}$.	158
V-54. CL spectrum of $\text{Al}_{0.20}\text{Ga}_{0.80}\text{N}$ (sample C2-2) before and after 1.0 MeV electron irradiation with a fluence of $1.1 \times 10^{17} \text{ cm}^{-2}$.	159
V-55. CL spectrum of $\text{Al}_{0.20}\text{Ga}_{0.80}\text{N}$ (sample D2-7) before and after 1.0 MeV electron irradiation with a fluence of $9 \times 10^{16} \text{ cm}^{-2}$.	160
V-56. CL spectrum of GaAs (sample F1-8) before and after 1.0 MeV electron irradiation with a fluence of $9 \times 10^{16} \text{ cm}^{-2}$.	161
A-1. Plot of $1/C^2$ versus applied bias for unirradiated GaN (sample A2-4b) at $T=290 \text{ K}$. Inset is the extrapolated carrier concentration versus depletion depth.	166
A-2. Plot of $1/C^2$ versus applied bias for unirradiated GaN (sample A2-4b) at $T=150 \text{ K}$. Inset is the extrapolated carrier concentration versus depletion depth.	167
A-3. C-V curves at various temperatures for unirradiated GaN (sample A2-4b).	168
A-4. I-V curves at various temperatures for unirradiated GaN (sample A2-4b).	169
A-5. Plot of $1/C^2$ versus applied bias for irradiated GaN (sample A2-5a) at $T = 150 \text{ K}$. Inset is the extrapolated carrier concentration versus depletion depth.	170
A-6. Plot of $1/C^2$ versus applied bias for irradiated GaN (sample A2-5a) at $T = 110 \text{ K}$. Inset is the extrapolated carrier concentration versus depletion depth.	171
A-7. I-V curves at various temperatures for 1.0 MeV electron irradiated GaN (sample A2-4a).	172
A-8. Plot of $1/C^2$ versus applied bias for unirradiated $\text{Al}_{0.14}\text{Ga}_{0.86}\text{N}$ (sample B2-21d) at $T=294 \text{ K}$. Inset is the extrapolated carrier concentration versus depletion depth.	173
A-9. Plot of $1/C^2$ versus applied bias for unirradiated $\text{Al}_{0.14}\text{Ga}_{0.86}\text{N}$ (sample B2-21d) at $T = 240 \text{ K}$. Inset is the extrapolated carrier concentration versus depletion depth.	174
A-10. Capacitance versus temperature in $\text{Al}_{0.14}\text{Ga}_{0.86}\text{N}$ (sample B2-21b) following 1.0 MeV electron irradiation.	175
A-11. I-V curves of irradiated $\text{Al}_{0.20}\text{Ga}_{0.80}\text{N}$ (sample C1-38a) before and after annealing at $350 \text{ }^\circ\text{C}$ for 15 min.	176

List of Tables

Table	Page
II-1. Selected physical properties of GaN and AlN at T = 300 K (from [20] and references contained therein).	22
II-2. Reported defect energy levels in GaN.	30
II-3. Reported defect energy levels in $\text{Al}_x\text{Ga}_{1-x}\text{N}$ ($x < 0.5$)	31
II-4. Maximum energy transferred to AlGaIn atomic constituents for given incident electron energies.	35
III-1. Wafer properties and designations.	54
III-2. Irradiation parameters.....	59
V-1. Measured DLTS trap parameters in GaN and references to similar reports.....	84
V-2. Measured defect parameters in 1.0-MeV electron irradiated $\text{Al}_{0.14}\text{Ga}_{0.86}\text{N}$ and references to similar reports.....	112
V-3. Measured defect parameters in 1.0-MeV electron irradiated $\text{Al}_{0.20}\text{Ga}_{0.80}\text{N}$ and references to similar reports.....	118
V-4. Measured defect parameters in unirradiated $\text{Al}_{0.30}\text{Ga}_{0.70}\text{N}$ and references to similar reports.	125

DEEP LEVEL DEFECTS IN ELECTRON-IRRADIATED ALUMINUM GALLIUM NITRIDE GROWN BY MOLECULAR BEAM EPITAXY

I. Introduction

Throughout the last decade, GaN and related III-nitride alloys have emerged as the leading materials for many optoelectronic devices operating in the blue to ultra-violet (UV) spectrum. More recently, GaN-based electronic devices, such as AlGaN/GaN high electron mobility transistors (HEMTs), have received much attention for their superior high-power, high-frequency performance characteristics [1, 2]. The GaN and AlGaN device technologies are still immature relative to those of GaAs and AlGaAs, but a great deal of scientific and engineering effort has been focused on the advancement of the GaN-based device technologies. The last five years have witnessed a steep increase in the number of defect studies involving thin epitaxial films of $\text{Al}_x\text{Ga}_{1-x}\text{N}$, particularly epitaxial GaN ($x = 0$). These studies have been driven by several different technological challenges. One pressing challenge has been to reduce the concentration of interface-related defects such as dislocations and stacking faults [3]. These can generally be attributed to the large lattice mismatch and difference in thermal expansion coefficient between $\text{Al}_x\text{Ga}_{1-x}\text{N}$ and available substrates such as Al_2O_3 and SiC. Another pressing challenge is to achieve efficient p-type doping. For example, as-grown native defects create problems by compensating the impurity dopant. Even after these fundamental growth problems have been solved, optimization of device performance requires characterization of the remaining defects that have energy levels in the band gap. Radiation-induced defects must be well characterized to ensure reliable device operation

in a space or nuclear environment. Processing steps, such as electrical isolation via high-energy ion bombardment [4, 5, 6] and dopant activation via low-energy electron irradiation [7] can also be improved when the relevant defect characteristics are understood.

Native defects have been studied extensively for epitaxially grown GaN ($x = 0$), and some useful conclusions have been drawn. For example, as-grown undoped GaN always has a net background concentration (typically $10^{16} - 10^{19} \text{ cm}^{-3}$, depending on the growth technique) of uncompensated shallow donors. For three decades, this was attributed to the nitrogen vacancy, V_N , until the mid-1990's when first-principles theoretical calculations indicated that the formation energy for a V_N is too high to occur so readily during growth [8, 9, 10]. To date, the experimental consensus is that the dominant residual shallow donors are, in most cases, oxygen or silicon impurities, or both [8, 9, 10]. Furthermore, theoretical studies have explained why native donor defects are more readily formed as GaN material is made more p-type, and why native acceptor defects are more readily formed as GaN material is made more n-type. That is, the most likely mechanisms responsible for the efficient self-compensation observed in GaN are now well understood [8]. Although there are still fundamental questions that remain unanswered, much has also been reported recently about radiation-induced defects in GaN. There exists, for example, some consensus about the primary radiation-induced defect energy levels in GaN. However, no such consensus exists for AlGaN [11], because only a couple of experimental results are available for irradiated AlGaN. In fact, a clear picture has still not emerged regarding the dominant as-grown defects in AlGaN because DLTS measurements have not been reported for varying aluminum mole

fractions. Specifically, it is unclear how any given deep defect level in GaN would change with aluminum mole fraction in AlGaN. Consequently, the understanding of performance-limiting radiation effects in AlGaN electronic devices is usually based on hypothesized defect energy levels that have yet to be verified [12]. Additionally, there is a lack of dose-dependent data on carrier concentration n and mobility μ in AlGaN. Of particular motivation to this dissertation research is the fact that no single study has correlated measurements of radiation-induced carrier removal with aluminum mole fraction and silicon dopant concentration. These and other such gaps in knowledge are compounded by the different growth techniques in common use. GaN and AlGaN layers grown by vapor phase epitaxy (VPE) techniques such as metal-organic vapor phase epitaxy (MOVPE) and hydride vapor phase epitaxy (HVPE) have received the most comprehensive treatment to date. Epitaxial layers of $\text{Al}_x\text{Ga}_{1-x}\text{N}$ grown by MBE generally contain fewer impurities and more dislocation-related defects. These different initial conditions for the thin films on substrates may affect the radiation response of the material, and thus there exists the need for a comprehensive study of radiation effects in MBE-grown $\text{Al}_x\text{Ga}_{1-x}\text{N}$.

In this dissertation research, the electrical and optical properties of high energy electron-irradiated $n\text{-Al}_x\text{Ga}_{1-x}\text{N}$ epitaxial films are characterized for aluminum mole fractions from $x = 0.0$ to 0.3 using deep level transient spectroscopy (DLTS), temperature-dependent Hall, and cathodoluminescence (CL) measurements, and the results are compared with those of the as-grown $n\text{-Al}_x\text{Ga}_{1-x}\text{N}$. The main purpose of the DLTS measurements was to obtain accurate DLTS signatures (total activation energies and capture cross-sections) of as-grown and radiation-induced electron traps. Hall effect

measurements were performed in order to characterize room temperature carrier removal due to 1.0 MeV electron radiation. Additionally, the temperature dependent carrier concentration was fit with a simple theoretical model in order to extract radiation-induced defect concentrations and activation energies. The CL characterization was performed before irradiation and after each of two consecutive 1.0 MeV electron radiation. The scope of the CL analysis was limited to looking for significant radiation-induced spectral variation and quantifying the radiation-induced degradation of the dominant luminescence peaks.

This dissertation research resulted in the first observation and characterization of the main radiation-induced electron traps in AlGa_N. Also, the energy levels of radiation-induced and as-grown electron traps were correlated with aluminum mole fraction for the first time. Furthermore, the degradation of carrier concentration and luminescence intensity in AlGa_N was correlated with aluminum mole fraction and initial carrier concentration for the first time. The new findings enable detailed modeling that can be used to engineer radiation-hardened device designs. The findings also validate some previous speculations and invalidate others about radiation effects in AlGa_N compared to Ga_N.

The following chapters begin by introducing semiconductor device physics and Al_xGa_{1-x}N properties relevant to this dissertation research. Then, the necessary background of defect properties and radiation effects is presented with review of related Al_xGa_{1-x}N literature. The experimental and analytical procedures used to obtain the data in this dissertation research are presented next. Then, the experimental results are

presented and discussed. Finally, the major conclusions resulting from this dissertation research and recommendations for future research are presented.

II. Background

2.1 Physics of Semiconductor Devices

2.1.1 Semiconductor Properties

In a crystalline material, the quantum mechanical interaction of conduction electrons with the periodic potential of the host atoms gives rise to allowed energy bands in which the electrons may exist. For semiconductors, this phenomenon gives rise to the existence of an energy gap between the band of electrons tightly bound in atomic orbitals (valence band) and the energy band of electrons that can move freely throughout the crystal (conduction band). The valence band is normally filled and the conduction band is normally empty with the exception of a small percentage of electrons that are thermally excited from the valence band to the conduction band. This concentration is given as

$$n = N_C \exp\left(\frac{-(E_C - E_f)}{kT}\right). \quad \text{II-1}$$

In this expression, E_C is the energy at the conduction band minimum, E_f is the Fermi energy, and N_C is the conduction band density of states given by

$$N_C = 2M_C \left(\frac{2\pi \cdot m^* kT}{h^2} \right)^{3/2}, \quad \text{II-2}$$

where M_C is the number of equivalent conduction band minima, and m^* is the electron effective mass. Because the electrons in the conduction band are thermally excited from the otherwise full valence band, the intrinsic concentration of holes is equal to the intrinsic concentration of electrons given by equation II-1. Holes have charge $+e$ ($e = 1.6022 \times 10^{-19}$ Coulombs) and can move freely throughout the valence band. The Fermi

energy of an intrinsic semiconductor is located near the middle of the energy band gap, E_g . Many commonly used semiconductors have E_g on the order of 1 eV, and in these semiconductors the intrinsic carrier concentration at room temperature ($kT \approx 0.026$ eV) is many orders of magnitude less than N_C . For many applications, the intrinsic carrier concentration is too low and thus extrinsically raising the concentration of conduction band electrons or valence band holes via doping is desirable. In fact, extrinsic doping takes place to some degree in all semiconductors due to unintentional impurities and defects in the crystal lattice. A donor level is introduced when an impurity dopant has one more valence electron than the atom that it replaces in the crystal lattice, and an acceptor level is introduced when the impurity dopant has one less valence electron than the atom that it replaces in the crystal lattice. Defects in the crystal lattice can also introduce centers in the band gap that behave as donors or acceptors. A donor transition involving one of these centers is said to occur when a neutral center loses an electron, or when a positively charged center gains or loses an electron [13:109]. An acceptor transition is said to occur when a neutral center gains an electron or a negatively charged center gains or loses an electron [13:109]. Usually the term “level” is used to indicate the energy of a particular transition [13:109]. The occupation of a donor (acceptor) level is determined by the electron distribution function as

$$f(E_{D(A)}, T) = \frac{1}{1 + \frac{g_o}{g_l} \exp\left(\frac{E_{D(A)} - E_f}{kT}\right)}, \quad \text{II-3}$$

where $E_{D(A)}$ is the donor (acceptor) energy with respect to the conduction band minimum (valence band maximum), and the constant (g_o/g_l) accounts for the degeneracy of the level with (g_l) and without (g_o) the trapped electron. The appropriate value for g_o/g_l is

often 1/2 for donor levels and 4 for acceptor levels [13:108]. With a donor concentration, N_D , the concentration of donor electrons thermally excited to the conduction band is

$$n = N_D(1 - f(E_D, T)). \quad \text{II-4}$$

In the presence of other discrete energy levels in the band gap, an analogous expression may be determined from the charge neutrality condition expressed as [13]

$$n + \sum_k N_{Ak}^- = p + \sum_m N_{Dm}^+. \quad \text{II-5}$$

This expression simply states that at thermodynamic equilibrium, the sum of conduction band electrons and ionized acceptors at k different levels must be equal to the sum of valence band holes and ionized donors at m different levels. In extrinsic semiconductors, either n or p in equation II-5 will become vanishingly small, with the remaining carrier concentration dictating whether the semiconductor is n-type or p-type. Considering n-type material, for which the hole concentration is vanishingly small, equation II-5 may be written as

$$n = \sum_m N_{Dm}^+ - \sum_k N_{Ak}^-. \quad \text{II-6}$$

In order for a semiconductor to conduct electricity, it must possess partially filled electron energy bands and the carriers must have a net direction of motion [14]. The first condition requires thermal ionization processes that place electrons in the conduction band or holes in the valence band as discussed above. The second condition requires the action of an electric field or the existence of a carrier concentration gradient in the material. In the presence of an electric field, \vec{E} , the coulombic force, $\vec{F} = q\vec{E}$, causes holes ($q = +e$) to accelerate in the direction of the field and electrons ($q = -e$) to accelerate in the direction opposite the field. This acceleration is interrupted by various

temperature-dependent scattering mechanisms in the semiconductor material. There exists a mean time, τ , between these scattering events called the momentum relaxation time because it determines the average velocity of carriers under the influence of a given electric field. Using the notation pertaining to electron conduction alone, this relationship between the average electron velocity (called drift velocity) and electric field is given as

$$\vec{v}_n = \frac{e\tau_n}{m^*} \vec{E} = -\mu_n \vec{E}, \quad \text{II-7}$$

where $\mu_n = e\tau_n/m^*$ is the electron mobility. This mobility is related to electron current density by the expression

$$\vec{J}_{drift}^n = ne\mu_n \vec{E}. \quad \text{II-8}$$

The total drift current density due to electron and hole conduction is given by the sum of electron and hole current densities as

$$\vec{J}_{drift} = e(n\mu_n + p\mu_p) \vec{E} = \sigma \vec{E}, \quad \text{II-9}$$

where $\sigma = e(n\mu_n + p\mu_p)$ is defined as the conductivity of the given material. The same carrier mobilities are also important to diffusion currents that result from carrier concentration gradients. Due to random motion of carriers alone, there will be a net movement of carriers from regions of high density to regions of low density, reflected by a net current density. The diffusion current due to electrons is expressed as

$$\vec{J}_{diff}^e = \mu_n kT \vec{\nabla} n = eD_n \vec{\nabla} n, \quad \text{II-10}$$

where $D_n = \mu_n kT/e$ is defined as the diffusion coefficient of the given material. If an electric field is present as well as a concentration gradient, the current densities of electron and holes are given by [14].

$$\vec{J}_n = -en\mu_n \vec{E} + eD_n \vec{\nabla} n, \quad \text{II-11}$$

and
$$\vec{J}_p = ep\mu_n \vec{E} - eD_n \vec{\nabla} n. \quad \text{II-12}$$

If conduction by both electrons and holes is present, the total current density is then

$$\vec{J} = \vec{J}_n + \vec{J}_p. \quad \text{II-13}$$

The concepts outlined above lay the groundwork for understanding electrical characterization of semiconductors and electronic devices. The same concepts are also relevant to the characterization of optoelectronic semiconductor devices, as these devices are nearly all based on the creation or annihilation of electron-hole pairs [14]. An electron-hole pair is created when an electron is excited from the valence band to the conduction band. As mentioned above, this excitation can take place spontaneously with enough thermal energy, or it can take place upon interaction with various types of radiation that have energy greater than the band gap. In either case, the excited electron will eventually recombine with the hole and lose its excess energy in the process. This energy loss can be radiative or non-radiative, or it can be a combination of the two. In a radiative recombination, this excess energy is emitted as a photon. In a non-radiative recombination, this excess energy is emitted as a phonon. Radiative recombination is the basis of light emitting devices and luminescence characterization techniques. Figure II-1 shows different ways in which radiative recombination transitions frequently take place. In figure II-1, transition (a) is a band-to-band transition producing a photon of energy

$$\hbar\omega = E_g + kT/2, \quad \text{II-14}$$

where the second term on the right hand side of the equation accounts for the peak in the density distribution of electrons above the conduction band edge [14]. Transition (b) is an excitonic transition, of which there are two types. A free exciton is formed when a

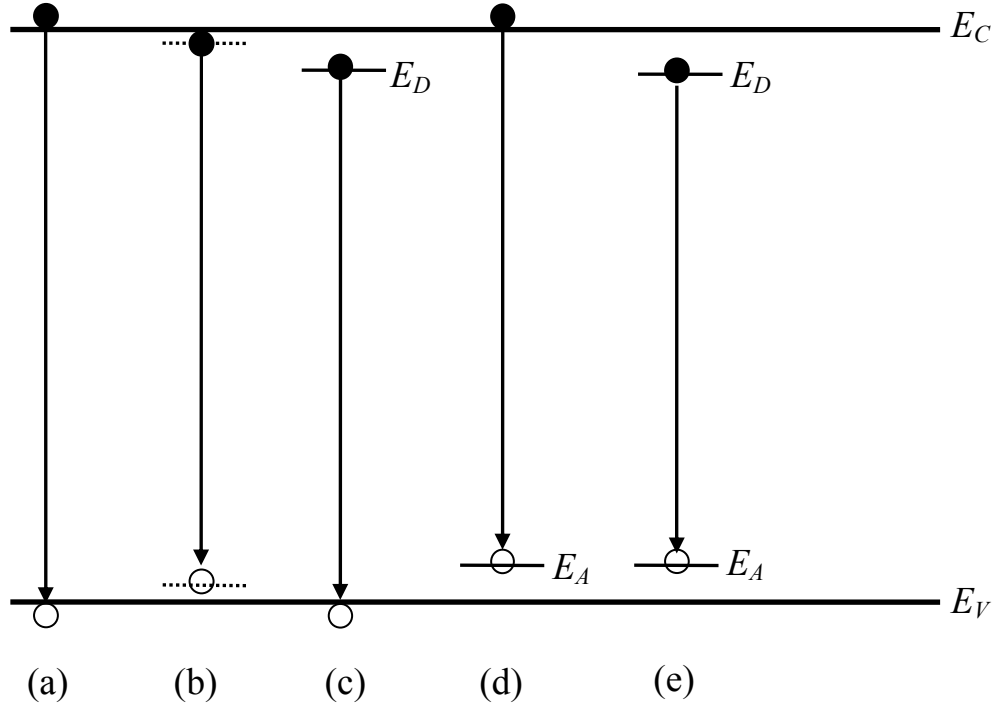


Figure II-1. Various radiative transitions observed in semiconductor luminescence spectra.

conduction band electron and valence band hole are bound by Coulombic attraction. The energy of the electron-hole system is reduced by a small free exciton binding energy.

When the electron and hole recombine, a photon is produced with energy [15]

$$\hbar\omega = E_g - \frac{m_r^* e^4}{2\kappa^2 \hbar^2}, \quad \text{II-15}$$

where $\kappa = 4\pi\epsilon_r\epsilon_0$, m_r^* is the reduced effective mass of the exciton. The exciton thus formed can also form a bound state with a donor or acceptor, and this is referred to as a bound exciton. When a bound exciton recombines, the emitted photon energy is reduced further from that of equation II-15 by an additional small binding energy that is typically $\sim 1/10^{\text{th}}$ the donor or acceptor energy level [14]. Transitions (c) and (d) are

donor/acceptor-band transitions. The energy of the photon emitted from such a transition is given by [15]

$$\hbar\omega = E_g - E_{D(A)} + \frac{1}{2}kT. \quad \text{II-16}$$

Here, $E_{D(A)}$ is the ionization energy corresponding of the donor (acceptor) level.

Transition (e) is a donor acceptor pair (DAP) transition. The photon energy released in a DAP transition is given by [15]

$$\hbar\omega = E_g - E_D - E_A + \frac{e^2}{\kappa r}, \quad \text{II-17}$$

where r is the separation distance of the donor-acceptor pair. Phonons can be emitted in any of the above transitions, and whenever that is the case, the photon energy is reduced by the energy of the phonon(s) involved. In the case of sharp peaks, these phonon replicas can be clearly identified because their energies are shifted down from the fundamental peak by integer multiples of a known phonon energy.

2.1.2 Metal-Semiconductor Contacts

In order to fabricate a useful electronic or optoelectronic semiconductor device, it is necessary to make electrical contact with the semiconductor. This is usually accomplished by depositing metal onto a clean semiconductor surface in a vacuum. Figure II-2(a) shows the energy band diagram of an isolated metal adjacent to an isolated n-type semiconductor having shallow donor concentration N_D . The Fermi level E_f of both the metal and semiconductor are labeled as well as the energy difference between E_f and the vacuum level. This energy difference, called the work function, is labeled $e\phi_m$ for the metal and $e\phi_s$ for the semiconductor. In the case considered here, $\phi_m > \phi_s$. The

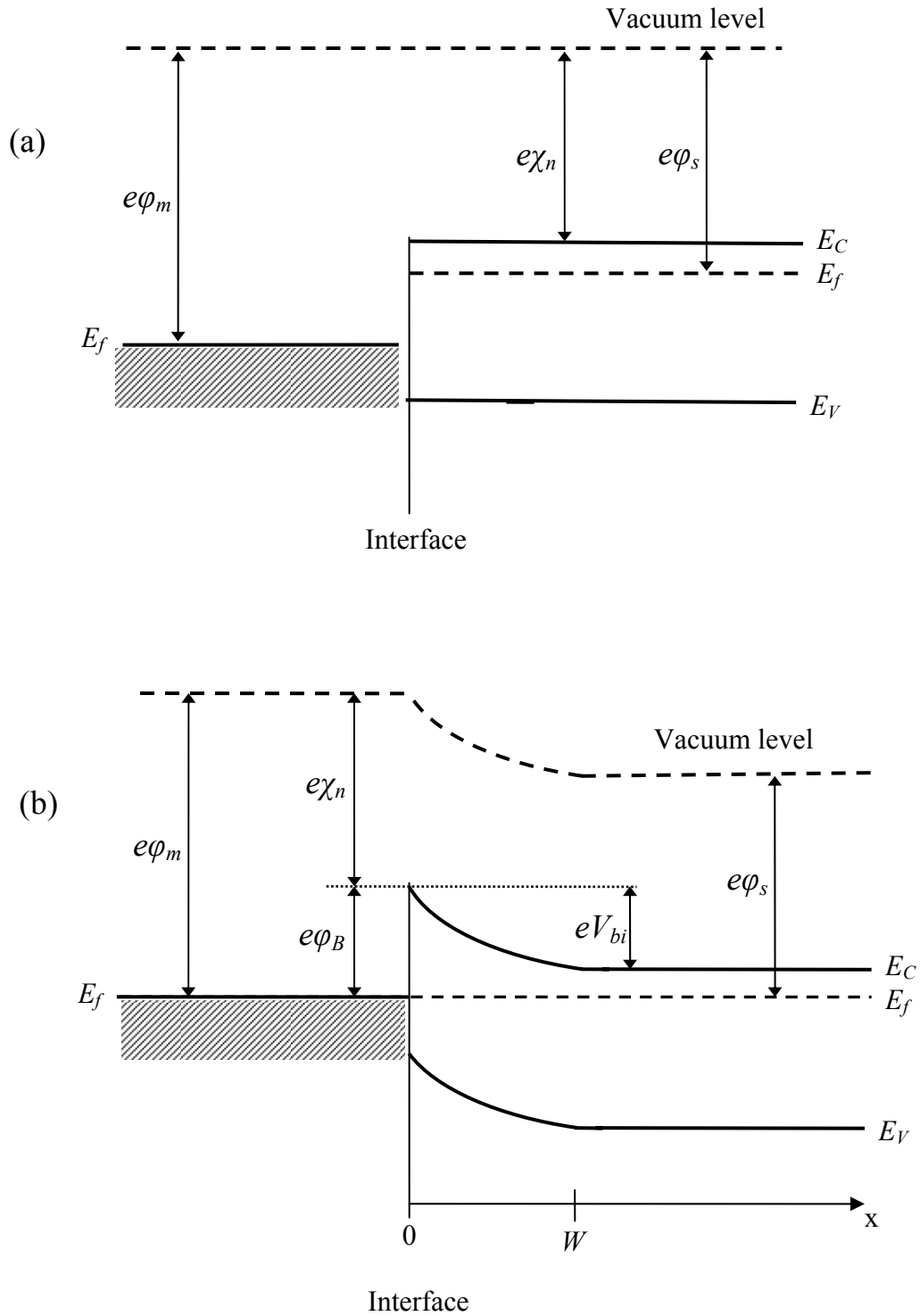


Figure II-2. (a) Energy band diagram of an isolated metal adjacent to an isolated n-type semiconductor. (b) Energy band diagram of a metal-semiconductor contact in thermal equilibrium (after Sze [16]).

energy difference $e\chi_n$ between the conduction band minimum and the vacuum level is called the electron affinity. When the metal comes into contact with the semiconductor as depicted in figure II-2(b), the Fermi levels of the two materials must be equal at thermal equilibrium. The vacuum level must also be continuous. These two requirements dictate that the semiconductor energy bands will bend such that E_C of the semiconductor is eV_{bi} ($= e\phi_s - e\phi_m$) higher at the interface than in the neutral region of the semiconductor [16]. The quantity V_{bi} is referred to as the built-in voltage. The physical process that corresponds to this energy band diagram is diffusion of donor electrons from the semiconductor to the metal. This diffusion process leaves a depletion region of ionized donor atoms which results in an electric field directed from the semiconductor toward the metal. This field opposes the diffusion current of electrons, and the depletion region increases to the depth W required to exactly counteract the diffusion current. Thus, as required by definition, no net current flows across the interface at thermal equilibrium. Applying the depletion approximation that $\rho_s = +eN_D$ for $x < W$ and $\rho_s = 0$ for $x \geq W$, solution of Poisson's equation allows W to be expressed as [16]

$$W = \sqrt{\frac{2\epsilon_s}{eN_D} V_{bi}}, \quad \text{II-18}$$

where $\epsilon_s = \epsilon_r \epsilon_o$ is the static dielectric constant of the semiconductor. If the potential of the neutral semiconductor region can be controlled, the depletion width can be increased or decreased by the application of a bias voltage V across the interface. With the applied bias voltage, the expression for W becomes

$$W = \sqrt{\frac{2\epsilon_s}{eN_D}(V_{bi} - V)}. \quad \text{II-19}$$

The applied bias voltage V in equation II-19 is a positive quantity when the voltage on the metal is made positive with respect to the n-type semiconductor. As mentioned above, the electric field in the depletion region points in the x-direction (figure II-2(b)) and the field strength F is given as a linear function of x by

$$F(x) = \frac{eN_D}{\epsilon_s}(W - x). \quad \text{II-20}$$

A capacitance is associated with the fixed charge in the depletion region. This “space charge” capacitance per unit area is given by [16:164]

$$Q_{sc} = eN_D W = \sqrt{2e\epsilon_s N_D (V_{bi} - V)}, \quad \text{II-21}$$

and the capacitance C is given by

$$C = A \left| \frac{\partial Q_{sc}}{\partial V} \right| = A \sqrt{\frac{e\epsilon_s N_D}{2(V_{bi} - V)}} = \frac{\epsilon_s A}{W}, \quad \text{II-22}$$

where A is the metal-semiconductor contact area. The metal-semiconductor contact described above is called a Schottky contact.

In the case that $\phi_s > \phi_m$ in figure II-2(a), the n-type semiconductor energy bands bend downward upon contact with the metal, and there is an accumulation rather than depletion of electrons in the interface region of the semiconductor. In this case, the application of bias V causes current to flow through the contact according to Ohm’s law which can be expressed as

$$V = IR_c. \quad \text{II-23}$$

This expression simply states that the current I is directly proportional to the applied bias voltage V by the contact resistance R_c of the metal-semiconductor contact. A contact

which exhibits this behavior is called an Ohmic contact. For semiconductor devices, it is also desirable to make Ohmic contacts having very small contact resistances such that current flows nearly unimpeded through the metal-semiconductor interface. For this reason, an Ohmic contact is commonly defined as one for which $R_c \approx 0$. Practically, metals and semiconductors for which $\phi_s > \phi_m$ are not usually available, so Ohmic contacts must be fabricated by an alternative method to that described above [14]. Alternatives include making the semiconductor interface region highly n-type by implantation, diffusion, or alloying [14]. Implantation and diffusion are both ways of obtaining a large concentration of chosen shallow donors in the interface region of the semiconductor. Alloying is usually accomplished by depositing a properly selected material on the semiconductor surface and annealing at temperatures which can range from 400 to 1000 °C. As the name implies, Ohmic alloys of the contact material and the semiconductor are formed.

Schottky and Ohmic contacts are essential to semiconductor device fabrication. A simple and important device called the Schottky Barrier Diode (SBD) consists of a Schottky contact as described above with an Ohmic contact placed elsewhere on the semiconductor. The Ohmic contact provides control of the semiconductor potential and thus permits the bias V to be applied across the Schottky contact. A diagram of a SBD is shown in figure II-3. In figure II-3, the Ohmic contact is placed on the back surface of a bulk semiconductor, but in the case of thin epitaxial semiconductor layers it is commonly placed on the front surface next to the Schottky contact. The energy band diagram of the SBD is shown in figure II-4 under applied bias voltage conditions of a) no bias voltage;

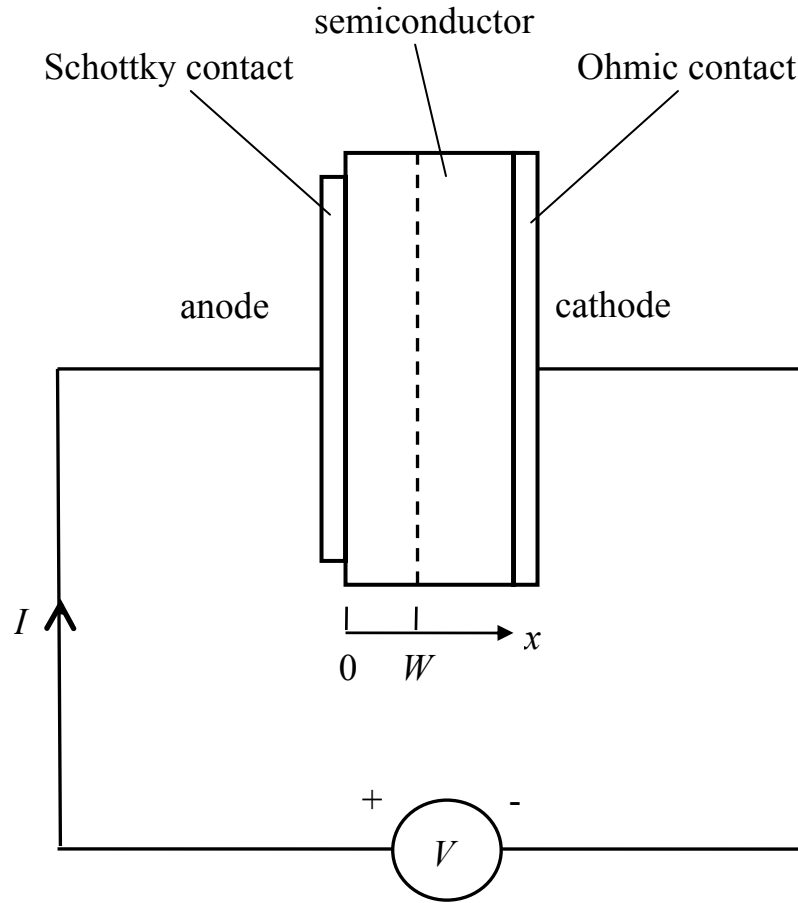


Figure II-3. Diagram of a Schottky Barrier Diode (SBD).

b) forward bias voltage; and c) reverse bias voltage. In the figure, it is shown that a forward bias voltage $+V_f$ causes the built-in voltage barrier to decrease by an energy eV_f . Also, it is shown in figure II-4 that a reverse bias voltage $-V_r$ increases the built-in voltage bias by an energy eV_r . Figure II-4 also shows that an applied bias voltage causes the Fermi levels of the metal and semiconductor to misalign, indicating a non-equilibrium condition whereby a net current may flow across the metal-semiconductor interface. Under all three applied bias conditions, it is seen that the Schottky barrier energy $e\phi_B$

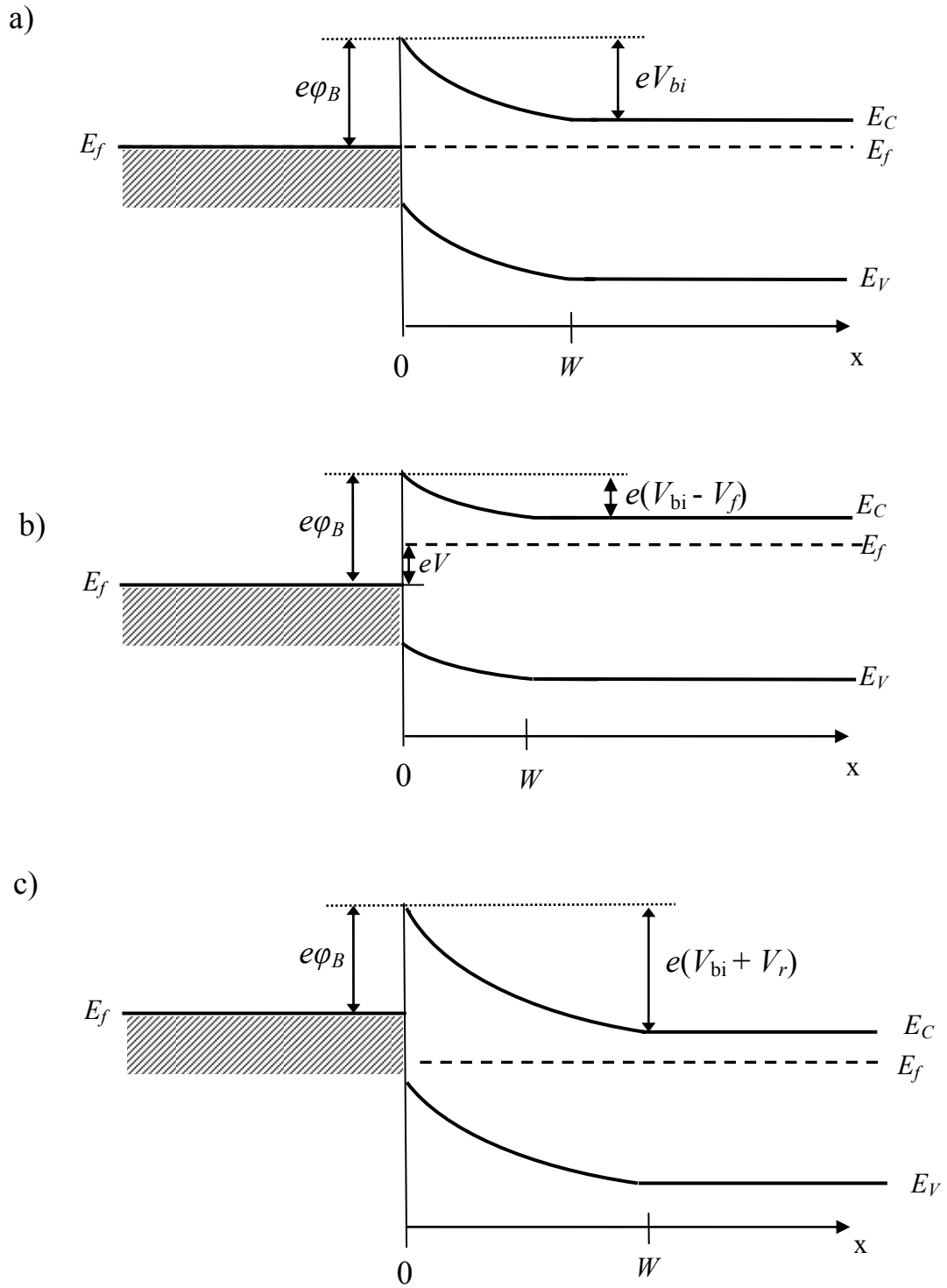


Figure II-4. Schottky barrier diode under a) no bias; b) forward bias; and c) reverse bias.

faced by electrons approaching the semiconductor from the metal side remains the same. Decreasing the built-in energy barrier eV_{bi} relative to $e\phi_B$ allows more conduction band electrons on the upper end of the Boltzmann energy distribution to overcome the barrier and create a net electron current across the interface. The transport mechanism thus described is called thermionic emission. At reverse bias, eV_{bi} is increased relative to $e\phi_B$, so a net electron current flows from the metal to the semiconductor. However, $e\phi_B$ is relatively large in a good SBD, so this net current due to thermionic emission is approximately zero at reverse bias. Thus, the SBD is a rectifier with electrical current density given by [14]

$$J = A^{**} T^2 \exp\left(-\frac{e\phi_B}{kT}\right) \left[\exp\left(\frac{eV}{n_f kT}\right) - 1 \right], \quad \text{II-24}$$

where A^{**} is the Richardson constant, a material specific quantity; and n_f is the ideality factor that introduces a correction to account for other transport mechanisms besides thermionic emission. Various tunneling mechanisms and carrier generation in the depletion region are examples of non-ideal carrier transport. At reverse bias, tunneling through the Schottky barrier is an important current transport mechanism that causes undesirable leakage currents.

2.2 Properties of $Al_xGa_{1-x}N$ Material and Devices

The wurtzite crystal structure of GaN is shown in figure II-5. Though a zinc-blende crystal phase of GaN can be grown epitaxially on properly chosen substrates, the wurtzite phase is the most widely grown and studied [17]. Only the wurtzite crystal

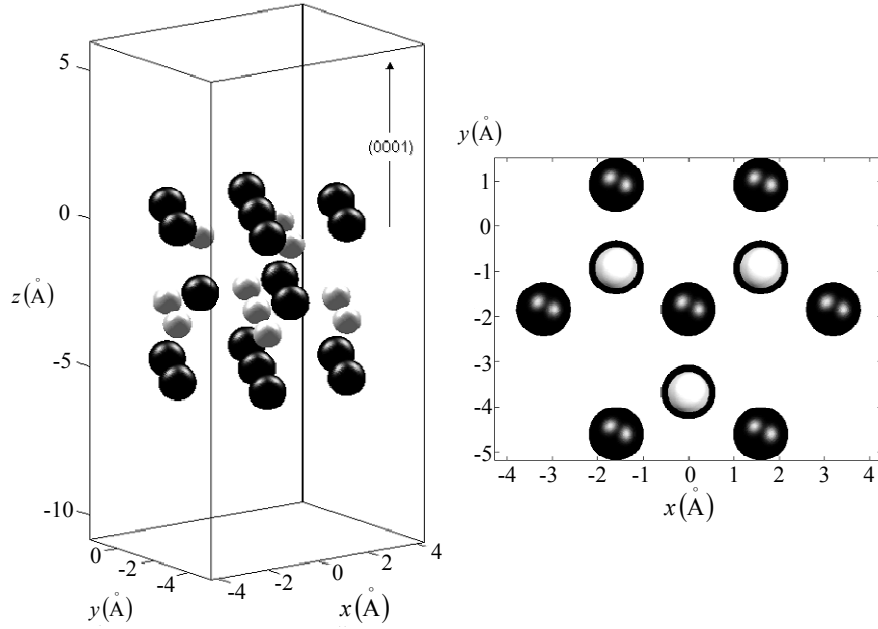


Figure II-5. Atomic locations for wurtzite crystal structure of GaN. The graph on the left illustrates the orientation of the (0001) direction, with Ga represented by black and N by white balls. The graph on the right is presented looking down the $(000\bar{1})$ direction for a Ga face surface [17].

phase of GaN and AlGa_N will be discussed in this dissertation. In figure II-5, the gallium atom positions are represented by black balls and the nitrogen atom positions are represented by white balls. The axis units are in angstroms and the lattice constants are $a = 3.189 \text{ \AA}$ and $c = 5.185 \text{ \AA}$. The energy band structure of GaN is shown in figure II-6. It is seen in this figure that GaN is a direct band gap semiconductor. That is, the conduction band minimum and valence band maximum are located at the same point (Γ) in momentum space. The band gap energy is $E_g = 3.39 \text{ eV}$ at $T = 300 \text{ K}$. This wide band gap affects nearly all of the other physical properties presented here. These properties enable the desirable performance capabilities of GaN-based electronic and optoelectronic

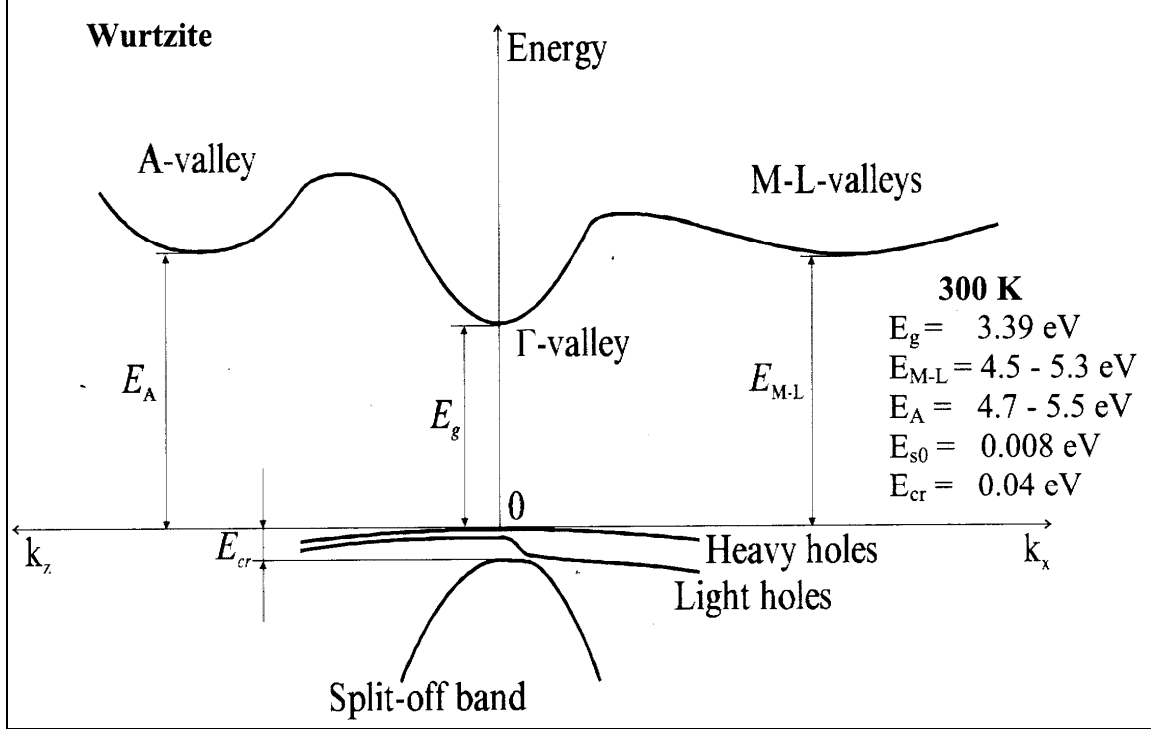


Figure II-6. Wurtzite GaN band-structure as computed by Suzuki [18], *et al.* via a plane-wave pseudopotential calculation method. All energy values are at 300 K.

devices. AlN has the same wurtzite crystal structure as GaN, but aluminum atoms have lower covalent radii than gallium atoms [19:13]. The crystal lattice constants in AlN are smaller than those in GaN, and the tighter packing of atoms contributes to larger band gap energy. The band gap energy in AlN is 6.2 eV at $T = 300 \text{ K}$. Table II-1 contains some selected physical properties of GaN and AlN that are directly relevant to the analyses and discussions in this dissertation.

In the case of $\text{Al}_x\text{Ga}_{1-x}\text{N}$ where aluminum substitutes for gallium on x % of the cation lattice sites, the physical parameter values are somewhere in between those of GaN and AlN. For many physical parameters, Vegard's law is a very good way to determine the parameter value in $\text{Al}_x\text{Ga}_{1-x}\text{N}$ for a given aluminum mole fraction x . Vegard's law,

Table II-1. Selected physical properties of GaN and AlN at T = 300 K (from [20] and references contained therein).

Property (units)	Symbol	GaN Value	AlN Value
Energy Gap (eV)	E_g	3.39	6.2
Density (g/cm ³)	ρ	6.15	3.23
Thermal Conductivity (W/cm·K)	κ	1.3	2.85
Static Dielectric Constant (8.854 x 10 ⁻¹⁴ F/cm)	ϵ_r	8.9	8.5
Lattice Constant (Å)	a	3.189	3.11
Lattice Constant (Å)	c	5.185	4.98
Electron Effective Mass (m_o)	m_{eff}	0.20	0.48
Electron mobility, bulk (cm ² /V·sec)	μ_n	1000	135
Hole mobility, bulk (cm ² /V·sec)	μ_p	30	14
Saturation Velocity (cm/s)	v_{sat}	2.5x10 ⁷	1.4x10 ⁷
Breakdown Field (V/cm)	F_b	> 2.5x10 ⁶	

applied to GaN and AlN may be expressed as [14]

$$\Gamma(\text{Al}_x\text{Ga}_{1-x}\text{N}) = x \Gamma(\text{AlN}) + (1-x) \Gamma(\text{GaN}), \quad \text{II-25}$$

where Γ represents any physical parameter for which the relation holds. One noteworthy physical parameter for which equation II-25 may not be adequate is band gap energy E_g . When calculating E_g of a ternary alloy it is often necessary to introduce a quadratic term to equation II-25 to obtain the expression

$$\Gamma(\text{Al}_x\text{Ga}_{1-x}\text{N}) = x \Gamma(\text{AlN}) + (1-x) \Gamma(\text{GaN}) - b x(1-x), \quad \text{II-26}$$

where b has the same units as Γ and is called the bowing parameter. In the case of E_g in $\text{Al}_x\text{Ga}_{1-x}\text{N}$, reported bowing parameters have ranged from $b = 0$ [21] (no bowing) to $b = 1.3$ [22], so equation II-26 can not presently be applied with much certainty. The

temperature dependence of E_g is given by the Varshni equation as [17]

$$E_g(T) = E(0) - \frac{\alpha T^2}{(T + \beta)}. \quad \text{II-27}$$

In GaN, $\alpha = -7.7 \times 10^{-4}$ eV/K, $\beta = 600$ K, and $E(0) = 3.49$ eV. In AlN, $\alpha = -1.8 \times 10^{-3}$ eV/K, $\beta = 1462$ K, and $E(0) = 6.28$ eV. Figure II-7 shows the room temperature band gap of $\text{Al}_x\text{Ga}_{1-x}\text{N}$ calculated with equation II-26 and various choices of b . In figure II-8, the temperature dependence of the $b = 0.35$ curve is calculated with equation II-27.

Upon application of equation II-1 and II-2 it is found that the intrinsic carrier concentration n_i of $\text{Al}_x\text{Ga}_{1-x}\text{N}$ ($0 \leq x \leq 1$) is essentially zero at $T = 300$ K, and n_i remains small enough so as to have a negligible effect on the operation of most devices until $T \approx 1000$ K. This property makes these and other wide band gap semiconductors well suited to use in high temperature environments. The wide band gap of $\text{Al}_x\text{Ga}_{1-x}\text{N}$ also makes the material resistant to electrical breakdown in high electric fields. The breakdown field strength of GaN is approximately 10 times higher than that of GaAs and Si. GaN also has an electron saturation velocity more than 2 times greater than that of GaAs and Si. The high breakdown field and electron velocity make GaN an excellent material for high power and high frequency electronic devices. As are all III-nitride semiconductors $\text{Al}_x\text{Ga}_{1-x}\text{N}$ is highly polar. The tensile strain caused by the growth of AlGaN on GaN gives rise to a piezoelectric polarization that combines with a spontaneous polarization to create a net positive charge at the AlGaN/GaN interface [2]. The polarization charge induces a 2-dimensional "gas" of electrons (2DEG) at the GaN side of the interface. This 2DEG forms the basis for a very important GaN-based electronic device known as a high electron mobility transistor (HEMT). A schematic cross section of such an AlGaN/GaN

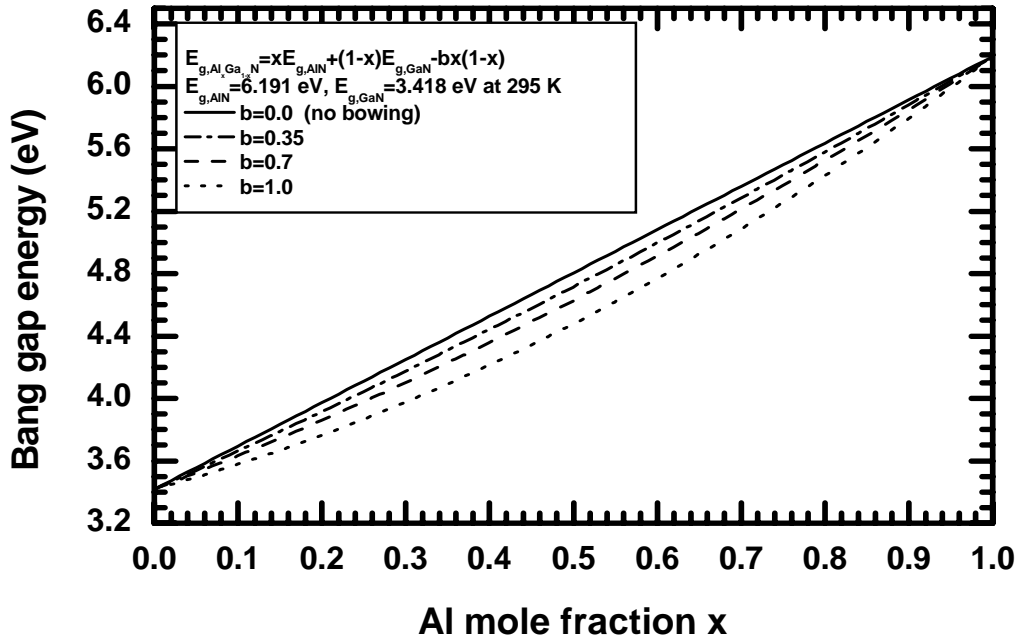


Figure II-7. Calculated room temperature band gap energy of $\text{Al}_x\text{Ga}_{1-x}\text{N}$ versus aluminum mole fraction for different bowing parameters.

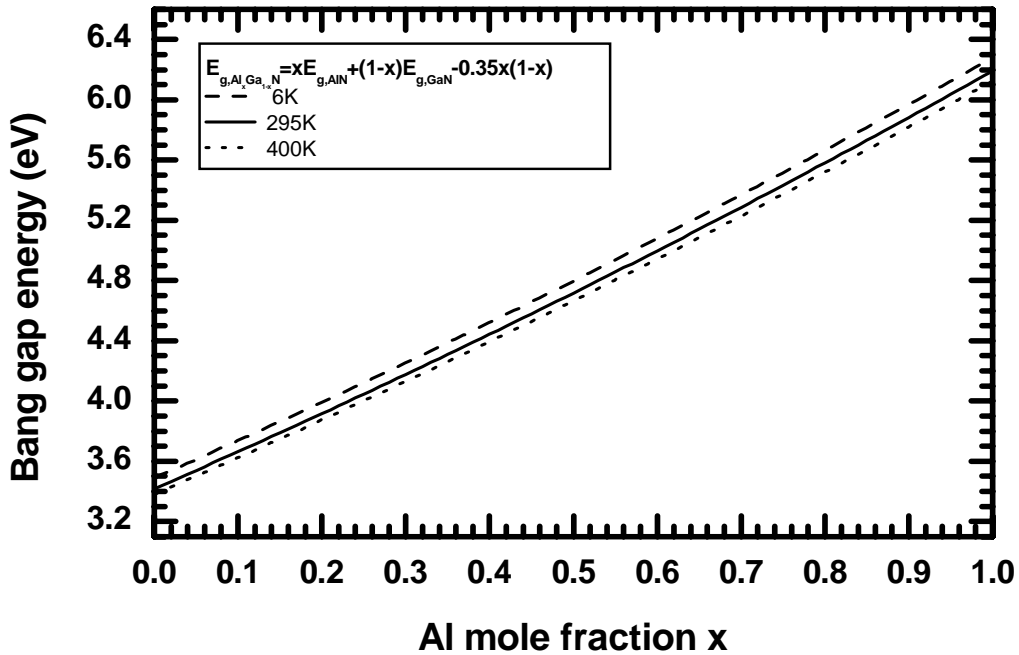


Figure II-8. Calculated band gap energy of $\text{Al}_x\text{Ga}_{1-x}\text{N}$ versus aluminum mole fraction at three different temperatures. A bowing parameter of $b=0.35$ is assumed.

HEMT is shown in figure II-9. In figure II-9, a dashed line indicates the location of the 2DEG. The metal-AlGa_N contact labeled "gate" is a Schottky contact. The contact regions labeled "source" and "drain" are Ohmic contacts. When a bias voltage is applied to the source and drain contacts current flows readily in the 2DEG channel. This channel has a very high mobility, especially when the GaN is undoped. Upon application of a negative voltage to the gate contact, the 2DEG diminishes in proportion to the magnitude of the applied gate voltage until a voltage is reached at which current is no longer carried between the biased source and drain. The speed with which channel conduction can be switched on and off and the high source-drain bias voltages that can be supported make AlGa_N/GaN HEMTs well suited to advance the state-of-the-art in high frequency power applications. The demonstrated power performance of AlGa_N/GaN HEMTs is generally 6-10 times better than that of GaAs or InP up through 20 GHz [23].

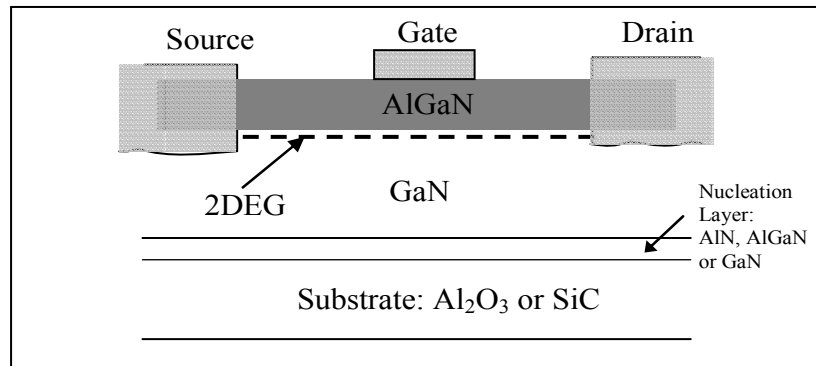


Figure II-9. Schematic of an AlGa_N/GaN HEMT.

The continuous choice of direct band gap energies from 3.4 to 6.2 eV make Al_xGa_{1-x}N a very attractive material for optoelectronic device applications in the spectrum ranging from blue to ultraviolet. Functionally, such devices can be categorized as those which detect light and those which emit light. The metal-Al_xGa_{1-x}N SBD, when

properly designed, functions as a solar-blind detector for $x \approx 0.35$. This $\text{Al}_{0.35}\text{Ga}_{0.65}\text{N}$ SBD operates at reverse bias. When a photon having energy greater than the band gap enters the depletion region, an electron-hole pair is created. The depletion region field causes the electron and hole to move in opposite directions out of the depletion region. A current thus flows, and it can be measured in external circuitry. The term "solar-blind" indicates that the detector is blind to the spectrum of solar photons found at the surface of the earth. These solar photons have wavelengths λ longer than ~ 285 nm, and they accordingly can not excite electrons across a band gap greater than 4.35 eV. In the light emitter category, GaN-based light emitting diode (LED) and laser diode technology have been developed to the point of significant commercial success in recent years. The physics of various LED and laser diodes is discussed in several good texts [14, 16] and will not be presented here.

2.3 Defect Characteristics

There are many types of native point defects in a ternary alloy such as $\text{Al}_x\text{Ga}_{1-x}\text{N}$. Example point defects include vacancies ($V_N, V_{\text{Ga}}, V_{\text{Al}}$), interstitials ($N_I, \text{Ga}_I, \text{Al}_I$), and antisites ($N_{\text{Ga}}, \text{Ga}_N, \text{Al}_N$). Two or more of these point defects can also couple with each other (or with impurity atoms) to form electrically active defect complexes. Additionally, each defect type can have more than one possible charge state. In ternary alloys like AlGa_N , there exist additional variations due to different cation nearest-neighbor configurations (e.g. the number of gallium versus aluminum atoms surrounding a nitrogen vacancy). Which of these defects are of interest depends on the intended $\text{Al}_x\text{Ga}_{1-x}\text{N}$ device application and on the relative concentrations of the various defect species. The relative concentration of a given point defect in as-grown semiconductor

material can depend on the formation energy and thermal stability of the defect species [24], the stoichiometry and purity of feed material [8], and the Fermi level [24]. In irradiated semiconductor material, the concentration of a given defect can depend on the type, energy, and flux of radiation; the threshold energy for atomic displacements; the thermal stability of the defect species; the existence of defect precursors; and the Fermi level [25, 26, 27].

An electrically active defect (that is, a donor or acceptor) is normally categorized as being either shallow or deep. This terminology refers to the magnitude of the defect's ionization energy, but there are more fundamental characteristics that distinguish the two categories. A shallow defect level tends to behave as a "hydrogenic" donor or acceptor with ionization energy defined by the carrier effective mass in the conduction (valence) band. A carrier occupying one of these states tends to be delocalized in space, and thus have well defined momentum according to the Heisenberg uncertainty principle. Conversely, the large ionization energy of a deep level suggests a more tightly bound electron orbit that is localized in space. Accordingly, deep levels tend to be delocalized in momentum space. This results in two significant properties of deep levels [28]. First, deep level defects are efficient recombination centers because the large extent in momentum space allows the level to couple with a variety of phonons. Nonradiative recombinations involving deep states are then much more likely than radiative recombinations, with phonon emission replacing photon emission for energy conservation. Second, the entire band structure must be involved in a theoretical description of a deep defect, making its energy level difficult to calculate from first principles. The nitrogen vacancy is observed in both as-grown and irradiated GaN layers.

First-principles calculations predict that V_N is a donor with three possible charge states (0, 1+, and 3+) in $Al_xGa_{1-x}N$ [29, 9, 30]. The 2+ state is unstable. The T_2 state of the neutral nitrogen vacancy is resonant with the conduction band in GaN. The single donor electron in that state automatically ionizes to the bottom of the conduction band where it forms an effective mass state bound by the Coulomb tail of the vacancy potential [24]. A central cell correction potential (the short range component due to local chemical structure) apparently causes this level to be 40-50 meV deeper than a pure effective mass donor, leading to the measured thermal activation energy of 60-70 meV [8, 31]. Thus, V_N behaves somewhat like a shallow single-electron donor. Under the effective mass donor model, this shallow level is expected to become deeper with increased Al mole fraction. To date, these energy levels have not been systematically measured (i.e. temperature dependent Hall (TDH) and deep level transient spectroscopy (DLTS) for incremental steps in x). Around $x = 0.45$, first principles calculations have indicated that a fundamental change in the electronic structure takes place [30], in that the V_N neutral state enters the band gap and continues deeper into the band gap for increasing Al mole fraction. Zhou, *et al.* [32] observed this behavior using visible absorption spectroscopy of proton-irradiated $Al_xGa_{1-x}N$. For $x < 0.45$, one might expect the V_N donor in AlGaIn to be similar in nature to V_N in GaN, though it is unclear how the hypothesized central cell potential that is so significant in GaN would change in AlGaIn. The triply ionized state is expected to have an energy level about 300 meV above the VBM in GaN. This charge state is metastable in n-type GaN. The ubiquitous electron trap in GaN that is often associated with V_N would correspond to the singly ionized state. Look *et al.* [33] reported this donor level to be 64 ± 10 meV below the CBM, and almost all other defect

studies report a similar level. This donor energy level was determined by temperature dependent Hall effect measurements, and it has been observed as an electron trap in many different DLTS studies as well. Most of these DLTS studies reported a trap level around 200 meV, but it was shown that this is probably a multi-component manifestation of the same V_N level having different capture cross-section and capture barrier heights [31].

One plausible explanation for these different components is variation in the spacing of V_N - N_I Frenkel pairs [8]. Several considerations detailed by Look [8] make it appear that V_N (either isolated or complexed in a way that changes the energy slightly) is the dominant radiation-induced donor-type point defect. The dominant acceptor-type defect induced by radiation is less clear. Theory [24, 29] points unambiguously to V_{Ga} , a triple acceptor, as the dominant acceptor-type defect in as-grown n-type material. In irradiated material, N_I point defects are also created which act as deep-level single acceptors. Look [8] makes the case that N_I is the dominant acceptor in irradiated GaN. The as-grown and radiation-induced defect levels reported in GaN and AlGaN to-date are summarized in table II-2 and table II-3. The format of the tables is similar to that presented by Look [8].

The annealing behavior of the above point defects helps correlate different characterization techniques such as DLTS and cathodoluminescence. The typical annealing trend in III-V materials is for interstitials and cation vacancies (N_I , Ga_I , and V_{Ga}) to anneal out at temperatures below 150 °C. Anion vacancies (V_N) tend to anneal out in the temperature range of 200-400 °C, and antisites (N_{Ga} and Ga_N) tend to anneal out at temperatures higher than 600 °C [32]. Look *et al.* [33] applied a first-order analysis to GaN isochronal (fixed time and varied temperature) annealing data following

Table II-2 Reported defect energy levels in GaN.

Category	Experimental Energy as-grown (eV)	Introduced/ Increased by Radiation (eV)	Thermal Energy (eV)	Type of Radiation	Observation Technique	Material	I.D.	Ref.
Donors	0.06 0.018	0.06	0.06	e^- (1 MeV)	TDH	undoped HVPE $n \approx 10^{17}$	V_N Si_{Ga}	33
Acceptors			deep	e^- (1 MeV)	TDH	"	N_I	33
			deep	e^- (2 MeV)	Positron Annihil.	Semi-insulating bulk $[Mg] \approx [O] \approx 10^{20}$	V_{Ga}	44
Electron Traps	0.21, 0.27, 0.45, 0.61	0.22	<u>0.22 peak fit:</u> 0.06, 0.10, 0.20	e^- (^{90}Sr)	DLTS	undoped MOVPE ELO $n \approx 10^{16}$	V_N	34
	0.21, 0.27, 0.45, 0.61	0.13, 0.16, 0.20		H^+ (2 MeV)	DLTS	undoped MOVPE ELO $n \approx 10^{16}$	V_N	35
	0.21, 0.27, 0.45, 0.61	0.20, 0.78 0.90		He^+ (5.4 MeV)	DLTS	undoped MOVPE ELO $n \approx 10^{16}$	V_N Spike	36
	0.20	0.12, 0.16, 0.52, 0.59, 0.90	0.08	H^+ (24 GeV)	DLTS	undoped HVPE $n \approx 10^{17}$	$V_N?$ N_I or $V_{Ga}-N_I$	37
	0.27, 0.36, 0.58	0.09, 0.13		γ -ray (^{60}Co)	DLTS	Si-doped MOCVD $n \approx 10^{17}$	V_N	38
	0.24, 0.45, 0.62	0.18, 0.85	0.06	e^- (1 MeV)	DLTS	undoped MOCVD $n \approx 10^{16}$	V_N	39
	0.2, 0.55, 0.65, 0.9				DLTS	undoped freestanding HVPE $n \approx 10^{16}$		40
Hole Traps	$E_v + 0.6, 0.9$				ODTLS	undoped freestanding HVPE $n \approx 10^{16}$		40

Table II-3 Reported defect energy levels in $\text{Al}_x\text{Ga}_{1-x}\text{N}$ ($x < 0.5$)

Category	Experimental Energy as-grown (eV)	Introduced/ Increased by Radiation (eV)	Thermal Energy (eV)	Type of Radiation	Observation Technique	Material	I.D.	Ref.
Electron Traps	0.61					$x = 0.12$ [Si] $\approx 3 \times 10^{17}$ MOVPE on SiC	similar to 0.5 eV GaN level	41
	0.77, 0.83, 1.01							
	0.274	0.187		He^{+2} (1.8 MeV)	DLTS TSCAP	$x = 0.12$ and 0.42 [Si] $\approx 5 \times 10^{17}$ MBE from SVTA	Similar to 0.234 eV GaN level Similar to 0.61 eV level in [41]	42
	0.567							

0.7 MeV electron irradiation. The equation that describes first-order annealing of mobility is

$$\mu_i^{-1} = \mu_{\infty}^{-1} + (\mu_{i-1}^{-1} - \mu_{\infty}^{-1}) \exp(-\nu t \exp[-E / kT_i]), \quad \text{II-28}$$

where i denotes the annealing temperature step, ν is a frequency factor (commonly set equal to 10^{13} s^{-1}), and E is the activation energy for defect migration. Look *et al.* used this model to fit the data precisely. In order to do so, they increased E linearly with temperature in the range 250-400 °C. This would be expected if the mobility degradation is caused by Frenkel-pairs with different separations [33]. Achieving an accurate first-order fit to the data in this way suggests that vacancies are recombining with their initial interstitials, i.e. Frenkel-pair annealing. Gallium interstitials and related complexes were tentatively identified by optically detected magnetic resonance (ODMR) [43]. The doubly-charged gallium interstitial, Ga_I^{2+} , apparently anneals near room temperature and complexes to form a different paramagnetic center [43,44]. A 0.85 eV photoluminescence (PL) band appeared along with this complex. Gallium vacancies are detectable by positron annihilation spectroscopy. Saarinen *et al.* [44] reported that the V_{Ga} created by 2 MeV electron irradiation anneal in a long-range migration process at 200-300 °C. On the other hand, this group reported that the V_{Ga} in as-grown GaN is stable up to 1000-1200 °C, and thus posited that V_{Ga} forms complexes with oxygen impurities.

Two other general defect categories besides point defects are line and areal defects. The important areal defects in as-grown GaN are stacking faults, and these are especially concentrated in a 0.2 μm thick region at the GaN/sapphire interface. This region often has a degenerate donor defect concentration which may be related to

stacking faults [45]. It has also been proposed, however, that this interface conduction layer is caused by an impurity band of oxygen [46]. Of certain consequence to the electrical measurements in this study are line defects; specifically threading edge and screw dislocations, which are believed to be electrically active in GaN [47]. These defects, with typical densities of the 10^8 - 10^{10} cm⁻² in epitaxial GaN grown on sapphire, are a consequence of the 14% lattice size mismatch and 34% thermal expansion coefficient mismatch between the GaN and the sapphire substrate [47]. Some theoretical calculations suggest that the core of such defects is composed of V_{Ga} [48]. Being acceptor-like and deep in the band gap, these ionized defects would cause a significant reduction in mobility. Indeed, an inverse relationship between dislocation concentration and mobility has been noted by many observers [47]. It has been suggested that a variety of point defect species segregate around core dislocations in GaN [49].

2.4 Radiation Damage Mechanisms

2.4.1 Interactions

To first-order, degradation of electrical and optical characteristics of a semiconductor usually scale with non-ionizing energy loss (NIEL). NIEL is a measure of the fraction of energy that is transferred from the bombarding particle to primary knock-on atoms (PKAs) as opposed to ionization and excitation in the crystal lattice. This concept is very useful in that it allows a direct comparison of the dose imparted from different radiation types and energies. One can thus analytically determine the fluence of 2 MeV electrons necessary to produce the same displacement damage as a 10^{12} cm⁻²

fluence of 14 MeV neutrons. Additionally, the popular Monte-Carlo program "Transport and Range of Ions in Matter" (TRIM) [50] may be used to calculate the actual defect concentration due to collision chains. Whereas NIEL is an analytically determined value proportional to the product of PKA collision cross-section and average recoil energy, TRIM uses the PKA recoil energy spectrum to incorporate the range of possible collision chains [25:18]. The TRIM output gives the concentration of displacements generated at a given material depth, but this says nothing about the thermal stability and electrical/optical characteristics of the resultant defects.

A Frenkel-pair is generated by any radiation that can impart the necessary displacement energy. In GaAs, the average displacement energy is about 9.8 eV for both Ga and As atoms [25]. The precise value can range from 7-11 eV depending on crystal orientation [25:110]. For a relativistic electron to impart this much energy in an elastic collision, it must have energy greater than or equal to the threshold energy, E_{thr} . The maximum imparted energy is given in units of MeV by the following equation [8]:

$$E_{\max} = \frac{2E(E + 2m_o c^2)}{Mc^2} = \frac{0.002147E(E + 1.022)}{A}, \quad \text{II-29}$$

where c is the speed of light, m_o is the rest mass of an electron, M is the mass of the target atom, A is the atomic weight of the target atom in units of amu, and E is the energy of the bombarding electron in MeV. The E_{\max} value of each constituent atom in AlGaIn is listed in table II-4 for the given electron energies. By substituting E_d for E_{\max} , equation II-29 may be solved to obtain E , which in this case is equivalent to E_{thr} . It is thereby calculated that the threshold electron energy for Ga and As atoms in GaAs is 0.25 and 0.27 MeV, respectively. Additional transferred energy will produce Frenkel-pairs with larger separations and secondary displacement due to the recoiling target atom.

Electrons in the laboratory testing environment and in the near-earth space environment typically have energies less than 5 MeV [27]. At these energies, electrons create simple Frenkel pairs uniformly in semiconductor material. For example, 1 MeV electrons have a range of about 0.2 cm in GaN [51]. The 1 MeV electrons traverse a 1 μm epitaxial layer with

Table II-4. Maximum energy transferred to AlGaIn atomic constituents for given incident electron energies.

Incident Energy (MeV)	Max Energy Transferred to Ga Atom (eV)	Max Energy Transferred to Al Atom (eV)	Max Energy Transferred to N Atom (eV)
0.42	18.7	48.2	92.9
0.62	31.4	81.0	156
1.0	62.3	161	310
1.2	82.1	212	409

equal displacement probability per unit depth and, following a displacement collision, the energy of the electron drops below E_{thr} . The displaced atom becomes an interstitial relatively close to the remaining vacancy.

If E_d is known, the Rutherford cross section for displacements by relativistic electrons is given in units of cm^2 by [33],

$$\sigma_d(E) = 2.5 \times 10^{-25} \cdot \frac{Z^2 \gamma^2}{(\gamma^2 - 1)^2} \left\{ \frac{E_{\max}}{E_d} - 1 - \beta^2 \ln \left(\frac{E_{\max}}{E_d} \right) + \frac{\pi Z \beta}{137} \left[2 \left(\frac{E_{\max}}{E_d} \right)^{1/2} - 2 - \ln \left(\frac{E_{\max}}{E_d} \right) \right] \right\}, \quad \text{II-30}$$

where Z is the target nucleus charge, e is the electron charge, $\beta = [(\gamma^2 - 1)^{1/2}]/\gamma$, $\gamma = 1 + E/m_e c^2$, and E is the electron beam energy. This expression includes a quantum mechanical correction formulated by McKinley and Feshbach [52]. The displacement cross section thus calculated is used to predict the displacement introduction rate, η_d , of certain atomic displacements during electron irradiation by

$$\eta_d = \sigma_d N_t, \quad \text{II-31}$$

where N_t is the target concentration of the particular atomic species. The displacement introduction rate has units of cm^{-1} gives the concentration of the displaced atoms, N_d , resulting from a given fluence, Φ , by

$$N_d = \eta_d \Phi. \quad \text{II-32}$$

In this way, an introduction rate is analogous to a macroscopic cross section in nuclear engineering. Figure II-10 shows the calculated η_d in GaN and $\text{Al}_{0.30}\text{Ga}_{0.70}\text{N}$ for a range of assumed displacement energies (E_d) based on the displacement cross section given by equation II-30. The displacement energies of the atomic components are not well known, but various theoretical considerations and experimental results [53, 44, 33, 54] limit the possible range of values to $10 < E_d < 50$ meV for Ga and N in GaN with perhaps the strongest consensus being that $20 < E_d < 25$ meV [33, 54].

Another factor that can conceivably produce different damage from two irradiations having the same NIEL is beam flux. Increased flux causes an increase in ionization throughout the material during irradiation. This can affect the mobility of certain defects during irradiation via the increase in defect charge states and non-radiative recombination energy (phonons). Additionally, the overlap of damage trails within a short time period can cause changes in the stable defect concentrations. In the case of high-energy electron irradiation, the most important consideration concerning flux is the rate at which heat is generated in the sample. If the sample is not cooled adequately for a given flux, the sample temperature will rise and increased dynamic annealing will take place.

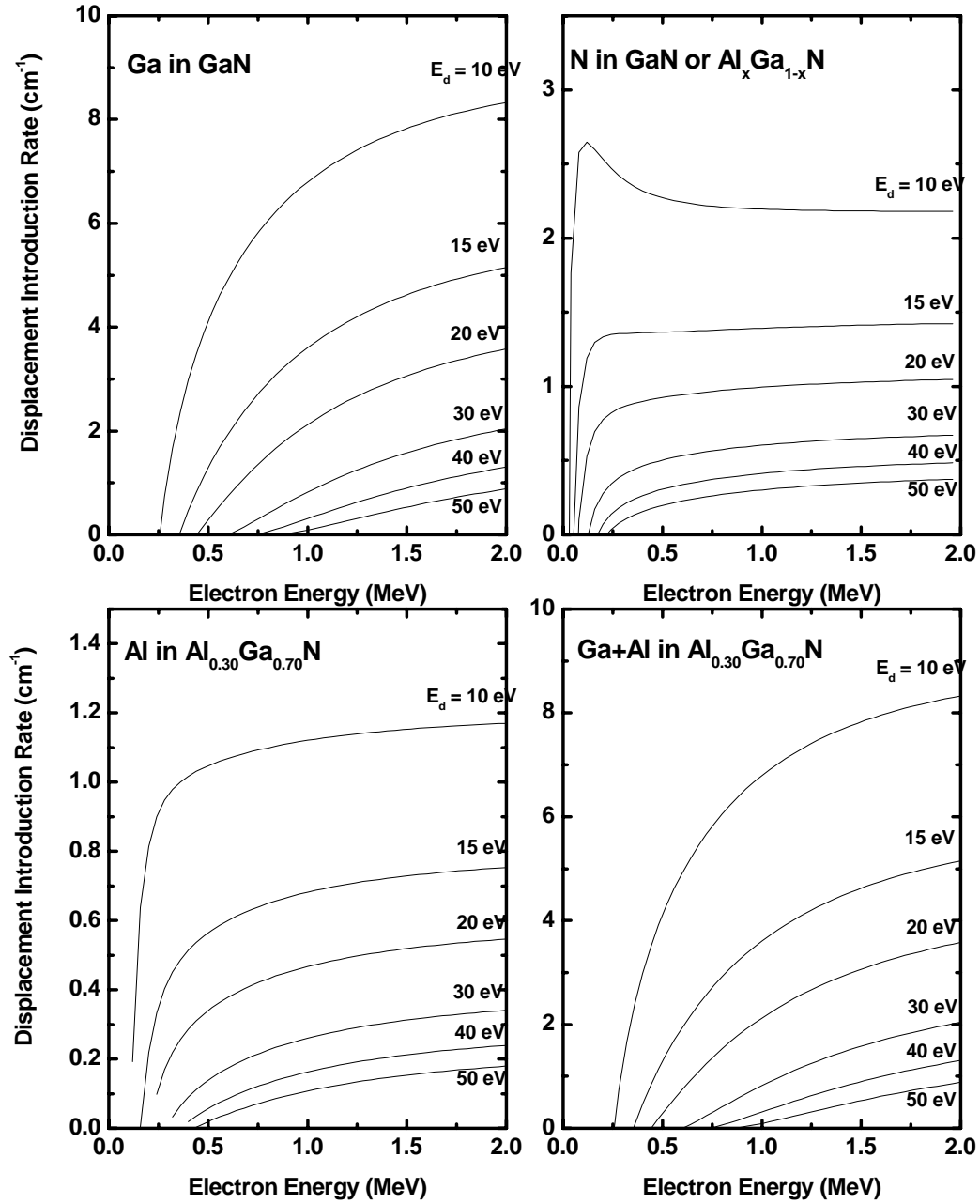


Figure II-10. Calculated displacement introduction rates in GaN and Al_{0.30}Ga_{0.70}N for a range of assumed displacement energies (E_d) based on the displacement cross section given by equation II-30.

2.4.2 Carrier Removal

Carrier removal is a general term referring to the decrease in majority carrier concentration following irradiation. The two established mechanisms of carrier removal are carrier compensation and donor passivation. In an n-type semiconductor, the existence of any acceptor-type traps below the Fermi level will lower the free carrier concentration. The acceptor-type traps that are more than a few kT below the Fermi level must be totally (practically speaking) filled in thermal equilibrium, and those electrons are supplied by the donor-type impurities and/or traps above and near the Fermi level. This phenomenon is called carrier compensation, and it occurs, to some degree, in every real semiconductor. Donor-type traps that are well below the Fermi level are filled and are thus unable to contribute to the free carrier concentration. Radiation generally creates both donor and acceptor-type traps, but the net effect is to decrease the majority carrier concentration, as described above. The stability of certain traps depends on their charge states (i.e. the location of the Fermi level). So, the relative concentrations of stable donors and acceptors also vary based on whether the material is n-type or p-type. This additional mechanism is apparently responsible for type conversion in n-type GaAs [55] (that is, the n-type material not only becomes more intrinsic, but proceeds to become p-type under irradiation).

At low doses, the carrier concentration n is reduced as a function of fluence Φ according to

$$n(\Phi) = n_0(1 - \alpha\Phi) , \quad \text{II-33}$$

where the constant α has units of cm^2 and is applicable only to a given type and energy of radiation. The constant n_0 is the initial carrier concentration, and Φ is the fluence (units

of cm^{-2}) of the given type of radiation. The carrier removal rate, defined as $\eta = dn/d\Phi$, is equivalent to $n_o\alpha$ in equation II-33 and has units of cm^{-1} . Though a simple proportionality of removal rate to initial free carrier concentration is implied by II-12, the constant α can in principle be proportional to the inverse of n_o or a fractional power thereof. For energetic ion and neutron irradiation of GaAs, α is inversely proportional to a fractional power of the initial carrier concentration, as will be discussed below.

When the fluence is large enough to cause a significant decrease in majority carrier concentration, equation II-33 begins to become less reliable. The main reason for the deviation from the linear model is that trap filling is a non-linear function of the existing concentration of majority carriers, which is decreasing significantly with fluence []. In other words, at high doses the Fermi level begins to move towards the middle of the band gap and trap filling in the upper half of the band gap decreases accordingly. Dose-dependent carrier removal in GaAs has been studied extensively in the past decade for the purpose of electrical isolation via ion implantation [56, 57]. Prior to that, a number of neutron [58, 59, 60] and electron [61, 55] irradiation studies were performed in order to characterize intrinsic defects in GaAs and understand radiation effects in GaAs devices.

For GaAs, the linear model of equation II-33 is only applicable up to doses where carrier concentration decreases by 25% [58]. At higher doses, the decrease is seen to be approximately exponential, corresponding to a linear shift in the Fermi level with dose. That is,

$$n(\Phi) = n_o \exp(-\alpha\Phi), \quad \text{II-34}$$

where the constant α takes on a value that is different than in equation II-33.

An additional consideration that is certain to apply to GaN is the efficient dynamic annealing that takes place during room temperature irradiation. That is, the introduction rate of stable and observable defects is may be much less than the introduction rate of primary point defects (vacancies, interstitials, and antisites). This behavior has been studied in connection with electrical isolation via ion implantation damage in GaN. In one study [62], point defects were found to anneal efficiently during irradiation at both 77 K and room temperature. Stable defect complexes were formed in the process, but no amorphization was observed by Rutherford backscattering (RBS) and transmission electron microscopy (TEM) until a threshold dose was reached. At that threshold dose, an amorphization layer formed on the surface and grew toward the bulk. At this point, it is important to clarify that the doses required to achieve electrical isolation are several orders of magnitude lower than those required to achieve amorphization. In the former case, the threshold dose is that required to produce defect concentrations on the order of the number of initial free carriers ($\sim 10^{18} \text{ cm}^{-3}$). In the latter case, the threshold dose is that required to produce defect concentrations on the order of the crystal atomic concentration ($\sim 10^{23} \text{ cm}^{-3}$). What the RBS study makes clear is that some defects anneal in GaN at temperatures as low as 77 K.

Dose-dependent studies of carrier removal are not widely reported for either GaN or AlGaN. Irradiation with 1 MeV electrons was reported to introduce compensating acceptors at a rate of approximately 1 cm^{-1} in GaN having $n_o = 2.3 \times 10^{16} \text{ cm}^{-3}$ [31]. Green [17] reported a carrier removal rate of 0.14 cm^{-1} for 1.0 MeV electron irradiation of unintentionally doped freestanding GaN layers grown by HVPE. For 1 MeV proton irradiation of unintentionally doped GaN ($n_o = 1.2 \times 10^{17} \text{ cm}^{-3}$), Auret *et al.* [63] found a

carrier removal rate of $3880 \pm 380 \text{ cm}^{-1}$ using C-V measurements. They also used DLTS to measure the introduction rate of the ER3 defect as being $290 \pm 50 \text{ cm}^{-1}$.

Some groups have measured dose-dependent sheet resistance *in-situ*. Boudinov *et al.* [64] reported that sheet resistance in n-type GaN ($n_o = 3 \times 10^{17} \text{ cm}^{-3}$) increases by 50% when exposed to a 0.6 MeV proton fluence of $5 \times 10^{13} \text{ cm}^{-2}$. The threshold dose (the dose at which resistivity reaches a plateau following several orders of magnitude increase) is $5 \times 10^{14} \text{ cm}^{-2}$. It was also reported that the threshold dose is directly proportional to the initial carrier concentration in silicon doped GaN [64]. This is in qualitative agreement with the linear carrier removal model of equation II-33. More recently, TDH measurements were reported for the same type of GaN sample discussed above [62]. Following a single dose of $2.4 \times 10^{14} \text{ cm}^{-2}$, the sheet carrier density dropped by about 5 orders of magnitude whereas the effective Hall mobility dropped by about 1 order of magnitude. A recently proposed model [65] with a simple theoretical basis is consistent with the above observations (specifically, the resistivity vs. dose curve and the threshold dose dependence on n_o). The model is based on the transformation of shallow dopant levels into deep levels via complexes that are formed between point defects and the dopants.

It is, at present, unclear how the aluminum mole fraction in $\text{Al}_x\text{Ga}_{1-x}\text{N}$ affects dose-dependent carrier removal. A carrier removal rate (applicable at low doses) has been reported for $\text{Al}_{0.12}\text{Ga}_{0.88}\text{N}$ [42] and a threshold dose for isolation has also been reported [66]. Legodi *et al.* [42] concluded that the carrier removal rate in $\text{Al}_x\text{Ga}_{1-x}\text{N}$ ($x = 0.12$ or 0.41) due to 1.8 MeV He^{2+} ions is 80 times higher than in similarly irradiated GaN. This may be the only published statement on the subject, thus far, and the result is

not at all conclusive. The GaN carrier removal study used for comparison is not cited. One of the few published reports of carrier removal rate in GaN is that done by two of Legodi's co-authors, Auret and Goodman [36] for 5.4 MeV He^{2+} irradiated GaN. The dose deposited through a gold contact in both studies can be compared using the TRIM program [50]. Such a calculation reveals that the damage created per unit fluence in Auret's study is 1.35 times greater than in Legodi's study. Thus, the irradiation conditions of these two studies are indeed similar. The GaN carrier removal rate reported by Auret is $6200 \pm 300 \text{ cm}^{-1}$. After accounting for the ion energy difference, this is only 5 times lower (not 80 times!) than the carrier removal rate reported for AlGa_xN by Legodi. Additionally, the GaN sample in Auret's study was unintentionally doped with $n_o = 3 \times 10^{16} \text{ cm}^{-3}$. The AlGa_xN sample in Legodi's study was silicon-doped with $n_o = 5\text{-}9 \times 10^{17} \text{ cm}^{-3}$. Thus, it is unclear from these studies how carrier removal would compare in GaN and AlGa_xN with similar doping levels.

Structural disorder was measured in proton and heavy ion-irradiated Al_xGa_{1-x}N [62]. Increasing the Al mole fraction (from $x = 0.05$ to $x = 0.60$) was shown to increase the dynamic annealing at room temperature [32]. Thus, the samples with the highest Al mole fraction were the most resistant to amorphization. In contrast with GaN, preferential surface disordering was not observed in Al_xGa_{1-x}N [32].

2.4.3 Carrier Trapping, Generation, and Recombination

The occupation of the defect-related energy levels mentioned above was discussed in the context of the semiconductor being in thermodynamic equilibrium. That is, the occupation probability of each level was defined by its energetic proximity to the Fermi level. When a non-equilibrium situation is created by a stimulus, such as the

application of an external electric field or exposure to ionizing photons, a non-equilibrium distribution of electrons is created. When the stimulus is removed, the carrier distribution at each level will return to thermodynamic equilibrium with an emission rate defined by its energetic proximity to the conduction band minimum and the temperature of the material. The situation described above is referred to as carrier trapping. Specifically, an electron trap is defined as a defect for which the electron capture rate constant, c_n , is much larger than the hole capture rate constant, c_p [28]. A microscopic capture cross section $\sigma_{n,p}$, having units of cm^2 , may be defined as

$$c_n = \sigma_n \langle v_n \rangle n \quad \text{II-35}$$

and

$$c_p = \sigma_p \langle v_p \rangle p \quad \text{II-36}$$

for electron and hole capture, respectively. The symbol $\langle v_{n,p} \rangle$ denotes the root mean square (rms) value of the carrier thermal velocity given as

$$\langle v_{n,p} \rangle = \sqrt{\frac{3kT}{m^*}}, \quad \text{II-37}$$

where m^* is the effective mass of the applicable carrier type. The emission rate constant, e_n , of a trapped electron to the conduction band has the form [28]

$$e_n = A_n \exp\left(\frac{-E_{th}}{kT}\right), \quad \text{II-38}$$

where E_{th} in the Boltzmann factor is the energy difference between the conduction band minimum and the trap energy level ($E_{th} = E_C - E_T$), and the constant A_n is a property of the specific defect. Applied to an electron trap, the statistical principle of detailed balance states that in a neutral material at thermal equilibrium the capture and emission rates must be equal. This principle is expressed as [72]

$$e_n P = c_n (1 - P), \quad \text{II-39}$$

where P is defined as the probability that the trap is filled by an electron. This probability is given by the Fermi-Dirac distribution function of equation II-3,

$$P = f(E_T) = \frac{1}{1 + \frac{g_o}{g_1} \exp\left(\frac{E_T - E_f}{kT}\right)}. \quad \text{II-40}$$

The coefficient A_n in equation II-38 may be determined by inserting equations II-35 and II-40 into equation II-39. Equation II-38 can then be expressed as

$$e_n = \sigma_n <v_n> n \cdot \left(\frac{g_o}{g_1}\right) \cdot \exp\left(\frac{E_T - E_f}{kT}\right). \quad \text{II-41}$$

The explicit dependence on the Fermi level can be removed from this expression by substituting for n from equation II-1 to obtain

$$e_n = \sigma_n <v_n> N_C \cdot \left(\frac{g_o}{g_1}\right) \cdot \exp\left(\frac{-E_{th}}{kT}\right). \quad \text{II-42}$$

It is often observed that the capture cross section of a particular trap has a temperature dependence of the form [28]

$$\sigma_n(T) = \sigma_n(\infty) \cdot \exp\left(\frac{-E_\sigma}{kT}\right), \quad \text{II-43}$$

where E_σ is effectively a capture energy barrier and $\sigma_n(\infty)$ is the high temperature limit of the capture cross section. Showing this explicit temperature dependence of σ_n , and that of the N_C and $<v_n>$, equation II-42 becomes

$$e_n = \gamma \cdot \sigma_n(\infty) \cdot \left(\frac{g_o}{g_1}\right) \cdot T^2 \cdot \exp\left(\frac{-(E_{th} + E_\sigma)}{kT}\right), \quad \text{II-44}$$

where $\gamma = 4\sqrt{6\pi^3} M_c m_{eff} k^2 h^{-3}$. The temperature dependence of one more term is still implicit in equation II-44. The temperature dependence of E_{th} is given by

$$E_{th} = E_{T0} - \alpha T. \quad \text{II-45}$$

Thermodynamically, E_{th} , E_{T0} , and α are the respective changes in Gibbs free energy, enthalpy, and entropy due to the change in the occupation of the trap level [28]. Upon substitution of equation II-45 into equation II-44, and some rearrangement, the explicit temperature dependence of e_n is given by

$$e_n(T) = \gamma \cdot \sigma_n(\infty) \cdot \left(\frac{g_o}{g_i} \right) \cdot e^{\left(\frac{\alpha}{k} \right)} T^2 \cdot \exp\left(\frac{-(E_{T0} + E_\sigma)}{kT} \right). \quad \text{II-46}$$

This expression is critical to the analysis of the DLTS data. Both capture and emission rate constants (often simply referred to as capture and emission rates) have units of s^{-1} , and the specific ways in which they describe carrier trapping and detrapping in the depletion region of a Schottky diode will be discussed in chapter IV.

Deep traps are known to be responsible for causing significant degradation of electrical device performance. In GaAs-based electrical devices, for instance, deep traps have been shown to be responsible for I-V hysteresis loops, “backgating phenomena” (where a voltage on one device affects the current on another device), and low frequency oscillations [13:187].

A recombination center is a defect for which both c_n and c_p are large. In this case, a trapped electron is likely to recombine with a hole before it has the chance to be emitted back into the conduction band. In generation, an electron is trapped from the valence band and subsequently emitted into the conduction band. A trap level must be located near the middle of the band gap to be an efficient generation center.

A specific example of an electron trap observed by DLTS is the nitrogen vacancy single donor level located 60-80 meV below the conduction band minimum of GaN. Polenta *et al.* [31] proposed that the ED1 and ED2 trap levels originate from the auto-ionized T₂ state of the nitrogen vacancy. Equation II-46 was applied in an attempt to model these two overlapping peaks, and the fitting suggested ED1 had an activation energy of about 60 meV. Thus, it was concluded that ED1 corresponds to the isolated V_N, whereas ED2 was suggested to be related to V_N but with some difference in microscopic configuration causing it to have a different capture cross section and activation energy [31].

2.4.4 Mobility Degradation

In many cases of interest, the degradation of mobility can be described as a linear function of fluence by the equation [25:138],

$$\mu^{-1} = \mu_0^{-1} (1 + b\Phi), \quad \text{II-47}$$

where b has units of cm². In analogy to the carrier removal rate, a damage constant $K_\mu = b/\mu_0$ may be defined and used to determine the expected increase in μ^{-1} with fluence.

The degradation in mobility due to radiation-induced defects is expected to be greatest at low temperature, because ionized impurity (or defect) scattering is the dominant scattering mechanism in semiconductors at low temperature.

2.4.5 Luminescence Degradation

Radiation generally causes the luminescence intensity of a semiconductor to decrease by creating defects that act as non-radiative recombination centers. Previous investigations of luminescence degradation in GaN have placed more emphasis on GaN-

based LEDs [67, 53] than on epitaxial layers. The radiation response of GaN-based LEDs is of practical importance and the luminescence can be measured with less experimental uncertainty than is found in photoluminescence and cathodoluminescence measurements, however, LEDs have additional degradation mechanisms than those measured directly in epitaxial GaN layers. Several different expressions for damage constants have been proposed depending on the device design, as changes in series resistance and other factors can affect the electroluminescence of LEDs [25]. Gaudreau *et al.* [67] reported that a GaN-based LED was about two orders of magnitude more resistant to 2 MeV proton radiation than GaAs LEDs. The same type of GaN-based LED was irradiated with 2.5 MeV electrons and the damage was observed to disappear after 16 hours of room temperature annealing [53]. The photoluminescence degradation in thin epitaxial films of GaN grown by MBE was characterized with 2 MeV proton radiation by Khanna *et al.* [68]. Following previous work in GaAs, the dose dependence of the photoluminescence intensity I was expressed as

$$\frac{I_0}{I} - 1 = K\Phi, \quad \text{II-48}$$

where I_0 is the PL intensity before irradiation, Φ is the fluence in units of cm^{-2} , and K is the damage constant in units of cm^2 . Equation II-48 was not applicable until $\Phi \sim 10^{13} \text{ cm}^{-2}$. For lesser values of Φ some luminescence degradation was apparent, but the change in $(I_0/I - 1)$ was considered to be within the margin of error of the pre-irradiated measurement. The damage constant obtained for $\Phi > 10^{13} \text{ cm}^{-2}$ was $K = 1.4 \times 10^{-13} \text{ cm}^2$. This damage constant was determined for the dominant donor bound exciton transition in the PL spectrum. Comparing with a damage constant pertaining to the dominant excitonic peak in neutron-irradiated GaAs, Khanna *et al.* concluded that GaN is ~ 100

times more tolerant to radiation than GaAs with regard to luminescence degradation. It does not appear that any comparable study has been performed on AlGa_N to date.

2.5 Radiation Effects on $Al_xGa_{1-x}N$ Devices

The radiation damage mechanisms outlined above can work independently or in concert to affect the functionality of a particular semiconductor device. Because AlGa_N/Ga_N high electron mobility transistors (HEMTs) have shown great promise for military and space applications, several researchers have focused on the radiation response of these devices, and their findings are discussed below. The Schottky barrier diode (SBD) forms an integral part of the HEMT structure. A stand alone SBD is also useful as a photodetector or an electrical rectifier. An overview of radiation effects on both of these devices is presented below.

2.5.1 SBD Response

As majority carrier devices, SBDs are inherently more radiation tolerant than p-n junctions [27]. The most radiation sensitive parameter in SBDs is usually reverse leakage current, caused by trap-assisted carrier generation in the depletion region [69]. Radiation can also cause a decrease in Schottky barrier height due to carrier removal. However, the Schottky barrier height of real devices is often determined by surface defects [14, 16]. These can be present in large densities and relatively insensitive to carrier removal. The SBD ideality factor, n_f , also increases with increases in radiation dose due to the increase in non-thermionic currents. Analytical expressions have been formulated for defect related contributions to the SBD forward and reverse currents [70, 71] and defect concentrations and activation energies may be extracted from temperature dependent I-V data [72]. This technique is generally not as reliable as DLTS, however.

2.5.2 HEMT Response

The primary DC performance parameters of standard GaN field effect transistors (FETs) that decrease with radiation displacement damage are maximum transconductance and drain saturation current. Additionally, low-frequency and generation-recombination noise have both been observed to increase with increase in defect concentration [79]. In GaN-based HEMTs specifically, radiation damage in the thin n-doped AlGaN layer causes a decrease in the two-dimensional electron gas (2DEG) concentration. This could be caused by compensation from acceptor-type defects in the AlGaN layer, but the effect may in fact be dominated by a radiation-induced reduction in the piezoelectric field within the AlGaN layer. Bradley *et al.* [73] correlated the reduction of as-grown 2DEG carrier density in certain MBE-grown HEMTs with an $\text{Al}_{0.3}\text{Ga}_{0.7}\text{N}$ defect luminescence peak at 2.34 eV. Cai *et al.* [74] reported a 68% and 62% reduction in the transconductance and drain saturation current of an MBE-grown $\text{Al}_{0.15}\text{Ga}_{0.85}\text{N}/\text{GaN}$ HEMT following irradiation with 1.0×10^{14} protons/cm² at 1.8 MeV. After annealing for 40 seconds at 800 °C, the transconductance and drain saturation current returned to 70% and 85% of the respective pre-irradiation values. Hall measurements revealed that an increase in electron carrier concentration was responsible for the recovery, whereas mobility decreased after the annealing. Luo *et al.* [75] performed a radiation study on similar HEMTs of varying channel geometries which were fabricated by SVT Associates [76]. The devices were irradiated with 40 MeV protons from 5×10^9 to 5×10^{10} cm⁻², followed by isothermal annealing at 300 °C. Transconductance decreased by less than 15% for a dose of 5×10^9 cm⁻². The authors attributed this to an increase in channel resistance. Additionally, Luo *et al.* found that reverse bias breakdown voltage increased

in magnitude with dose, suggesting that carrier removal dominated the rise in resistivity. The decrease in saturation current was 30-50% for the highest dose of $5 \times 10^{10} \text{ cm}^{-2}$. They reported a significant increase in both transconductance and saturation current following 60 seconds of annealing at 300 °C. There was no systematic effect of gate width or length on the HEMT parameters. Gaudreau *et al.* [67] recently reported temperature dependent Hall effect measurements on 2 MeV proton-irradiated MBE-grown $\text{Al}_{0.3}\text{Ga}_{0.7}\text{N}/\text{GaN}$ 2DEG test structures. Between a fluence of 3×10^{14} and $3 \times 10^{15} \text{ cm}^{-2}$, the structures changed from being a conductor to being an insulator. The sheet charge density dropped to about 50% of its original value and the mobility dropped to about 20% of its original value. A further increase in resistivity beyond a fluence of $3 \times 10^{15} \text{ cm}^{-2}$ was due to a large drop in mobility, whereas sheet charge density remained mostly unchanged.

III. Experimental Procedures

This chapter describes the procedures used to obtain the experimental data presented in chapter V. The reasons for choosing the given test materials are discussed first, followed by a description of the preparation of test samples. Next are described the procedures by which electron radiation doses were applied to the samples. Finally, the three main characterization techniques; DLTS, Hall Effect, and CL are introduced along with specific procedures followed when applying these characterization techniques.

3.1 Sample Selection and Preparation

The $\text{Al}_x\text{Ga}_{1-x}\text{N}$ material used in this study was purchased from SVT Associates [76]. Previous experience proved that this company was capable of producing good quality GaN for electrical and optical characterization as well as good quality $\text{Al}_x\text{Ga}_{1-x}\text{N}$ ($x \leq 0.3$) for optical characterization. The $1\mu\text{m}$ thick $\text{Al}_x\text{Ga}_{1-x}\text{N}$ layers were grown by plasma-assisted MBE on the c-plane of 0.5 mm thick polished sapphire substrates with low-temperature grown AlN buffer layers between the two. Each wafer was custom ordered with a requested aluminum mole fraction and silicon doping level. Before choosing the requested silicon doping levels, a simple estimate of room temperature carrier concentration was made by solving the charge neutrality equation with the assumption of a single hydrogenic donor level and a given background concentration of acceptors [77],

$$\frac{n(n + N_A)}{N_D - N_A - n} = \frac{N_C}{g} \exp\left(-\frac{E_D}{k_B T}\right) . \quad \text{III-1}$$

Here, n is the carrier concentration, N_D is the intentionally doped donor concentration, N_A is the unintentionally doped acceptor concentration, and g is the degeneracy, which is equal to 2. E_D is the donor ionization energy given by

$$E_D = 13.6 \left(\frac{m^*}{m_o} \right) \left(\frac{\epsilon_o}{\epsilon_r} \right)^2 \text{ eV}, \quad \text{III-2}$$

where m^* and ϵ_r are the electron effective mass and static dielectric constant of $\text{Al}_x\text{Ga}_{1-x}\text{N}$ for the given Al mole fraction. From equation III-2, the ϵ_r values in table II-1, and the effective mass $m^* = 0.22 m_o$ the donor ionization energies are 38, 48, and 53 meV for $x = 0, 0.2$, and 0.3 , respectively. Theory indicates that the V_{Ga} acceptor formation energy decreases as E_f increases in GaN [29]. Thus, more V_{Ga} acceptors are formed during growth of GaN that is more n-type. Another source of compensation is Si atoms that reside on N lattice sites, acting as acceptors instead of donors. Thus, N_A is not independent of N_D , and can be approximated as being a constant fraction, called the compensation ratio of N_D . This constant fraction is typically equal to 0.6 ± 0.1 [77,78]. Using this compensation ratio and $N_D = 10^{17} \text{ cm}^{-3}$, equation III-2 yields a 295 K carrier concentration of $n = 2.9 \times 10^{16}$ and $2.5 \times 10^{16} \text{ cm}^{-3}$ for $x = 0$ and 0.3 , respectively. In both cases, then, the donor level is sufficiently shallow for nearly complete ionization at room temperature. At 77 K, the carrier concentrations are 3.2×10^{14} and $3.4 \times 10^{13} \text{ cm}^{-3}$ for $x = 0$ and 0.3 , respectively. Actual silicon ionization energies are generally shallower (for $x \leq 0.3$) than those predicted by the simple theory above due, in part, to free carrier screening. For $x = 0$ and $N_D = 3 \times 10^{17} \text{ cm}^{-3}$, it is found experimentally that $E_D = 17 \text{ meV}$ [41]. For $x = 0.3$ and $N_D = 4 \times 10^{17} \text{ cm}^{-3}$, $E_D = 20 \text{ meV}$ [79]. The effect of screening upon donor ionization energy can be approximated by

$$E_D(N_D) = E_{D0} - \alpha N_D^{1/3},$$

III-3

where the screening factor, α , was empirically determined to be 2.1×10^{-5} meV-cm for Si in GaN [80]. A screening factor of 2.5×10^{-5} meV-cm has been reported for $\text{Al}_{0.23}\text{Ga}_{0.77}\text{N}$ [81].

The actual measured ionized carrier concentrations (for $x > 0$) proved to be somewhat unpredictable. One reason for this was that the carrier concentration measured by the growers for quality assurance was artificially high due to an impurity conduction layer near the sapphire substrate interface. However, it was also apparent that precise control of silicon doping concentration was fundamentally more difficult for $x > 0$ than it was for $x = 0$. The aluminum mole fraction of the wafers was reported by SVT Associates based on CL and X-ray diffraction measurements. The CL measurements performed at AFIT showed a small variation in the radial direction such that aluminum mole fractions were greatest at the center of each wafer. A $2 \mu\text{m}$ thick GaAs epitaxial layer doped at $6.0 \times 10^{17} \text{ cm}^{-3}$ with silicon was also included in this study. This epitaxial layer was grown by MBE on a GaAs substrate at the Air Force Research Laboratory. The purpose for including this wafer was to compare the radiation hardness of $\text{Al}_x\text{Ga}_{1-x}\text{N}$ with the better known GaAs grown by a comparable epitaxial technique. An $\text{Al}_{0.27}\text{Ga}_{0.73}\text{N}/\text{GaN}$ single heterostructure grown by Cree, Inc. [82] was also included in this study to compare the effects of radiation doses on the heterostructure transport properties. Table III-1 lists the alpha-numeric designations of the wafers used in this study as well as their measured properties. The third and forth columns of this table show the apparent carrier concentration and mobility determined by room temperature

Table III-1. Wafer properties and designations.

I.D.	Material Type	Apparent Carrier Conc. (e^-/cm^3)	Apparent Mobility ($\text{cm}^2/\text{V-s}$)	Corrected Carrier Conc. (e^-/cm^3)	Corrected Mobility ($\text{cm}^2/\text{V-s}$)	CL Peak Energy (eV)
A1	$\text{Al}_x\text{Ga}_{1-x}\text{N}$ $x = 0$	0.65×10^{17}	139	0.65×10^{17}	140	3.49
A2	$\text{Al}_x\text{Ga}_{1-x}\text{N}$ $x = 0$	1.6×10^{17}	324	1.6×10^{17}	324	3.49
B1	$\text{Al}_x\text{Ga}_{1-x}\text{N}$ $x = 0.10$	2.3×10^{17}	78	$< 1.0 \times 10^{17}$		3.71
B2	$\text{Al}_x\text{Ga}_{1-x}\text{N}$ $x = 0.14$	2.7×10^{17}	56	8.2×10^{16}	64	3.87
C1	$\text{Al}_x\text{Ga}_{1-x}\text{N}$ $x = 0.20$	6.5×10^{17}	44.3	3.0×10^{17}	49.4	4.00
C2	$\text{Al}_x\text{Ga}_{1-x}\text{N}$ $x = 0.20$	1.0×10^{17}	13.3	0.8×10^{17}	14.6	4.00
D1	$\text{Al}_x\text{Ga}_{1-x}\text{N}$ $x = 0.30$	2×10^{17}	25-35	1×10^{17}	30-45	4.26
D2	$\text{Al}_x\text{Ga}_{1-x}\text{N}$ $x = 0.30$	8.6×10^{17}	15.7	$7-8 \times 10^{17}$	16.1	4.26
E1	$\text{Al}_{0.27}\text{Ga}_{0.73}\text{N}$ /GaN	Sheet conc. $1.1 \times 10^{13} \text{ cm}^{-2}$	1410			
F1	GaAs	6.4×10^{17}	2980			1.52

Hall measurement of a representative sample from the wafer. The fifth and sixth columns show the corresponding carrier concentration and mobility corrected for interfacial layer conduction as described in section 3.4.2 below.

The last column of table III-1 lists the $T = 6 \text{ K}$ peak CL energies of the samples used in this work, and these energies are plotted as data points in figure III-1 to compare with the predicted band gap energy assuming different bowing parameters. It is seen that a bowing parameter, $b = 0.35$, provides the best fit to the plot of band gap versus aluminum mole fraction x in these samples.

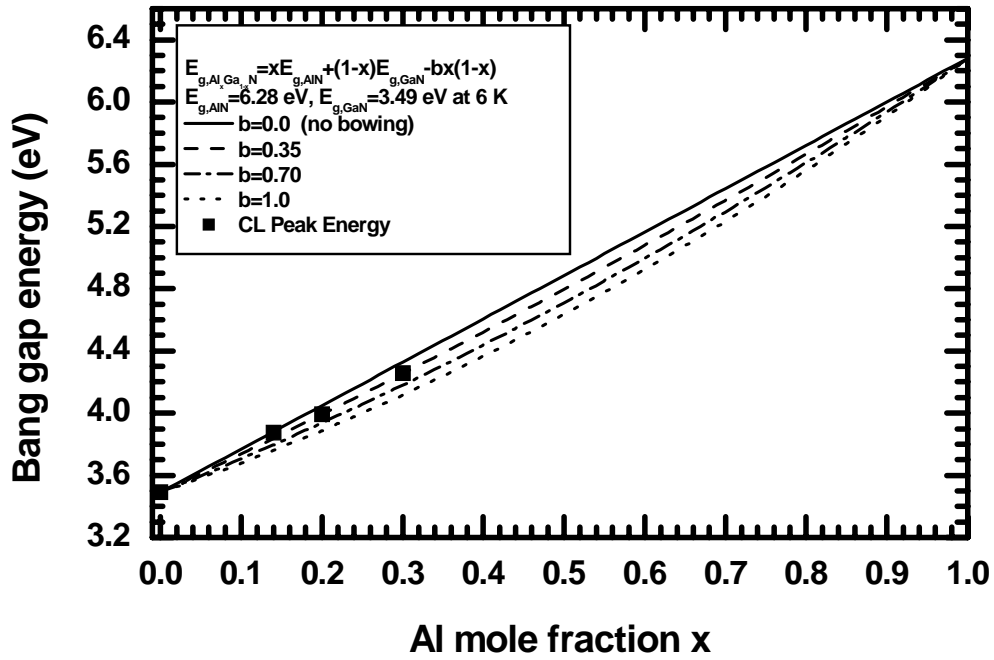


Figure III-1. Measured CL peak energies (black squares) of $Al_xGa_{1-x}N$ samples versus x . The CL measurements are performed at $T = 6$ K.

Most sample preparation including cleaning, masking, metal deposition, and contact annealing was performed in the AFIT clean room. Each 2" diameter wafer arrived with a thin titanium backing that had to be etched away in a hydrofluoric acid solution. The titanium backing had been necessary to distribute heat across the substrate during MBE growth. The wafer was then cut into 5x5 mm squares (die) with a diamond blade saw. A number was marked on the back of each sample with a diamond scribe in order to keep track of the sample's original location on the wafer. The oxidized layer expected to be on the surface of each sample was removed by immersion in boiling aqua regia (1:3 $HNO_3:HCl$) for 2-4 minutes. Ohmic contact areas were then defined by photolithography (discussed below) for the DLTS samples and by a perforated stainless

steel mask for the Hall samples. The Ohmic metal was deposited by electron beam evaporation. The Ohmic metallization used for GaN samples was Ti(400Å)/Al(2000Å), where the notation indicates that 400 Å of titanium is deposited first, followed by 2000 Å of aluminum. The standard Ohmic metallization used for AlGaN samples was Ti (300 Å)/Al (800 Å)/Ti (1200 Å)/Au (500 Å). Following Ohmic metal deposition (and photoresist lift-off in the case of the DLTS samples), the samples were annealed at 900 °C for 45 s in a nitrogen gas ambient. This step was performed in the rapid thermal annealing furnace located in the AFIT clean room. At this point, the Hall samples were ready for characterization. The DLTS samples required the additional steps involved in making Schottky barrier contacts. As with the Ohmic contact areas, the circular Schottky contact areas (diameters of 200, 300, and 400 μm) were defined via photolithography. In this process, 1813 photoresist was spread into a uniform layer on the surface of the sample at 4000 rpm. The sample was then placed on a 100 °C hot plate for 5 minutes in order to dry the photoresist. The sample was then placed in contact with the photographic mask in the mask aligner and exposed to UV light for 20 s. The exposed areas of the sample were then removed by immersing the sample in 351 developer solution for 30 s. The sample was then rinsed in de-ionized water (DIW) for 30 s followed by a 30 s dip in dilute hydrochloric acid solution (1:10 HCl:DIW) and subsequent DIW rinse. The dilute HCl is used to remove surface oxidation that grew since the previous oxidation removal step. Following every DIW rinse, the sample was blown dry with nitrogen gas. At this point, the sample had a photoresist-defined pattern of exposed circular areas that were clean and de-oxidized. The sample was then placed in the electron beam evaporator such that the entire masked surface was exposed to metal

deposition. The metallization used for Schottky barrier contacts was Ni (350 Å)/Au (4000 Å). Following metallization, lift-off of the photoresist was accomplished by placing the sample in acetone and exposing it to ultrasonic agitation for 10-20 minutes. At this point the sample could be diced and packaged for DLTS measurements. The 5x5 mm samples were typically diced into four square quarters using a diamond-tip scribing tool. This step yielded samples small enough to fit onto the TO-5 cans used for DLTS characterization. A manual ultrasonic gold wire bonder was used to make a gold wire connection between one of the circular Schottky contacts on the sample and one of the gold posts on the can. The wire bonder was also used to make a gold wire connection between the Ohmic area on the sample and another gold post on the can. A complication was encountered in this step, as it was found that the wire bond would not adhere to the annealed Ohmic contact area directly. Consequently, the procedure was altered such that Au was deposited to connect at least one of the Schottky pads and the Ohmic contact area. This step was accomplished by masking off the appropriate area with rubber cement or the sticky part of a Post-it™ note, and then sputtering gold onto the surface in a table-top sputterer. After this step, the exposed Schottky pad served as an Ohmic contact.

3.2 Irradiation Procedures

The electron irradiations were performed at the Wright State University Van de Graff (VDG) generator facility. The available electron beam energy range is approximately 0.40-1.8 MeV. The available beam current depends on the chosen energy. Typical beam currents that allow for stable operation fall in the range of 1-30 μA . At the lowest achievable energies, the beam current drops off considerably, and the beam energy tends to be unstable. A current integrator attached to the cold head keeps a running count

of the negative charge impinging on the cold head. The total fluence is then given with explicit dimensional analysis as

$$\Phi = \frac{Q_{TOT}}{A} \cdot \frac{Coulomb}{cm^2} \cdot \frac{1}{1.602 \times 10^{-19}} \cdot \frac{e^-}{Coulomb} = \frac{Q_{TOT}}{1.602 \times 10^{-19} A} \cdot \frac{e^-}{cm^2}, \quad \text{III-4}$$

where A is the irradiated area, and Q_{TOT} is the total integrated charge. Before January of 2003, this area was approximately equal to 3.3 cm^2 . In January of 2003, however, a two inch spacer tube was inserted between the aperture and the cold head. The beam focal point is in front of the aperture. Thus, the beam diverges after this point in the beam line. It was found, by irradiating a plastic sheet at the plane of the cold head, that the new beam area was approximately 7.9 cm^2 , and this is the number used in calculating the fluence in all the doses of table III-2, with the exception of the dose applied on 30 Apr 04. At that time, the samples were mounted on a different cold head, and this other cold head was further from the aperture than the normal cold head. The divergence angle was determined from the previous spot size measurement to be approximately equal to 0.25 radians. This angle was used to determine that the beam area at the plane of this second cold head was 18.6 cm^2 . Because it took several weeks to complete the post-irradiation characterization, the samples were stored in liquid nitrogen following irradiation. This reduced the risk of obtaining conflicting results due to long-term room temperature annealing. All of the samples were exposed to at least 3 hours of room temperature annealing before being characterized. Table III-2 lists the parameters pertaining to irradiations performed in the course of this work.

Table III-2. Irradiation parameters.

Irradiation Date/ Facility	Energy/ Type	Beam Current	Irradiated Area	Effective Beam Flux	Total Fluence
20 Oct 03 WSU	1.0 MeV electrons	15 μ A	7.9 cm ²	1×10^{13} cm ⁻² s ⁻¹	9×10^{16} cm ⁻²
30 Apr 04 WSU	1.0 MeV electrons	10 μ A	18.5 cm ²	6×10^{12} cm ⁻² s ⁻¹	2×10^{16} cm ⁻²
9 Jun 04 WSU	1.0 MeV electrons	10 μ A	7.9 cm ²	8×10^{12} cm ⁻² s ⁻¹	9×10^{16} cm ⁻²
31 Aug 04 WSU	0.62 MeV electrons	1.5 μ A	7.9 cm ²	8×10^{12} cm ⁻² s ⁻¹	2.5×10^{16} cm ⁻²

3.3 Deep Level Transient Spectroscopy (DLTS)

The core components of the DLTS system used in this dissertation research (figure III-2) consist of an evacuated JANIS Corp. sample chamber with closed cycle refrigerated helium cold head and coaxial electrical feedthroughs, a Lake Shore 330 temperature controller, a SULA Corp. capacitance meter, which supplies a 100 mV test waveform at 1 MHz to measure capacitance, a Lecroy 1 GHz pulse generator for system timing signals, and a PC and data acquisition board, which supply all pulsed and steady-state bias voltages to the diode and control the entire data acquisition process in an automated manner. The temperature range of the sample chamber is 50 to 450 K, and temperature control is good to ± 0.1 K in most temperature ranges. All measurements in this study are made on a 100 pF capacitance range setting. The auxiliary equipment includes a Keithley 237 Source Measurement Unit (SMU), which is used for I-V measurements, and a Lecroy 9410 oscilloscope, which is used to monitor diode input and output voltage waveforms. Additionally, a low-pass filter with a cutoff frequency of

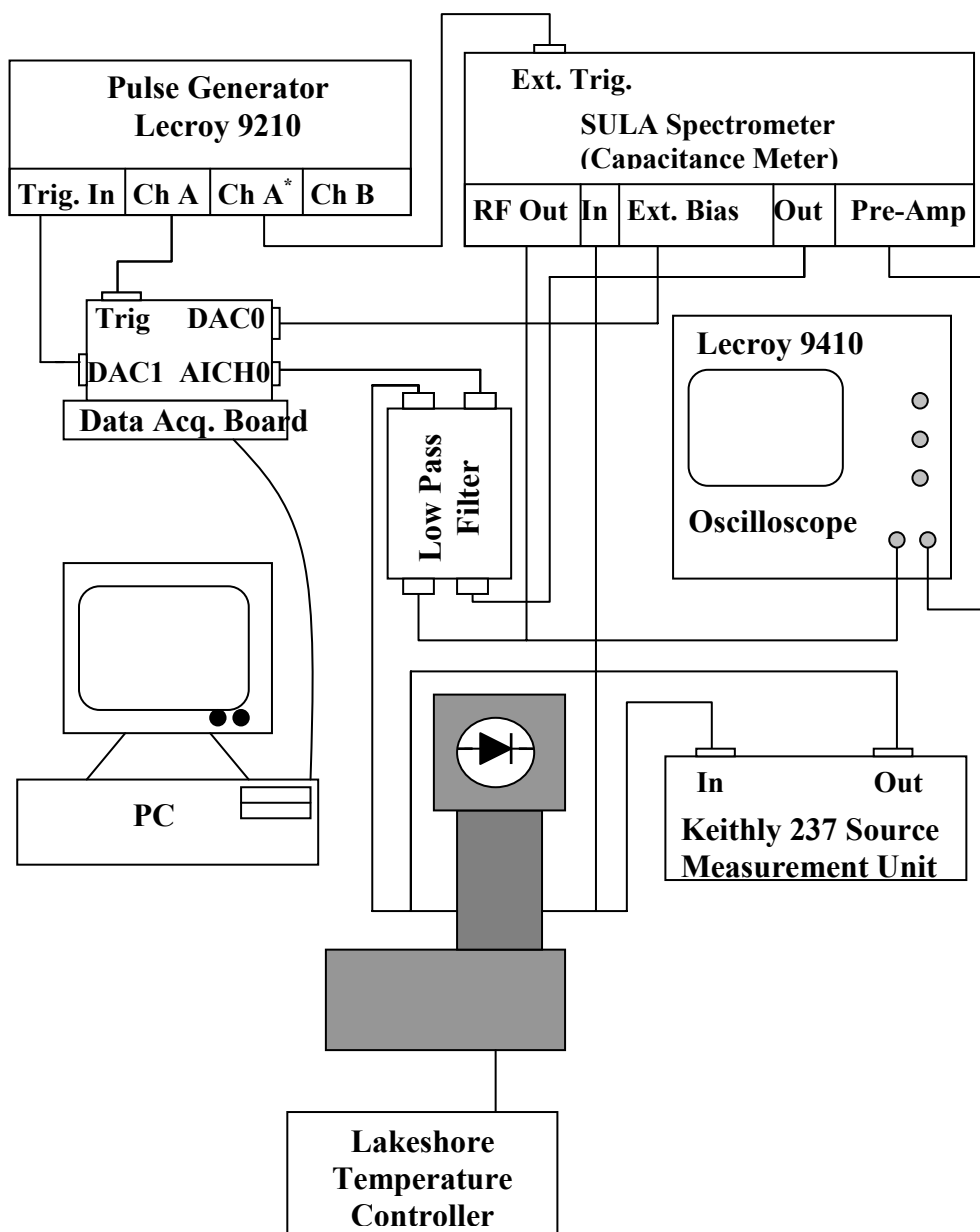


Figure III-2. Schematic diagram of DLTS system used in this study. The Keithly 237 SMU is used for I-V measurements (after Scofield [72])

slightly greater than 1 MHz was inserted in the signal path for improved signal-to-noise ratio.

The wire-bonded SBD is placed in good thermal contact with the cold head and fine coaxial wires are connected to the Ohmic and Schottky leads that protrude from the TO-5 can. These wires run to a coaxial feedthrough outside of which BNC cables run to the capacitance meter. Before beginning the DLTS temperature scan, room temperature capacitance vs. voltage (C-V) and current vs. voltage (I-V) measurements were performed at room temperature. These measurements, which were also performed at about 20 K increments throughout the 50-450 K temperature range, are essential diagnostic tools for determining the quality of the SBD, and thus the suitability for DLTS measurements. Additionally, the computer control program that makes the C-V measurement also determines the ionized shallow donor concentration N_D from the slope of the $1/C^2$ vs. V curve. This calculation is based on the relationship [83]

$$N_D = \frac{2}{e\epsilon_s A^2 \left[d(1/C^2)/dV \right]}, \quad \text{III-5}$$

where ϵ_s is the static dielectric constant and A is the area of the Schottky contact. These two values are given as inputs to the program.

The data which are directly obtained by the DLTS procedure are digitized capacitance transients recorded at 2 K temperature intervals across a certain temperature range. Capacitance transients are depicted in figure III-3. The bias voltage applied to the SBD during DLTS measurement is depicted in the upper section of figure III-3. The SBD is initially held at a reverse bias voltage of magnitude V_r . The capacitance corresponding to the SBD thus biased, C_o is as shown in the lower section of figure III-3. This static situation is interrupted by a forward bias voltage pulse V_f of duration t_p . This

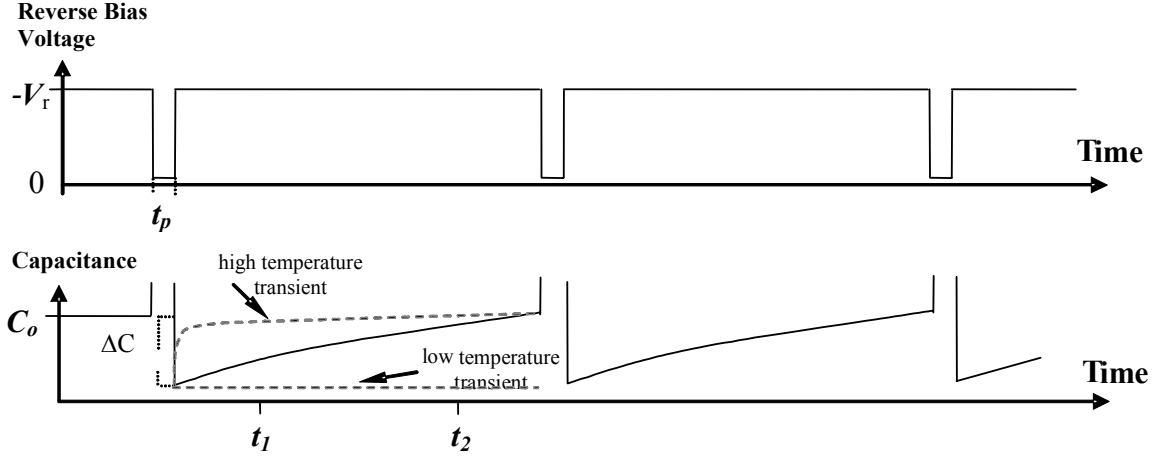


Figure III-3. Applied voltage pulses and corresponding capacitance transients in the DLTS measurement procedure.

V_f pulse causes the depletion region of the SBD to collapse and capacitance C to spike upward as shown. During this time, the introduction of majority carriers into the previously depleted region allows previously empty majority carrier traps to be filled. When the V_f pulse is removed, the depletion region returns to the usual width W plus an extra amount ΔW in response to the trapped majority carrier charge. This extra depletion width corresponds to a decrease in SBD capacitance indicated by ΔC in figure III-3. At reverse bias, the majority carrier traps emit the trapped carriers in an exponentially decaying manner with time constant e_n described in section 2.4.3. The emission corresponds to the exponential decay of $\Delta C(t)$ to the quasi-equilibrium value of C_o . This capacitance transient is expressed as

$$\Delta C(t) = \Delta C(1 - \exp(-e_n t)), \quad \text{III-6}$$

where $t = 0$ at the end of the filling pulse. In order to increase the signal-to-noise ratio in the measured capacitance transient, 500-800 transient signals are collected and averaged at each temperature step. The recorded capacitance transients may then be analyzed according to the methods of section 4.1.

One other way in which capacitance transients may be obtained is by double-correlated DLTS (DDLTS). The DDLTS technique simply subtracts the capacitance transient obtained with a smaller magnitude of forward voltage pulse V_{f2} from the capacitance transient obtained with a larger magnitude of forward voltage pulse V_{f1} . The resulting DDLTS capacitance transient represents the carrier trapping and emission in a narrow width of the depletion region defined by the choices of V_{f1} and V_{f2} .

3.4 Hall Effect Measurements

3.4.1 Room Temperature Hall Effect Measurements

The Hall effect has long been the standard method for measurement of free carrier concentration and mobility as well as resistivity. Figure III-4 shows a diagram of the basic components of the Lake Shore HMS 7700 Hall effect measurement system used in this study. As usual for measurement of epitaxial layers, the van der Pauw technique is used to measure resistivity and Hall voltage. In this technique, four Ohmic contacts are placed on the periphery of a sample as illustrated in figure III-5. The Ohmic metallization layers were deposited and annealed as described previously. In order to make electrical connection between the sample and the Hall measurement system, the sample was affixed with rubber cement to a removable sample mount, indium was soldered to the Ohmic contacts, and the four wires from the sample mount were then easily soldered to the indium.

The physical concept of the Hall measurement will be described here, briefly. A fixed current, I , is sourced between two opposing (across the diagonal) contacts under the

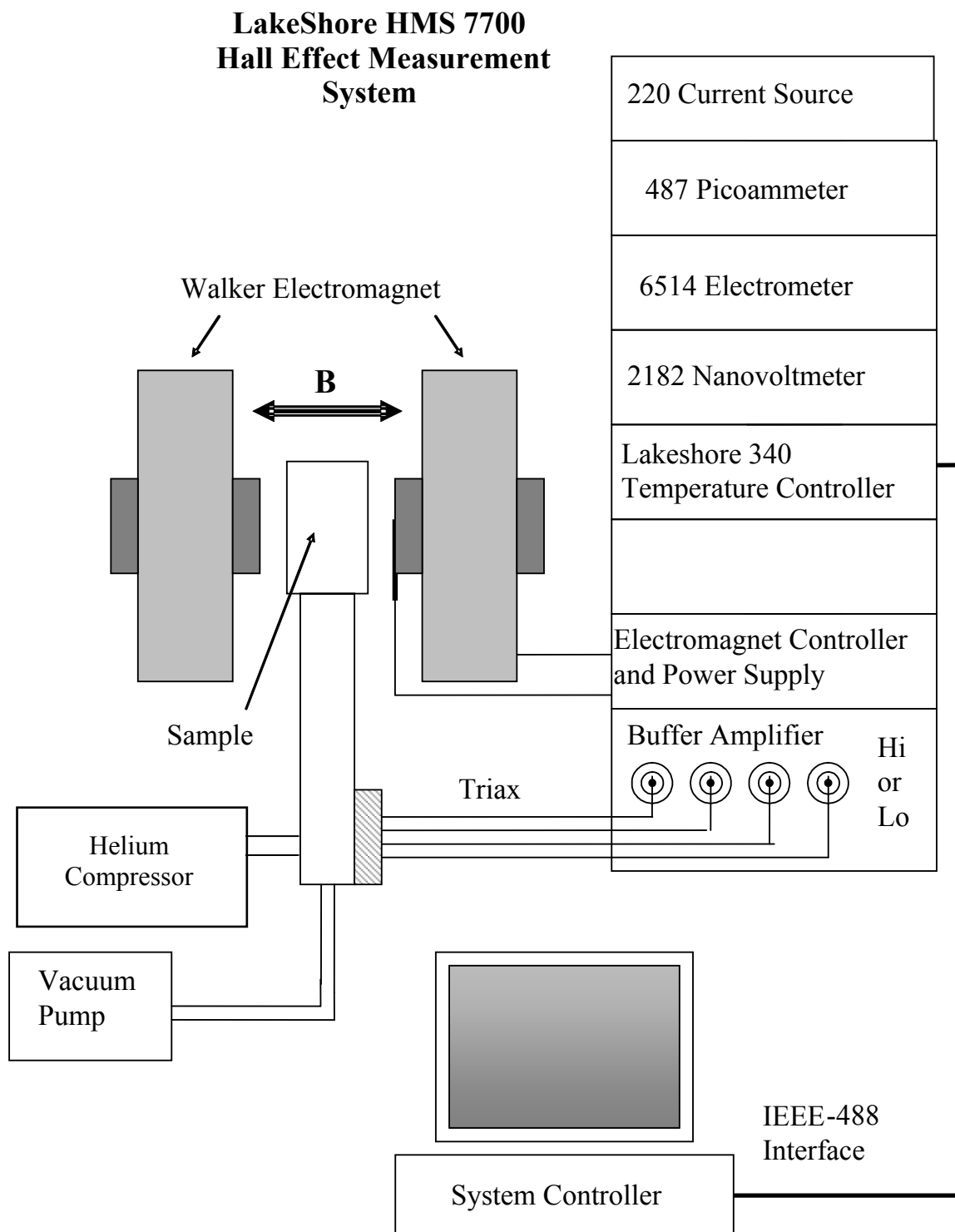


Figure III-4. Schematic of Temperature Dependent Hall measurement system.

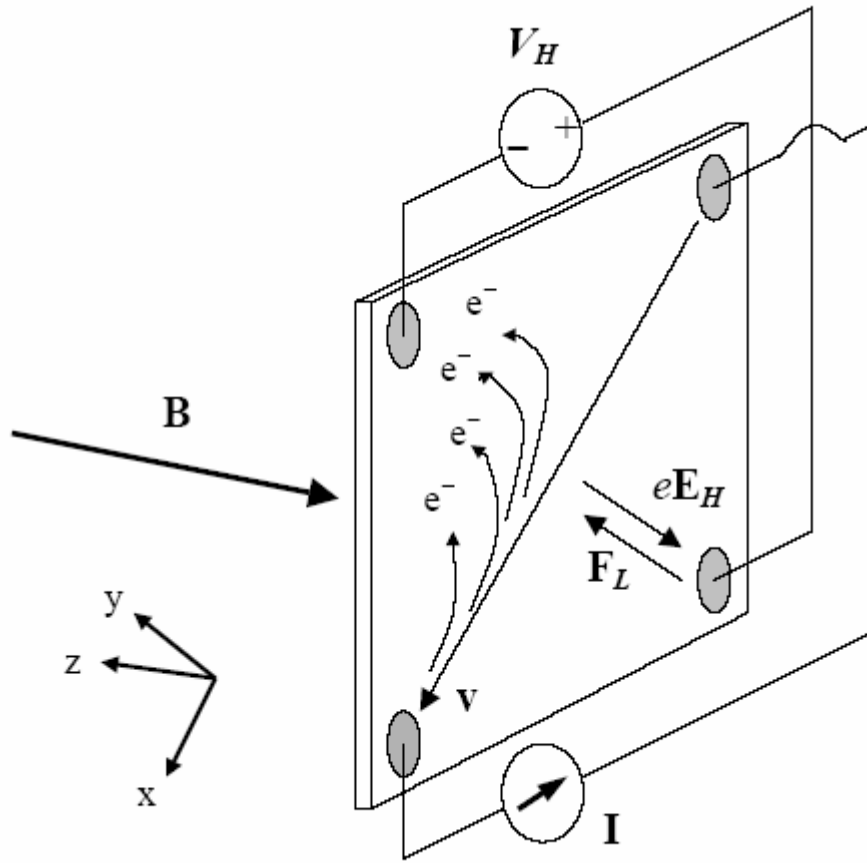


Figure III-5. Illustration of Hall effect in planar sample with Van der Pauw contact geometry [15].

influence of a perpendicularly directed magnetic field, \vec{B} . In this situation, the carriers experience the Lorentz force, given as

$$\vec{F} = q(\vec{v} \times \vec{B}), \quad \text{III-7}$$

where q is $-e$ for electrons and $+e$ for holes. Because electrons and holes have opposite charge and move in opposite directions under the applied electric field, the Lorentz force causes both carriers to be displaced in the same direction. The dominant carrier type causes a net dipole moment to result from this displacement, and it is measured as a

voltage between the opposing contacts. In a simplified Hall bar geometry, this Hall voltage would be given by the expression [15]

$$V_H = \frac{I_x B r_H}{e n_s} = R_{Hs} I_x B r_H. \quad \text{III-8}$$

In this expression, R_{Hs} is the sheet Hall coefficient and $r_H (= \langle \tau^2 \rangle / \langle \tau \rangle^2)$ is the Hall scattering factor, defined by τ , which is the mean time between scattering determined by a variety of scattering mechanisms [83]. R_{Hs} can be expressed as

$$R_{Hs} = \frac{V_H}{I_x B r_H}. \quad \text{III-9}$$

Assuming n-type material, the sheet carrier concentration, n_s , and the electron mobility, μ_n , are defined in terms of this coefficient as [83]

$$n_s = -\frac{r_H}{e R_{Hs}} \quad \text{III-10}$$

and

$$\mu_n = \frac{R_{Hs}}{r_H \rho_s}. \quad \text{III-11}$$

The Hall scattering factor can theoretically have any value in the range $1.0 \leq r_H \leq 2.0$, and 1.2 would be a typical values for many semiconductor samples. Because the individual scattering mechanisms are not characterized, r_H is assumed to be equal to 1.0. Thus, the quantities obtained from the Hall measurement are understood to be the Hall carrier concentration and Hall mobility, which overestimates the actual carrier concentration and underestimates the actual mobility by the factor r_H . In the van der Pauw geometry of figure III-5, ρ_s in equation III-11 is determined from a total of eight different current-voltage pair measurements, and then four different current-voltage pair

measurements are made under the application of the magnetic field to obtain R_{Hs} in equation III-10 and III-11. In the implementation here, the electromagnet current is reversed and R_H is also obtained under the reversed magnetic field. The average of the two R_H values is then used to calculate n_s and μ_n . These two values are calculated by the measurement system software. The volume carrier concentration is then obtained from the sheet concentration by

$$n = \frac{n_s}{d}, \quad \text{III-12}$$

where d is the thickness of the epitaxial layer. The source current used in this work ranged from 10^{-6} to 10^{-3} A, depending on the resistivity of the sample. Specifically, the current was chosen in order to keep the Hall voltage within the desired range of 10 to 500 mV.

3.4.2 Temperature-Dependent Hall Effect Measurements

In the case of temperature dependent Hall effect measurements, the above measurements and calculations are performed at different temperatures under automated computer control. The chamber is evacuated and an air-cooled helium compressor enables the cold head refrigerator to achieve 20 K sample temperature. The automated temperature control system then raises the temperature in programmed steps. Steps of 2.5 K were used when $20 \text{ K} \leq T \leq 70 \text{ K}$, and then 5 K steps were used when $70 \text{ K} \leq T \leq 320 \text{ K}$. A wait time of seven minutes was used at each temperature step to give the sample time to equilibrate with the sample holder. For shielding consistency and to avoid persistent photoconductivity effects, all of the measurements were performed in the dark, inside the vacuum chamber.

Because epitaxial layers of GaN and AlGaN are often observed to have a degenerate donor conduction layer near the substrate [45, 46], low temperature Hall effect measurements were necessary in order to deconvolve the conductivity contribution of the epitaxial layer from the conductivity contribution of the degenerate near-interfacial conduction layer. Following the deconvolution method outlined by Look [33], the measured sheet carrier density n_s and mobility μ at $T = 20$ K were taken to be equal to that of the sheet carrier density n_{s2} and mobility μ_2 of the near-interfacial conduction layer. This step was based on the assumption that the conduction in the near-interfacial layer is independent of temperature and that the epitaxial layer sheet carrier concentration n_{s1} and mobility μ_1 are very low at $T = 20$ K. With these assumptions, a two-layer conduction analysis [17] may be applied in order to extract the volume density n_1 and mobility μ_1 at temperatures higher than 20 K. This extraction is accomplished at each temperature step by the equations

$$\mu_1 = \frac{\mu^2 n - \mu_2^2 n_{s2} / d}{\mu n - \mu_2 n_{s2} / d} \quad \text{III-13}$$

and

$$n_1 = \frac{(\mu n - \mu_2 n_{s2} / d)^2}{\mu^2 n - \mu_2^2 n_{s2} / d}, \quad \text{III-14}$$

where d is the epitaxial layer thickness.

3.5 Cathodoluminescence

A diagram of the cathodoluminescence experiment is shown in figure III-6. The CL measurements were performed at 6 K under vacuum. The excitation source was a Kimball Physics EMG-12 electron gun. In this dissertation research, a beam energy of 5

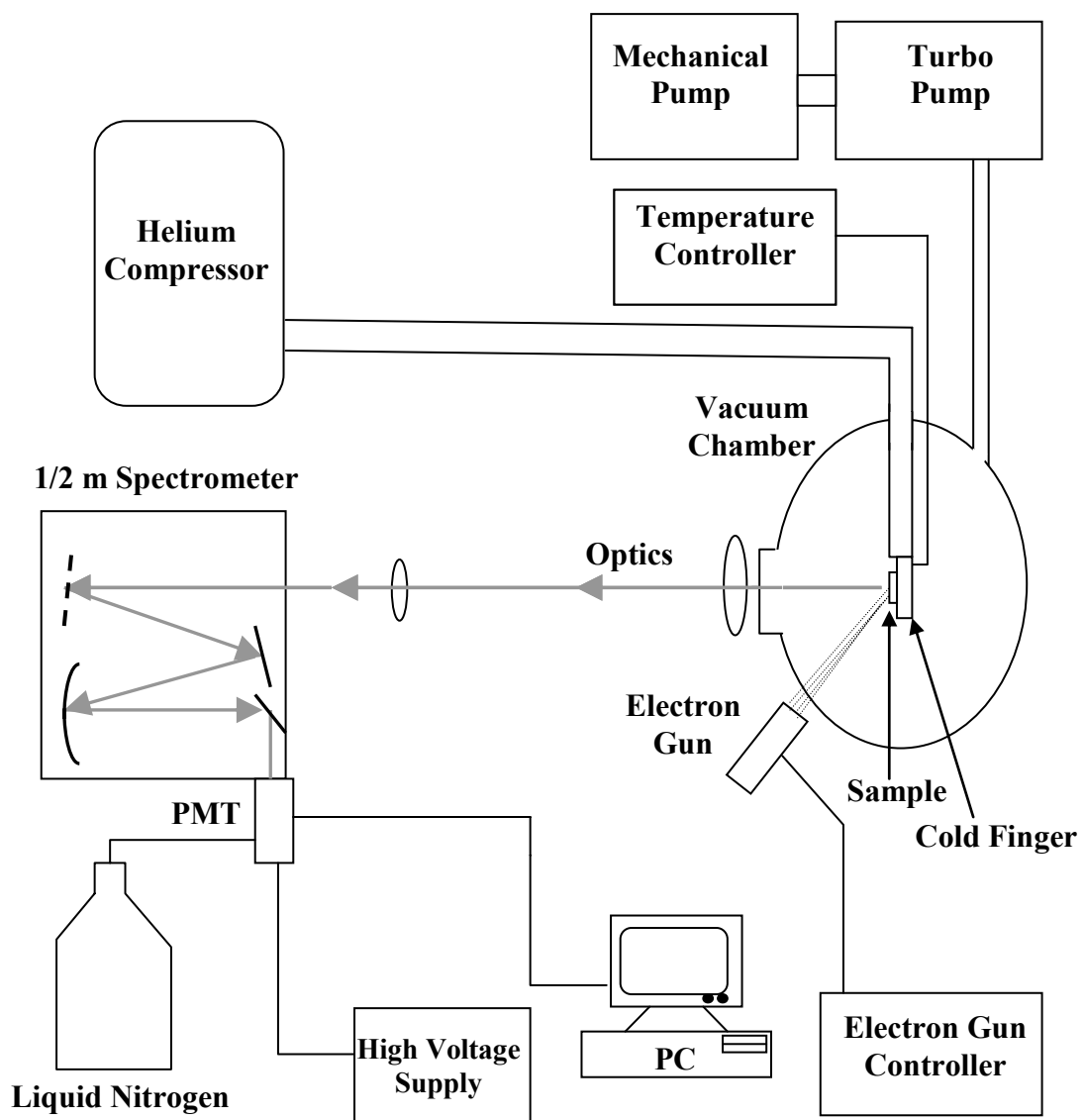


Figure III-6. Schematic of cathodoluminescence system [84].

keV was chosen with a beam current of 25 μA and focused spot size of approximately 2 mm diameter. The light emitted from the sample was dispersed by a SPEX 500M spectrometer with a 0.2 \AA resolution and directed into a liquid nitrogen-cooled photomultiplier tube (PMT) biased at 1500 kV. The PMT signal was recorded by the control computer at each wavelength step of the spectrometer. A typical scan of the spectrometer started at 2800 \AA and moved to 8000 \AA in 2 \AA steps. The chosen integration time was 0.1 s. CL characterization was performed on the Hall effect samples, and grounding wires were soldered to one Ohmic contact on each sample. The other ends of these wires were tied to the copper sample holder to prevent excess charge build-up on the sample surface during measurement.

IV. Analytical Procedures

4.1 Deep Level Transient Spectroscopy (DLTS)

4.1.1 Capacitance Transient Analysis

In this study, the digitized capacitance (C) transient data are analyzed according to the “boxcar” method (figure IV-1) whereby C is extracted at two different times, t_1 and t_2 . The difference $\delta C = C(t_1) - C(t_2)$ is a negative value for majority carrier trapping and a positive value for minority carrier trapping whether the material is n-type or p-type. In the remainder of this discussion the behavior of a majority carrier trap (specifically, electrons in n-type material) will be assumed, but the arguments are equally valid for minority carrier traps. As temperature is swept, a positive peak occurs in the signal – $\delta C(T)$ at temperature T_m (figure IV-1), and at this temperature it can be shown [83] that

$$e_n(T_m) = \frac{\ln(t_2/t_1)}{t_2 - t_1}. \quad \text{IV-1}$$

This emission rate constant, determined by the choice of t_1 and t_2 , is referred to as the “rate window.” Different combinations of t_1 and t_2 are chosen that will yield sufficiently different e_n . Taking the natural logarithm of both sides of equation II-46 and rearranging terms yields

$$\ln\left(\frac{e_n}{T^2}\right) = \ln\left(\gamma \cdot \sigma_n(\infty) \cdot \left(\frac{g_o}{g_1}\right) \cdot \left(\frac{\alpha}{k}\right)\right) + \frac{(E_{T0} + E_\sigma)}{1000k} \cdot \frac{1000}{T}. \quad \text{IV-2}$$

Equation IV-2 shows that a plot of $\ln(e_n/T^2)$ versus $1000/T$ (an “Arrhenius plot”) will produce a straight line having a slope equal to $(E_{T0} + E_\sigma)/1000k$ and a $T \rightarrow \infty$ intercept

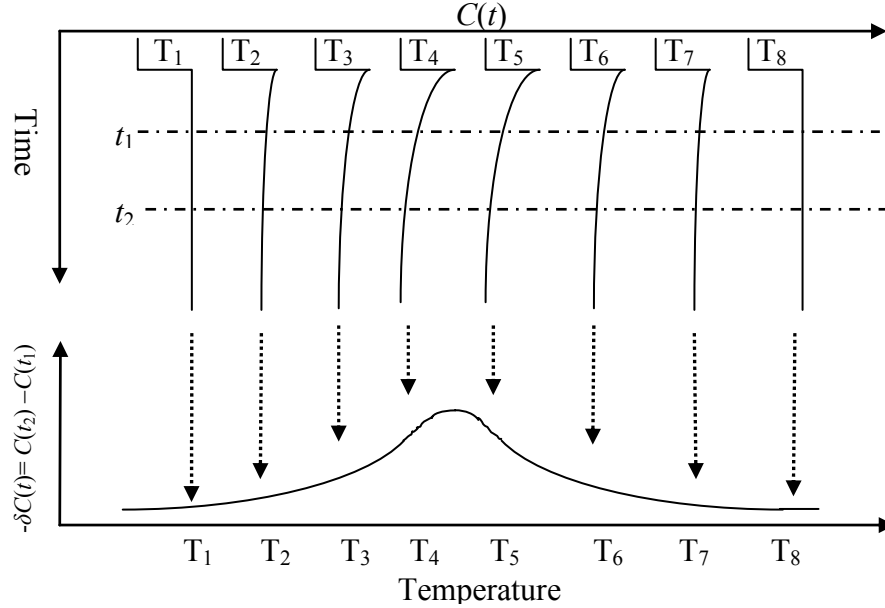


Figure IV-1. Illustration of how a rate window peak is obtained from temperature dependent capacitance transients (after Lang [85]).

equal to $\ln[\gamma (g_o/g_1)(\alpha/k) \sigma_n(\infty)]$. Accordingly, an Arrhenius plot is constructed from the measured $e_n(T_m)$ data and a linear fit reveals the total activation energy, $E_{TOT} (= E_{T0} + E_\sigma)$, and the apparent capture cross section, $\sigma_{na} (= (g_o/g_1)(\alpha/k) \sigma_n(\infty))$. These two values are often referred to as the “DLTS signature” of a trap level, and are often reported in the electrical characterization of deep trap defects. The measured activation energy and apparent capture cross sections can be used with the general expressions for emission from a single trap level [83],

$$\Delta C(T, t) = \Delta C(T, 0) \exp[-e_n t] \quad \text{IV-3}$$

and

$$e_n = v(T) \sigma_{na} N_c(T) \exp\left(-\frac{E_{TOT}}{kT}\right). \quad \text{IV-4}$$

in order to model the capacitance transient due to that level. In these expressions, $\Delta C(T, t)$ is the capacitance transient at time t following the end of the trap filling pulse, e_n the

emission rate, $v(T)$ the rms thermal velocity and $N_c(T)$ the conduction band density of states at temperature T . Peak broadening may be introduced into the above model by integrating equation IV-3 over a distribution of trap energies centered at E_{TOT} :

$$\Delta C(t) = \Delta C(0) \int_0^{\infty} g(E) \exp[-e_n(E)t] dE, \quad \text{IV-5}$$

where $g(E)$ is the Gaussian distribution function given by

$$g(E) = \left(\frac{1}{\sqrt{2\pi}S} \right) \exp\left[- (E - E_{TOT})^2 / 2S^2 \right] \quad \text{IV-6}$$

This simple model was applied to alloy-broadened DLTS data by Omling, *et al.* [86]. The parameter, S , is a measure of broadening. Care must be taken when applying this method to the case of overlapping peaks, as the choice of S for one peak can alter the positions and magnitudes of the adjacent peaks, with the magnitudes being the most susceptible to error.

4.1.2 Trap Concentration

It can be shown [83] that when the trap concentration, N_T , is much less than the net shallow donor concentration in the space charge region, $N_D^{net} (= N_D - N_A)$,

$$N_T \cong \frac{1}{f_\lambda} \cdot 2 \frac{\Delta C}{C_o} \cdot N_D^{net}, \quad \text{IV-7}$$

where it is also assumed that ΔC corresponds to complete filling of all the traps in the region of interest during the forward voltage pulse. The factor, f_λ , accounts for the thickness of the depletion region in which the trap level is already filled before application of the forward voltage pulse. The factor f_λ is given as [87]

$$f_{\lambda} = \frac{(w_r - \lambda)^2 - (w_f - \lambda)^2}{w_r^2}, \quad \text{IV-8}$$

and the thickness λ is given as [87]

$$\lambda = \left[\frac{2\varepsilon(E_F - E_T)}{e^2 \cdot N_D^{net}} \right]^{1/2}, \quad \text{IV-9}$$

where w_r is the depletion depth under the reverse bias voltage, and w_f is the depletion depth during the forward bias voltage pulse as depicted in figure IV-2. Equation IV-7 can be applied to specific rate window plot, where instead of $\Delta C/C_o$ ($= [C(0) - C(\infty)]/C_o$), the peak magnitude is a lesser value of $\delta C/C_o$ ($= [C(t_1) - C(t_2)]/C_o$). In this case, equation IV-7 can be re-written in terms of the ratio, $r = t_2/t_1$, as [83]

$$N_T \cong \frac{1}{f_{\lambda}} \cdot 2 \frac{\delta C}{C_o} \cdot \left[\frac{\exp\{[r/(1-r)] \ln r\}}{(1-r)} \right] N_D^{net}. \quad \text{IV-10}$$

For $r = 3$ and $r = 5$, two commonly used ratios in this dissertation research, the value in brackets becomes 5.20 and 3.74, respectively.

4.1.3 Pulse Width Dependence

During application of the forward bias voltage pulse, the previously empty point defect traps of a given species capture electrons according to [28]

$$N(t) = N_T [1 - \exp(-c_n t)], \quad \text{IV-11}$$

where $N(t)$ and N_T are, respectively, the filled and total concentrations of the specific trap species, and c_n is the electron capture rate (introduced in equation II-35) for that trap. By varying the filling pulse width t_p and recording the resulting $\Delta C/C$, equations IV-7 and IV-11 can be used to directly measure c_n at a given temperature. By inserting typical values of $n \sim 10^{17} \text{ cm}^{-3}$, $\langle v \rangle \sim 10^7 \text{ cm/s}$, and $\sigma_n \sim 10^{-16} \text{ cm}^2$ into equation II-35, it is found

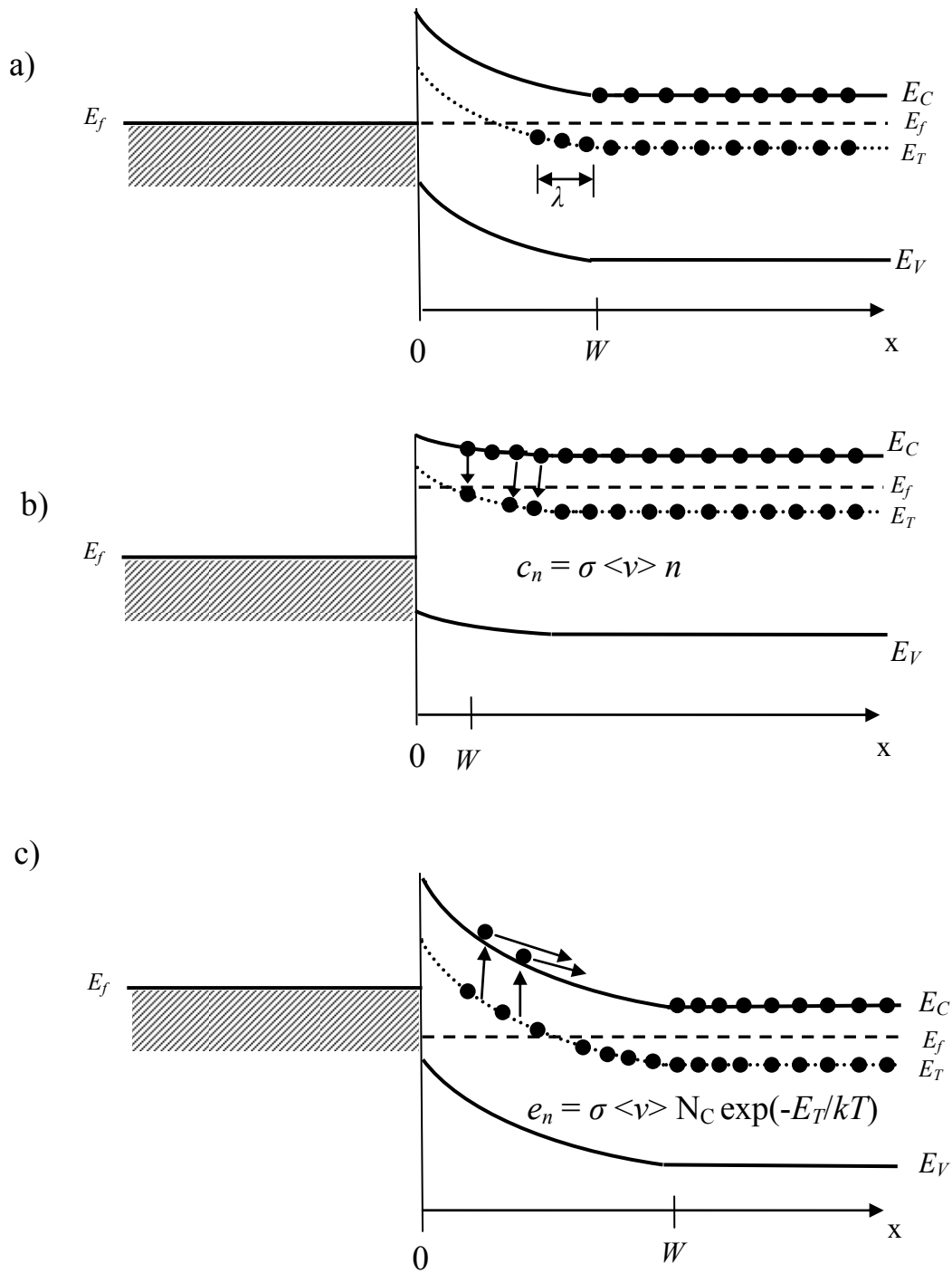


Figure IV-2. Energy band diagram of a Schottky barrier diode and single trap level: a) before; b) during; and c) after forward bias voltage pulse.

that $c_n \sim 10^8 \text{ s}^{-1}$. In this case, the traps would be 63% filled in 10 ns. Thus, a pulse width t_p on the order of 10 ns is required to measure trap filling versus t_p . For the DLTS system used in this study, the lowest available t_p is 20 μs , so such a measurement can not be performed.

Dislocation-related defects are known to display capture kinetics that deviate significantly from the form of equation IV-11. It has been observed in many materials including Si [88], GaAs [89], and GaN [90] that dislocation-related traps $N(t)$ do not approach a saturation value except when very long filling pulse widths ($>100 \text{ ms}$) are used. The increase in $N(t_p)$ (or $\Delta C(t_p)/C$) is linear when plotted versus $\log(t_p)$. It has been observed that the DLTS signature (E_a and σ_{na}) for these dislocation-related traps is often the same as for known point defects in the material. It was also observed [88] that for short pulse widths (when only a small fraction of N_T are filled) normal trap filling takes place according to equation IV-11. A simple model [91] was proposed to describe this dislocation-related capture behavior in terms of a repulsive Coulomb potential, ϕ_d , that reflects the number of charges captured at the dislocations. Figure IV-3 shows an energy band illustration of this model. With the addition of this repulsive potential, the electron capture rate valid for all filling pulse widths becomes

$$\frac{dN}{dt} = (N_T - N)n \langle v \rangle \sigma_n \exp\left[-q\phi_d(t_p)/kT\right] \quad \text{IV-12}$$

where $\phi_d(t_p)$ increases with t_p and has the effect of reducing the total number of electrons, n_ℓ , available for trapping in close proximity to the defect. As suggested in figure IV-3, the basic physical properties of the defect-related point defect remain the same as those of

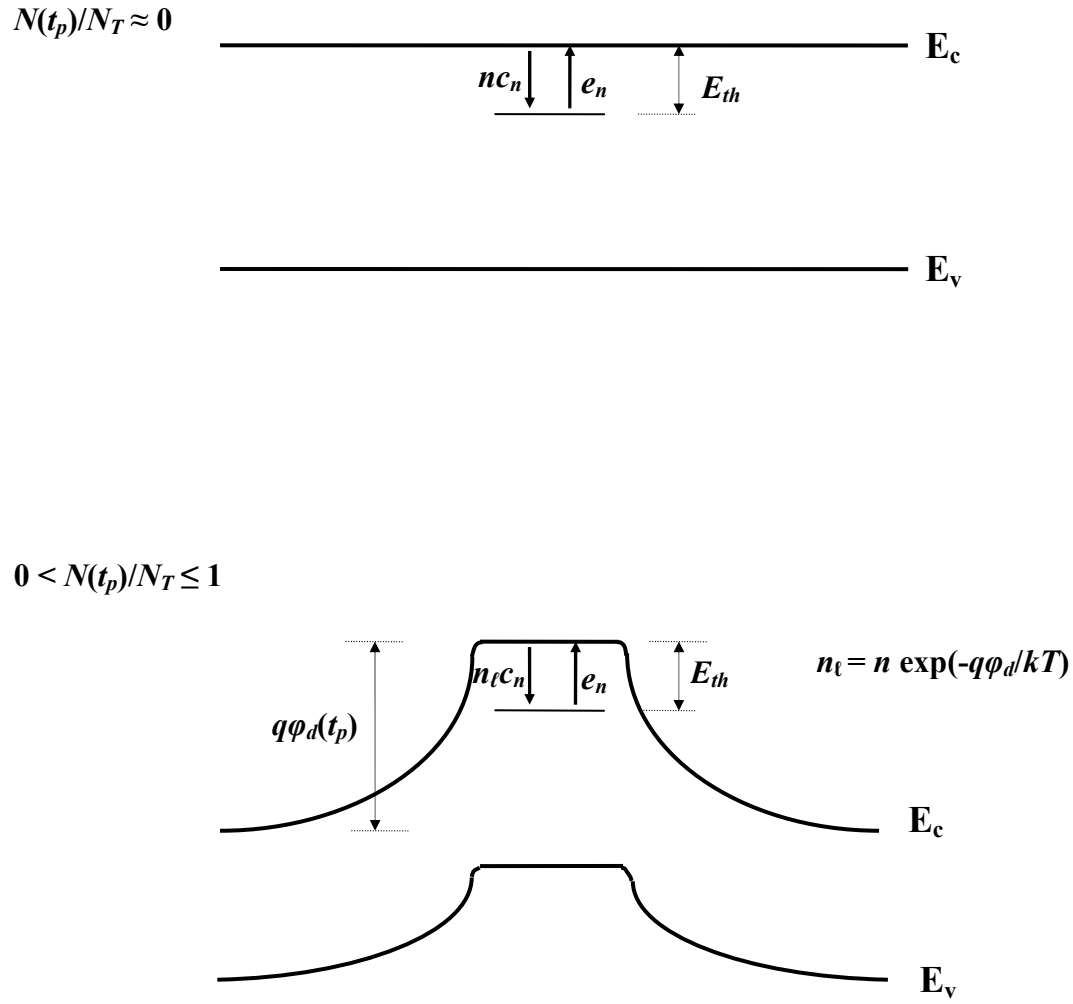


Figure IV-3. Energy band illustration of trapping at dislocation-related point defects. The situation for small occupation numbers ($N(t) \ll N_T$) resembles that for isolated point defects (after Omling *et al.* [88]).

the isolated point defect.

4.1.4 Field Dependence

In all DLTS measurements, carrier emission is measured under the influence of an electric field. If a trap is a single acceptor, it starts out neutral and becomes negatively charged upon capture of an electron. If a trap is a single donor, it starts out positively charged and becomes neutral upon capture of an electron. In the latter case, emission of the electron takes place against the Coulombic attraction to the positively charged donor ion. Expressed as a function of distance r from the donor ion, the potential energy is $U(r) = -q^2/\epsilon r$. Under the application of the electric field F in the x-direction the potential energy may be expressed in one dimension as [72]

$$U(x) = -\frac{e^2}{\epsilon x} + eFx. \quad \text{IV-13}$$

Differentiating with respect to x and setting the expression equal to zero yields the distance x_{min} at which the Coulombic attraction peaks. Plugging this value back into equation IV-13 yields the new Coulombic energy barrier that must be overcome, and this energy barrier is seen to be lower than the zero-field energy barrier by an amount ΔU given as

$$\Delta U = 2e\left(\frac{eF}{\epsilon}\right)^{1/2}. \quad \text{IV-14}$$

This so-called Poole-Frenkel barrier lowering becomes apparent in DLTS measurements as a decreasing linear plot of E_a or $\ln(e_n)$ versus $F^{1/2}$. Whenever such field-dependent behavior occurs, the trap may be assumed to be donor-like. The absence of such behavior, however, is not necessarily confirmation that the trap is acceptor-like [92]. A

classic example is the EL2 deep donor in GaAs, for which it has been shown that the Poole-Frenkel effect is greatly suppressed. Ganichev *et al.* [92] presented a model that showed how the presence of an E_b can cause this suppression. It was also shown that classical Poole-Frenkel emission can only be expected at low field strengths, whereas phonon assisted and direct tunneling begin to dominate at higher field strengths [92]. The latter two processes dominate at all field strengths in the case of neutral traps. The field-enhanced emission processes are illustrated in figure IV-4 for: a) a donor-type electron trap; and b) an acceptor-type electron trap.

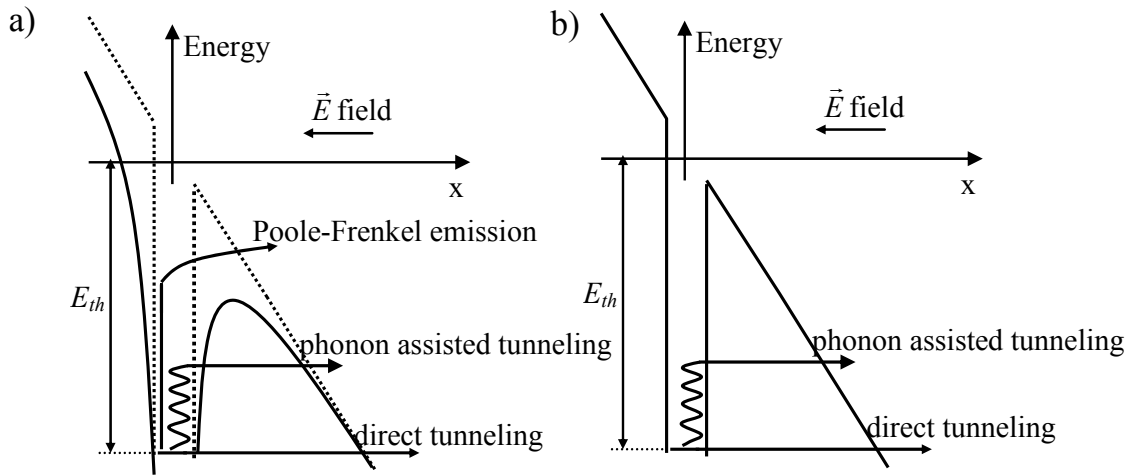


Figure IV-4. Potential barrier and emission processes a) for a charged (donor-type) electron trap and b) for a neutral (acceptor-type) electron trap (after Ganichev [92]).

4.2 Temperature Dependent Hall Effect Measurements

The corrected $n(T)$ data obtained using the procedures of section 3.4.2 may in principle be fitted by equation II-6 in order to model the given donor and acceptor levels

and concentrations. In this dissertation research, the fit was performed with the assumptions that $n(T)$ is determined by two dominant donor levels located within several kT of the Fermi level and that all other donor and acceptor energies are more than several kT below the Fermi level at all temperatures. The assumption of two dominant donors is based on previous results by Look [33] and Green [17] for epitaxial layers of GaN grown by HVPE. In those studies, $n(T)$ fitting indicated that a shallow donor level believed to be an impurity dominated the carrier concentration in addition to a deeper donor level believed to be the V_N donor. The introduction of a third donor with any chosen concentration and energy level provides the opportunity to obtain a better fit to the data at the expense of weakening the model with too many parameters. The second assumption that all acceptors are located more than a few kT below the Fermi level and thus ionized for $20\text{ K} \leq T \leq 300\text{ K}$ allows the summation of k acceptors in equation II-6 to be simplified as

$$\sum_k N_{Ak}^- \approx \sum_k N_{Ak} \equiv N_A^{eff}, \quad \text{IV-15}$$

where the parameter N_A^{eff} is the sum of all acceptor levels. This second assumption is based on the findings of Look [33] and Green [17]. Using equations II-3, II-4, and IV-15, equation II-6 may be expressed in the two donor model as

$$n = \frac{N_{D1}}{1 + \frac{1}{2} \frac{n}{N_C} \exp\left(\frac{E_{D1}}{kT}\right)} + \frac{N_{D2}}{1 + \frac{1}{2} \frac{n}{N_C} \exp\left(\frac{E_{D2}}{kT}\right)} - N_A^{eff}, \quad \text{IV-16}$$

where E_{D1} and E_{D2} are the ionization energies of the first and second donors. The fit was accomplished on a Mathcad worksheet by first plotting the carrier concentration data $n_d(T)$ and the modeled carrier concentration $n_m(T)$ from equation IV-16 versus $1000/T$ on

a logarithmic vertical scale. The model parameters N_{D1} , E_{D1} , N_{D2} , E_{D2} , and N_A were then individually adjusted until the model curve overlapped the data points over the widest temperature range possible. When the model could not match the data over the entire temperature range, parameters were chosen in order to fit to the higher data points. Data in higher temperature range ($T > 70 \text{ K}$) are less susceptible to error that is introduced from the near-interfacial conductive layer subtraction.

V. Experimental Results and Analysis

The data obtained and analyzed according to the procedures in chapters III and IV are plotted and discussed below. The results are grouped according to characterization technique, with DLTS results being presented, first; Hall effect results, second; and cathodoluminescence results, third. Analysis is presented along with experimental observations, with an additional analysis section being included to discuss the DLTS trends.

5.1 Deep Level Transient Spectroscopy (DLTS)

The DLTS rate window spectra of the pre-irradiated samples were found to vary significantly with aluminum mole fraction and silicon doping concentration. Experimental results from each wafer are thus presented separately, with comparisons being discussed in section 5.1.9.

5.1.1 Unirradiated GaN (wafer A2)

Figure V-1 shows the DLTS spectrum of unirradiated GaN (sample A2-4b) recorded with the pulse parameters $V_f = 0$ V, $V_r = -4$ V, and $t_p = 0.1$ s. Six separate peaks are labeled in the figure. An additional peak (labeled E) was revealed with DDLTS, but the DLTS signatures could not be measured for a reason discussed below. Arrhenius plots were obtained for the peaks A, B, C, and D, and these plots are displayed in the inset of figure V-1. The measured DLTS parameters corresponding to these peaks are listed in table V-1. It is seen that with the exception of trap A, the measured DLTS signatures agree well with those previously reported in the literature.

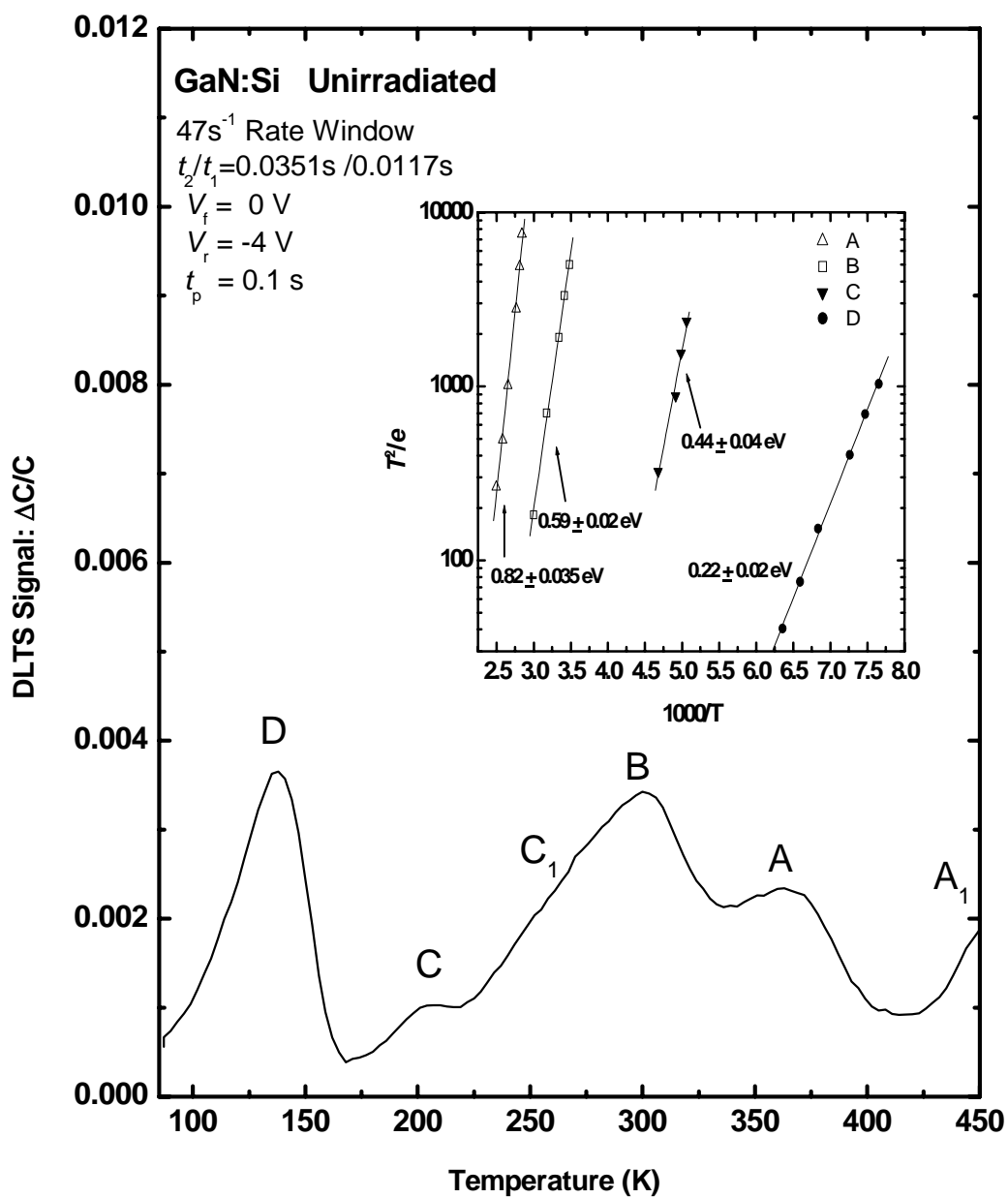


Figure V-1. DLTS spectrum of unirradiated GaN (sample A2-4b). Trap labels are assigned based on similarity to previously reported traps. The Arrhenius plots of peaks A, B, C, and D are shown in the inset.

Table V-1. Measured DLTS trap parameters in GaN and references to similar reports.

Parameter	E	D	C	C ₁	B	A
$T_{\text{peak}}^{\text{a}}$ (K)	~110	137	207	250-270	301	365
E_{TOT} (eV)		0.22±0.02	0.44±0.04	-	0.59±0.02	0.82±0.04
σ_{∞} (10 ⁻¹⁶ cm ²)		2.8	1300	-	56	1500
Similar traps and E_{TOT} (eV)	ED2 0.11 E1 ⁹⁰ 0.19 D2 0.16	D 0.25 EO2 0.27 E1 0.26 D ₁ 0.20 DLN ₁ ⁹³ 0.24	C 0.41 ES3 0.40	C ₁ 0.43-0.48 ES4 0.45±.1	B 0.62 E2 0.58 D2 0.60	A 0.67 EO5 0.61 E3 ⁹⁴ 0.67 D3 ⁹⁵ 0.67

^a Peak temperature determined with 47s⁻¹ rate window.

The peak that begins to develop at the high temperature end (~ 450 K) of the spectrum only appears for filling pulse widths larger than 1 ms. Limitations on the temperature and rate window do not allow the trap parameters to be extracted for this trap, but other people have observed a trap in this temperature range of 400-450K, and it has been labeled A₁, [49], DLN₄ [93], and E4 [94]. The reported activation energy of A₁ ranges from 0.86 to 0.91 eV. The concentration of this trap has been shown to increase with all kinds of radiation [8], and this increase shows a correlation with an increase in the density of trap E, which is believed to be the isolated nitrogen vacancy. In unirradiated GaN, however, the intensity of A₁ has been reported to be anti-correlated with trap E. As pointed out by Look [8], both of these observations are consistent with the identification of this trap as being nitrogen interstitial (N_i) related.

The next peak, labeled A, is seen at 365 K using a 47 Hz rate window. Other people have observed a trap in this temperature range which has been labeled A [49], EO5 [35], E3 [94], and D3 [95]. The Arrhenius fit indicates an activation energy $E_{\text{TOT}} = 0.82 \pm 0.04$ eV and cross section $\sigma_{na} = 1.5 \times 10^{-13}$ cm². This activation energy and cross section are both significantly greater than what has usually been reported for trap A [49]

(0.67 eV and $\sim 10^{-15} \text{ cm}^2$), but as will be seen below, the peak seen here appears to actually be a superposition of peaks with different activation energies. When this is the case, the Arrhenius plot from the combined peak sometimes indicates large activation energy and cross section. The next peak, labeled B, is seen at 301 K using a 47 Hz rate window. A trap has been reported in this temperature range by others, and it has been labeled B [49], E2 [94], and D2 [95]. The Arrhenius fit indicates an activation energy $E_{\text{TOT}} = 0.59 \pm 0.02 \text{ eV}$ and cross section $\sigma_{na} = 5.6 \times 10^{-15} \text{ cm}^2$. The activation energy and cross section agree with previously reported values for this trap (0.58-0.62 eV and $\sim 10^{-14} \text{ cm}^2$).

The next slightly perceptible shoulder peak on the low temperature side of trap B is seen in the 250-270 K temperature range, and is tentatively assigned to another trap labeled C₁. Other people observed a trap in the same temperature, and it has been labeled C₁ [49] and ES4 [96]. Fang *et al.* [49] reported that C₁ was peculiar to reactive molecular beam epitaxy (RMBE) GaN layers. They also reported that C₁ was concentrated close to the surface, and that the DLTS peak position was sensitive to electric field strength. Aurret *et al.* [96] reported that ES4 is created in the process of sputtered metal deposition, and that it was concentrated within 15 μm of the surface.

The next peak, labeled C, is seen at 207 K using a 47 Hz rate window. A similar trap reported in this temperature range has been labeled C [49] and ES3 [96]. The Arrhenius fit indicates an activation energy $E_{\text{TOT}} = 0.44 \pm 0.04 \text{ eV}$ and cross section $\sigma_{na} = 1.3 \times 10^{-13} \text{ cm}^2$. The activation energy and cross section agree with the two previously reported values for this trap (0.40-0.41 eV and 10^{-14} - 10^{-13} cm^2). Fang *et al.* [49] have reported that trap C is associated with ion-beam etching, and is concentrated within 27

μm of the surface. They have also observed this trap in GaN grown by plasma-assisted MBE. Aurret *et al.* [96] reported that as with ES4 (C_1), ES3 was created during sputtered metal deposition, and that it was concentrated within 15 μm of the surface.

An instance in which trap C dominated the DLTS spectrum is shown in figure V-2. Here, it is seen that the intensity of peak C increases considerably with pulse width. The inset shows that this peak height increase was only apparent with the larger rate windows. As shown in figure V-3 the increase in peak C was not observed in a subsequent scan, indicating that that this effect can be suppressed with annealing at 450 K under an applied reverse bias voltage.

The next peak in the DLTS spectrum of figure V-1, labeled D, is seen at 137 K using a 47 s^{-1} rate window. A similar trap reported in this temperature range has been labeled D [49], EO2 [35], E1 [94], and DLN1 [93]. The Arrhenius fit indicates an activation energy $E_{\text{TOT}} = 0.22 \pm 0.02\text{ eV}$ and cross section $\sigma_{na} = 2.8 \times 10^{-16}\text{ cm}^2$. The activation energy and cross section are close to previously reported values for this trap (0.24-0.27 eV and 10^{-15} - 10^{-14} cm^2), however, DDLTS measurements reveal that this peak has a strong electric field dependence.

Figure V-4 shows the DDLTS spectra (16.5 s^{-1} rate window) of the same GaN diode discussed above. The four pulsing conditions isolate four sections of the $V_r = 0$ to -4 V depletion region. It is seen that the summation of these four different signals (solid dark gray line) closely matches the signal obtained with the pulsing conditions $V_f = 0$, $V_r = -4\text{ V}$ (dashed light gray line). The figure suggests that peaks A and D are strongly affected by electric field, and thus by depth in the depletion region. Figure V-5 shows the detailed components of peak D under the indicated pulsing conditions. Arrhenius plots

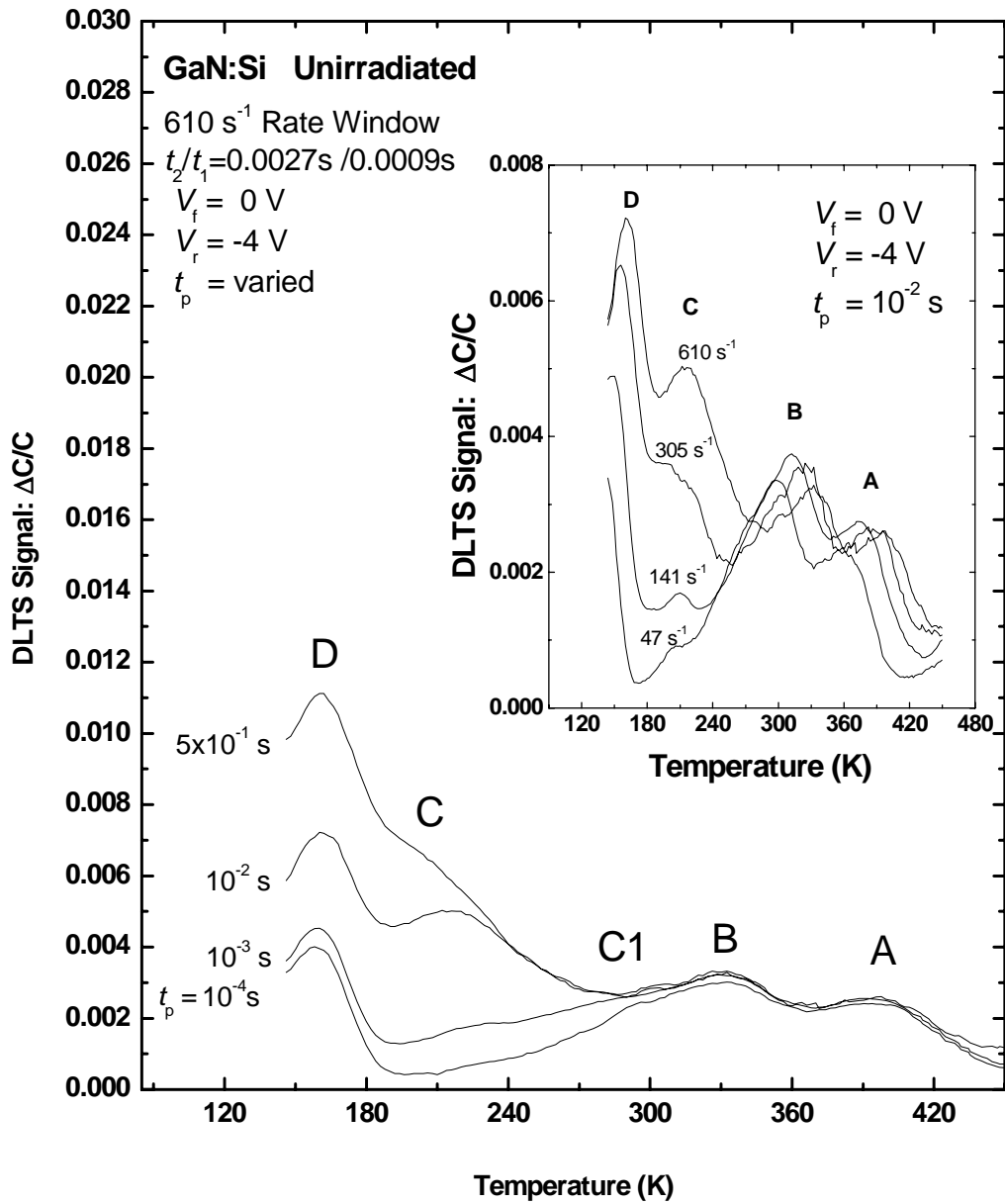


Figure V-2. DLTS spectrum of unirradiated GaN (sample A2-4b) at different filling pulse widths. The trap C dominates at large pulse width in this temperature scan, but it greatly diminished in a subsequent temperature scan. The inset shows various rate windows for $t_p = 10^{-2}$ s, illustrating that trap C is only dominant for large rate windows.

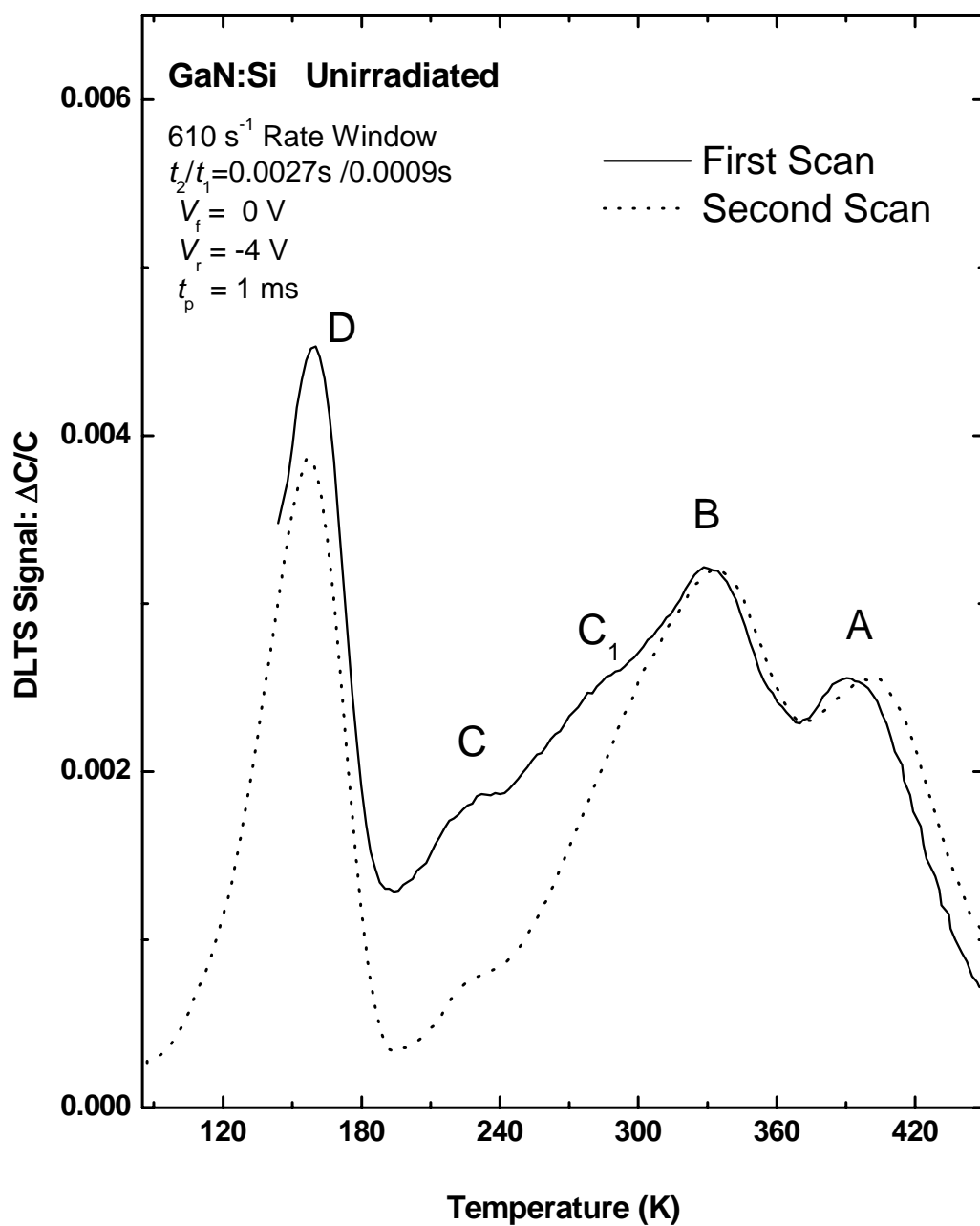


Figure V-3. DLTS spectrum of unirradiated GaN (sample A2-4b) produced by two consecutive temperature scans.

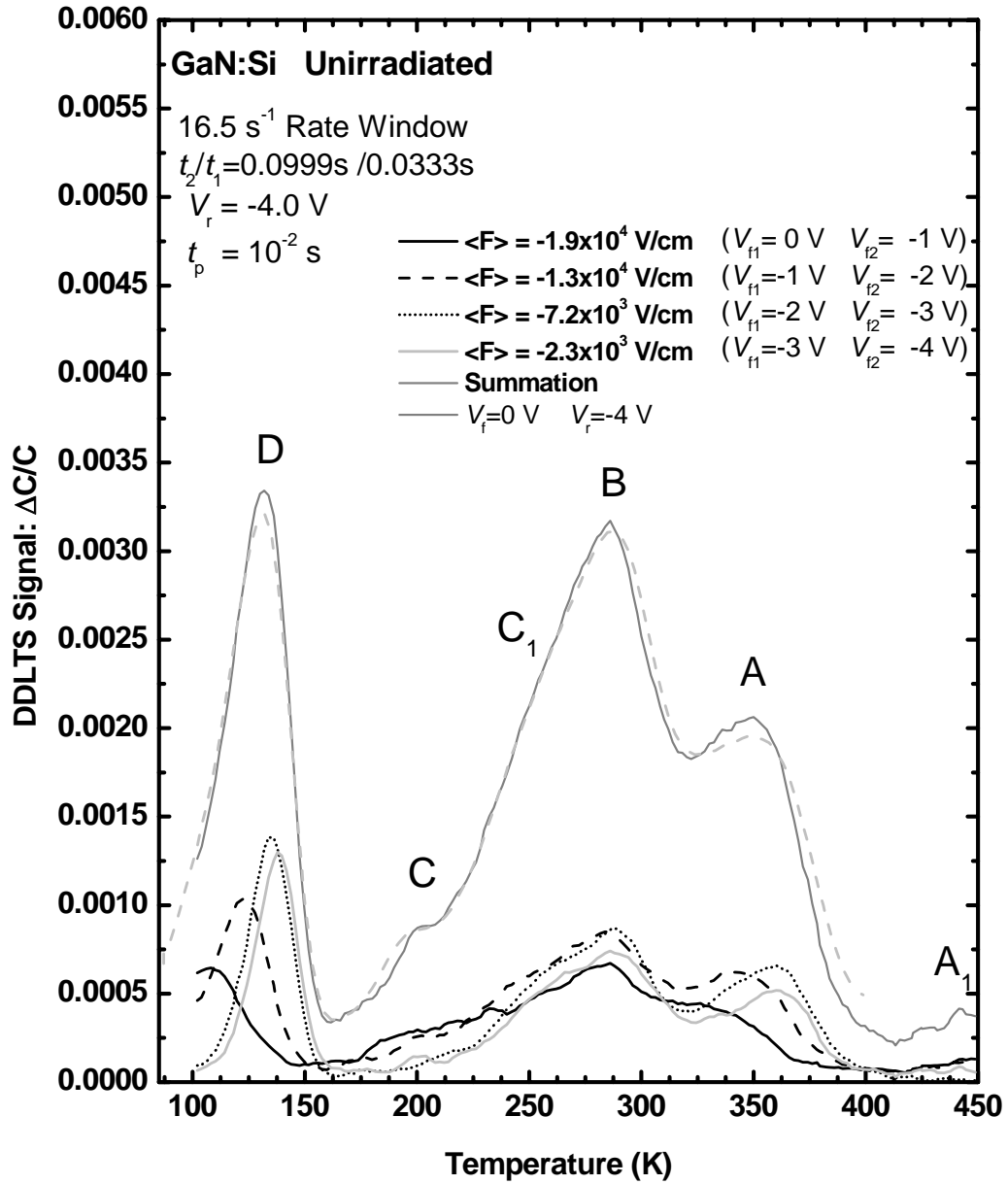


Figure V-4. Double correlated DLTS spectra of unirradiated GaN (sample A2-4b). The four pulsing conditions isolate four sections of the $V_r = 0$ to -4 V depletion region. The summation of these four different signals (solid dark gray line) closely matches the signal obtained with the pulsing conditions $V_f = 0$, $V_r = -4\text{ V}$ (dashed light gray line).

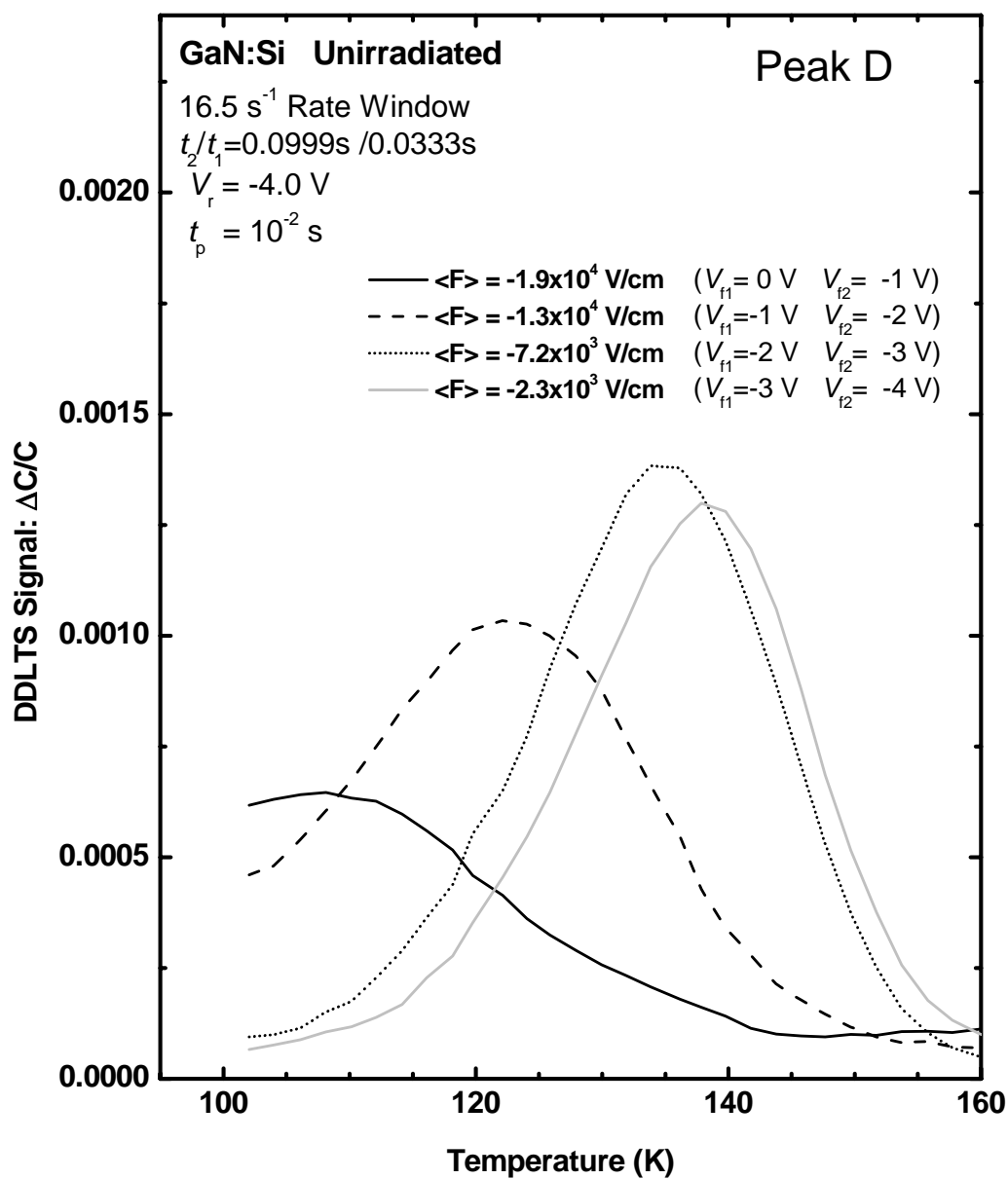


Figure V-5. Double correlated DLTS spectra of peak D in unirradiated GaN (sample A2-4b).

corresponding to these peaks are shown in figure V-6. The peak that appears under the lowest field condition has activation energy $E_{TOT} = 0.23$ eV and cross section $\sigma_{na} = 3.9 \times 10^{-16} \text{ cm}^2$, whereas the peak that appears under the highest field condition has activation energy $E_{TOT} = 0.13$ eV and cross section $\sigma_{na} = 1.1 \times 10^{-21} \text{ cm}^2$. The two low-field peaks are very similar, and their superposition dominates the emission properties of the combined peak D. The two high-field peaks have the same cross section but different activation energies (0.13 and 0.19 eV). This fact could indicate that two different electron traps are being revealed. In fact, shoulders on the low temperature side of trap D have often been reported [64]. In studies on GaN grown by MOCVD and HVPE, this has been labeled as trap E₁ [90], and has similarities to trap E (combination of ED1 and ED2 [31]) introduced by electron irradiation. In GaN grown by RMBE, deconvolution of trap D by fitting has revealed two traps, D₁ ($E_{TOT} = 0.25$ eV ; $\sigma_n = 1.4 \times 10^{-14} \text{ cm}^2$) and D₂ ($E_{TOT} = 0.16$ eV ; $\sigma_n = 2.1 \times 10^{-16} \text{ cm}^2$), where D₁ dominates the behavior of trap D, and D₂ appears as a shoulder on the low temperature side of D₁. In this case, however, the very low capture cross section may indicate that phonon assisted tunneling is dominating, and what is seen in figure V-5 is simply trap D with a strongly field-dependent emission rate.

Figure V-7 shows the DDLTS spectra (16.5 s^{-1} rate window) of trap A. In this case, the higher rate windows were too noisy for Arrhenius fitting to be accomplished. Figure V-8 shows the peak heights of traps A, B, C, and D versus filling pulse width. It is seen that traps A, B, and D exhibit a linear increase with $\log(t_p)$ up through $t_p = 10$ ms. Trap C increases in this manner without saturation up through $t_p = 500$ ms. As discussed in section IV, this behavior indicates that all four of these defects are concentrated in the vicinity of dislocations.

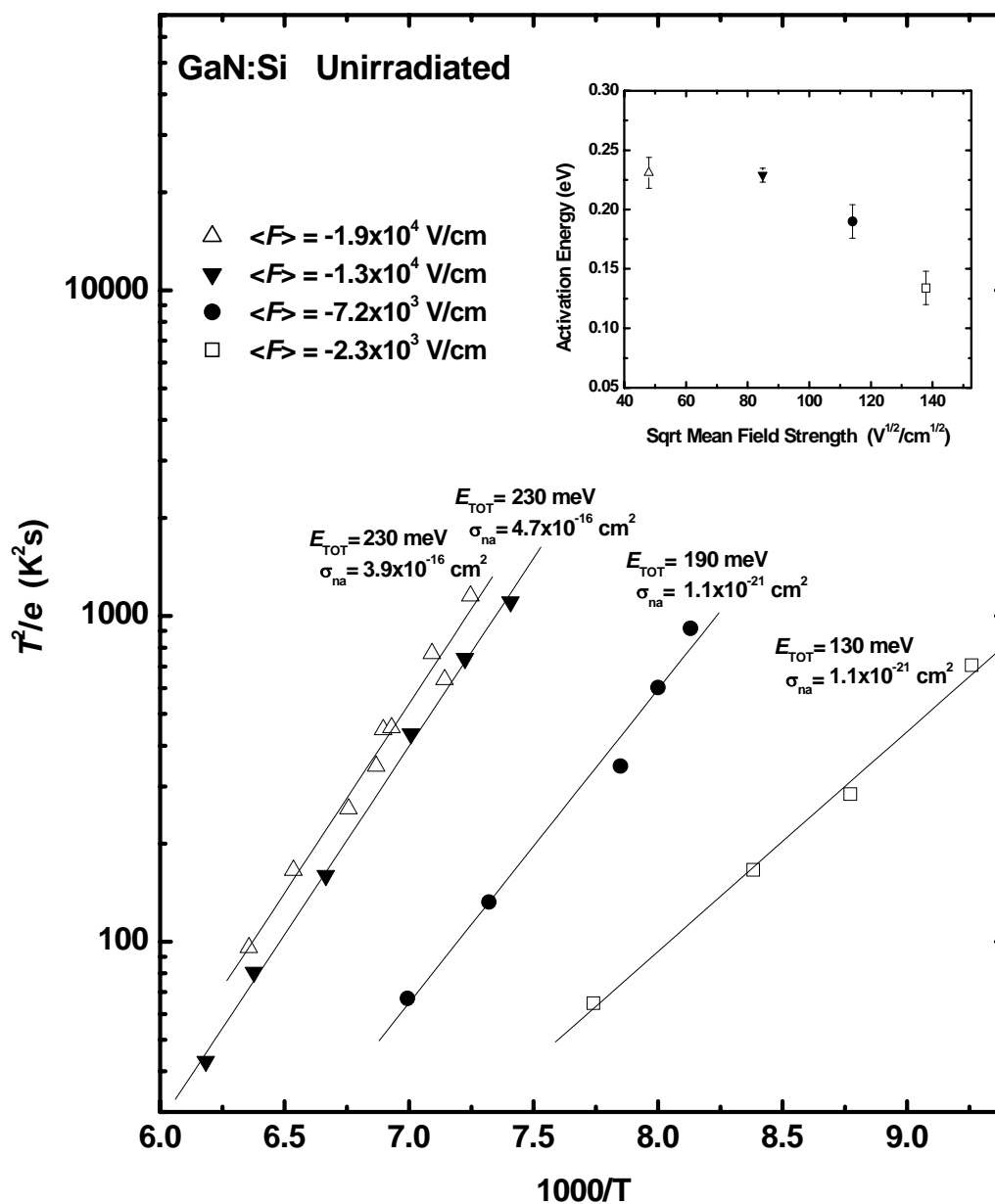


Figure V-6. Arrhenius plots corresponding to the low temperature peaks shown in figure V-5. Inset are the activation energies plotted against the square root of the mean field strength. The error bars represent the standard errors determined from data variance.

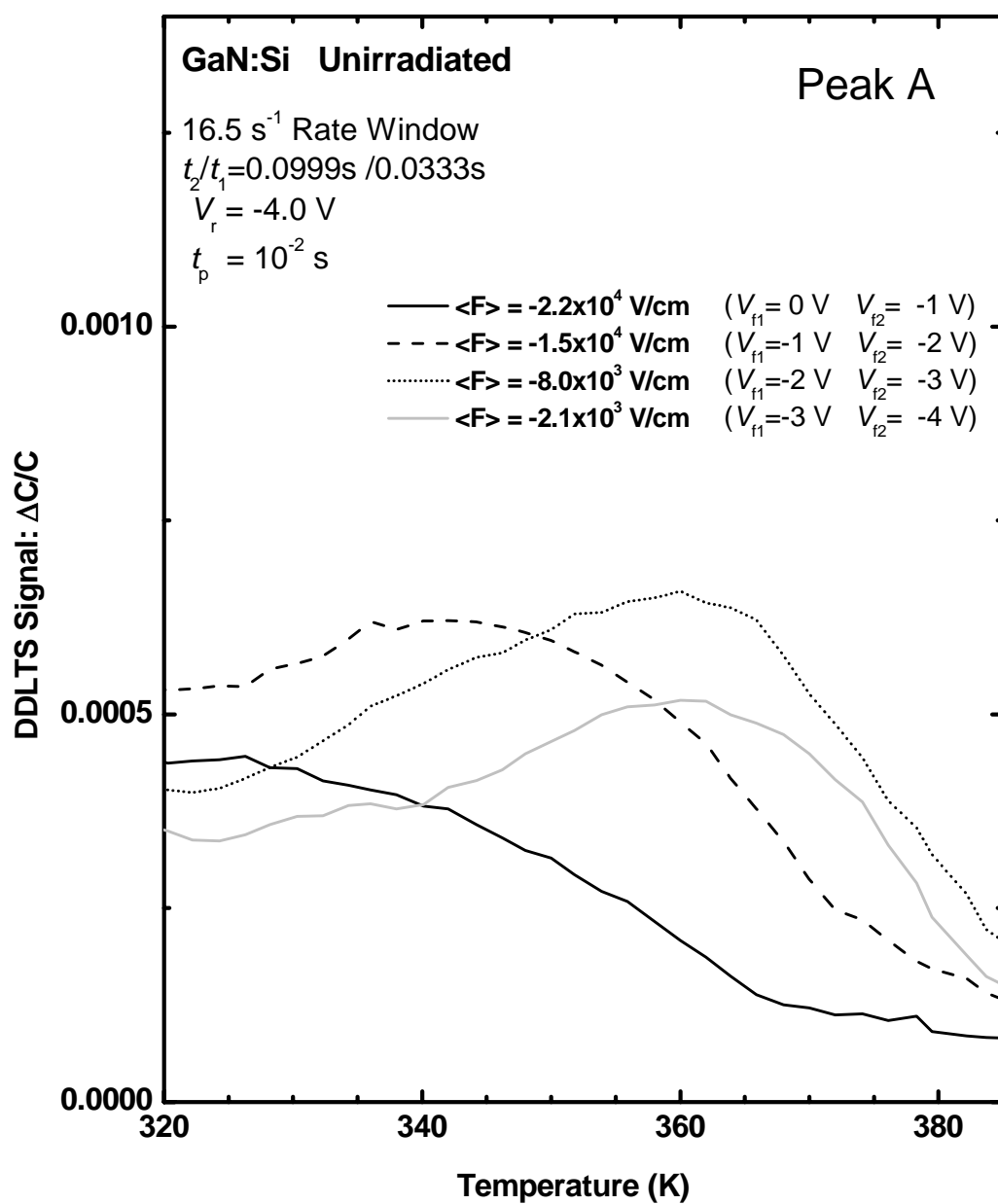


Figure V-7. Double correlated DLTs spectrum of peak A in unirradiated GaN (sample A2-4b).

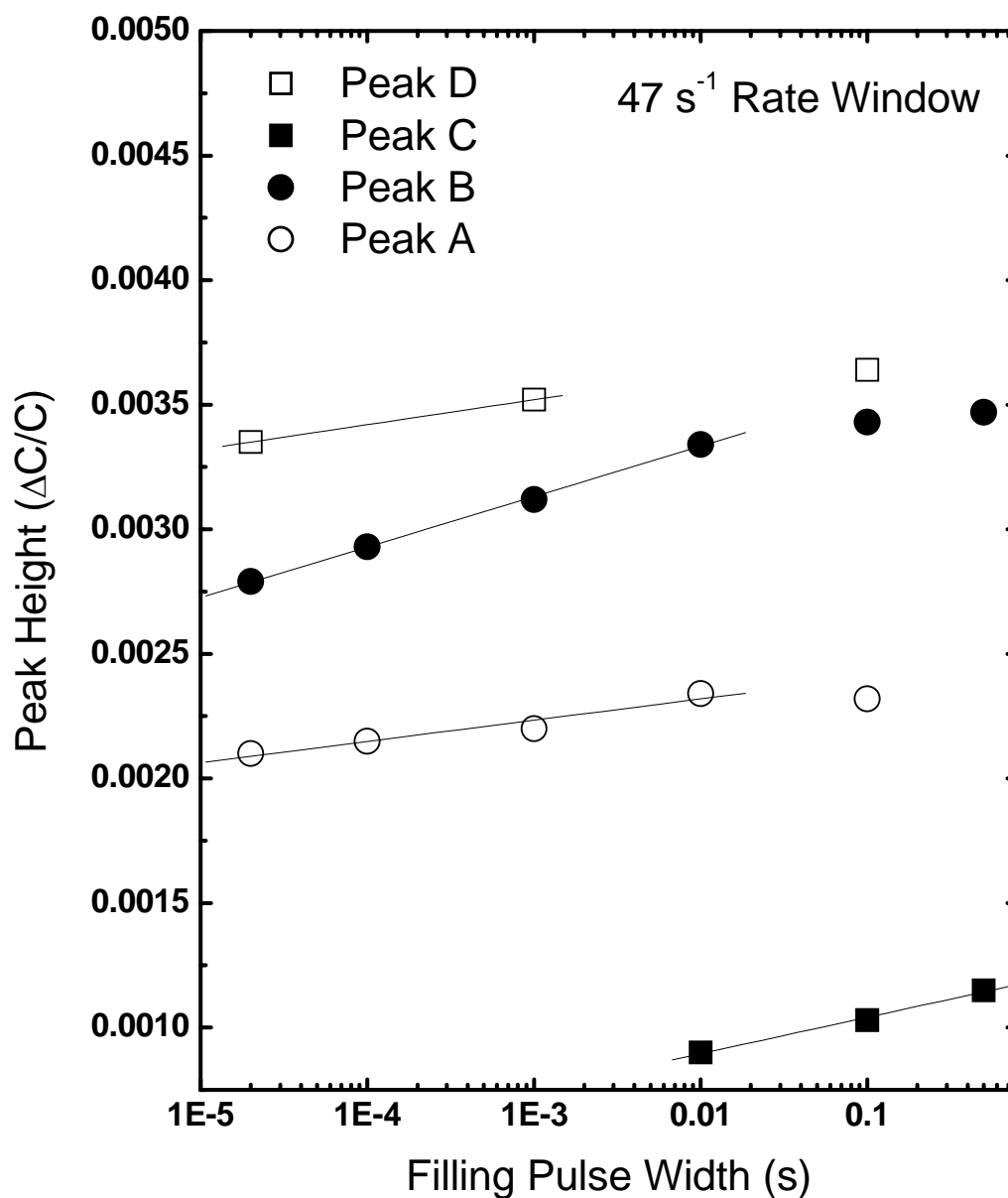


Figure V-8. Peak heights of four traps versus filling pulse width in GaN (sample A2-4b). The 47 s⁻¹ rate window was used for this comparison.

5.1.2 Irradiated GaN (Wafer A2)

Figure V-9 shows the DLTS spectrum of sample A2-4a irradiated at two consecutive 1.0 MeV electron doses. It is apparent that the peaks A, B, and C do not increase with radiation damage. A small decrease in some of these may be attributed to an increase in the Schottky barrier diode series resistance. Only one radiation-induced peak, labeled E, is shown. Arrhenius fitting could not be accomplished for this peak because of carrier freeze-out. In this situation, radiation-induced deep acceptor levels cause the carrier concentration to drop sharply as temperature is reduced. This phenomenon is especially severe at the second dose as shown in figure V-9. Figure V-10 shows that the diode capacitance drops off considerably at low temperatures due to carrier freeze-out. The C-V curves taken after the $1.1 \times 10^{17} \text{ cm}^{-2}$ dose are shown at various temperatures in figure V-11. In this figure, it is seen that a normal C-V relationship, showing a decrease in capacitance with increase in V_r , is not obtained for $T < 160 \text{ K}$. A comparison with a normal C-V curve at 130 K is shown in figure V-12 for samples before and after electron irradiation. Figure V-13 shows double-correlated DLTS spectra of GaN (sample A2-5a) irradiated with $2.5 \times 10^{16} \text{ cm}^{-2}$ of 0.62 MeV electrons. The rate window used in this figure is 610 s^{-1} , so the peaks are shifted upward in temperature relative to the 121 s^{-1} rate window of figure V-9. In figure V-13, it is seen that trap E is rather broad, and almost certainly is a combination of traps ER1 and ER2 reported in [35]. Figure V-14 shows the field dependence of the E and D peaks, where both DDLTS spectra are generated in the same spatial region defined by the forward pulse pairs $V_{f1} = 0 \text{ V}$ and $V_{f2} = -2 \text{ V}$. This figure demonstrates that the variations in the DDLTS spectra of figure V-13 are caused by the field variation in the

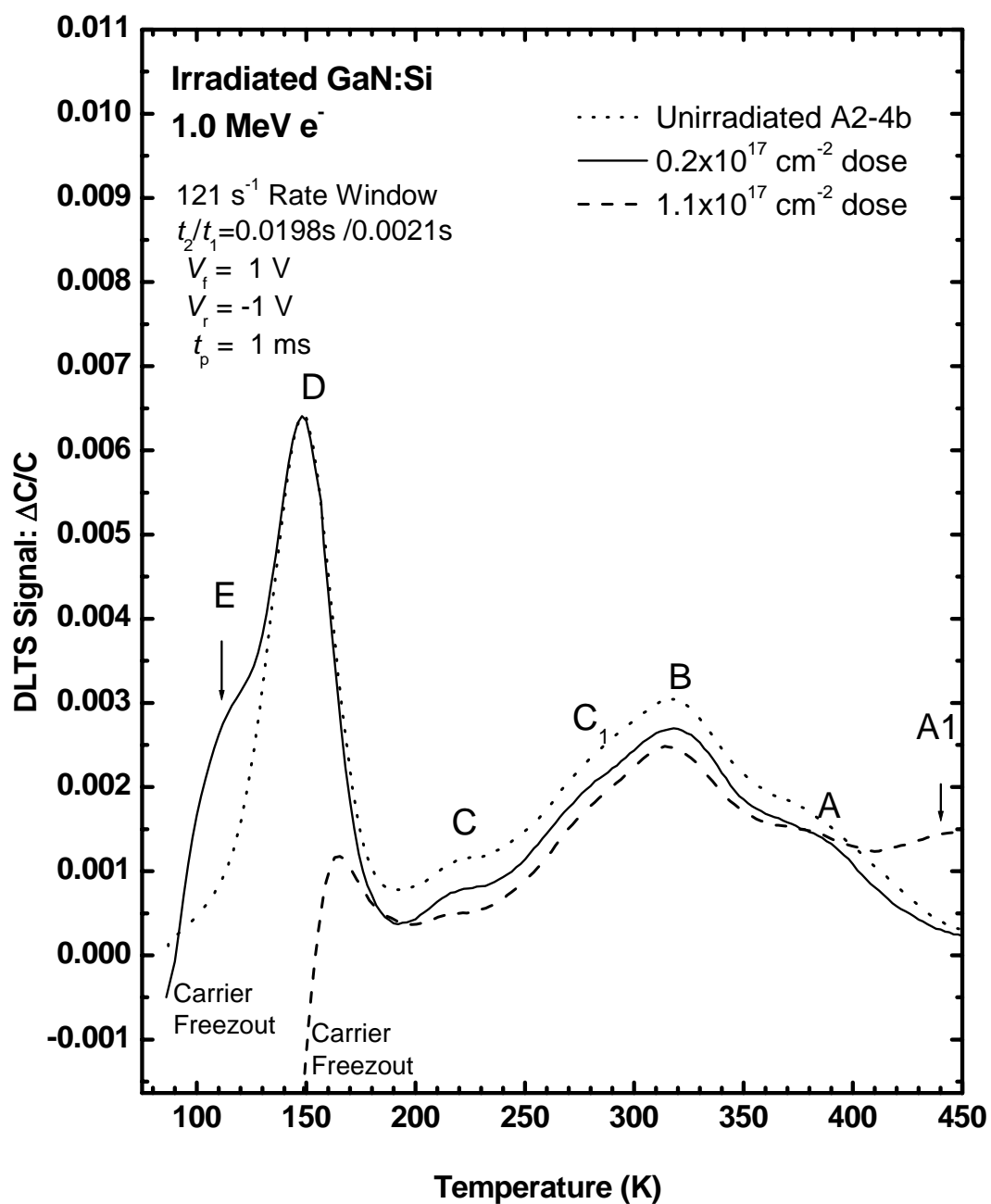


Figure V-9. DLTS spectra of GaN (sample A2-4a) irradiated at two consecutive 1.0 MeV electron doses. Unirradiated GaN (sample A2-4b) is overlaid for comparison.

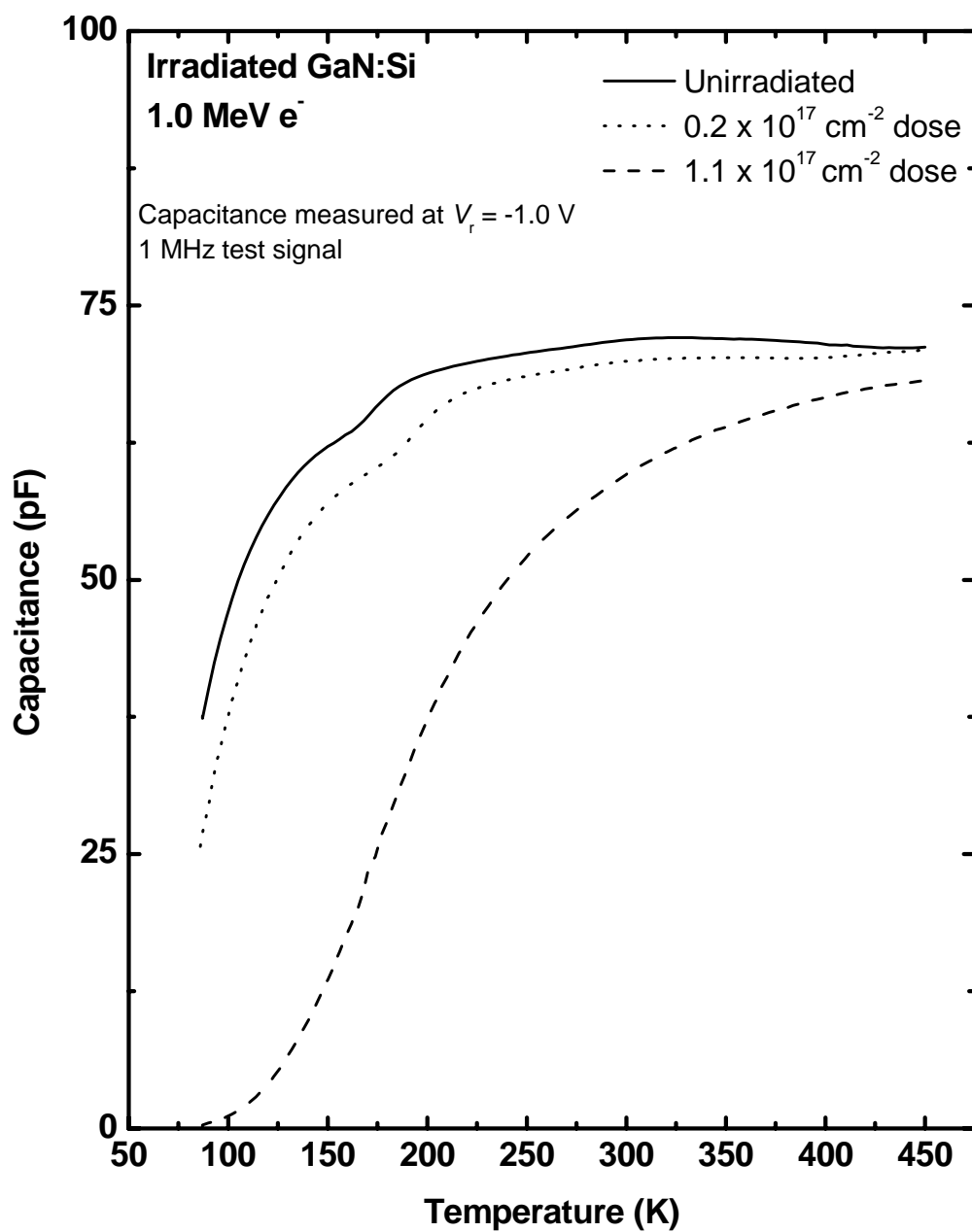


Figure V-10. Capacitance versus temperature for GaN (sample A2-4a) before and after two consecutive 1.0 MeV electron irradiations.

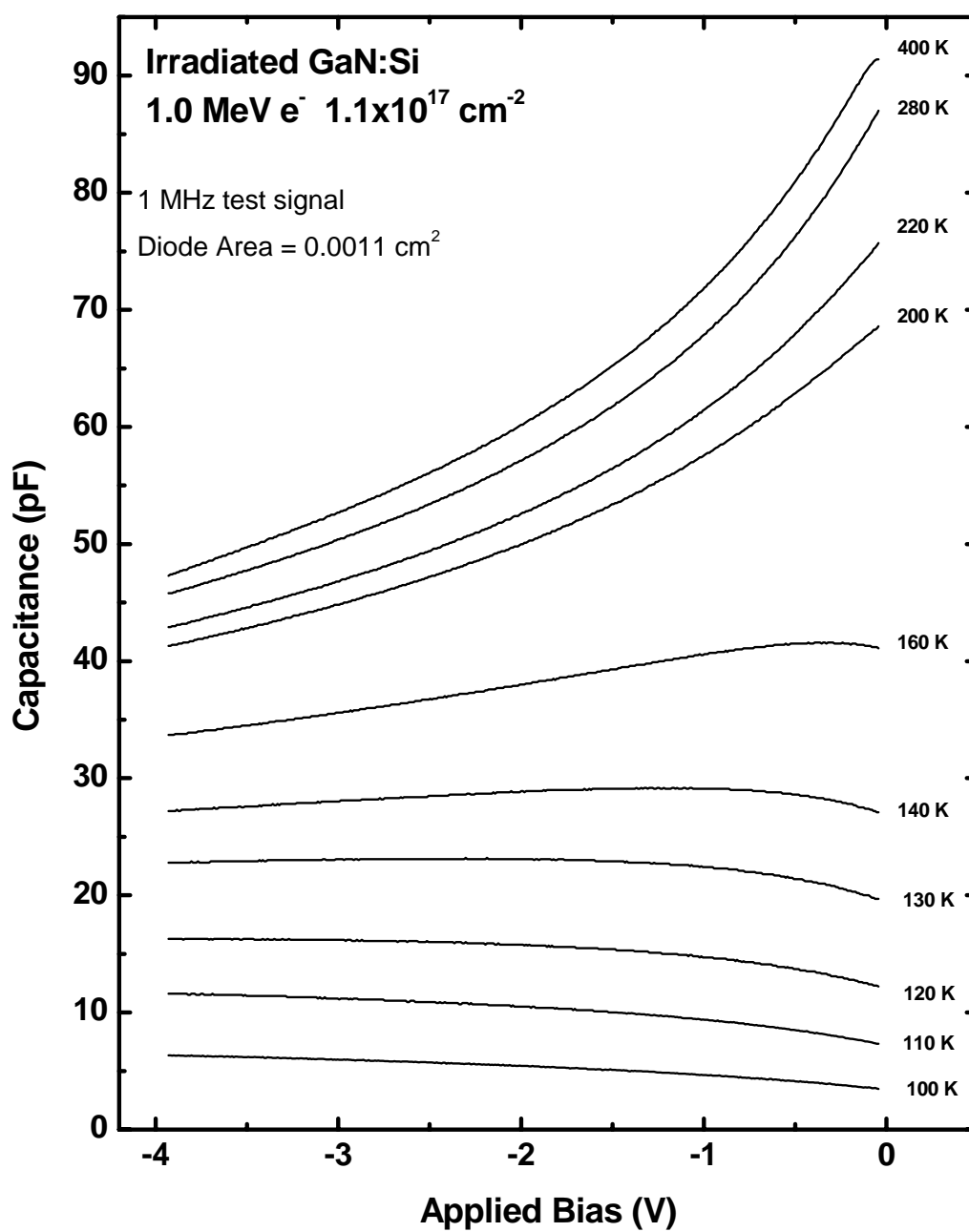


Figure V-11. C-V curves at various temperatures for 1.0 MeV electron irradiated GaN (sample A2-4a).

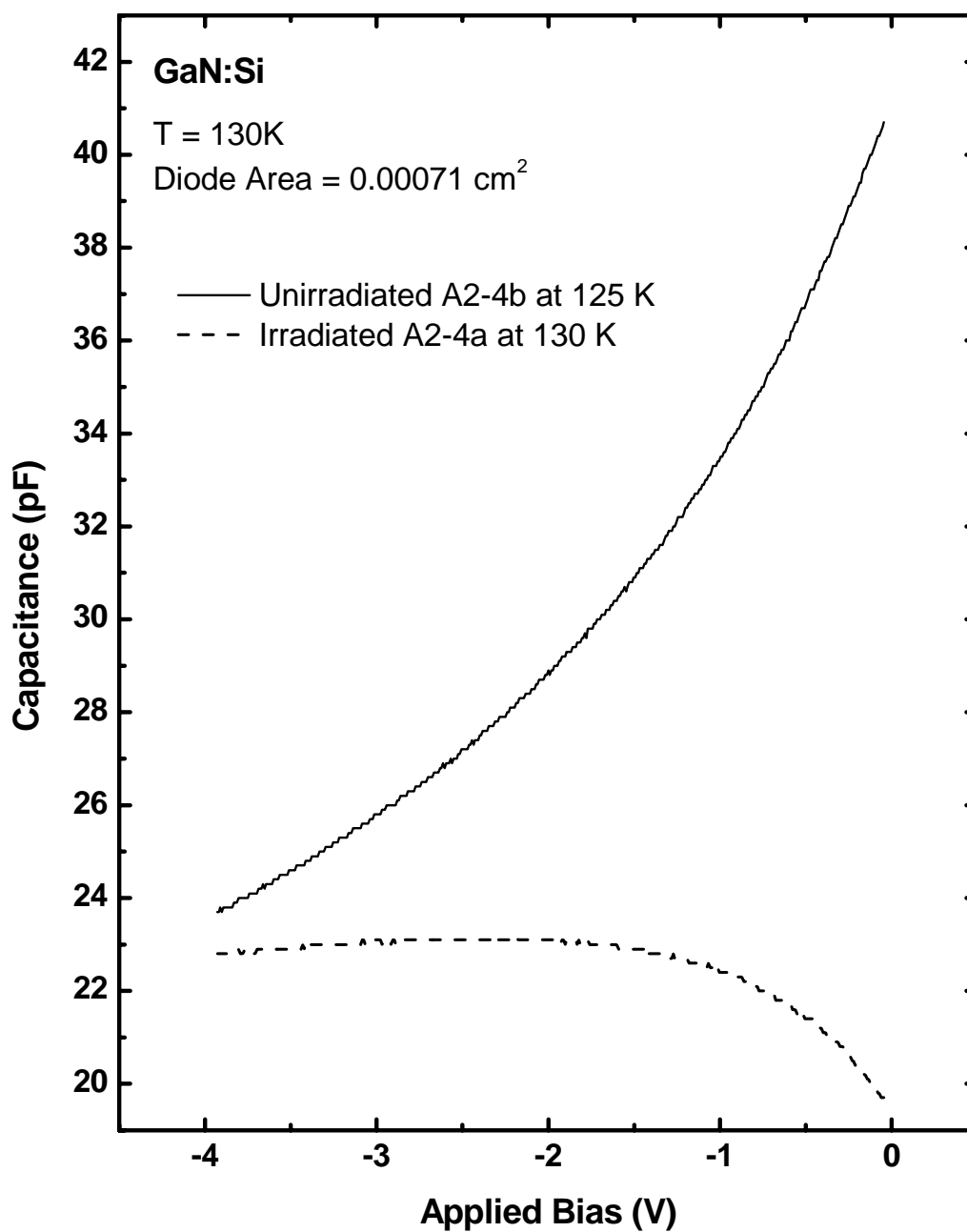


Figure V-12. C-V curve of 1.0 MeV electron irradiated GaN (sample A2-4a), showing the effect of carrier freeze-out at this temperature. The normal C-V curve from unirradiated GaN (sample A2-4b) is overlaid for comparison.

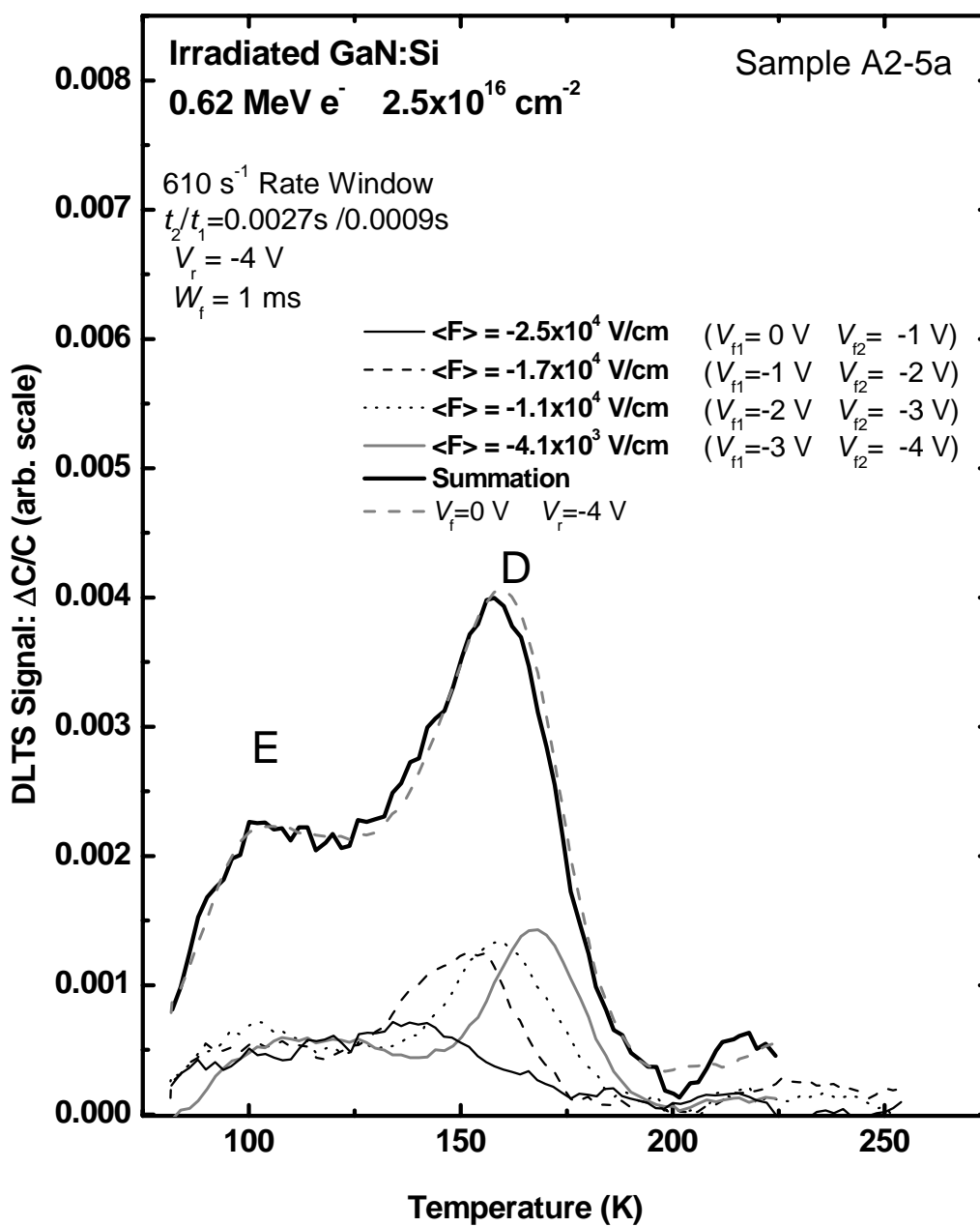


Figure V-13. Double correlated DLTS spectra of peaks D and E in irradiated GaN (sample A2-5a). The rate window is 610 s⁻¹.

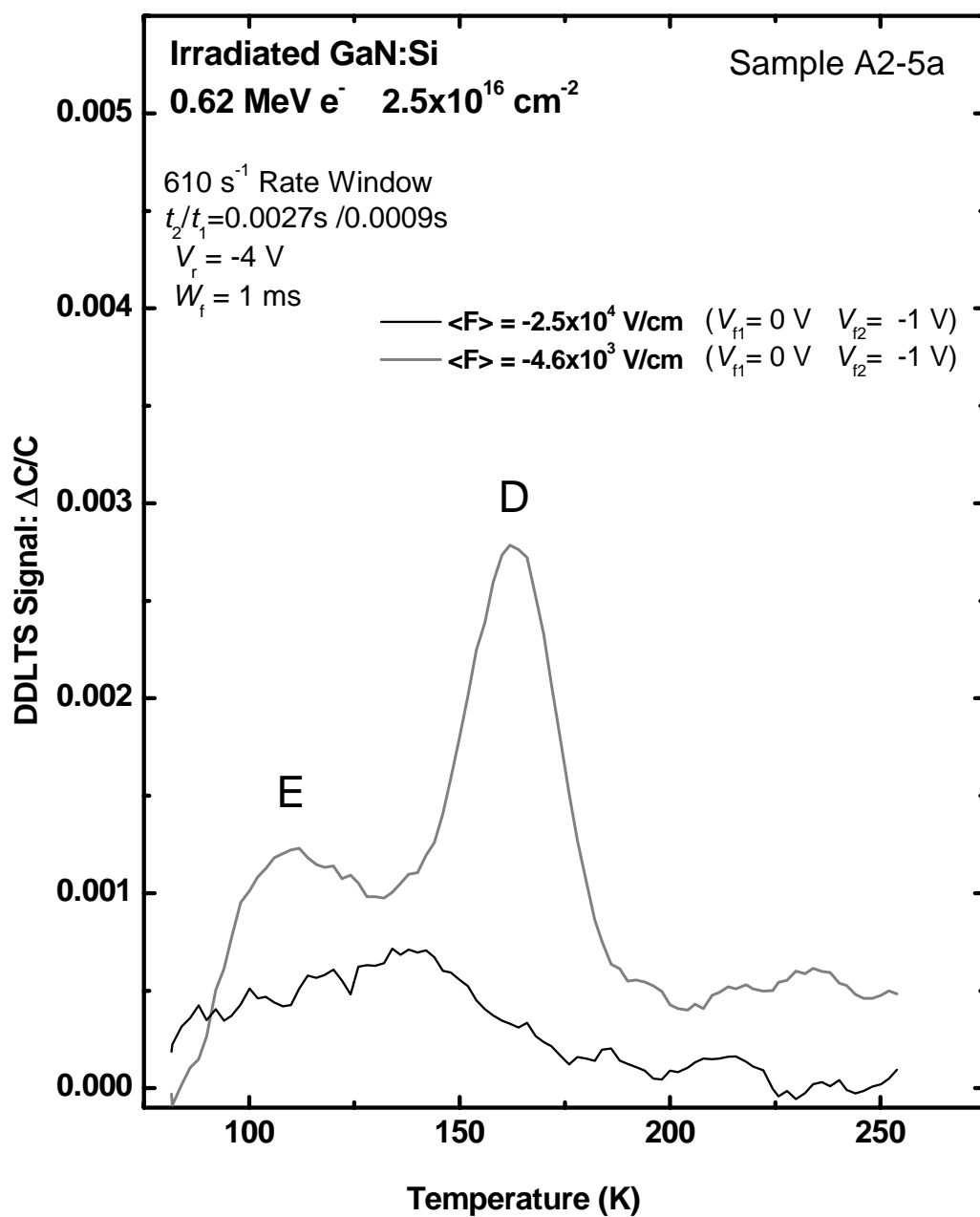


Figure V-14. Double correlated DLTS spectra of peaks D and E in irradiated GaN (sample A2-5a) showing the effect of field strength in the spatial region defined by forward pulse pair $V_{f1} = 0\text{ V}$ and $V_{f2} = -1\text{ V}$. The rate window is 610 s^{-1} .

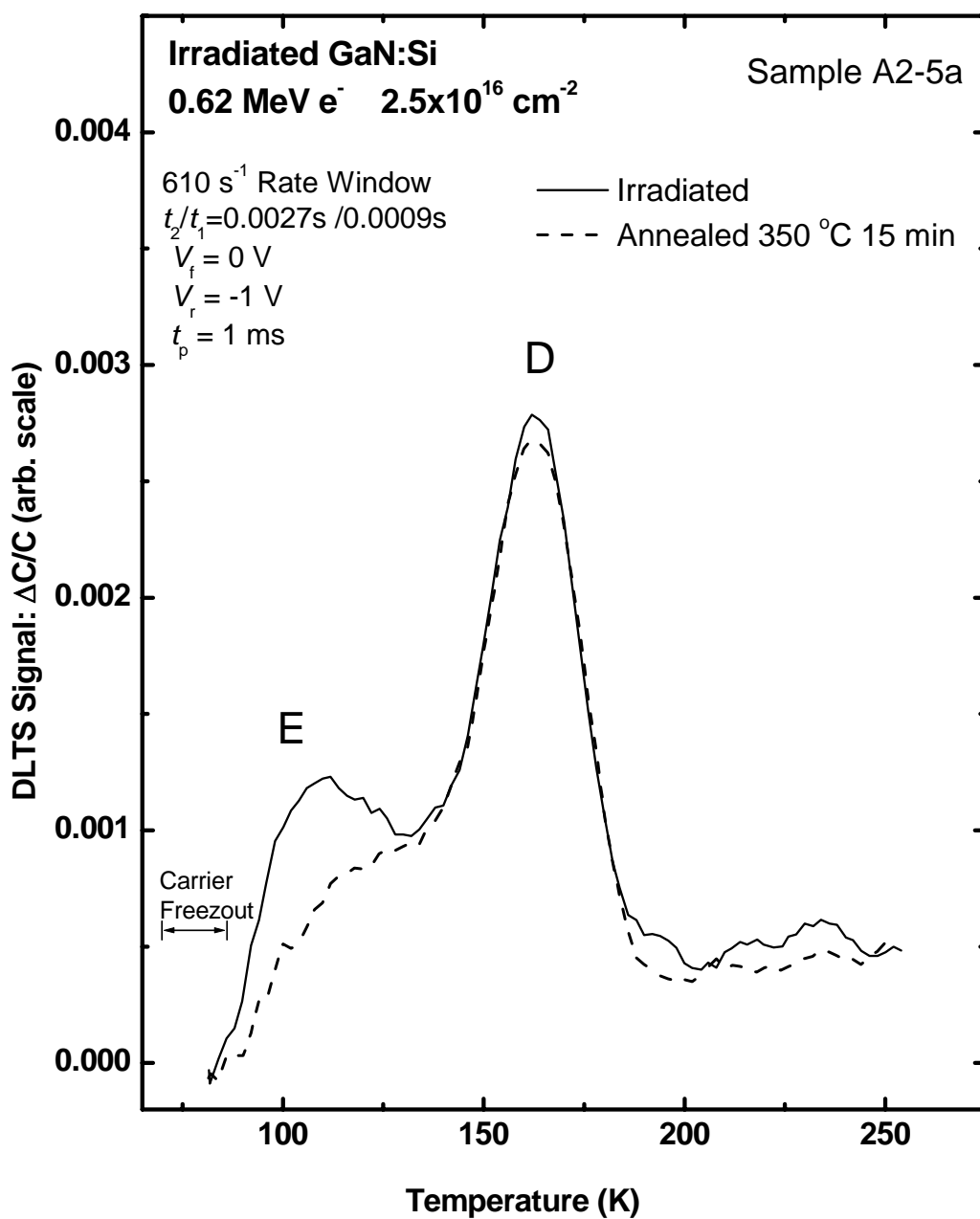


Figure V-15. DLTS spectra of peaks D and E in irradiated GaN (sample A2-5a) before and after annealing at 350 °C for 15 minutes. The rate window is 610 s⁻¹.

depletion region, and not by an inhomogeneous spatial distribution of defects. Figure V-15 shows that trap E diminishes greatly after annealing at 350 °C. The extent of the reduction caused by the annealing is obscured by carrier freeze-out, however, it appears that trap E anneals out considerably, and that the remaining low temperature shoulder of peak D may be similar to what was seen in the unirradiated GaN samples.

5.1.3 Unirradiated Al_{0.14}Ga_{0.86}N (Wafer B2)

Figure V-16 shows a DLTS spectrum of unirradiated Al_{0.14}Ga_{0.86}N typical of samples from wafer B2. A 47 s⁻¹ rate window is used, and the pulsing parameters are $V_f = 3$ V, $V_r = -3$ V, and $t_p = 20$ μs. Two electron traps, labeled P1 and P2 are apparent in the spectrum.

The peak of figure V-16 labeled P2 is noticeably broader than the peak that would be expected from a discrete trap level. This kind of broad peak can result from the superposition of a few traps with different closely spaced energy levels. With the measurement parameters shown in figure V-16, the central value of activation energy for P2 is $E_{TOT} = 0.98 \pm 0.10$ eV and the apparent capture cross section is $\sigma_{na} = 4 \times 10^{-12}$ cm². Using the 0.1 s filling pulse width, a much cleaner Arrhenius plot is obtained. In that case, the central value of activation energy for P2 is $E_{TOT} = 0.88 \pm 0.02$ eV and the apparent capture cross section is $\sigma_{na} = 5 \pm 3 \times 10^{-12}$ cm².

The most prominent electron trap level, P1, peaks at 255 K in the 47 s⁻¹ rate window. The Arrhenius fit, shown in the inset, indicates an activation energy of $E_{TOT} = 0.54 \pm 0.02$ eV and cross section of $\sigma_{na} = 3.9 \pm 1.0 \times 10^{-14}$ cm². This level was also observed by Legodi *et al.* [42] in Al_{0.12}Ga_{0.88}N grown by the same plasma-assisted MBE method. They suggested that this electron trap is similar to the one observed in MOCVD

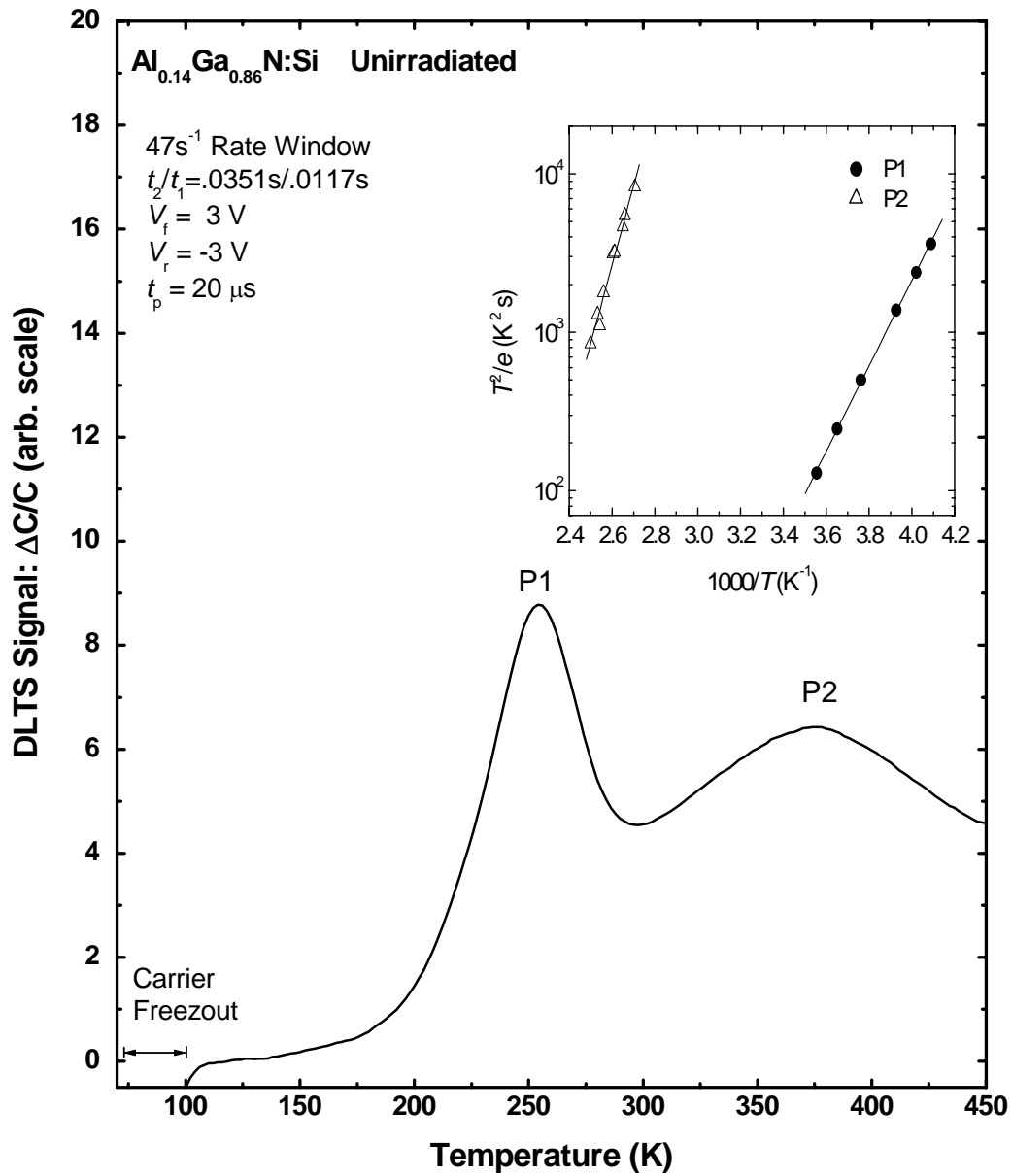


Figure V-16. DLTS spectrum of pre-irradiated Al_{0.14}Ga_{0.86}N (sample B2-21d). The Arrhenius plots of the two peaks are shown in the inset.

-grown $\text{Al}_{0.12}\text{Ga}_{0.88}\text{N}$ by Götz *et al.* [97]. Götz *et al.* labeled this electron trap DLN_2 and reported an activation energy of $E_{TOT} = 0.61 \pm 0.02$ eV. The authors also proposed that this DLN_2 trap in $\text{Al}_{0.14}\text{Ga}_{0.86}\text{N}$ corresponded to a trap in GaN having $E_{TOT} = 0.5$ eV. They also reported that the activation energy of DLN_2 decreased linearly with the increasing square root of field strength, indicating that the trap was donor-like. In order to determine if P1 shares this donor-like characteristic, the electric field dependence of E_{TOT} is measured by performing DDLTS measurements. Figure V-17 shows E_{TOT} versus the square root of the average electric field strength in a narrow spatial segment of the depletion region defined by the forward pulse pairs $V_{f1} = -1$ V and $V_{f2} = -2$ V. The reverse bias was increased from -2 to -6 V to obtain an average electric field strength ranging from 1.3×10^3 V/cm to 9.6×10^3 V/cm. It is apparent that there is no clear decreasing trend in E_{TOT} as the average electric field strength is increased in this range. The inset of figure V-17 shows the 47 s^{-1} rate window of P1 at electric field strengths 1.3×10^3 and 9.1×10^3 V/cm, where it is clear that the increase in electric field strength causes no significant shift in the peak position. This is quite different than the situation reported for DLN_2 by Götz *et al.*, however, in that work, the field strengths were an order of magnitude greater due to a higher carrier concentration $n \sim 5 \times 10^{17} \text{ cm}^{-3}$. Figure V-18 shows the increase in the P1 and P2 peak heights with pulse width. Here, it is seen that in the pulse width range of 20 μs to 1 ms, the peak heights increase linearly with the logarithm of pulse width. Again, this may indicate that the defects corresponding to these peaks are associated with line defects, as discussed in chapter IV. Because increasing occupation of the electron traps gives rise to a repulsive potential, it appears that these

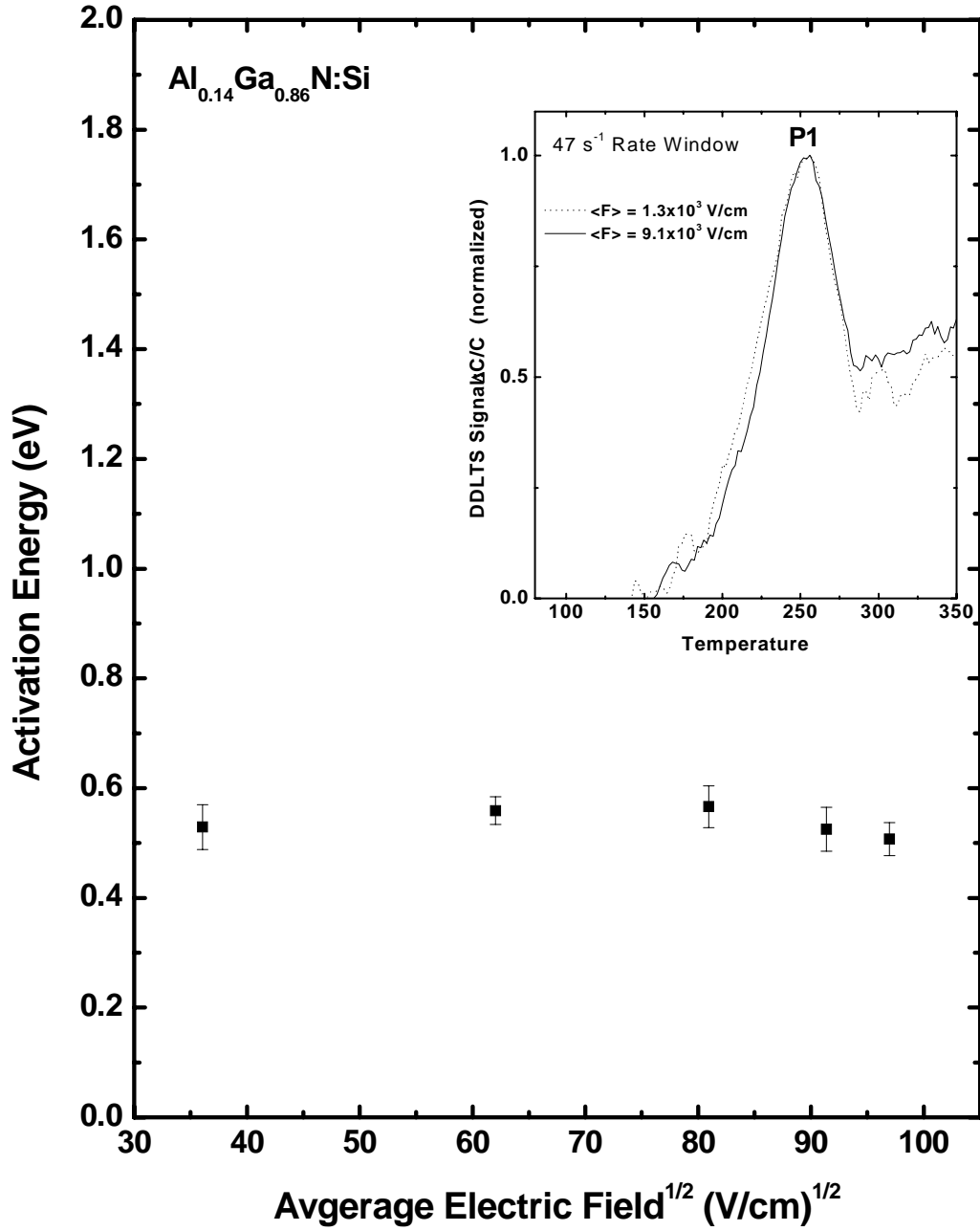


Figure V-17. Electric field dependence of electron trap P1 activation energy in $\text{Al}_{0.14}\text{Ga}_{0.86}\text{N}$ (sample B2-8b). DDLTS signals are measured in the spatial region defined by the forward voltage pulse pair $V_{f1} = -1$ and $V_{f2} = -2$ V, with field increase provided by increasing reverse bias V_r . Error bars apply to random sources of error in these comparative measurements. Inset shows 47s⁻¹ peak positions when field strength is raised nearly one order of magnitude. No peak temperature shift is observed.

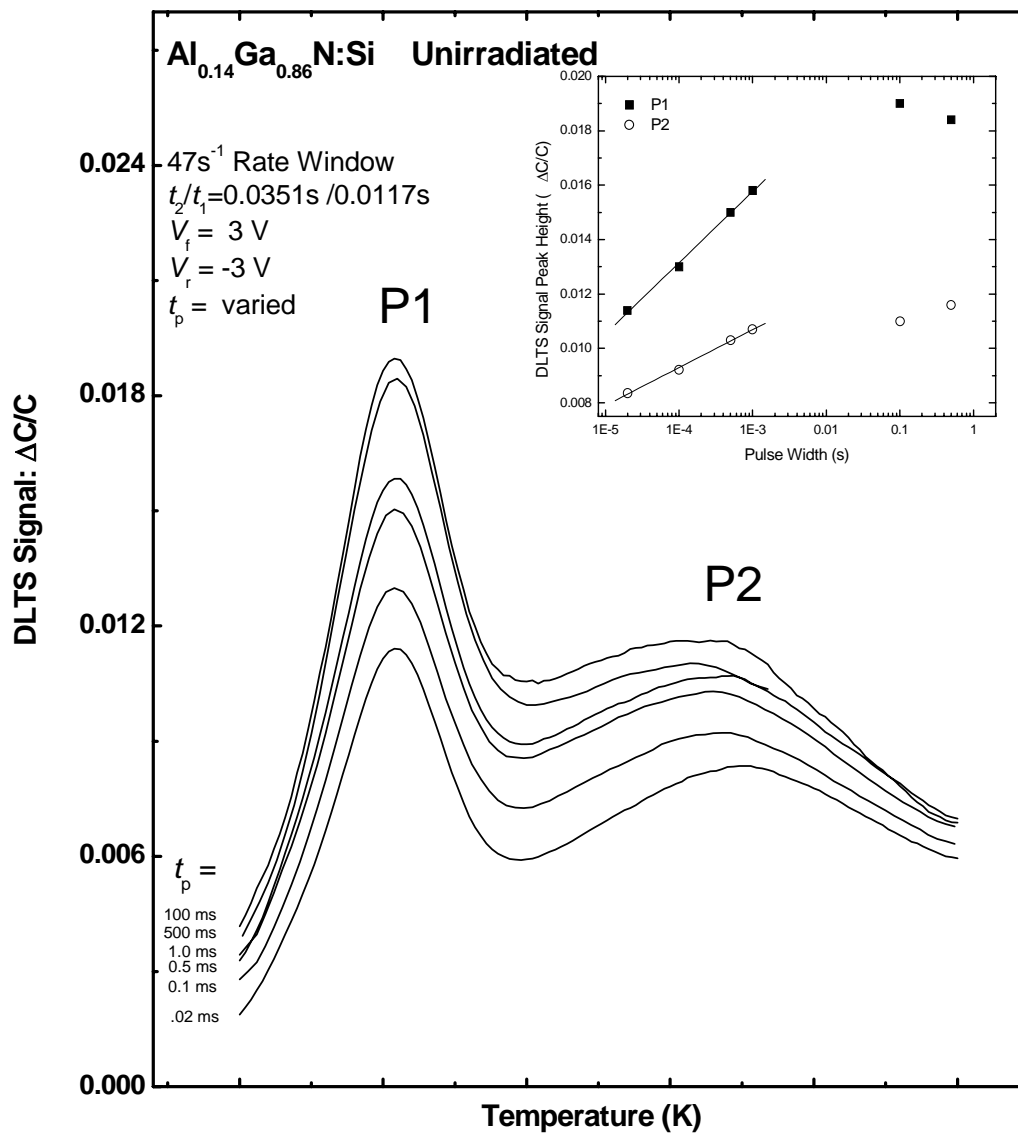


Figure V-18. DLTS spectrum of unirradiated $\text{Al}_{0.14}\text{Ga}_{0.86}\text{N}$ (sample B2-21d) at various pulse widths. The peak heights of P1 and P2 are plotted versus filling pulse width in the inset.

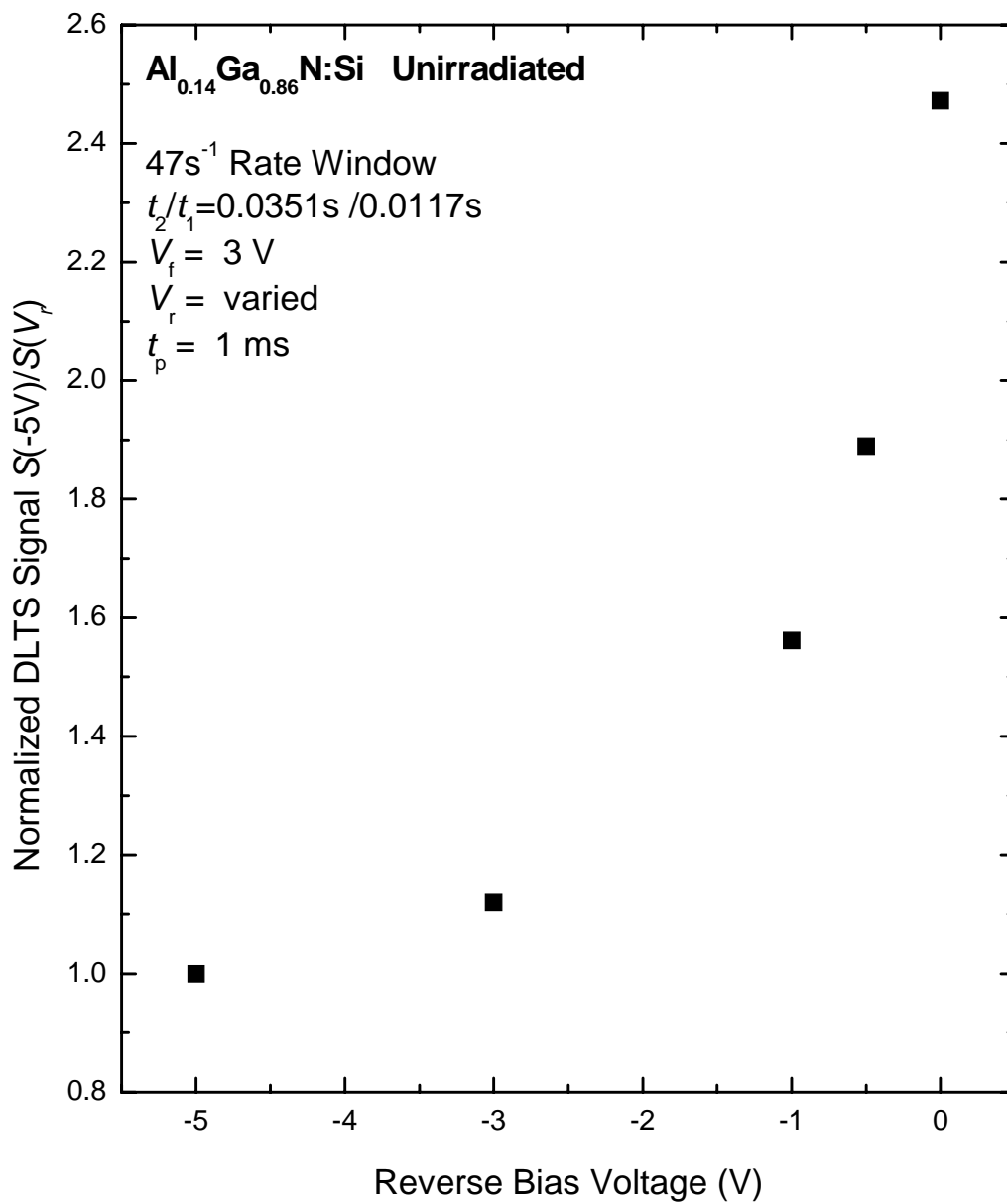


Figure V-19. Normalized peak height of electron trap P1 versus reverse bias voltage.

traps both behave as acceptors. The reverse bias voltage dependence of P1 peak height is shown in figure V-19. The resulting plot is characteristic of a trap distributed throughout the thickness of the epitaxial layer rather than being concentrated near the surface.

5.1.4 Irradiated Al_{0.14}Ga_{0.86}N (Wafer B2)

Figure V-20 shows the DLTS spectrum of the irradiated Al_{0.14}Ga_{0.86}N sample B2-21b measured after 1.0 MeV electron irradiation to a fluence of $9 \times 10^{16} \text{ cm}^{-2}$ and about 3 hours of room temperature annealing. Measurements taken with two different filling pulse widths are presented. It is apparent from the spectrum corresponding to the 0.1 s pulse width that four distinct electron traps indicated by R1, R2, R3, and R4 were generated from the radiation damage. Arrhenius analysis was most readily applied to peaks in the 20 μs pulse width spectrum. The apparent activation energy and the apparent cross section for the electron traps of R2, R3, and R4, determined from the inset of figure V-21 are 0.21 eV and $7 \times 10^{-17} \text{ cm}^2$, 0.26 eV and $1.4 \times 10^{-16} \text{ cm}^2$, and 0.33 eV and $1.3 \times 10^{-16} \text{ cm}^2$, respectively. An Arrhenius plot for R1 could not be made due to lack of resolution. In order to deconvolve the peaks in the 20 μs pulse width spectrum, the measured parameters from the Arrhenius plot were used with equations IV-4 to IV-6 to generate the radiation damage-induced peaks R1, R2, R3, and R4 seen as the dotted lines in figure V-21. In the application of these equations to each trap, the apparent cross section, σ_{na} , was allowed to vary, the activation energy, E_{TOT} , was held fixed at the measured value, and the broadening parameter, S , and DLTS signal magnitude, ΔC , were chosen. The σ_{na} that produced the best fit was within the error bounds of the measured σ_{na} for each trap. In this work, the S corresponding to trap P1 was determined from the

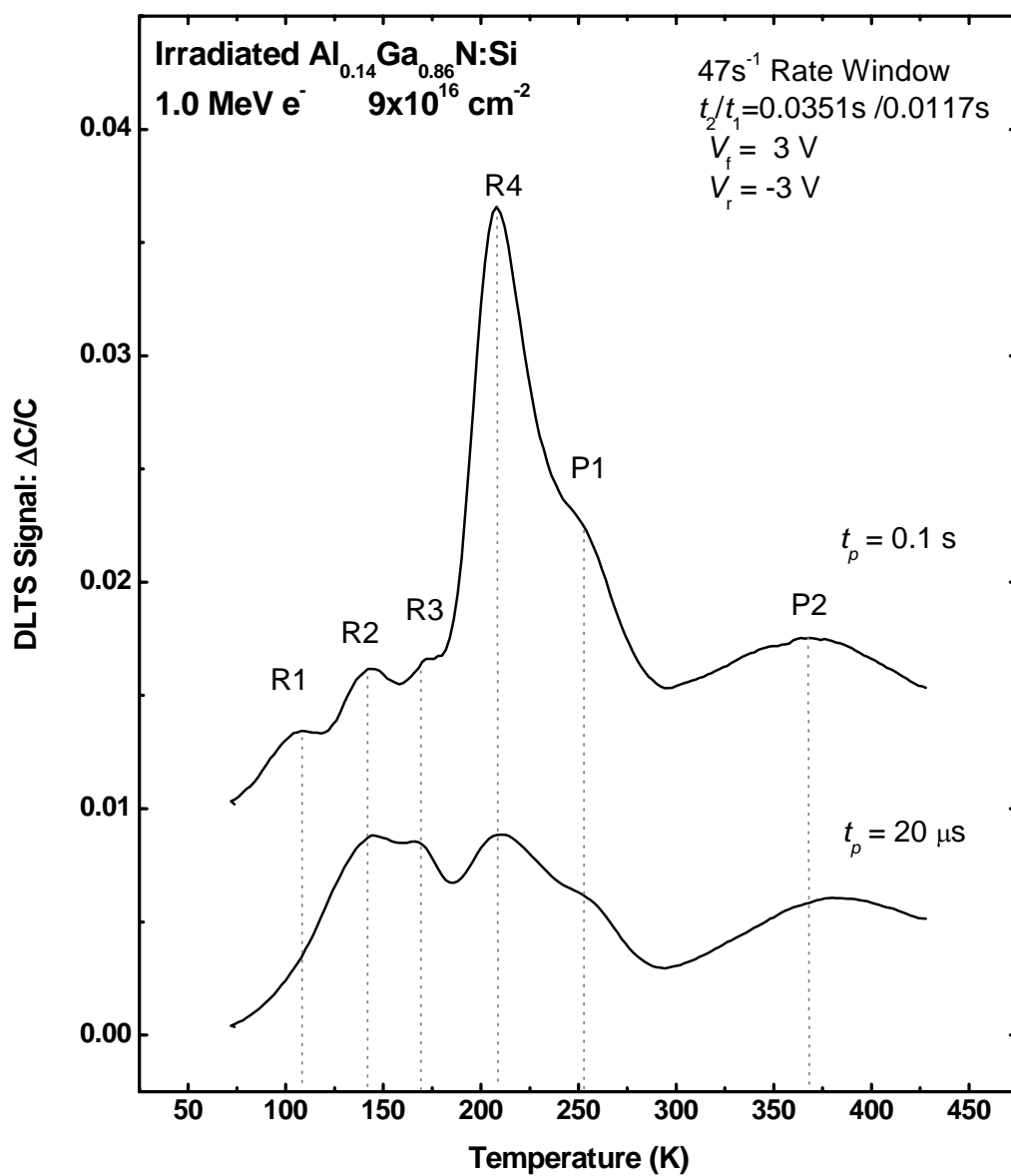


Figure V-20. DLTS spectrum of 1.0 MeV electron irradiated $\text{Al}_{0.14}\text{Ga}_{0.86}\text{N}$ (sample B2-21b) at short ($20 \mu\text{s}$) and long (0.1 s) pulse width.

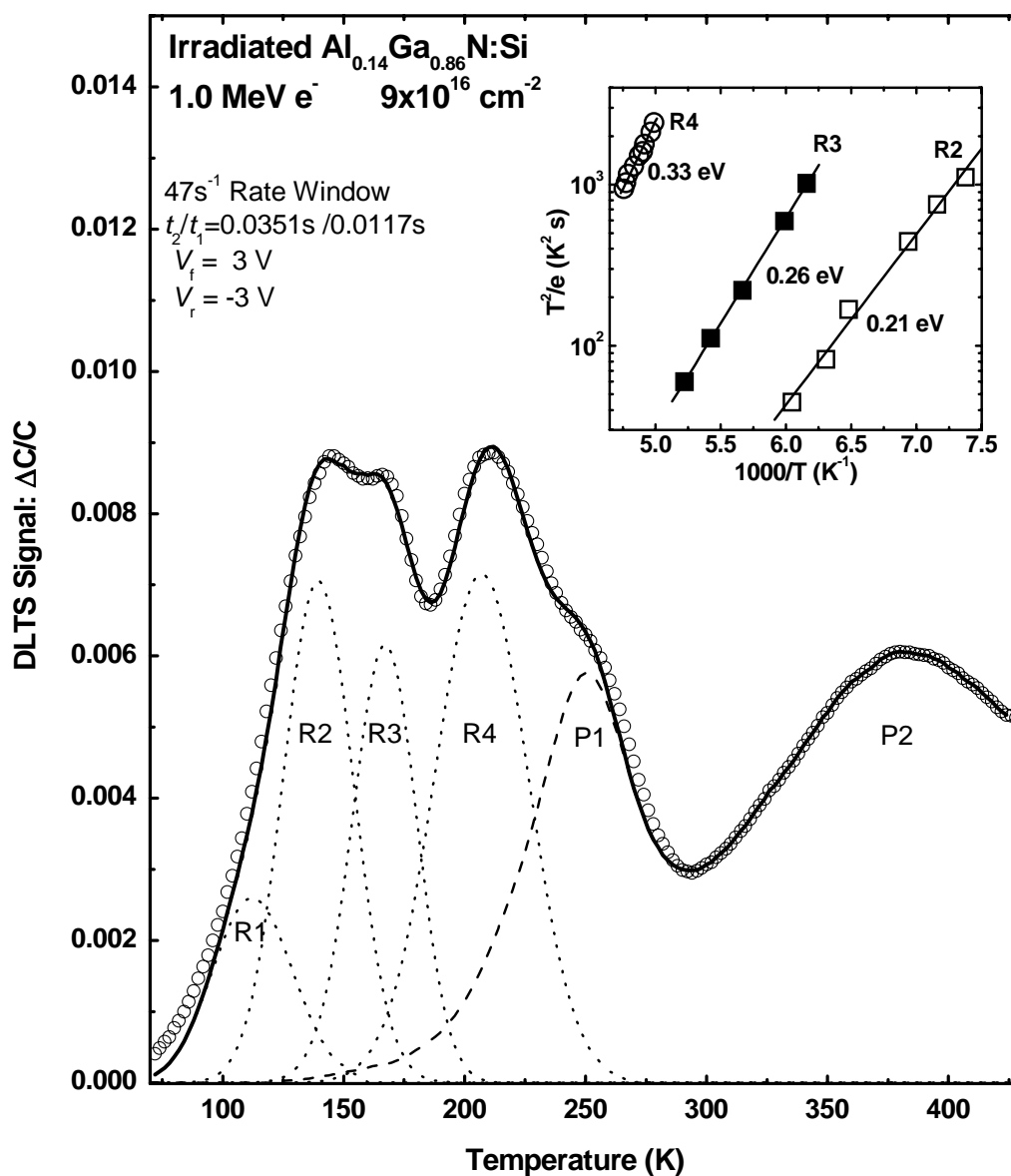


Figure V-21. DLTS spectrum of 1.0 MeV electron irradiated $\text{Al}_{0.14}\text{Ga}_{0.86}\text{N}$ (sample B2-21b) at 20 μs pulse width. Inset is the Arrhenius plot constructed from visible peak positions. Open circles are measured data. Dotted lines are the individual peaks modeled using equations IV-4 to IV-6. Dashed line is spectrum from the pre-irradiated data. The solid line is the sum of all the peaks.

pre-irradiated signal. It was then found that this value had to be scaled down for the lower energy peaks to produce a good fit to the data.

Traps R1, R2, and R3 have not been previously reported, as such, in AlGa_{0.14}N. One electron trap, EpR1 (0.187 eV), was previously reported in proton-irradiated Al_{0.12}Ga_{0.14}N using thermally stimulated capacitance (TSCAP) [42]. Though the authors drew no correlation with known defects in GaN, it appears likely to be the same as our observed trap R2, or perhaps a superposition of R1 and R2. Traps R1, R2, and R3 are similar to ER1, ER2, and ER3 observed in GaN [35]. As was discussed in chapter II, it has been reported that ER1 corresponds to the isolated nitrogen vacancy, and that ER2 is also related to the nitrogen vacancy with some difference in microscopic configuration, causing it to have different cross sections and activation energies [31]. It is noteworthy that R2 and R3 are 50 and 60 meV deeper than the corresponding traps in GaN. Equation III-2 indicates that the increase in electron effective mass would cause a shallow (hydrogenic) donor to be only 7 meV deeper. On the other hand, the band gap energy difference between Al_{0.14}Ga_{0.86}N and GaN is approximately 270 meV, so it is clear that the energy of these two traps is not fixed with respect to the vacuum level but is, in fact, partially related to the position of the conduction band minimum.

The electron trap parameters measured in unirradiated and irradiated Al_{0.14}Ga_{0.86}N are summarized in table V-2. Although an Arrhenius plot was not obtained for trap R1, a range of possible values for its activation energy can be proposed by assuming a capture cross section based on GaN reports in the literature. Two independent reports showed ER1 to have a cross section 5% that of ER2 [35, 31]. In another report, the cross section of ER1 is half that of ER2 [37]. Using these values as lower and upper bounds of the

Table V-2. Measured defect parameters in 1.0-MeV electron irradiated Al_{0.14}Ga_{0.86}N and references to similar reports.

Parameter	R1	R2	R3	R4	P1	P2
$T_{\text{peak}}^{\text{a}}$ (K)	~ 110	138	166	208	253	381
E_{TOT} (eV)	$0.15 \pm 0.02^{\text{b}}$	0.21 ± 0.02	0.26 ± 0.02	0.33 ± 0.03	0.54 ± 0.02	0.98 ± 0.10
σ_{∞} (10^{-16} cm ²)	0.05-0.5 ^b	0.7 1.0 ^b	1.4 1.25 ^b	1.3 1.25 ^b	400	40000
Similar Traps and E_{TOT} (eV) in GaN	ER1 0.13 ED1 0.06 ^b T1 0.12 (0.08 ^b)	ER2 0.16 ED2 0.11 ^b T1A 0.16	ER3 ³⁵ 0.20			
Similar Traps and E_{TOT} (eV) in Al _x Ga _{1-x} N		EpR1 0.19 ^c x = 0.12			EOA2 0.57 x = 0.12	

^a Peak temperature determined with 47s⁻¹ rate window.

^b Fitted value

^c Determined by TSCAP. Authors in Ref. 42 did not make attribution.

cross section of R1 relative to R2, activation energy of 0.15 ± 0.02 eV is obtained from the fitted R1 peak in figure V-21. Trap R4 does not have an obvious analog in irradiated GaN, suggesting that it is possibly related to aluminum displacement. Assuming binding energies comparable to GaN, the 1.0 MeV electron energy used here is above the threshold energy values needed for displacing the three constituents of Al_{0.14}Ga_{0.86}N.

Figure V-22 shows the DLTS spectrum before and after annealing at 430 and 450 K sequentially. After cycling the diode up to 430 K, the peak heights of both traps R2 and R3 decreased significantly. Some further reduction was observed after cycling up to 450 K. Trap R4, however, was thermally stable up to 450 K. Figure V-23 shows the DLTS spectrum of Al_{0.14}Ga_{0.86}N after 0.62 MeV electron irradiation with a fluence of 2.5×10^{16} cm⁻². In this sample, the carrier concentration was lower, and carrier freeze-out was a problem at low temperatures. Nevertheless, trap R4 is clearly induced by the radiation, and the introduction rate of this trap with 0.62 MeV electrons is comparable to the introduction rate with 1.0 MeV electrons. In this figure, it is also clear that the

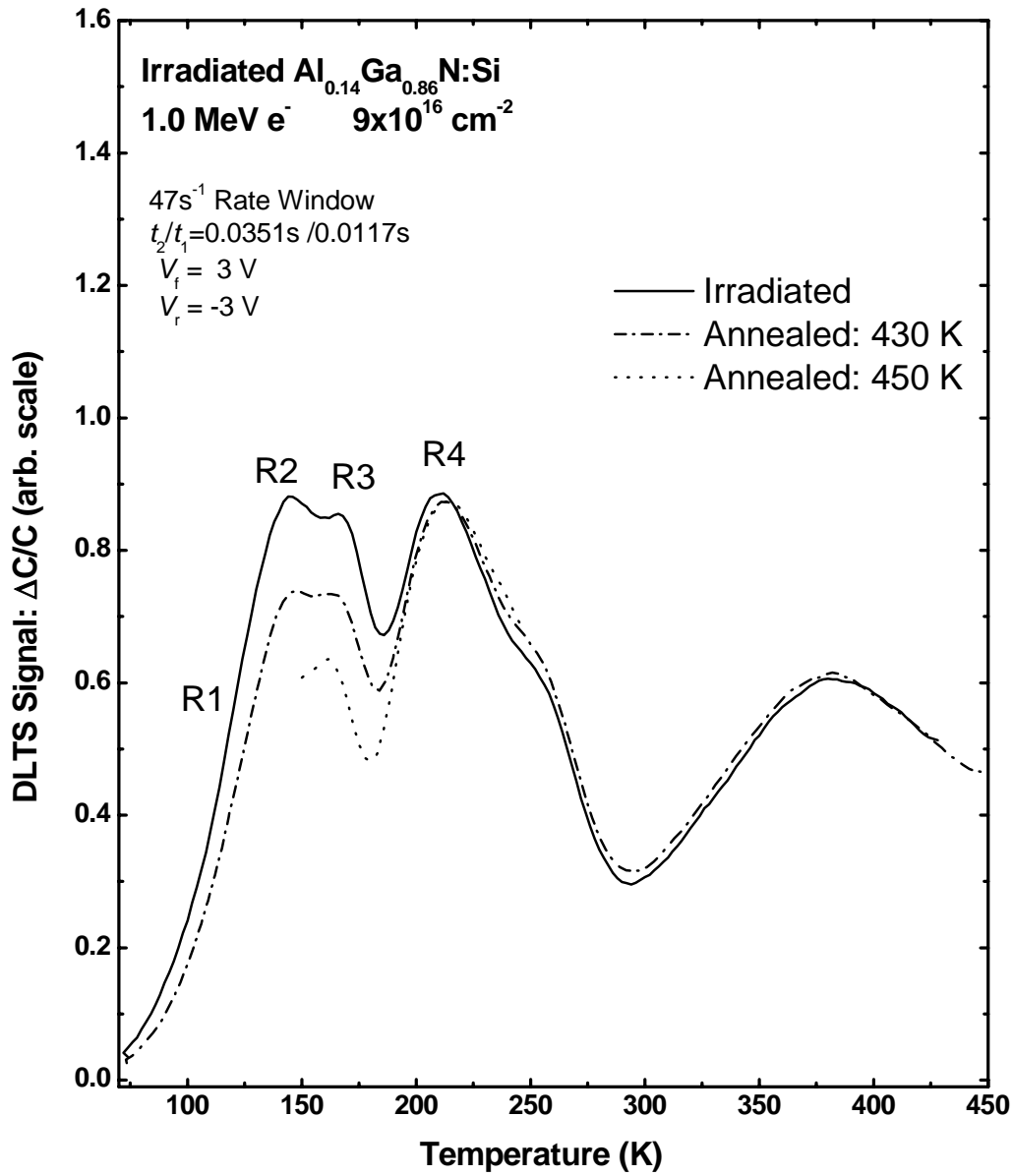


Figure V-22. DLTS spectrum of 1.0 MeV electron irradiated $\text{Al}_{0.14}\text{Ga}_{0.86}\text{N}$ (sample B2-21b) before and after annealing. The dashed and dotted lines represent the spectrum after cycling up to 430 and 450 K, respectively.

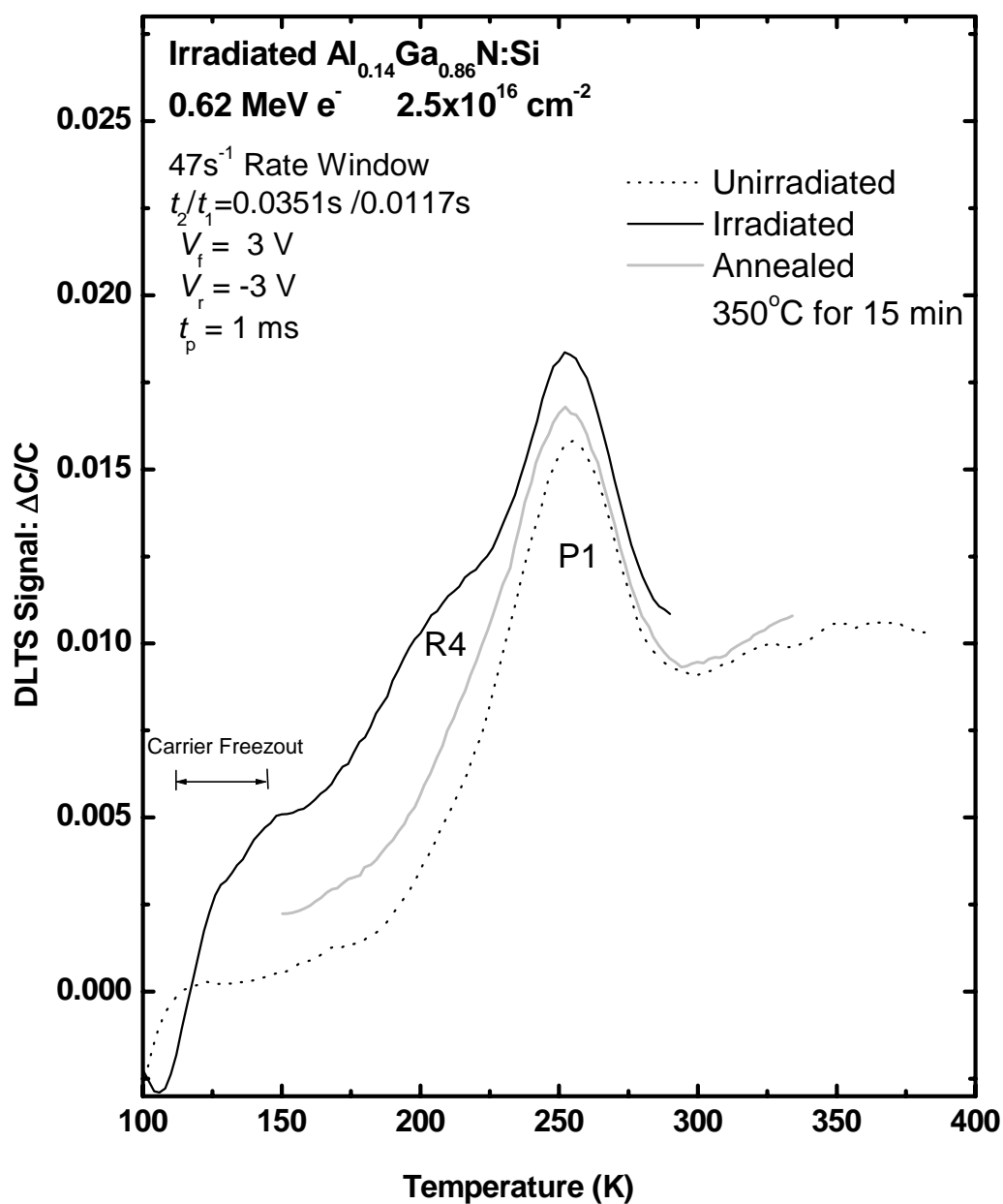


Figure V-23. DLTS spectrum of 0.62 MeV electron irradiated $\text{Al}_{0.14}\text{Ga}_{0.86}\text{N}$ (sample B2-21d) before and after 350 °C annealing. The spectrum of unirradiated $\text{Al}_{0.14}\text{Ga}_{0.86}\text{N}$ (sample B2-21d) is overlaid (dotted line).

concentration of trap R4, which was seen in figure V-22 to be stable at 177 °C (450 K), decreases considerably following annealing at 350 °C (623 K) for 15 minutes.

5.1.5 Unirradiated Al_{0.20}Ga_{0.80}N (Wafer C1)

Figure V-24 shows a DLTS spectrum of unirradiated Al_{0.20}Ga_{0.80}N typical of samples from wafer C1. A 46 s⁻¹ rate window is shown, and the pulsing parameters are $V_f = 1$ V, $V_r = -3$ V, and $t_p = 1$ ms. Three electron traps, labeled P0, P1, and P2 are apparent in the spectrum. The DLTS signals of all three traps are seen to be relatively small because of the larger carrier concentration ($\sim 3 \times 10^{17}$ cm⁻³ at 295 K) in samples from this wafer.

The peak that appears at 158 K in the 46 s⁻¹ rate window of figure V-24, labeled P0, may correspond to trap D in GaN. However, resolution of the DLTS signal is too poor for an Arrhenius plot to be constructed, so this assignment is tentative. The peaks labeled P1 and P2 correspond to the peaks given the same designation in Al_{0.14}Ga_{0.86}N. The Arrhenius plots corresponding to these two electron traps, shown in the inset of figure V-24, indicate activation energies of $E_{TOT} = 0.67 \pm 0.03$ and 0.92 ± 0.06 eV, and cross sections of $\sigma_{na} = 1.6 \times 10^{-13}$ and 9.0×10^{-14} cm² for P1 and P2, respectively.

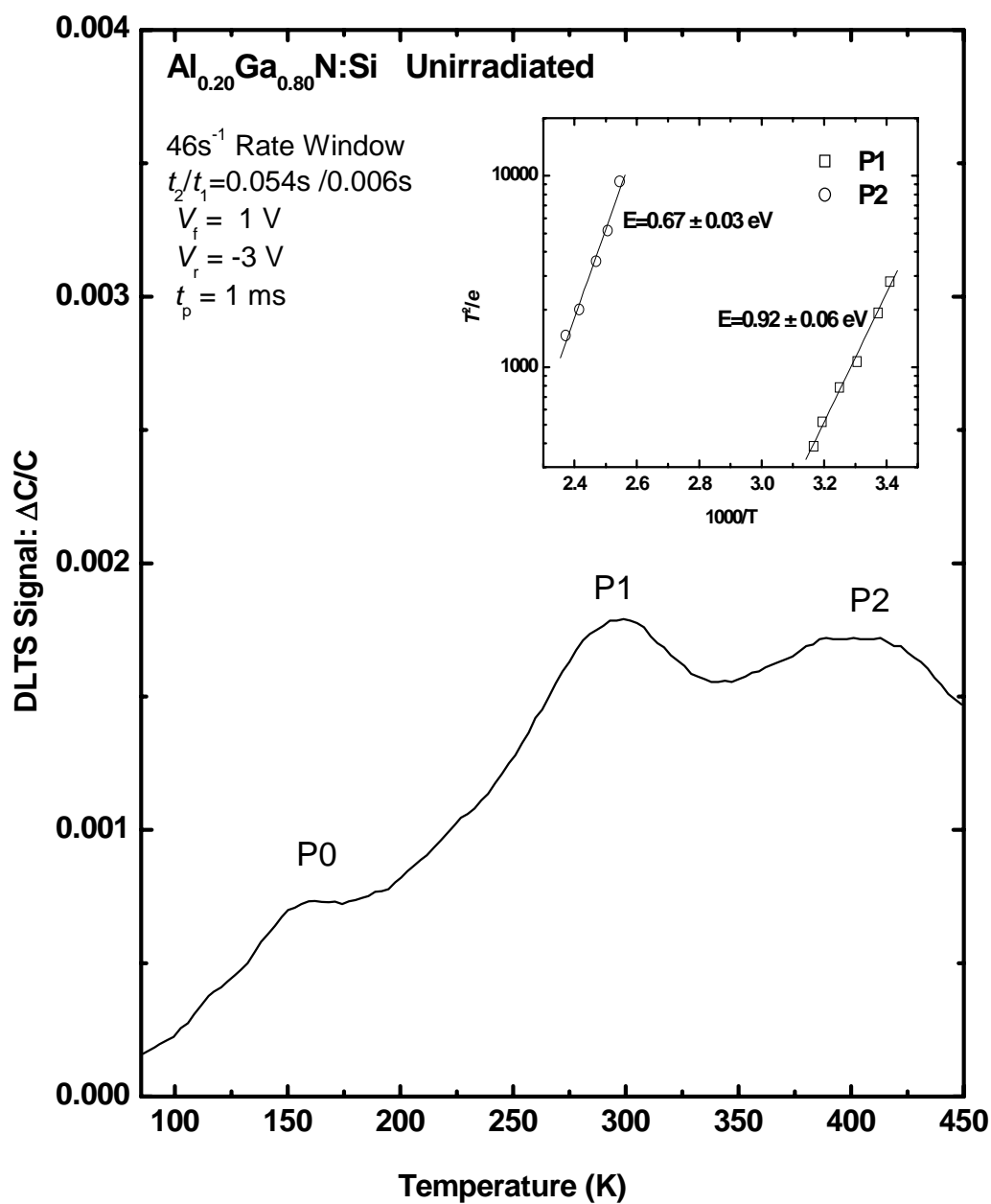


Figure V-24. DLTS spectrum of unirradiated Al_{0.20}Ga_{0.80}N (sample C1-38c). The Arrhenius plots of the two peaks are shown in the inset.

5.1.6 Irradiated Al_{0.20}Ga_{0.80}N (Wafer C1)

Figure V-25 shows the DLTS spectrum of irradiated Al_{0.20}Ga_{0.80}N sample C1-38c measured after 1.0 MeV electron irradiation to a fluence of $1.1 \times 10^{17} \text{ cm}^{-2}$ and about 3 hours of room temperature annealing. The rate window is 46 s^{-1} , and the pulsing parameters are $V_f = 1 \text{ V}$, $V_r = -3 \text{ V}$, and $t_p = 1 \text{ ms}$. The apparent activation energy and cross section of electron trap R4, determined from the Arrhenius plot shown in the inset of figure V-25, are $E_{\text{TOT}} = 0.38 \pm 0.02 \text{ eV}$ and $\sigma_{na} = 2.7 \times 10^{16} \text{ cm}^2$. Arrhenius plots for R1, R2, and R3 could not be made due to lack of resolution. The electron trap parameters measured in unirradiated and irradiated Al_{0.20}Ga_{0.80}N are summarized in table V-3. Also shown in figure V-25 is the DLTS spectrum of the same Al_{0.20}Ga_{0.80}N sample following annealing at 350 °C for 15 minutes. Figure V-26 shows a similarly irradiated Al_{0.20}Ga_{0.80}N sample, and in this case the sample was annealed at 400 °C for 15 minutes. Comparison of the two figures indicates that the radiation-induced traps anneal out nearly entirely in the 350 to 400 °C temperature range.

Table V-3. Measured defect parameters in 1.0-MeV electron irradiated Al_{0.20}Ga_{0.80}N and references to similar reports.

Parameter	R2	R3	P0	R4	P1	P2
$T_{\text{peak}}^a \text{ (K)}$	~177	~208	158	245	296	405
$E_{\text{TOT}} \text{ (eV)}$				0.38 ± 0.02	0.67 ± 0.03	0.92 ± 0.06
$\sigma_{\infty} (10^{-16} \text{ cm}^2)$				2.7	1600	900
Similar Traps and $E_{\text{TOT}} \text{ (eV)}$ in GaN	ER2 0.16 ED2 0.11 ^b T1A 0.16	ER3 ³⁵ 0.20	D 0.25 EO2 0.27 E1 0.26 DLN ₁ 0.24			
Similar Traps and $E_{\text{TOT}} \text{ (eV)}$ in Al _x Ga _{1-x} N	EpR1 0.19 ^c x = 0.12		P1 0.16 x = 0.09		EOA2 0.57 x = 0.12	

^a Peak temperature determined with 47 s^{-1} rate window.

^b Fitted value

^c Determined by TSCAP. Authors in Ref. 42 did not make attribution.

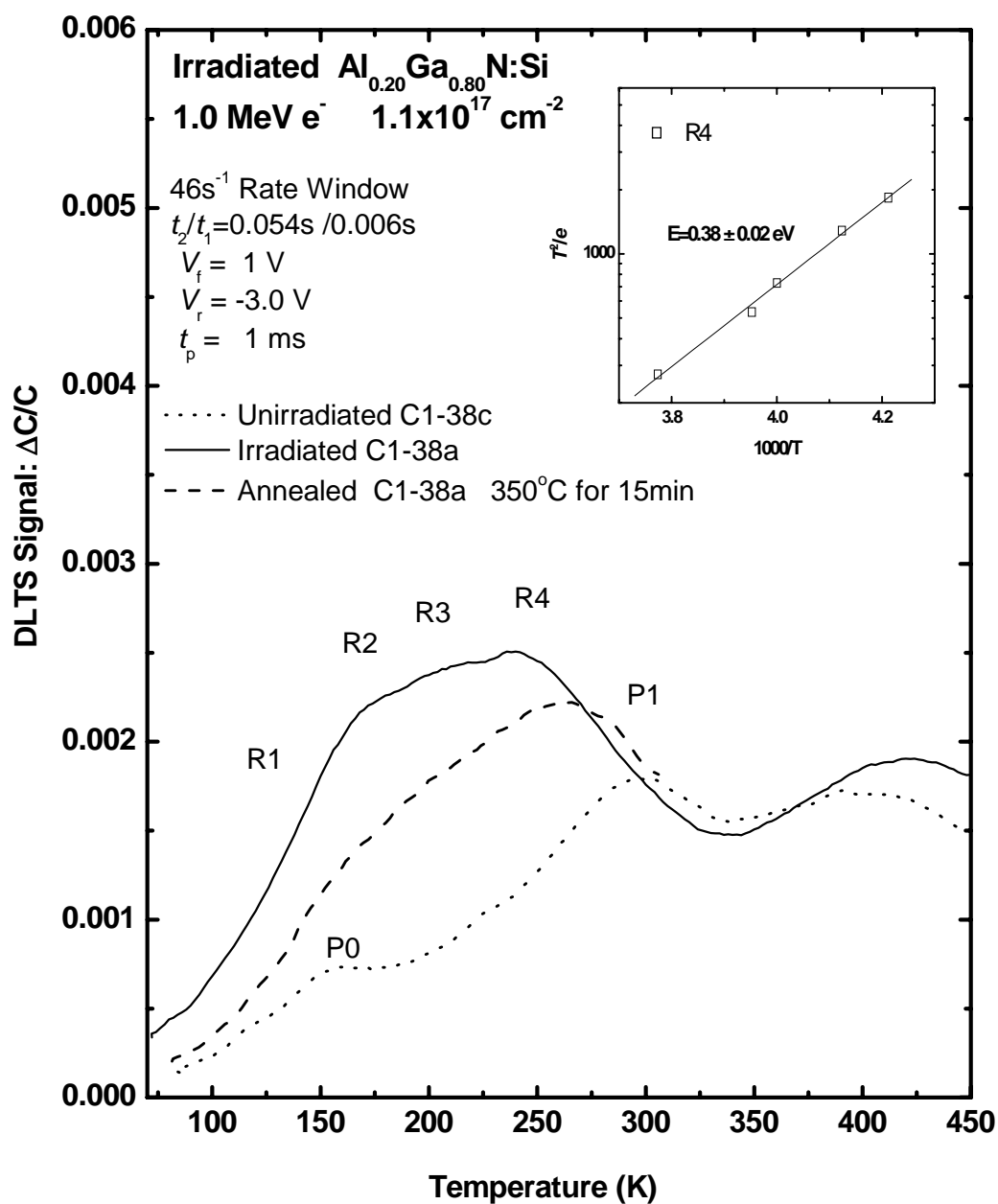


Figure V-25. DLTS spectrum of 1.0 MeV electron irradiated $\text{Al}_{0.20}\text{Ga}_{0.80}\text{N}$ (sample C1-38a) before and after 350 °C annealing. The spectrum of unirradiated $\text{Al}_{0.20}\text{Ga}_{0.80}\text{N}$ (sample C1-38c) is overlaid (dotted line).

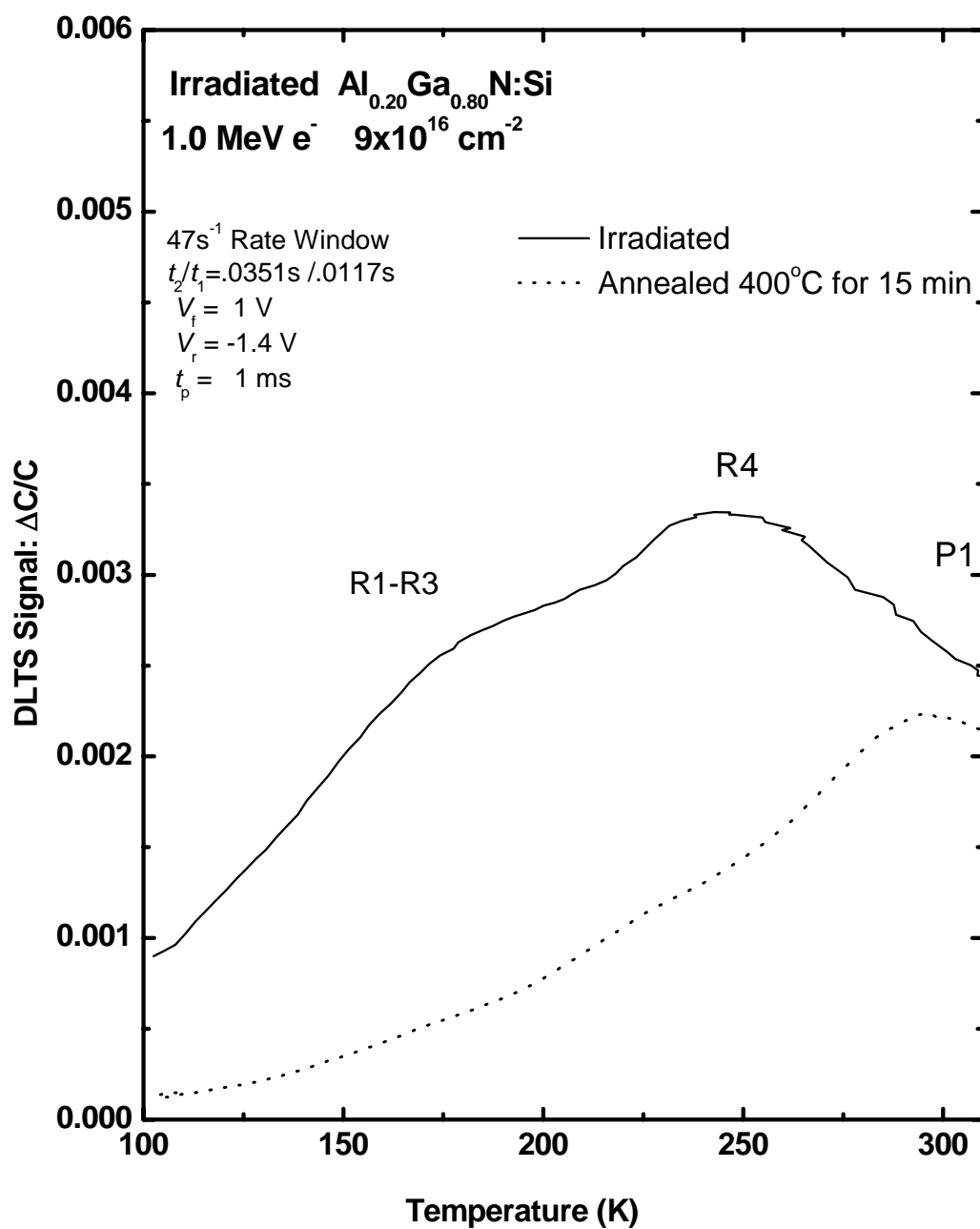


Figure V-26. DLTS spectrum of 1.0 MeV electron irradiated $\text{Al}_{0.20}\text{Ga}_{0.80}\text{N}$ (sample C1-40b) before and after 400 °C annealing.

5.1.7 Unirradiated Al_{0.30}Ga_{0.70}N (Wafer D1)

Figure V-27 shows a DLTS spectrum typical of Al_{0.30}Ga_{0.70}N samples from wafer D1. A 47 s⁻¹ rate window is shown, and the pulsing parameters are $V_f = 3$ V, $V_r = -5$ V, and $t_p = 20$ μ s. One electron trap, labeled P0, dominates the low temperature end of the spectrum. The apparent activation energy and cross section of electron trap P0, determined from the Arrhenius plot in the inset of figure V-27 are $E_{TOT} = 0.39 \pm 0.02$ eV and $\sigma_{na} = 2.5 \times 10^{-11}$ cm². The very large capture cross section of trap P0 is responsible for this trap having a 47 s⁻¹ rate window peak at such a low temperature as 152 K when the activation energy is so large. Under the pulsing parameters $V_f = 4.5$ V, $V_r = -1$ V, and $t_p = 1$ ms, two peaks labeled P1 and P2 are better resolved in the high temperature range of the 47 s⁻¹ rate window spectrum as shown in the figure. The apparent activation energy and cross section of electron trap P1, determined from the Arrhenius plot in the inset of figure V-27, are $E_{TOT} = 0.94 \pm 0.06$ eV and $\sigma_{na} = 3.0 \times 10^{-12}$ cm². Figure V-28 shows the DLTS spectrum with reverse bias voltage ranging from $V_r = 0$ to -5 V. The inset of this figure shows that the shape and location of peak P0 does not change appreciably with reverse bias voltage. Figure V-29 shows the normalized peak P0 peak height versus reverse bias voltage. The shape of this plot is characteristic of a trap distributed throughout the depth of the epitaxial layer. The electron trap parameters measured in unirradiated Al_{0.30}Ga_{0.70}N are summarized in table V-4.

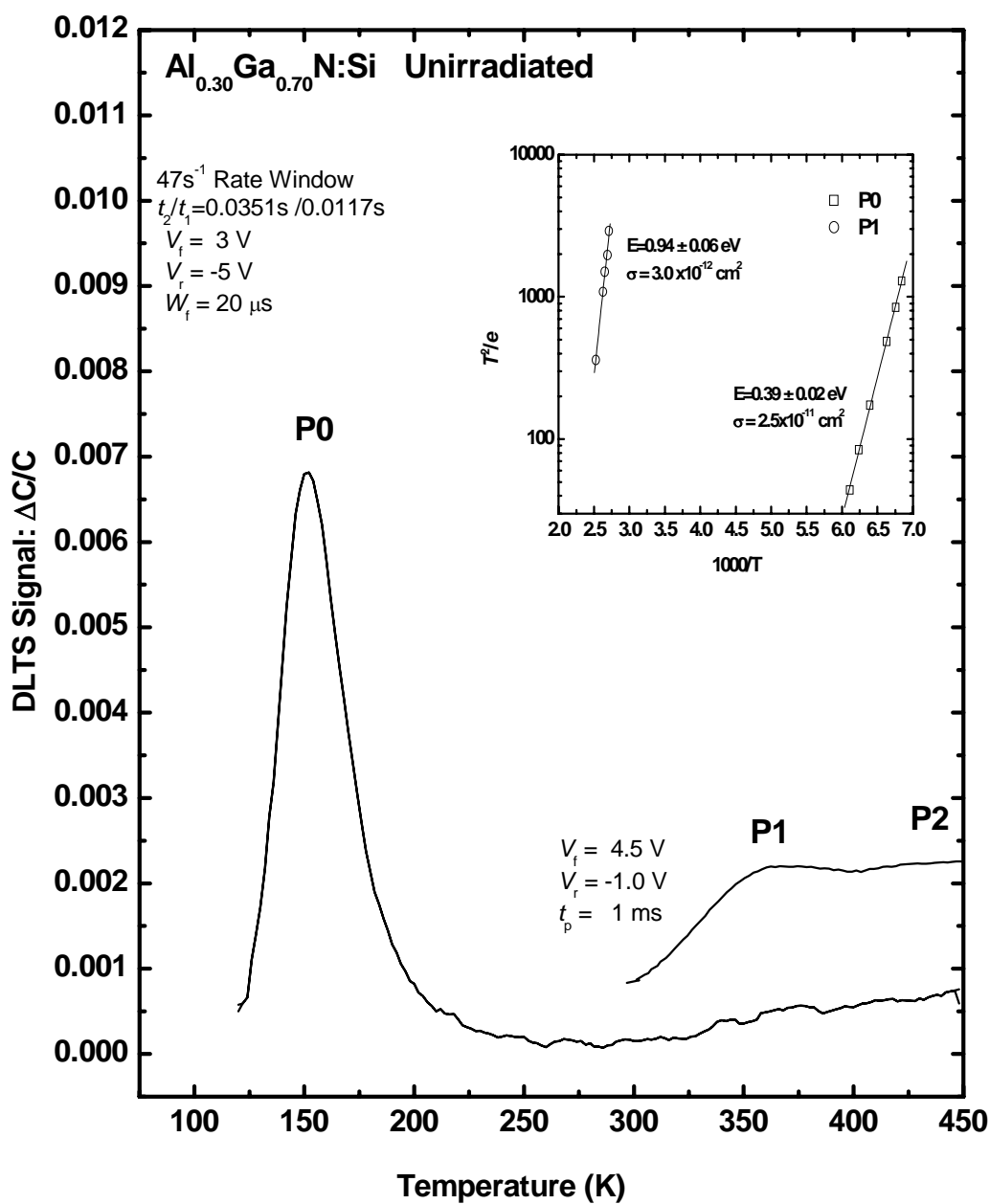


Figure V-27. DLTS spectrum of unirradiated sample D1-38c (Al_{0.30}Ga_{0.70}N). The Arrhenius plot of peaks P0 and P1 are shown in the inset.

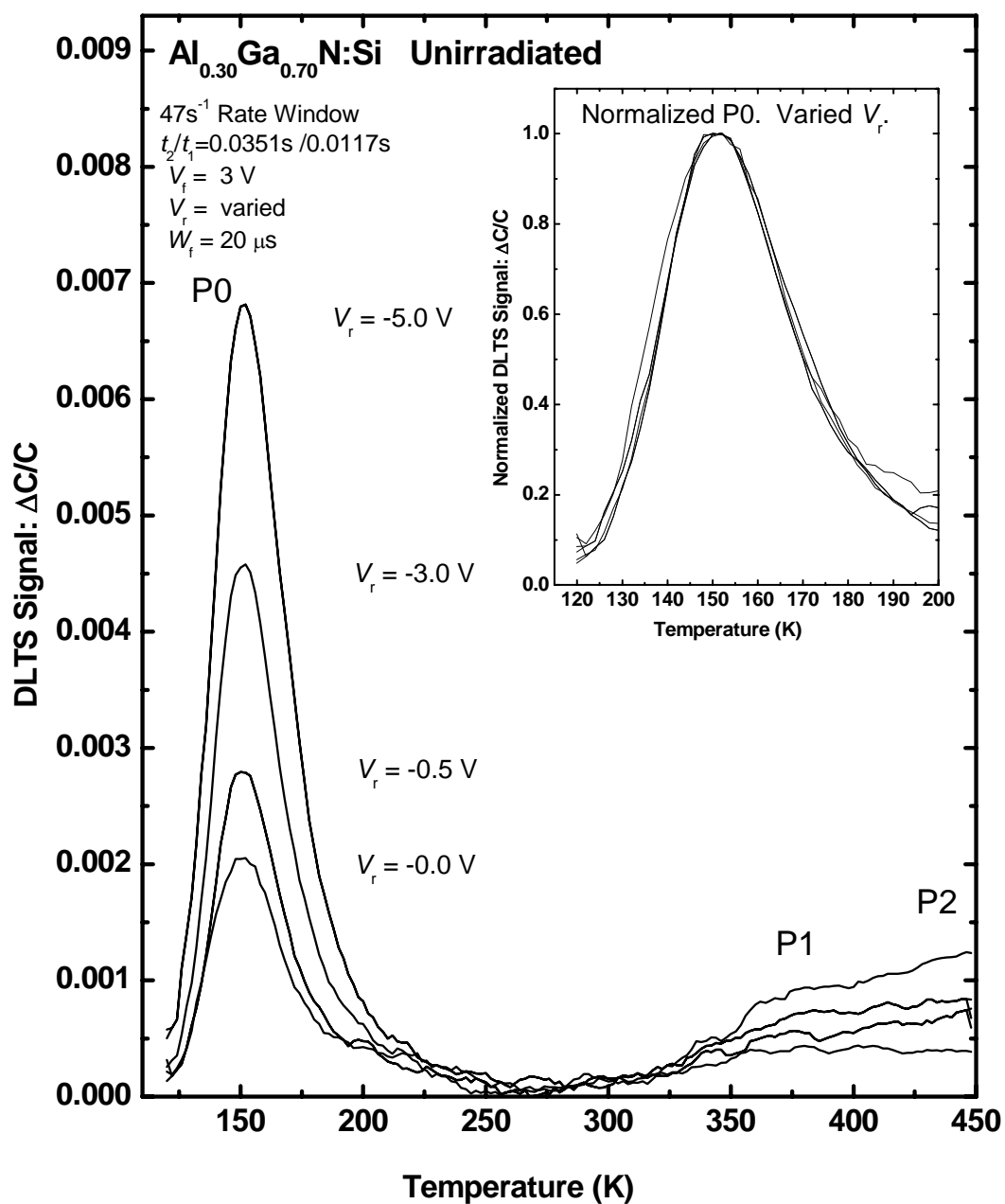


Figure V-28. DLTS spectra of unirradiated Al_{0.30}Ga_{0.70}N (sample D1-38c) at four different reverse bias voltages. Inset is the normalized peak P0 for each of the traces, showing that the peak shape is unchanged with reverse bias voltage.

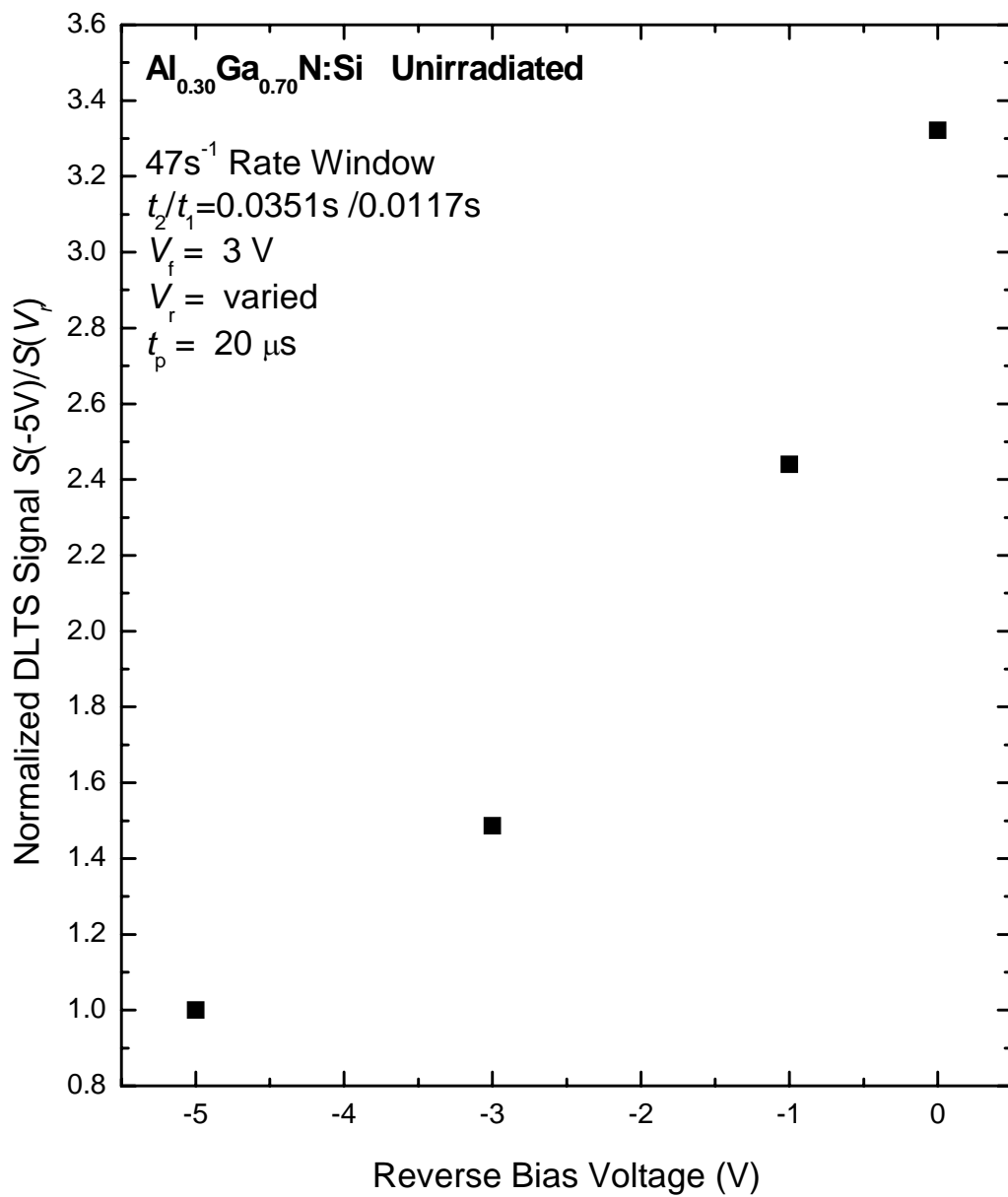


Figure V-29. Normalized peak height of electron trap P0 in $\text{Al}_{0.30}\text{Ga}_{0.70}\text{N}$ versus reverse bias voltage.

Table V-4. Measured defect parameters in unirradiated $\text{Al}_{0.30}\text{Ga}_{0.70}\text{N}$ and references to similar reports.

Parameter	P0	P1	P2
$T_{\text{peak}}^{\text{a}}$ (K)	152	369	440
E_{TOT} (eV)		0.94 ± 0.06	
σ_{∞} (10^{-16} cm^2)		30000	
Similar Traps and E_{TOT} (eV) in GaN	D 0.25 EO2 0.27 E1 0.26 DLN _i ⁹³ 0.24		
Similar Traps and E_{TOT} (eV) in $\text{Al}_x\text{Ga}_{1-x}\text{N}$	P1 ⁹⁸ 0.16 x=0.09	EOA2 0.57 x = 0.12	

^aPeak temperature determined with 47s^{-1} rate window.

5.1.8 Irradiated $\text{Al}_{0.30}\text{Ga}_{0.70}\text{N}$ (Wafer D1)

Figure V-30 shows the DLTS spectrum of irradiated $\text{Al}_{0.30}\text{Ga}_{0.70}\text{N}$ sample D1-38c measured after 0.62 MeV electron irradiation to a fluence of $2.5 \times 10^{16} \text{ cm}^{-2}$. The rate window is 47 s^{-1} , and the pulsing parameters are $V_f = 3 \text{ V}$, $V_r = -5\text{V}$, and $t_p = 20 \mu\text{s}$. Under these conditions, no radiation-induced peaks were observed in the 120 to 290 K temperature range. It should be noted that the C-V characteristics of samples from wafer D1 are poor due to high series resistance. Thus, the DLTS spectra of both the unirradiated and irradiated samples were suppressed in magnitude. This fact makes it difficult to determine whether or not the $2.5 \times 10^{16} \text{ cm}^{-2}$ fluence of 0.62 MeV electrons created electron traps corresponding to those seen in the $x = 0$ to 0.20 $\text{Al}_x\text{Ga}_{1-x}\text{N}$ samples.

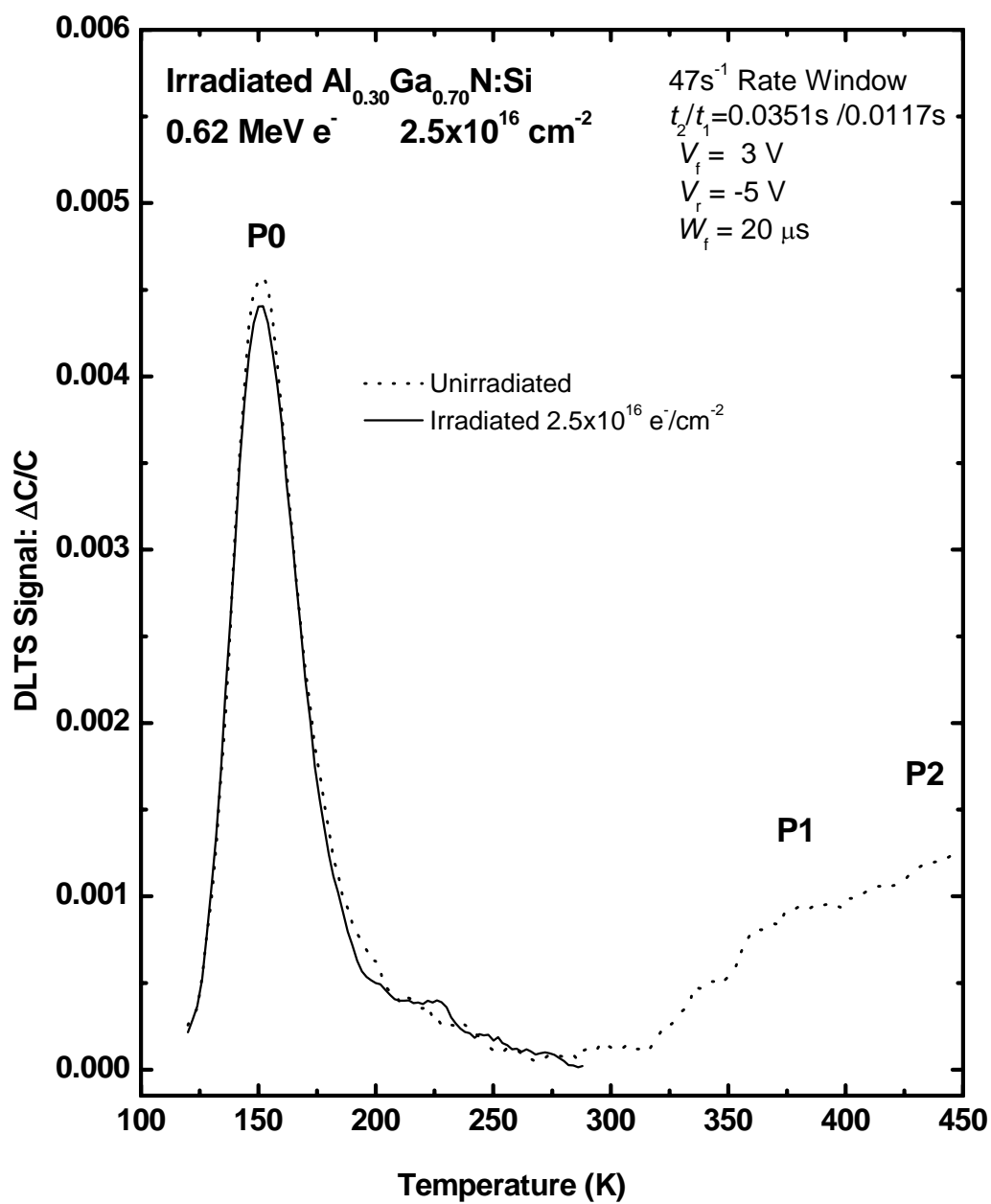


Figure V-30. DLTS spectra of $\text{Al}_{0.30}\text{Ga}_{0.70}\text{N}$ (sample D1-38c) before and after 0.62 MeV electron irradiation.

5.1.9 DLTS Analysis

Figure V-31 compares the 46 s^{-1} rate windows of unirradiated $\text{Al}_x\text{Ga}_{1-x}\text{N}$ for $x=0.0, 0.14, 0.20$, and 0.30 . Two significant electron traps, P1 and P2, appear in unirradiated AlGa_N at all aluminum mole fractions. The electron trap, P2, appears to be a superposition of traps, as yet, unidentified. However, the peak trends in figure V-31 suggest that P2 could be a superposition of traps A and B. These two traps are both thought to be related to V_{Ga} -shallow donor complexes [11], and are present in GaN grown by all kinds of methods. Trap P1, which has been previously reported in $\text{Al}_{0.12}\text{Ga}_{0.88}\text{N}$ [42], was discussed in terms of its relationship to another previously reported trap, DLN_2 . This DLN_2 trap was reported by Götz, *et al.* [97] as being donor-like. In figure V-17, it is shown that this trap does not exhibit Poole-Frenkel barrier lowering at low electric field strength. Additionally, the dislocation related capture kinetics shown in the inset of figure V-18 suggests that trap P1 is acceptor-like. It may be concluded that Götz, *et al.* were either observing a defect that was different from P1 or that they mistakenly attributed Poole-Frenkel barrier lowering to what was actually phonon-assisted tunneling at the high field strength. Figure V-32 compares DLTS spectra of the radiation-induced electron traps measured in $\text{Al}_x\text{Ga}_{1-x}\text{N}$ at $x=0.14$ and 0.20 . It is clear that the radiation-induced peaks R1, R2, R3, and R4 are induced at each aluminum mole fraction, and that the peak positions of these traps shift upward in temperature with aluminum mole fraction. Arrhenius analysis of radiation-induced traps R2, R3, and R4 indicates that this peak temperature shift is caused by an increase in E_{TOT} . The same can be confirmed for as-grown electron traps P1 and P2. Figure V-33 plots the

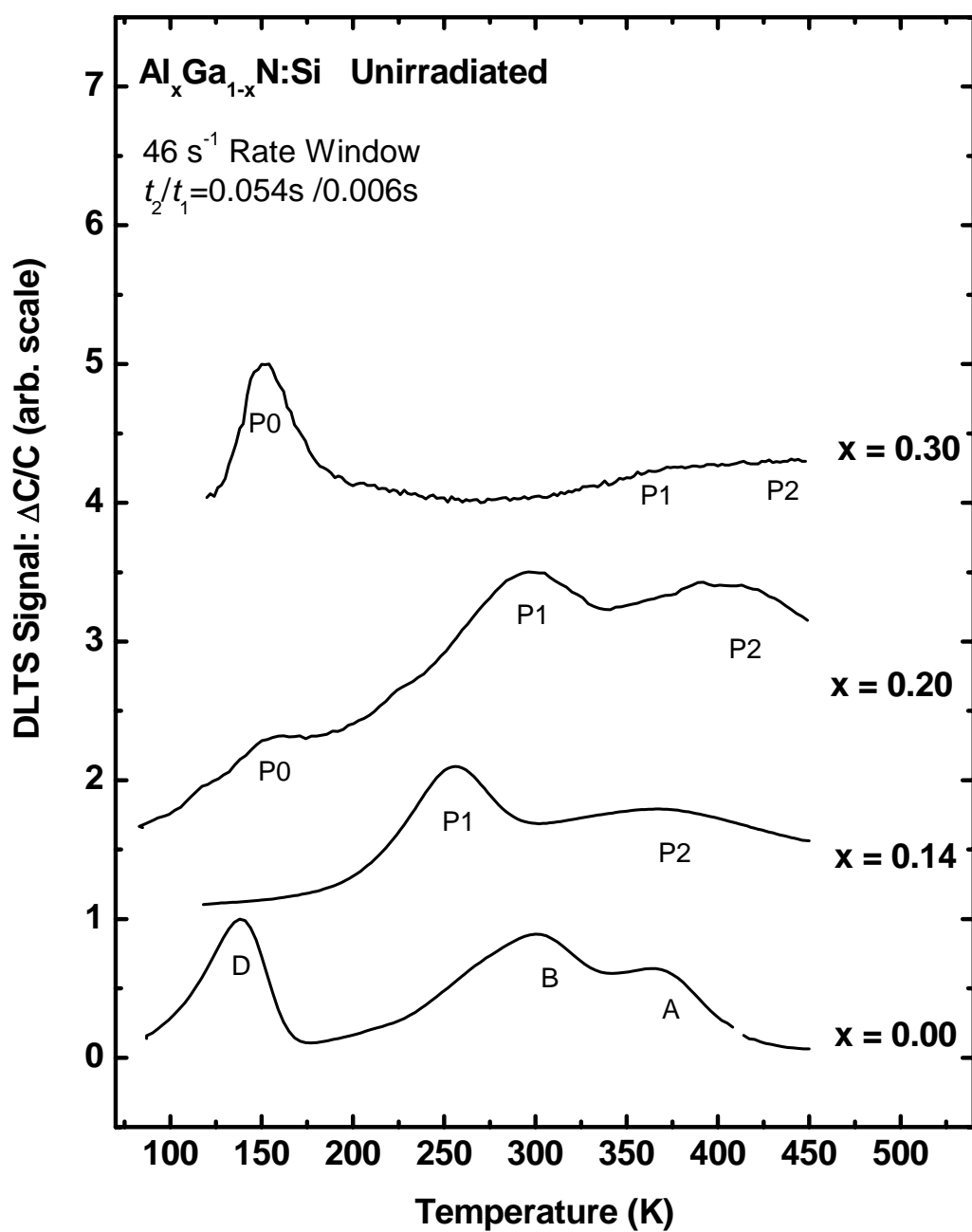


Figure V-31. DLTS spectra of unirradiated Al_xGa_{1-x}N for $x=0$, $x=0.14$, $x=0.20$, and $x=0.30$.

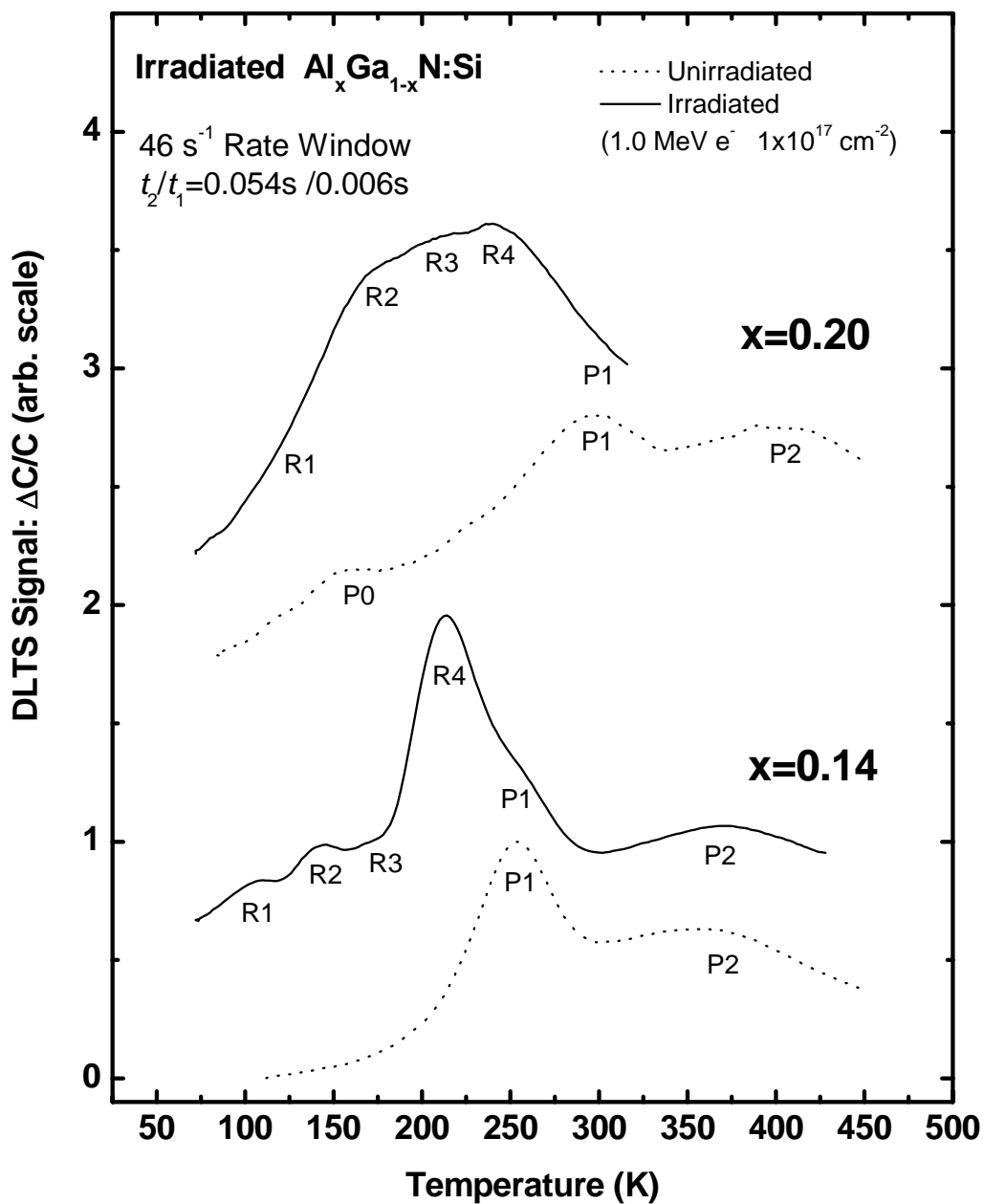


Figure V-32. DLTS spectra of $\text{Al}_x\text{Ga}_{1-x}\text{N}$ ($x=0.14$ and $x=0.20$) before and after 1.0 MeV electron irradiation.

measured E_{TOT} versus x for several different electron traps. The progression of E_{TOT} versus x for electron trap P1 is found to be equal to the increase in band gap energy as measured by CL (table III-1). This trend for P1 is shown clearly in figure V-34 where E_{TOT} is plotted versus band gap energy. In this figure, a straight line with a slope of 1.0 connects the three P1 data points, indicating that the increase in E_{TOT} is equal to the increase in band gap energy in this range. In figure V-34, the dotted line represents a possible extension of AlGaIn trap P1 to GaN trap D. The E_{TOT} of radiation-induced traps R2, R3, and R4 are found to increase significantly with increase in x , but by a lesser amount than the increase in band gap energy. The slope of each connecting line is labeled in figure V-34. It is apparent in this figure that E_{TOT} of the shallowest traps changes the least with increase in band gap energy and that E_{TOT} of the deepest traps changes the most with the increase in band gap energy. The radiation-induced defects in GaN corresponding to R1 and R2 are believed to be V_N related. Thus R1 and R2 in AlGaIn may also be related to V_N . While these defects are ubiquitous in irradiated GaN, the radiation-induced trap corresponding to R3 is not reported by all groups. However, it has been observed in HVPE GaN by Aurret *et al.* under a variety of different radiation conditions (Sr^{90} β -decay electron source, 5.4 MeV He-ions, and 2 MeV protons [96:262]). They reported that this trap did not exhibit typical Poole-Frenkel electric field enhanced emission. Given this fact, and that the capture cross section was relatively small ($\sigma = 8 \pm 4 \times 10^{-18} \text{ cm}^2$), the authors [96] suggested that ER3 is acceptor-like. The radiation-induced electron trap R4 observed here does not appear to correspond to the radiation-induced trap level reported previously in GaN. This raises the possibility that

R4 is related to aluminum displacement This trap is introduced with 1.0 MeV radiation at a greater rate than the

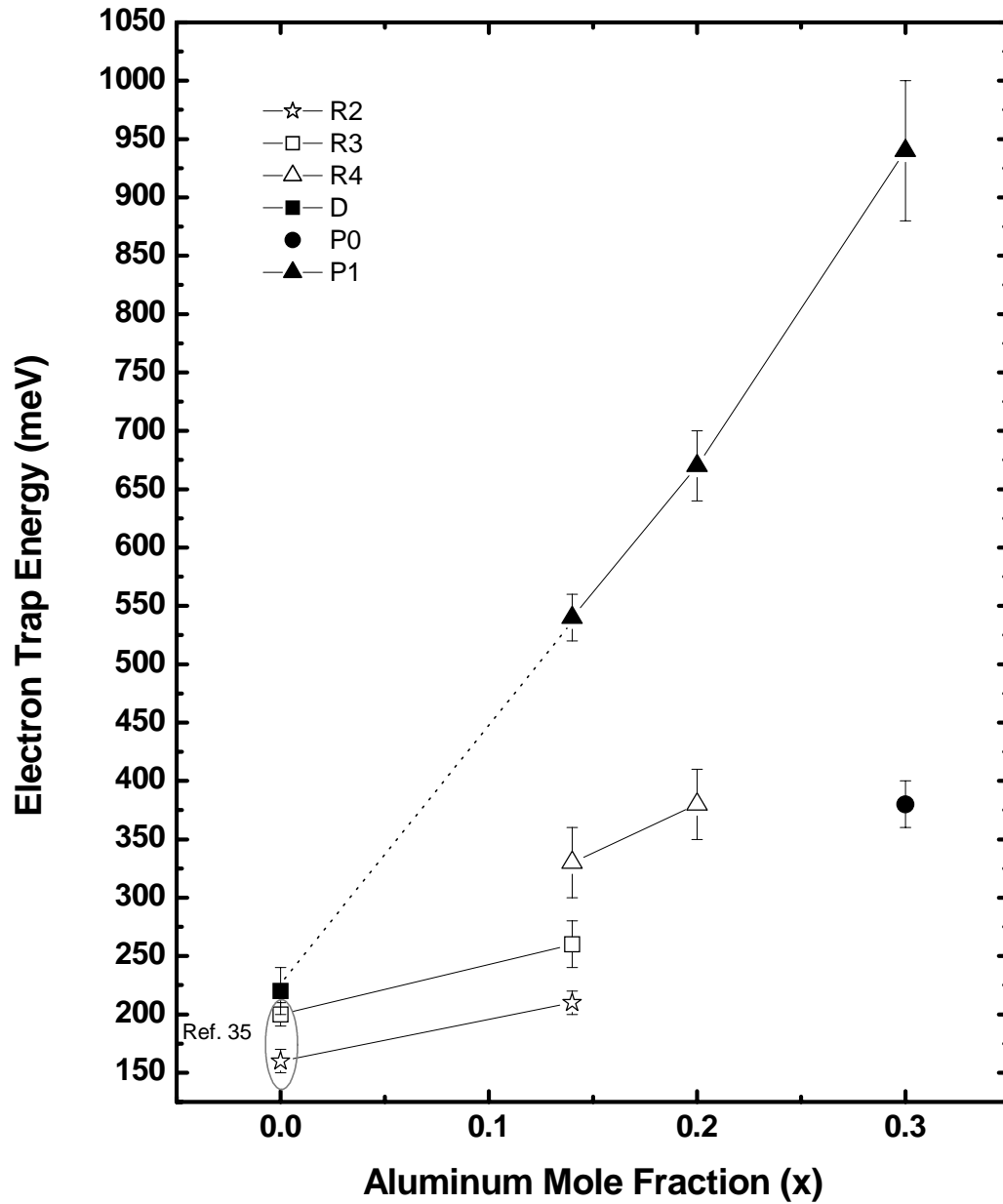


Figure V-33. Measured electron trap energy versus aluminum mole fraction for traps labeled R2, R3, R4, D, P0, and P1 in this study. The dotted line represents a possible extension to GaN trap D with decrease in aluminum mole fraction.

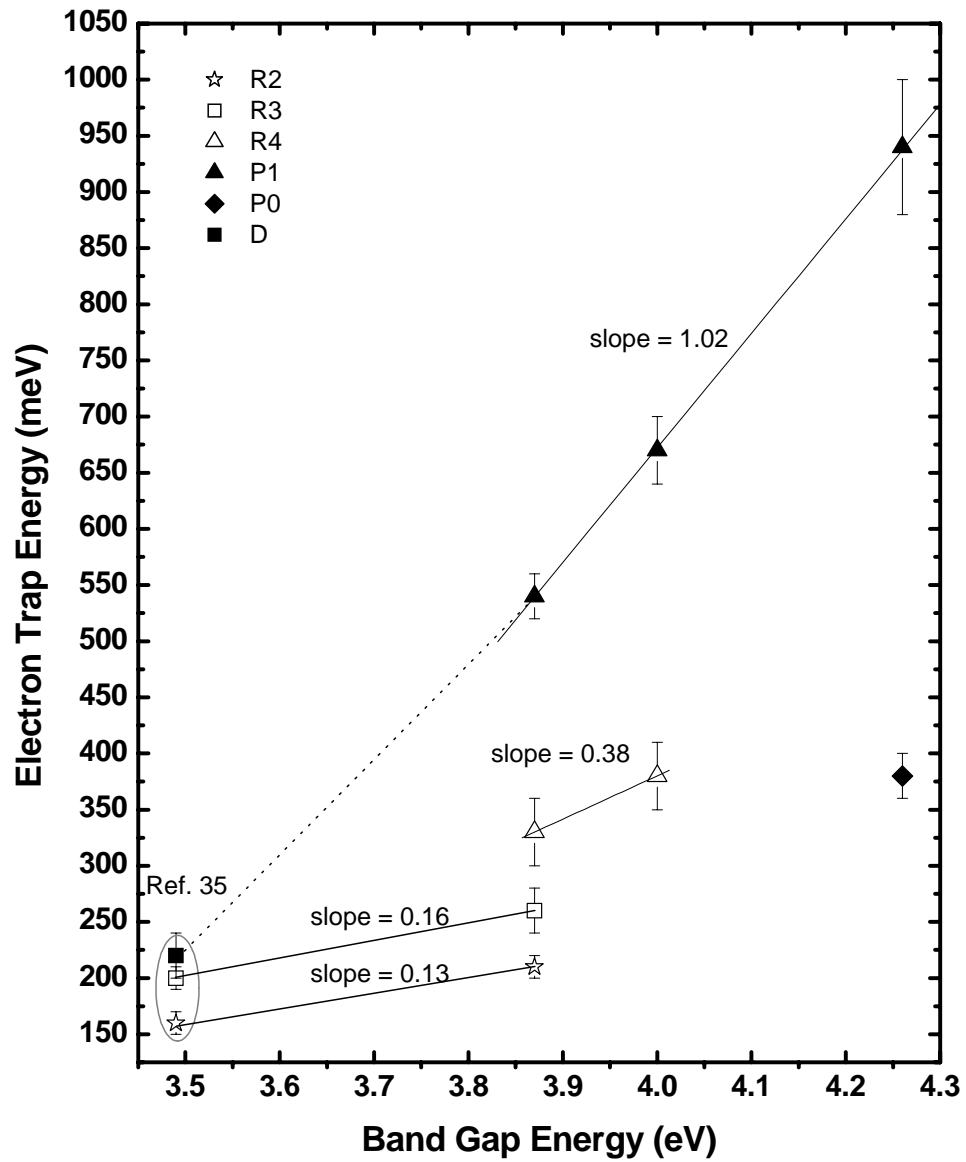


Figure V-34. Measured electron trap energy versus band gap energy for traps labeled R2, R3, R4, D, P0, and P1 in this study. The dotted line represents a possible extensions to GaN trap D with decrease in band gap energy.

individual introduction rates of R1, R2, and R3. Furthermore, R4 appears to have greater thermal stability than the other three traps. The existence of this trap, could, therefore, be a very important contributor to radiation-induced degradation of AlGa_N based devices.

Traps A, B, C, D, P0, P1, and P2 all exhibit dislocation-related capture kinetics as discussed in chapter IV. According to the theory that was discussed in that chapter, these traps are expected to be acceptor-like defects that are concentrated in the vicinity of the multiple dislocations expected in thin, epitaxial layers of GaN and AlGa_N. All of the radiation-induced traps anneal out almost entirely following annealing at 400 °C for 15 minutes, and traps R1 and R2 begin annealing (under a reverse bias electric field) below 200 °C in Al_{0.14}Ga_{0.86}N. Comparing figures V-22, V-23, and V-25, the radiation-induced traps, R2, R3, and R4 appear to have greater thermal stability in Al_{0.20}Ga_{0.80}N than those of the same traps in Al_{0.14}Ga_{0.86}N. The electron trap labeled P0 in Al_{0.30}Ga_{0.70}N is of unknown origin, and it has an unusually large capture cross section. This large cross section would normally indicate a donor-type trap, but the reverse bias voltage dependence and electron capture kinetics do not appear to support this conclusion. Figure V-35 shows the Arrhenius plots of all electron traps thus characterized in this study. The corresponding activation energies and capture cross sections can be found in tables V-1, V-2, V-3, and V-4

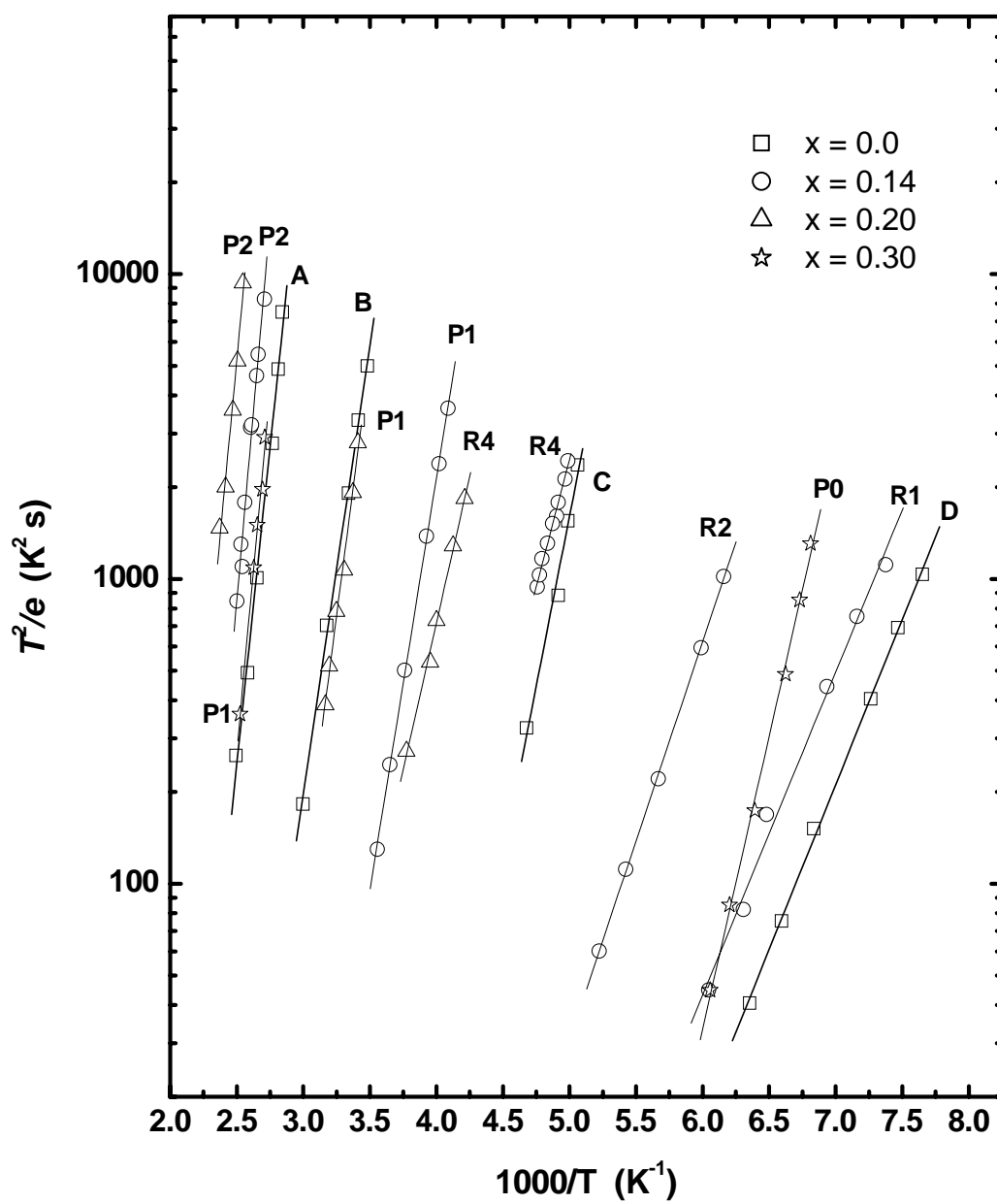


Figure V-35. Arrhenius plots of all $Al_xGa_{1-x}N$ traps characterized in this study.

5.2 Hall Effect Measurements

Hall effect measurements of $\text{Al}_x\text{Ga}_{1-x}\text{N}$ ($x=0.0$ to 0.30) samples were made following 1.0 MeV electron irradiation at a fluence of $1 \times 10^{17} \text{ cm}^{-2}$. The room temperature carrier removal rate, η , was calculated as the change in carrier concentration divided by the fluence. It is found that to first order, the carrier removal rate, η , is dominated by the initial carrier concentration, n_o . Figure V-36 shows that the carrier removal rate, η , has an approximately linear relationship to n_o , regardless of the aluminum mole fraction. This linear fit is quantified as $\eta = (3.96 \times 10^{-18} n_o - 0.15) \text{ cm}^{-1}$ for $6.5 \times 10^{16} \leq n_o \leq 8.2 \times 10^{17} \text{ cm}^{-3}$. Under the same irradiation and characterization conditions, the GaAs sample F1-8 ($n_o = 6.41 \times 10^{17} \text{ cm}^{-3}$) is found to have a carrier removal rate $\eta = 5.1 \text{ cm}^{-1}$, while the corresponding η in $\text{Al}_x\text{Ga}_{1-x}\text{N}$ having the same n_o is 2.4 cm^{-1} . Thus, the removal rate due to 1.0 MeV electron irradiation in this GaAs sample is two times greater than in $\text{Al}_x\text{Ga}_{1-x}\text{N}$.

Temperature dependent carrier concentration was analyzed in order to determine the mechanisms involved in this carrier removal processes. Figure V-37 shows the temperature dependent carrier concentration of GaN sample A2-6 before and after the $1.1 \times 10^{17} \text{ cm}^{-2}$ fluence of 1.0 MeV electrons. The fit lines are produced by using the two donor model of equation IV-16. Before irradiation, the fitting parameters indicate that there are $1.9 \times 10^{17} \text{ cm}^{-3}$ shallow donors, N_{D1} , having a screened thermal activation energy, E_{D1} , equal to 17 meV . Also, there are $7.5 \times 10^{16} \text{ cm}^{-3}$ deeper donors, N_{D2} , having a screened thermal activation energy, E_{D2} , equal to 59 meV . There are also $2.3 \times 10^{16} \text{ cm}^{-3}$ deep (always ionized) acceptors, N_A . Following irradiation, N_{D1} drops to $1.64 \times 10^{17} \text{ cm}^{-3}$,

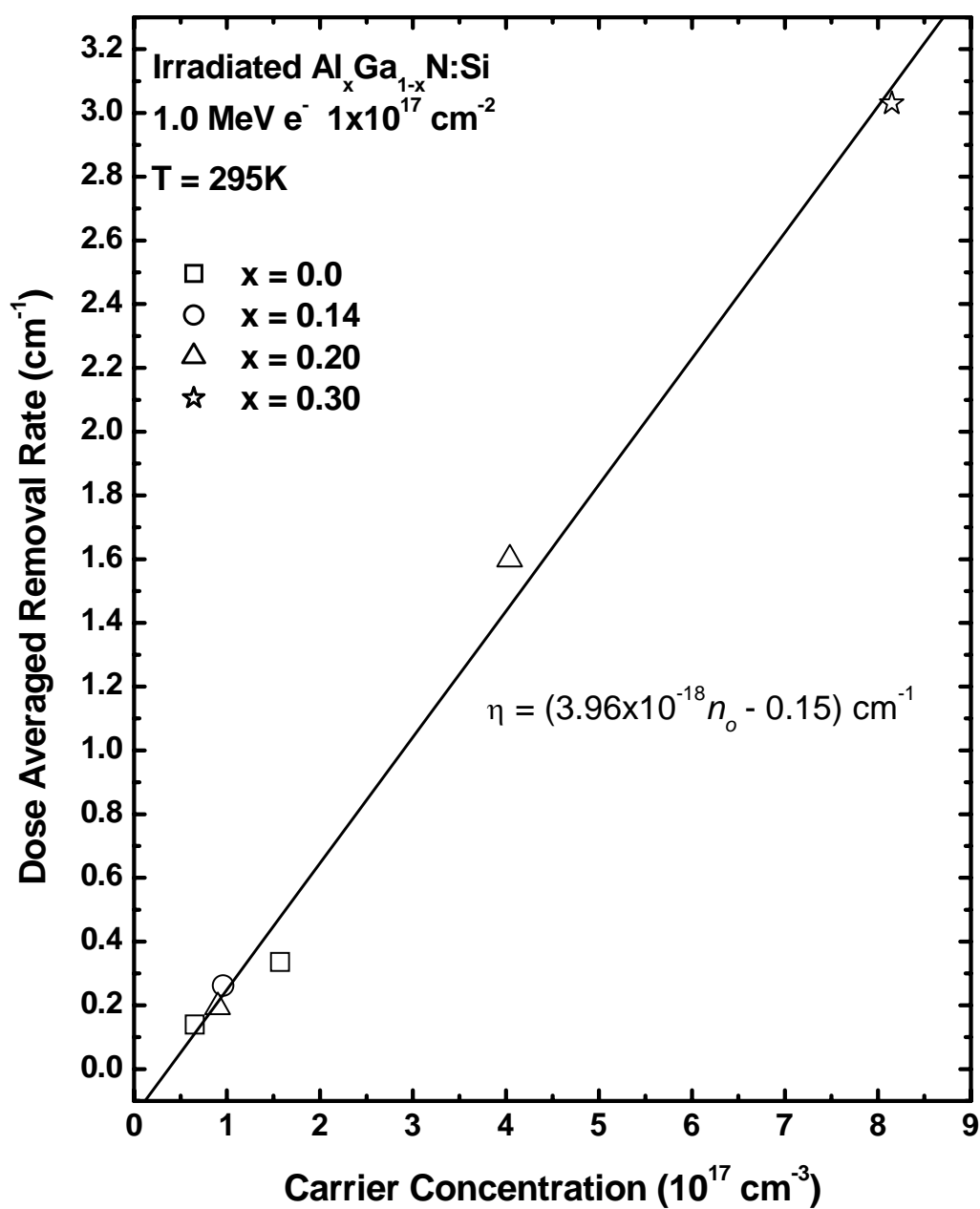


Figure V-36. Dose-averaged carrier removal versus initial room temperature carrier concentration in $\text{Al}_x\text{Ga}_{1-x}\text{N}$.

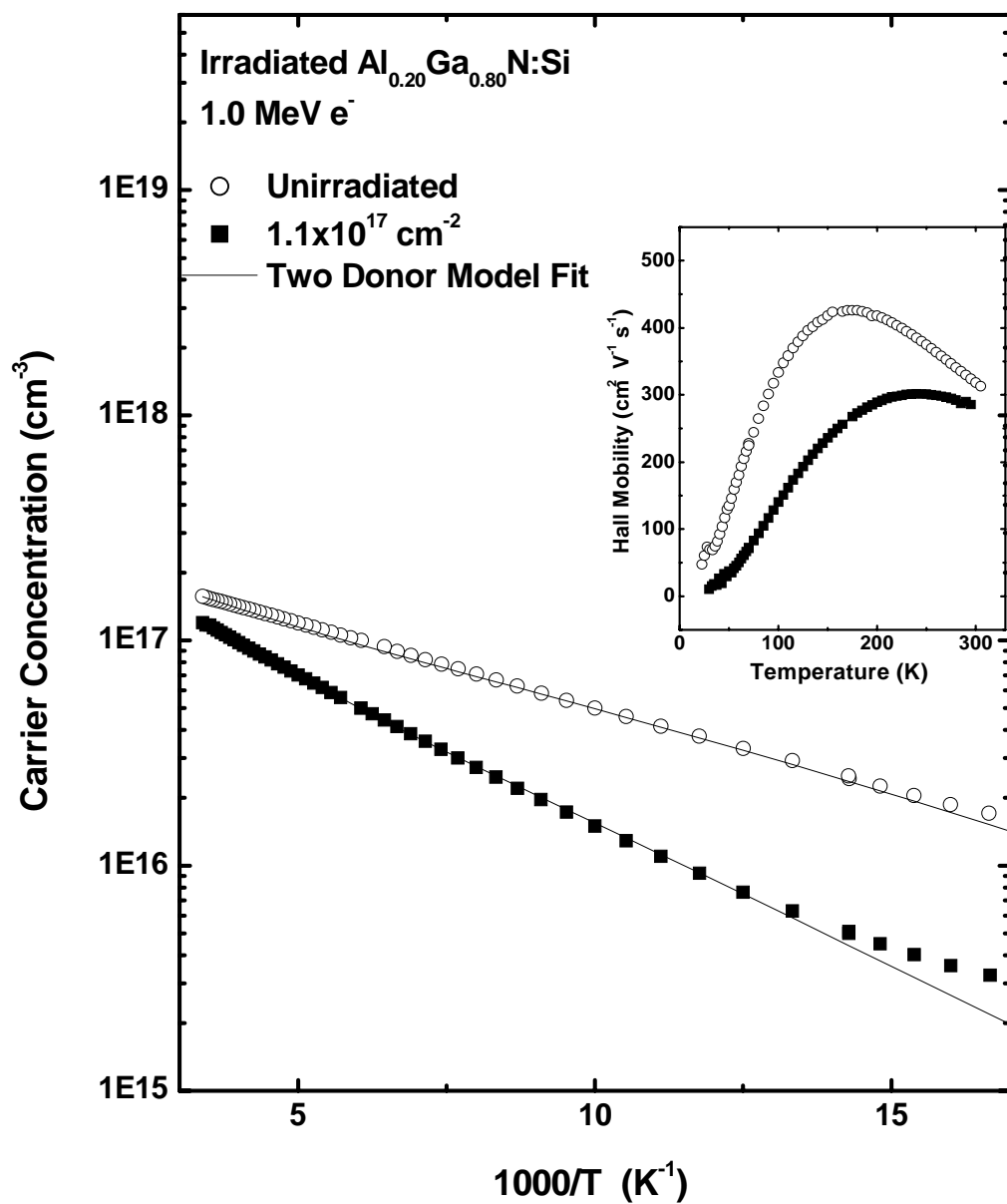


Figure V-37. Temperature dependent Hall data for GaN (sample A2-1) before and after 1.0 MeV electron irradiation. Model (lines) are for a two donor fit with ($N_{D1}=1.9 \times 10^{17}$, $E_{D1}=17$ meV, $N_{D2}=7.5 \times 10^{16}$, $E_{D2}=60$ meV, $N_A=2.3 \times 10^{16}$) and ($N_{D1}=1.64 \times 10^{17}$, $E_{D1}=19$ meV, $N_{D2}=1.55 \times 10^{17}$, $E_{D2}=59$ meV, $N_A=8.7 \times 10^{16}$) for the unirradiated and irradiated data respectively.

N_{D2} increases to $1.55 \times 10^{17} \text{ cm}^{-3}$ and N_A increases to $8.7 \times 10^{16} \text{ cm}^{-3}$. The unscreened thermal activation energy of the shallow donor is calculated by equation III-3 to be $E_{D1}^0 = 17 + (2.1 \times 10^{-5})(1.9 \times 10^{17})^{1/3} = 29 \text{ meV}$. This is a very reasonable value for Si in GaN. The deeper donor has an unscreened thermal activation energy $E_{D2}^0 = 59 + (2.1 \times 10^{-5})(7.5 \times 10^{16})^{1/3} = 68 \text{ meV}$. This is a very reasonable value for V_N in GaN, agreeing with that reported by Look, *et al.* [47]. With confidence in the assignment of the two donor levels, physical inferences may be drawn from the fitting parameters. Following irradiation, the total increase in the concentration of V_N is $8.0 \times 10^{16} \text{ cm}^{-3}$. This is nearly equal to the sum of the decrease in Si donors, $2.6 \times 10^{16} \text{ cm}^{-3}$ and the increase in N_A , $6.4 \times 10^{16} \text{ cm}^{-3}$. This situation can be understood as $5.4 \times 10^{16} \text{ cm}^{-3}$ nitrogen interstitials acting as deep single acceptors according to theory [24, 29], $2.6 \times 10^{16} \text{ cm}^{-3}$ nitrogen interstitials forming Si- N_i complexes that passivate some silicon donors [99], and $3.3 \times 10^{15} \text{ cm}^{-3}$ gallium interstitials acting as triple acceptors according to theory [24, 29]. Assuming no recombination of nitrogen Frenkel pairs, the introduction rate of V_N with 1.0 MeV electrons is 0.73 cm^{-1} according to the above analysis. Referencing figure II-10, it is seen that this introduction rate would correspond to a nitrogen displacement energy of approximately 25 eV, which falls within a theoretically reasonable range of 20 to 50 eV for GaN. Based on the above considerations, however, there is no reason that the carrier removal rate would be expected to increase as the initial carrier concentration is further increased. Normally, the increase in Si donors would raise the odds that a mobile N_i forms a Si- N_i complex before recombining with a V_N . In order for η to increase over the whole range shown in figure V-36, based on this mechanism alone, the nitrogen displacement introduction rate would have to be over 3 cm^{-1} . This displacement

introduction rate is 3 times larger than predicted by equations II-30 through II-32 and the lowest reasonable value of displacement energy, T_d . Thus, other mechanisms of carrier removal such as ionization-induced activation of acceptor impurities [7, 96] may be dominant for large n_o in figure V-36.

It was found that the substrate contribution to room temperature conductivity was greater than or equal to the bulk contribution in samples from AlGa_N wafers B1, B2, C1, C2, and D1. In these cases, the $\ln(n)$ versus $1000/T$ plot was very sensitive to the choice of two-layer correction parameters (low temperature values of n_s and μ_s). An example of this behavior is shown for unirradiated Al_{0.14}Ga_{0.86}N sample B2-16 in figure V-38 and for unirradiated Al_{0.30}Ga_{0.70}N sample D2-7 in figure V-39. A reliable two-donor fit could not be obtained for any of the AlGa_N samples, whether they were irradiated or unirradiated. It may be that for these samples, the two layer analysis of equations III-13 and III-14 is inadequate to yield the precise bulk carrier concentration and mobility. Despite the apparent inadequacy of the two layer analysis for precise temperature dependent Hall fitting of the AlGa_N, it is very necessary and helpful for determining the true carrier concentration and mobility at room temperature and is applied accordingly in this dissertation research. Figures V-40, V-41, and V-42 are representative of the temperature dependent Hall measurements, corrected for substrate conduction, in AlGa_N samples.

The Al_{0.27}Ga_{0.73}N/GaN single heterostructure sample E1-3 was subjected to the $9 \times 10^{16} \text{ cm}^{-2}$ electron fluence at 1.0 MeV and characterized with temperature dependent Hall measurements. The Ohmic contacts were diffused through the Al_{0.27}Ga_{0.73}N layer and brought into contact with the two-dimensional electron gas (2-DEG) by annealing at

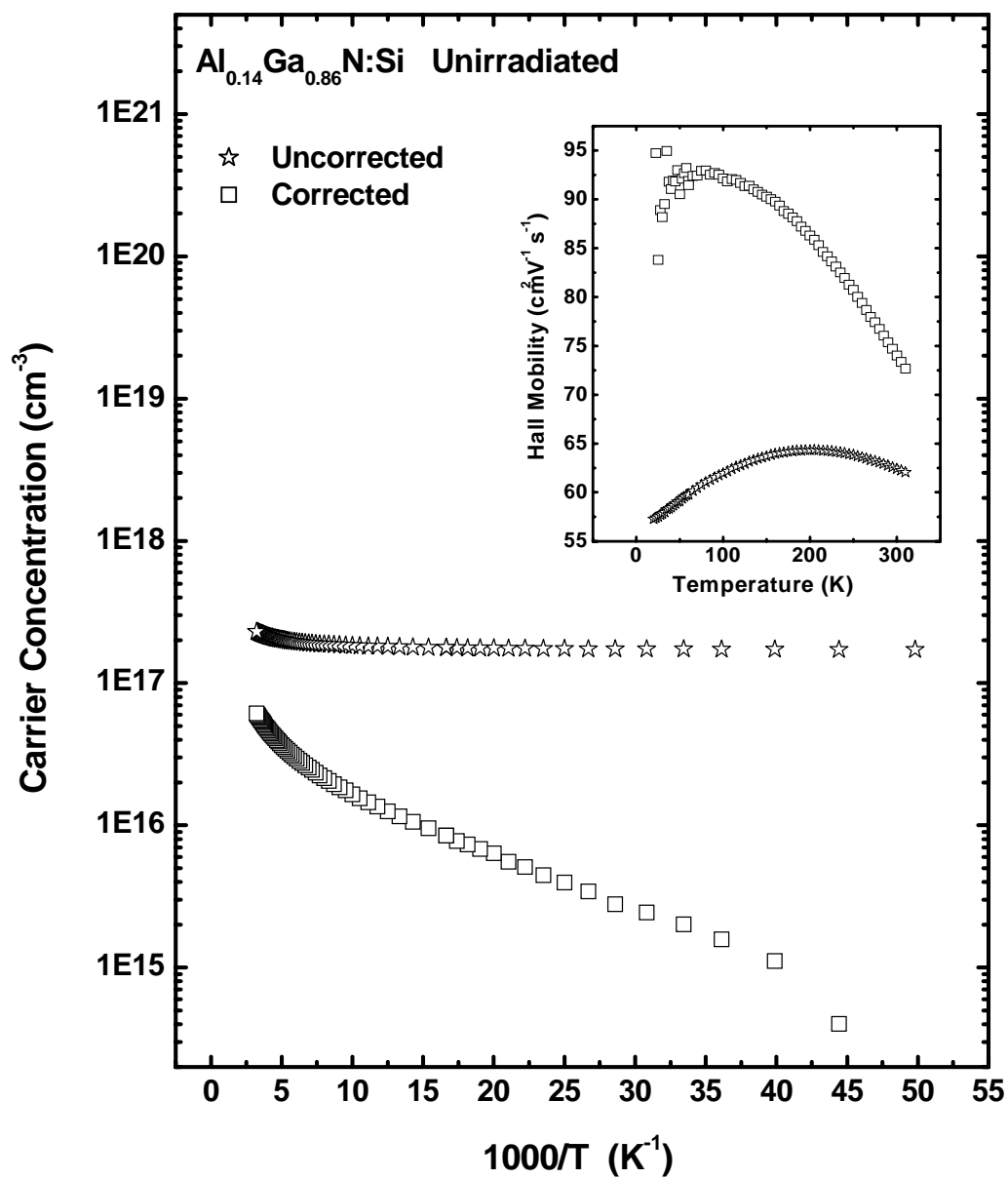


Figure V-38. Carrier concentration versus inverse temperature of unirradiated Al_{0.14}Ga_{0.86}N (sample B2-16) before and after correction for a secondary conduction layer. The corresponding mobility plots are shown in the inset.

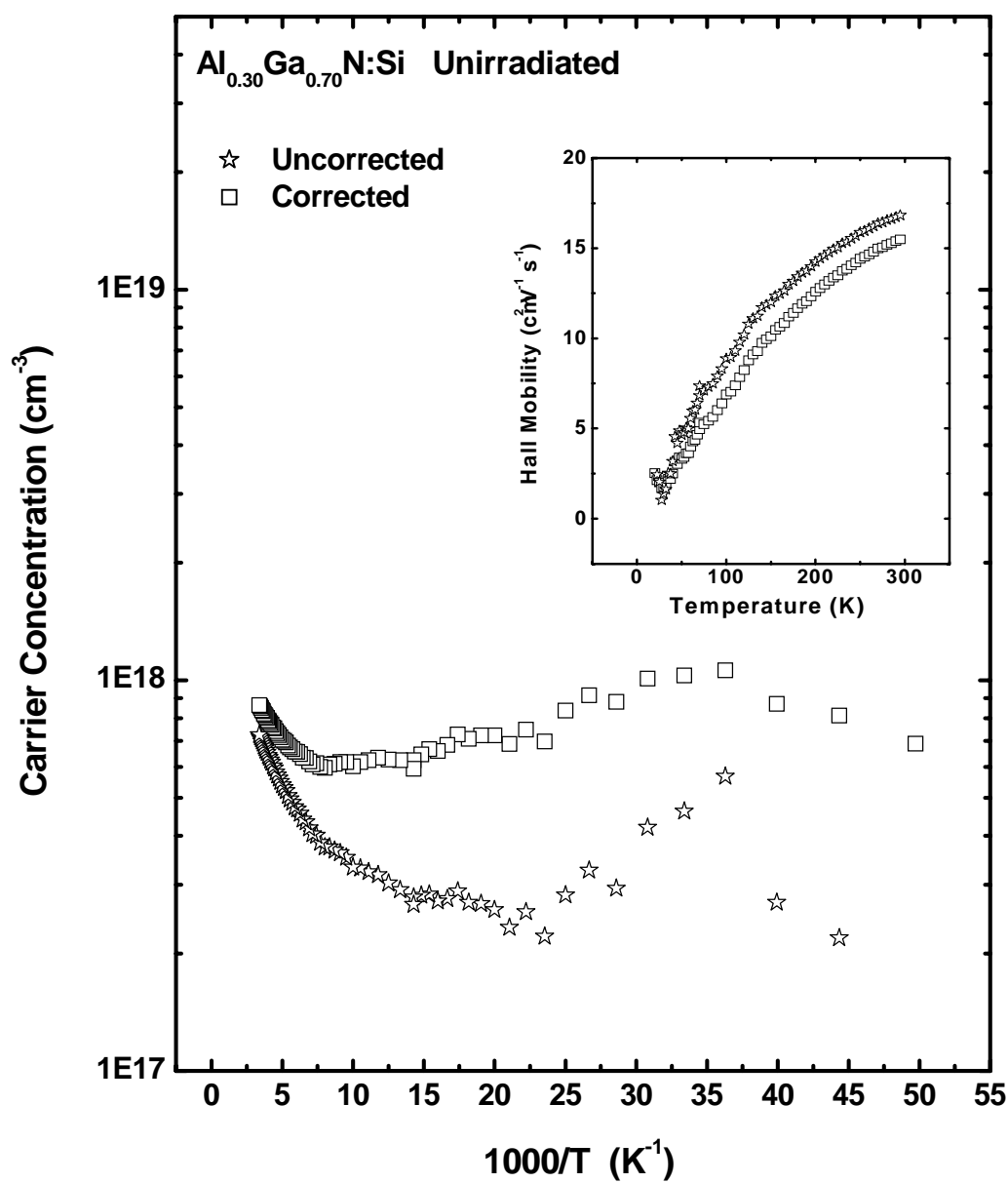


Figure V-39. Carrier concentration versus inverse temperature of unirradiated Al_{0.30}Ga_{0.70}N (sample D2-7) before and after correction for a secondary conduction layer. The corresponding mobility plots are shown in the inset.

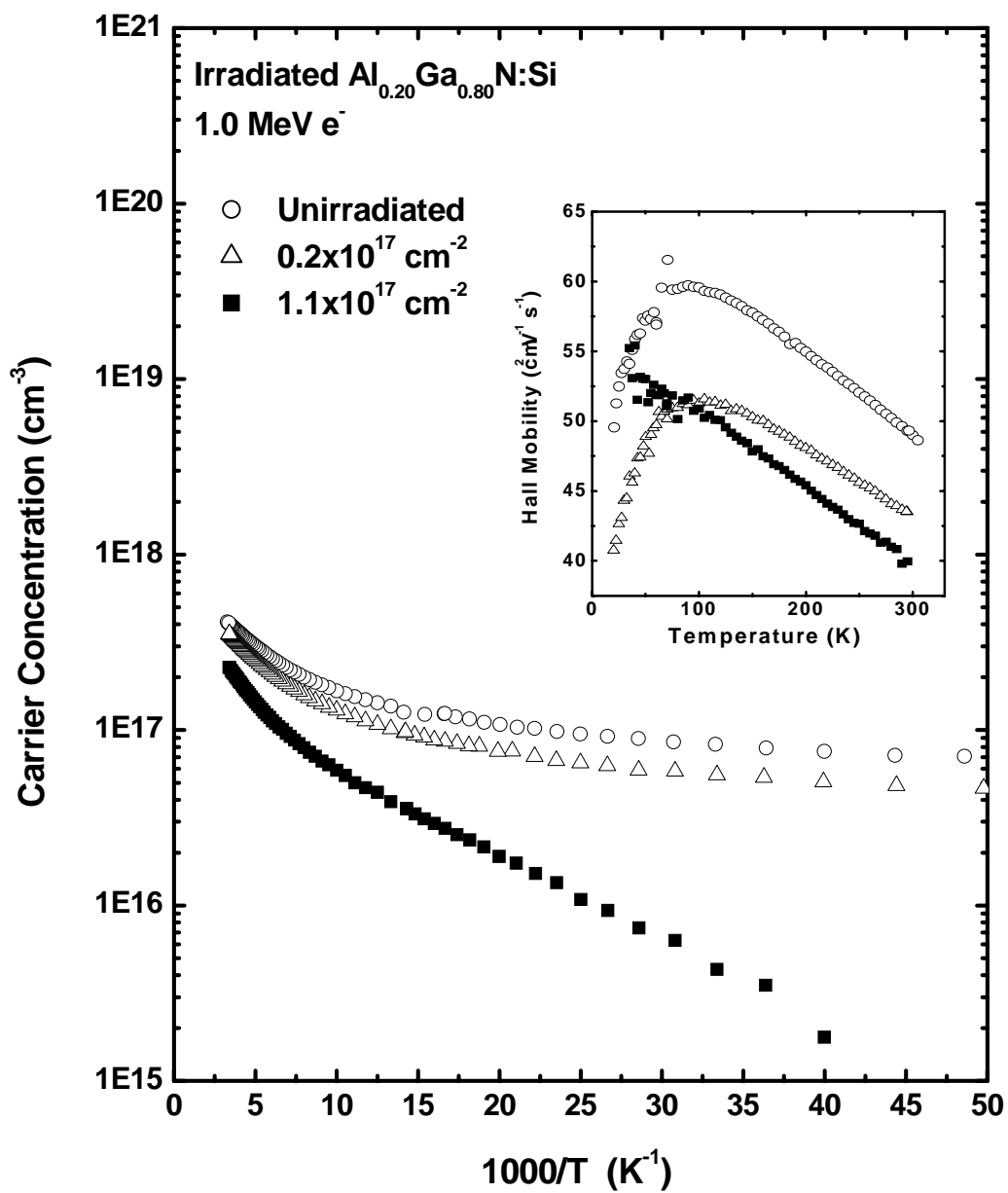


Figure V-40. Temperature dependent carrier concentration of $\text{Al}_{0.20}\text{Ga}_{0.80}\text{N}$ (sample C1-9) before and after 1.0 MeV electron irradiation at two consecutive doses.

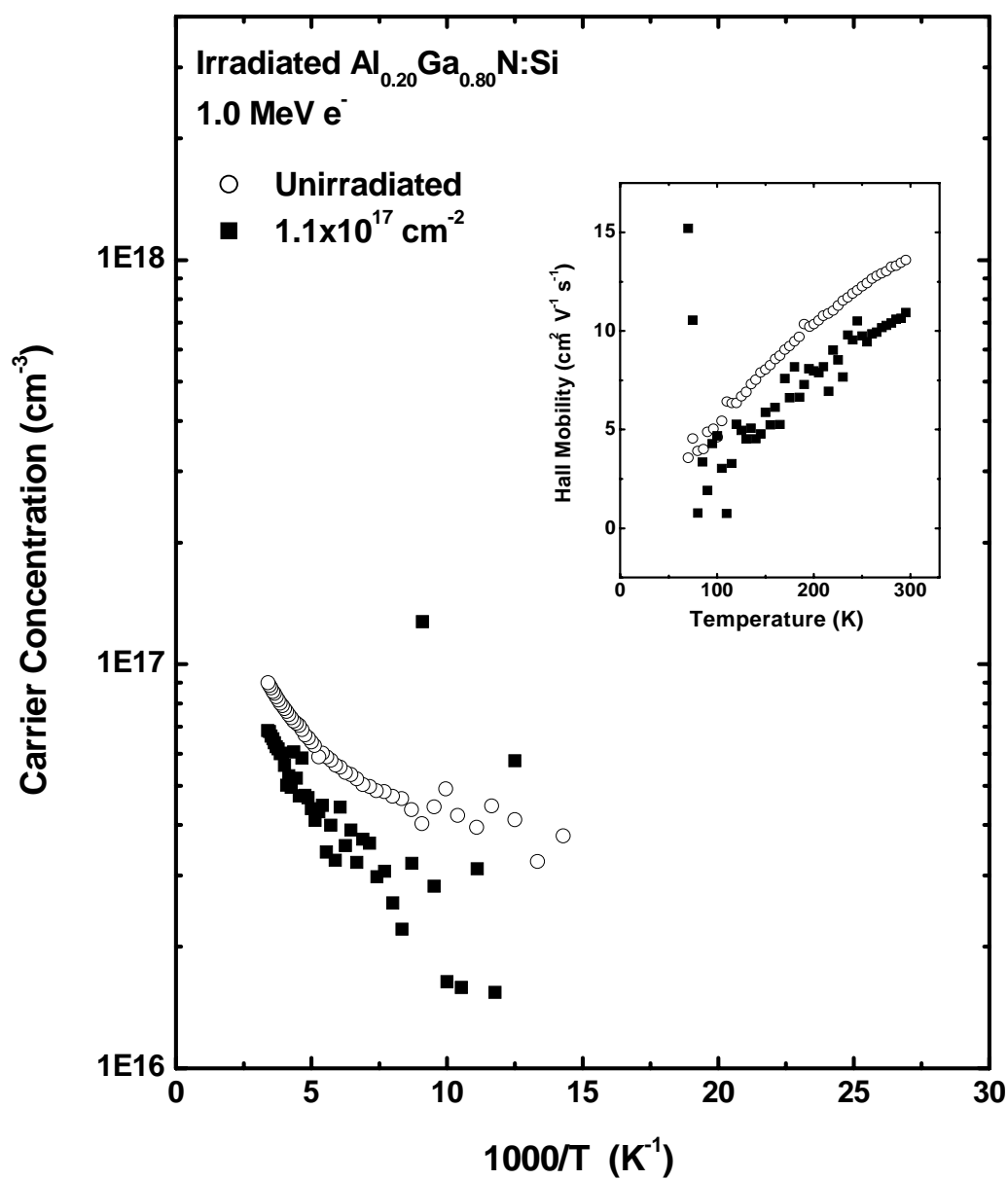


Figure V-41. Temperature dependent carrier concentration of $\text{Al}_{0.20}\text{Ga}_{0.80}\text{N}$ (sample C2-2) before and after 1.0 MeV electron irradiation.

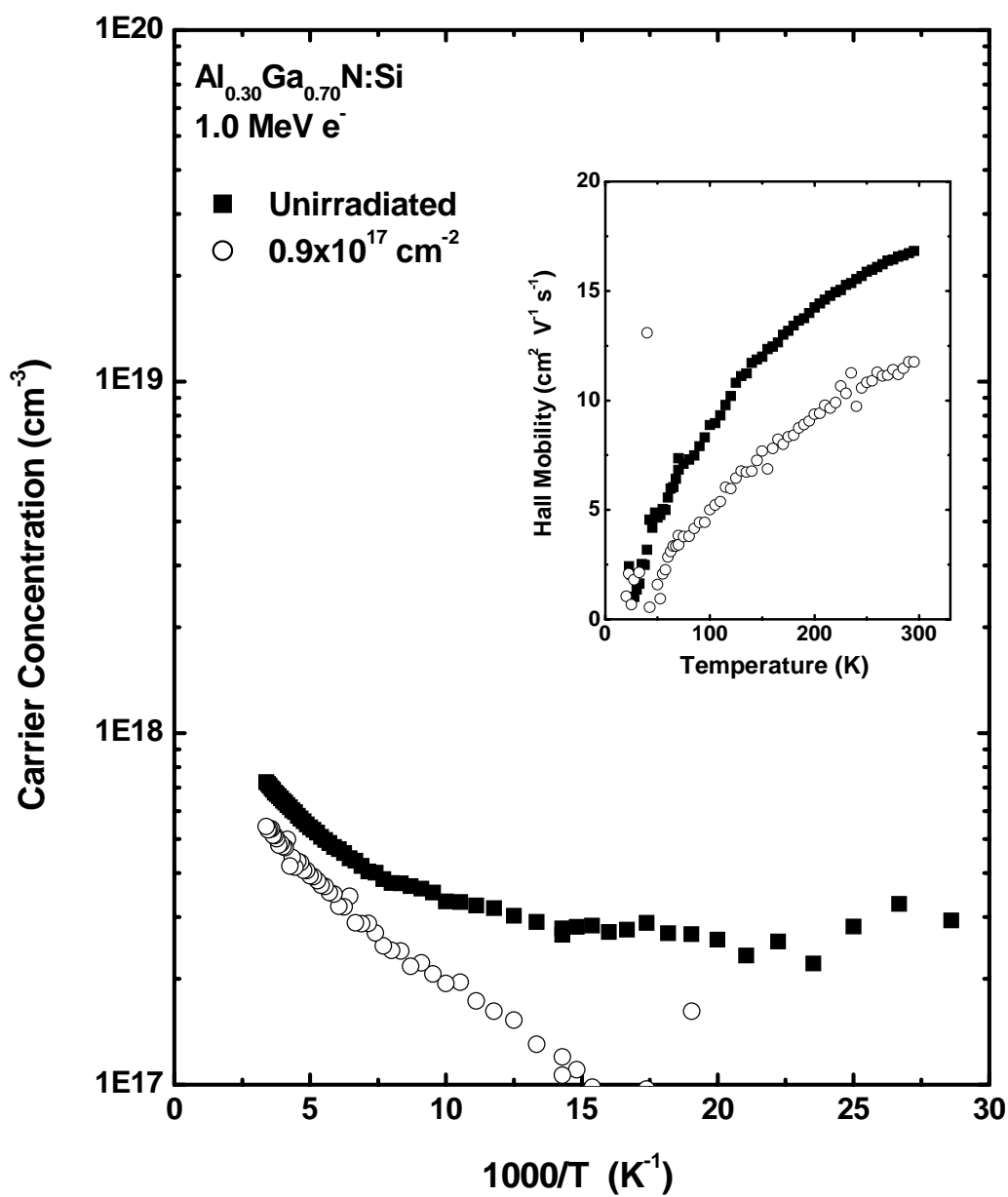


Figure V-42. Temperature dependent carrier concentration of $\text{Al}_{0.30}\text{Ga}_{0.70}\text{N}$ (sample D2-7) before and after 1.0 MeV e^- electron irradiation.

900 °C. The high conductivity of the 2-DEG region causes the AlGaIn layer to be shorted and it can be assumed that the measured sheet carrier concentration and mobility reflect that of the 2-DEG region. Figures V-43, V-44, and V-45 show the temperature dependent sheet carrier concentration, mobility, and sheet resistivity of the sample before and after irradiation. It is found that sheet carrier concentration and mobility are reduced by 13 % and 23%, respectively, at room temperature (295 K). This causes a 150 % increase in sheet resistivity. While sheet carrier concentration remains relatively constant with temperature before and after irradiation, the mobility is greatly affected at low temperatures, where ionized defect scattering dominates. Thus, it is confirmed that the 1.0 MeV electron doses used throughout this study ($\sim 1 \times 10^{17} \text{ cm}^{-2}$) and the accompanying defect introduction rates are relevant to HEMT device operation.

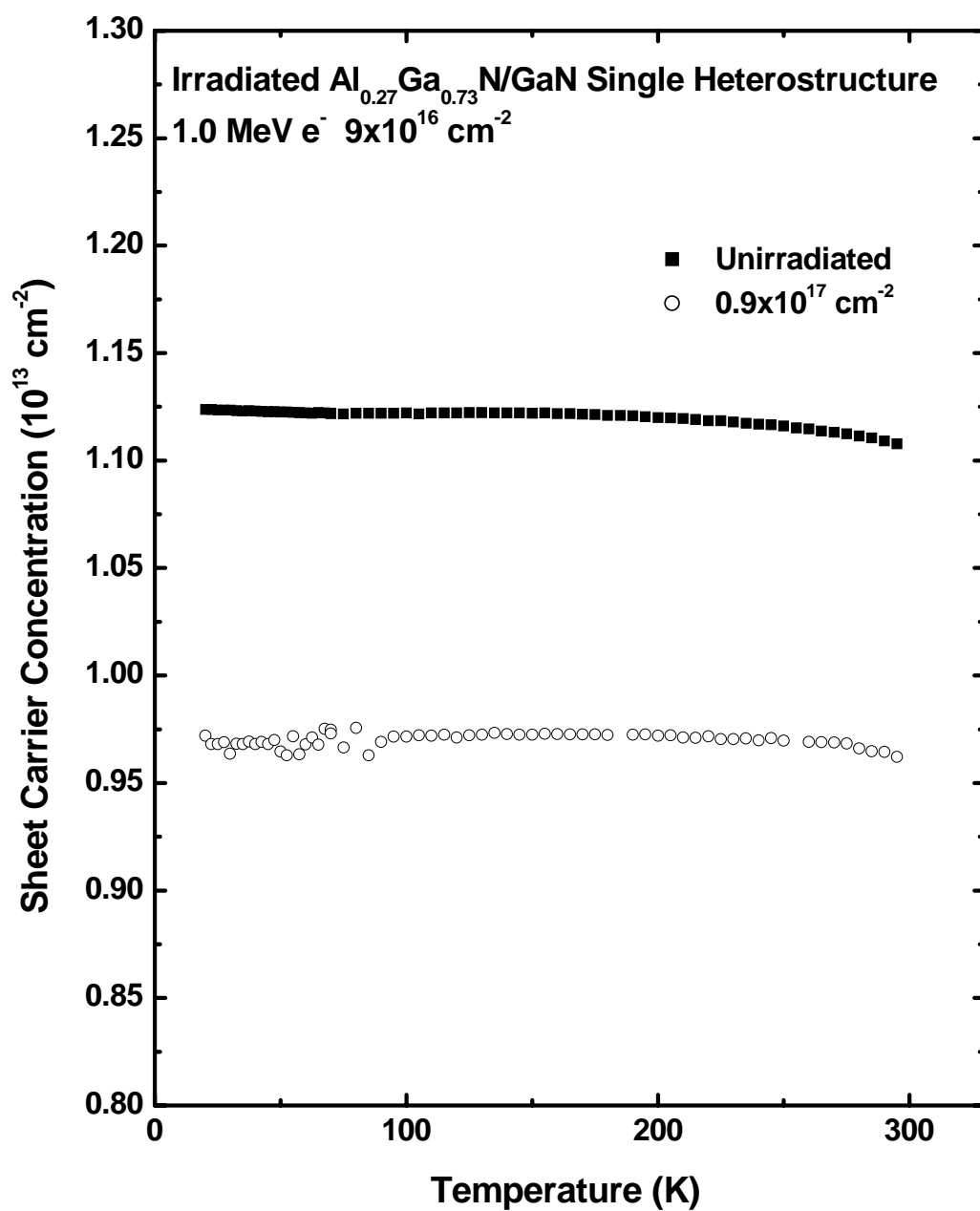


Figure V-43. Sheet carrier concentration versus temperature in $\text{Al}_{0.27}\text{Ga}_{0.73}\text{N}/\text{GaN}$ single heterostructure (sample E1-3) before and after 1.0 MeV electron irradiation.

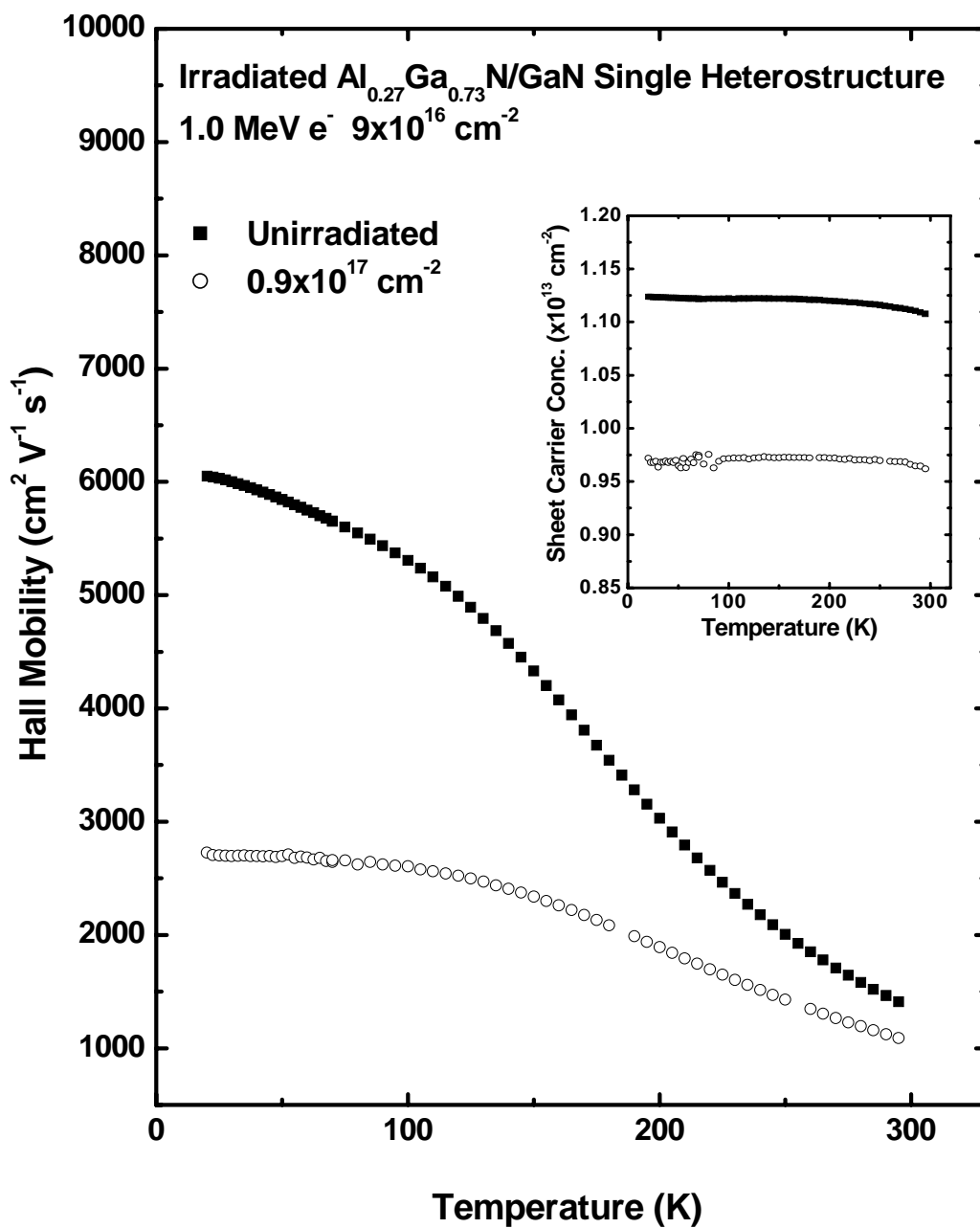


Figure V-44. Hall Mobility versus temperature in $\text{Al}_{0.27}\text{Ga}_{0.73}\text{N}/\text{GaN}$ single heterostructure (sample E1-3) before and after 1.0 MeV electron irradiation.

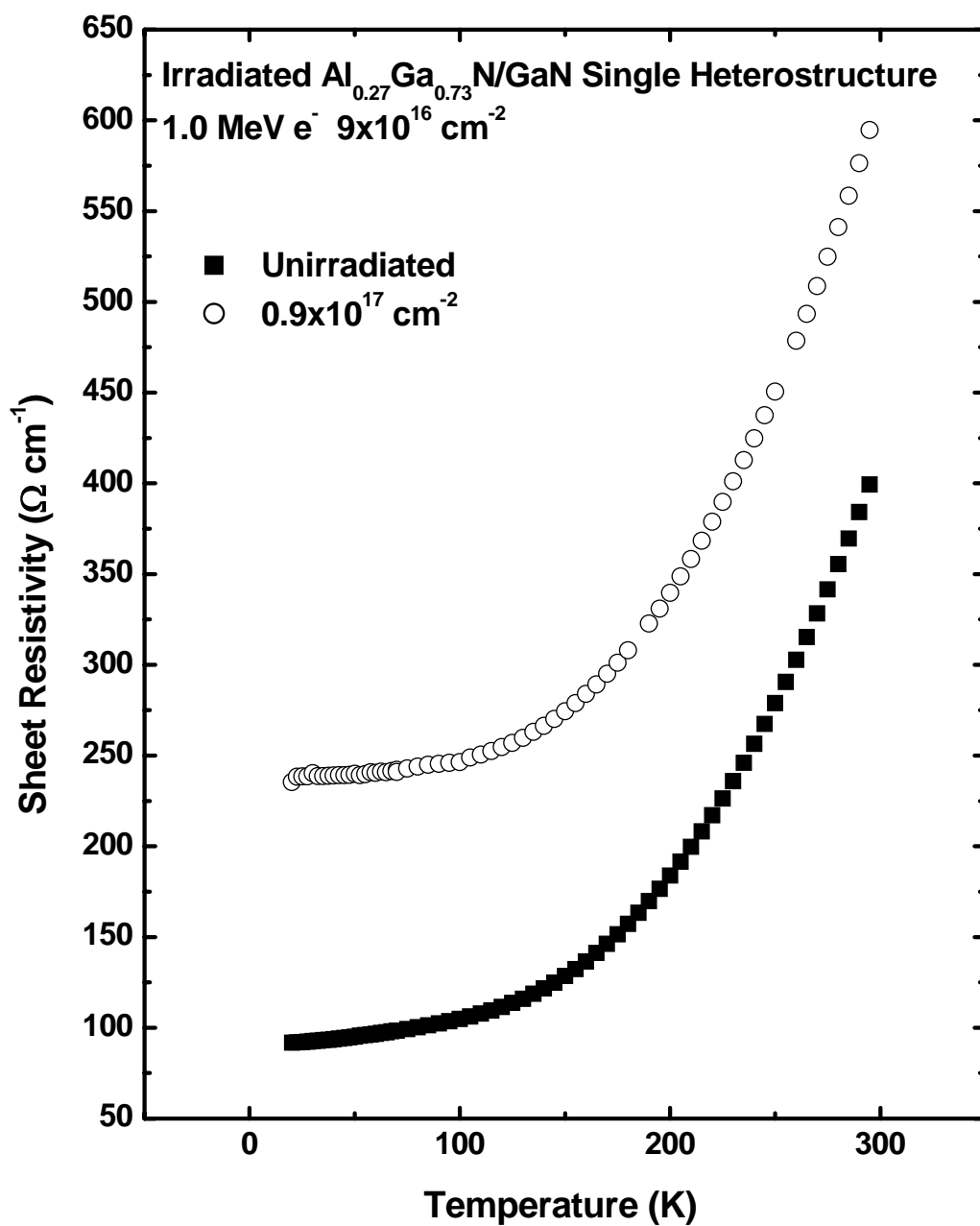


Figure V-45. Sheet resistivity versus temperature in $\text{Al}_{0.27}\text{Ga}_{0.73}\text{N}/\text{GaN}$ single heterostructure (sample E1-3) before and after 1.0 MeV electron irradiation.

5.3 Cathodoluminescence

The CL spectra of as-grown $\text{Al}_x\text{Ga}_{1-x}\text{N}$ samples are shown in figure V-46. These and all CL measurements presented here were made at $T = 6\text{ K}$ with a $25\text{ }\mu\text{A}$ excitation current of 5 keV electrons. In the GaN spectrum, a donor bound exciton (D^0, X) peak is dominant at 3.48 eV . Lesser features are typical of that previously reported in GaN. The CL spectrum of the $\text{Al}_{0.14}\text{Ga}_{0.86}\text{N}$ shows a (D^0, X) at 3.87 eV , and a secondary peak at 3.83 eV that may be a neutral-donor-to-free hole transition (D^0, h) [100]. The CL spectrum of the $\text{Al}_{0.20}\text{Ga}_{0.80}\text{N}$ shows the (D^0, X) peak at 4.00 eV , and the secondary peak at 3.92 eV . The CL spectrum of the $\text{Al}_{0.30}\text{Ga}_{0.70}\text{N}$ shows the (D^0, X) peak at 4.26 eV , and the secondary peak at about 4.19 eV . Two broad luminescence peaks appear at lower energies in the $\text{Al}_x\text{Ga}_{1-x}\text{N}$. One of these (as designated in figure V-46) corresponds to the ubiquitous yellow luminescence (YL) band in GaN. Interestingly, another broad luminescence, labeled UVL, is fixed at $1.00 \pm 0.05\text{ eV}$ below the band edge. It is probable that this luminescence is caused by a radiative transition from a defect band centered at about $1.00 \pm 0.05\text{ eV}$ below the conduction band minimum to holes in the valence band. This defect band may correspond to the observed peak P2 discussed in the DLTS results section above. There, it was shown that the apparent activation energy of P2 was $0.98 \pm 0.10\text{ eV}$ in $\text{Al}_{0.14}\text{Ga}_{0.86}\text{N}$ and $0.92 \pm 0.06\text{ eV}$ in $\text{Al}_{0.20}\text{Ga}_{0.80}\text{N}$. The CL spectra of as-grown and irradiated GaN and $\text{Al}_{0.20}\text{Ga}_{0.80}\text{N}$ samples are shown on a linear scale in figure V-47. The CL spectra measured from the as-grown samples are depicted in solid lines and the CL spectra from the irradiated samples are in dotted lines. Following 1.0 MeV electron irradiation at a fluence of $1.1 \times 10^{17}\text{ cm}^{-2}$, the peak CL luminescence intensities of both GaN and $\text{Al}_{0.20}\text{Ga}_{0.80}\text{N}$ decreased by about 50% as shown in the figure.

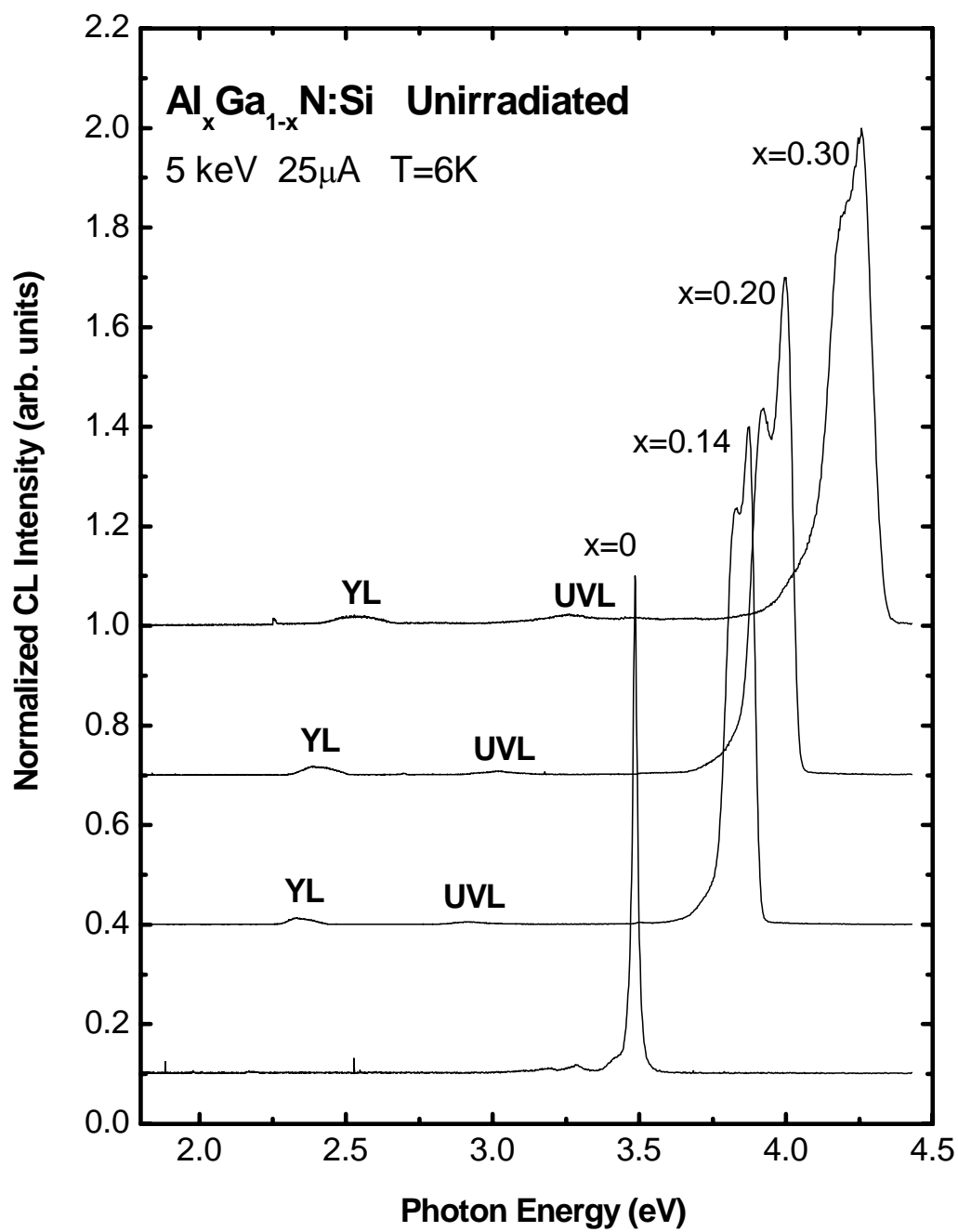


Figure V-46. Normalized CL spectra of unirradiated $\text{Al}_x\text{Ga}_{1-x}\text{N}$ for $x = 0, 0.14, 0.20$, and 0.30 .

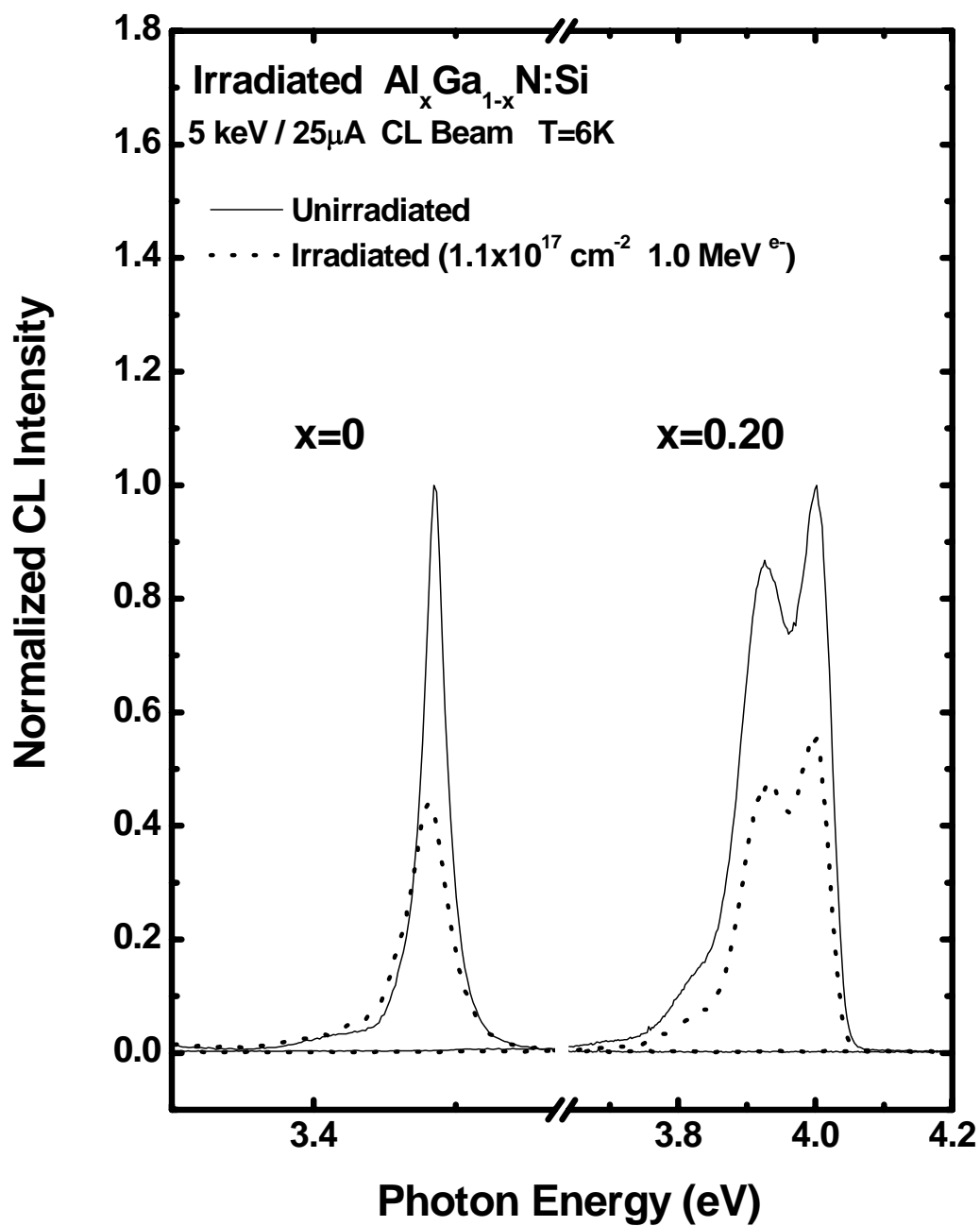


Figure V-47. Normalized CL spectra of $\text{Al}_x\text{Ga}_{1-x}\text{N}$ ($x=0.0$ and $x=0.2$) before and after 1.0-MeV electron irradiation with a fluence of $1.1 \times 10^{17} \text{ cm}^{-2}$

This reduction is found to be stable at room temperature and is attributed to the creation of non-radiative recombination centers. Figure V-48 shows a plot of the normalized CL peak luminescence intensity of five different $\text{Al}_x\text{Ga}_{1-x}\text{N}$ samples as a function of the 1.0 MeV electron fluence. The intensity is reduced by about 35 and 50% after electron irradiation at fluences of 2×10^{16} and $1.1 \times 10^{17} \text{ cm}^{-2}$, respectively from the value before irradiation. The margin of error can be rather large for these measurements, and it is not expected that any trend can be distinguished based on the compositional differences of the samples. Rather, the data of figure V-48 are averaged and taken to be representative of the $\text{Al}_x\text{Ga}_{1-x}\text{N}$ samples for $0 \leq x \leq 0.30$, and this average is shown in figure V-49. The lines overlaid in figure V-49 are the reported electroluminescence peak intensities from InGaN LEDs irradiated with 0.94 MeV (dotted line) and 1.14 MeV (dashed line) electrons [53]. Interestingly, the exponential character of all the curves is similar. In the referenced work, it was reported that the damage annealed out after 16 hours at room temperature. Figures V-50 to V-55 show the spectra of several $\text{Al}_x\text{Ga}_{1-x}\text{N}$ samples ($x = 0.0$ to 0.30) before and after 1.0 MeV electron irradiation. These are presented on a logarithmic scale to show the detail of the broad range of luminescence peaks. Generally, the entire spectrum decreases in intensity due to the introduction of non-radiative recombination centers. Figure V-56 shows the GaAs sample F1-8 before and after 1.0 MeV electron irradiation to a fluence of $9 \times 10^{16} \text{ cm}^{-2}$. The peak luminescence intensity decreases by 99.9 % following the irradiation. Thus, luminescence intensity in the $\text{Al}_x\text{Ga}_{1-x}\text{N}$ samples is much more tolerant to 1.0 MeV electron radiation than in the GaAs sample.

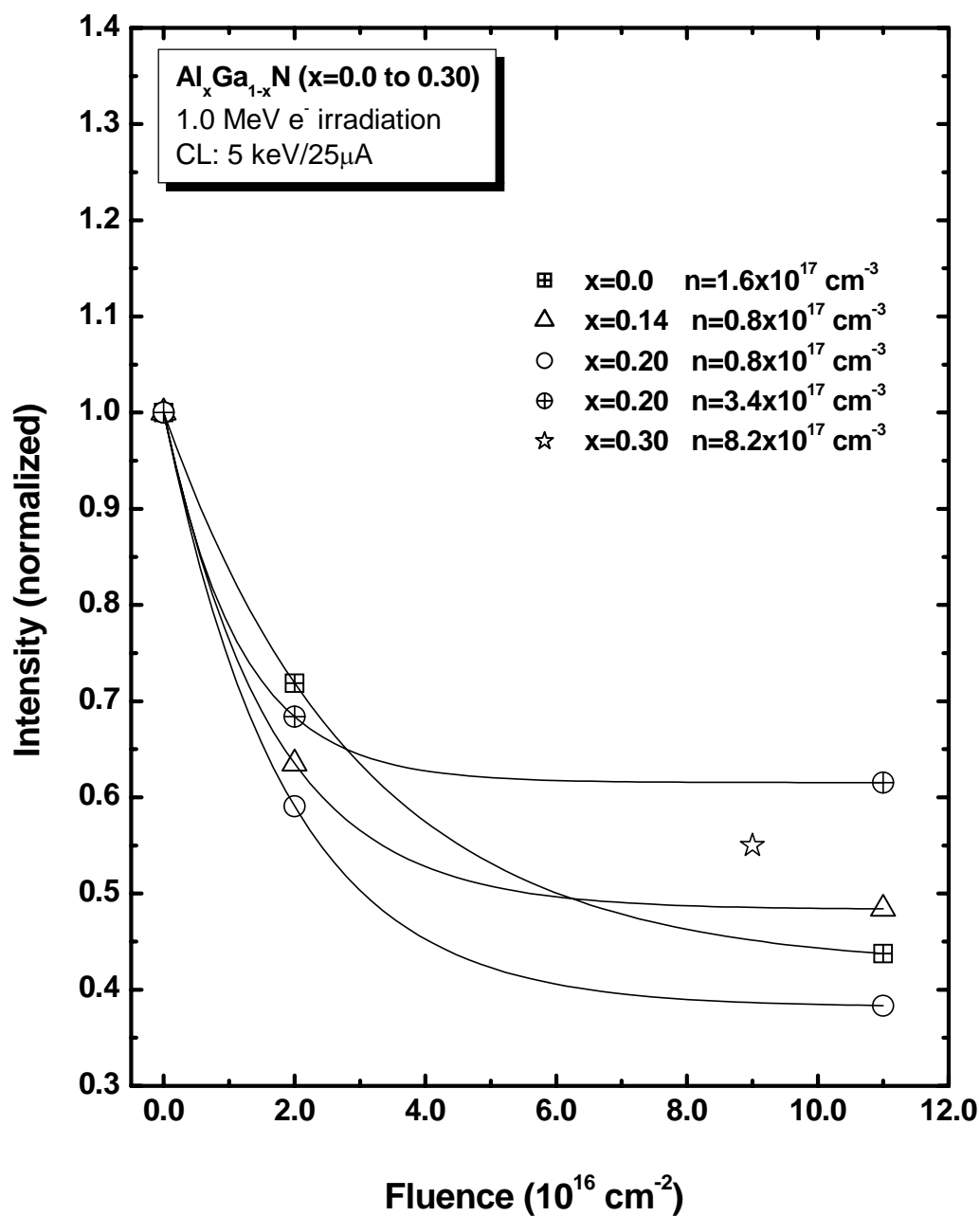


Figure V-48. Normalized luminescence intensity in Al_xGa_{1-x}N irradiated at two consecutive 1.0 MeV electron doses with 2×10^{16} and 1.1×10^{17} e⁻ cm⁻².

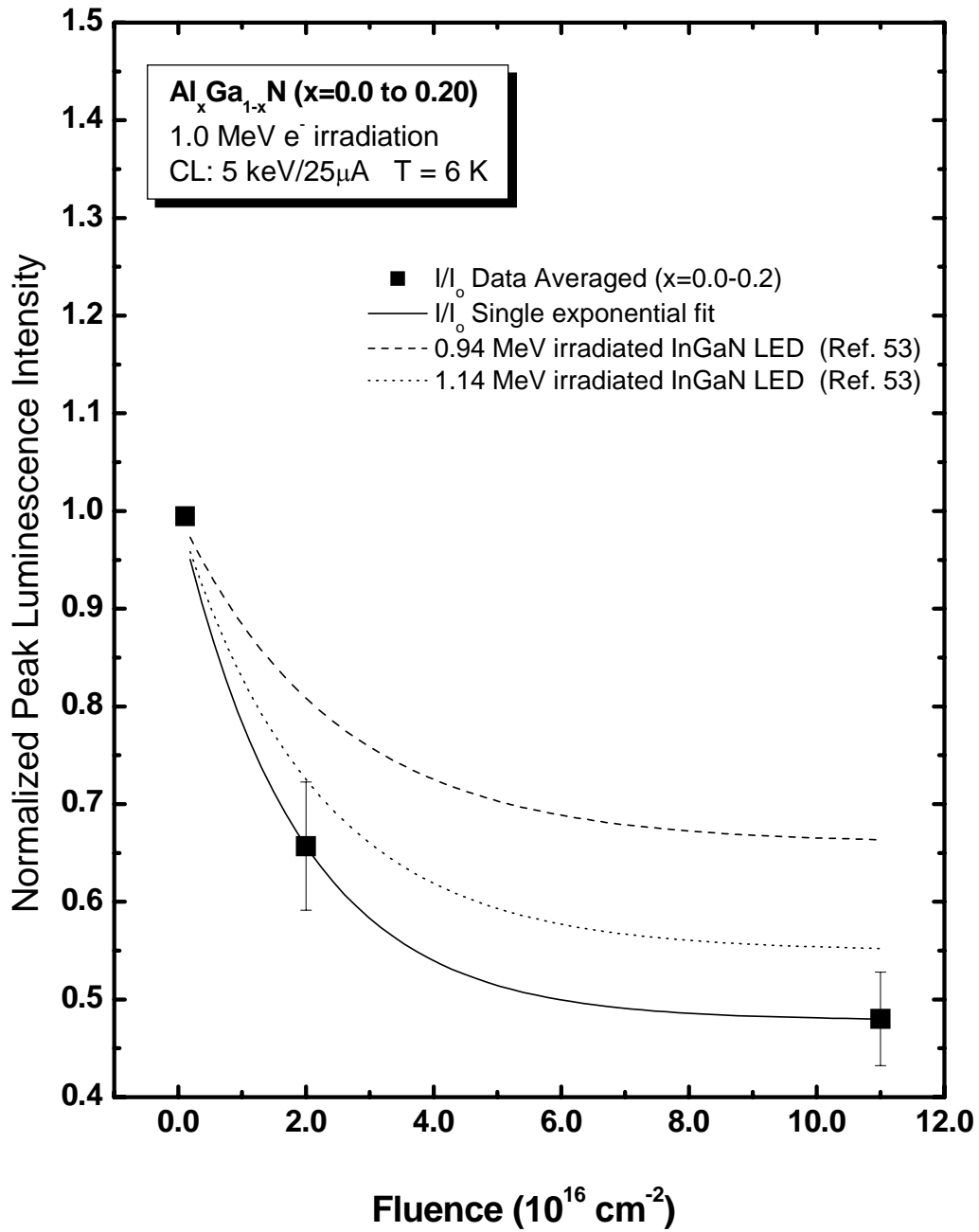


Figure V-49. Normalized luminescence intensity in Al_xGa_{1-x}N irradiated at two consecutive 1.0 MeV electron doses with 2×10^{16} and 1.1×10^{17} e⁻ cm⁻². Data are produced from the average of four samples (x=0.0 to 0.20). The reported degradation of an electron irradiated InGaN LED [53] is overlaid for comparison.

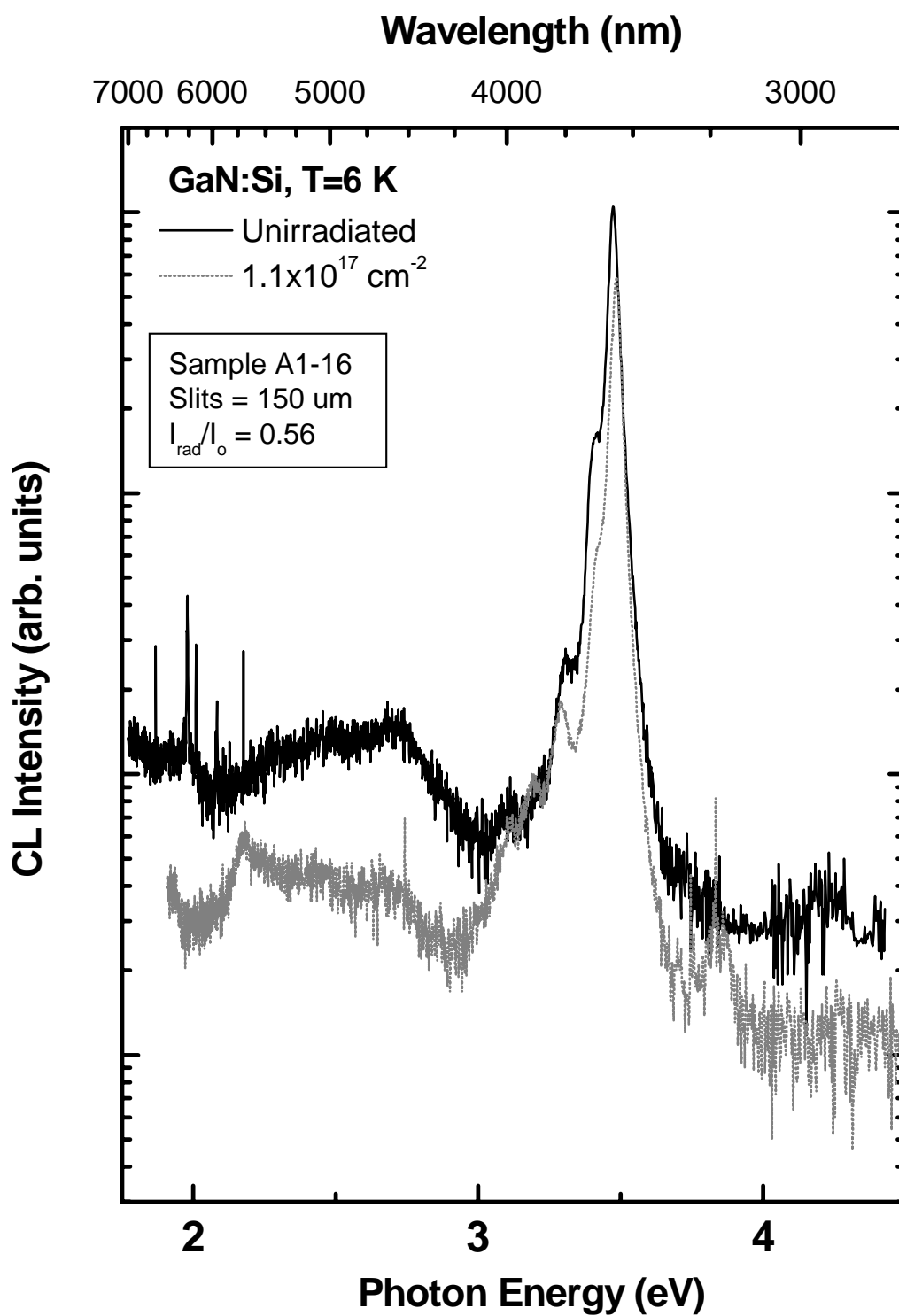


Figure V-50. CL spectrum of GaN (sample A1-16) before and after 1.0 MeV electron irradiation with a fluence of $1.1 \times 10^{17} \text{ cm}^{-2}$.

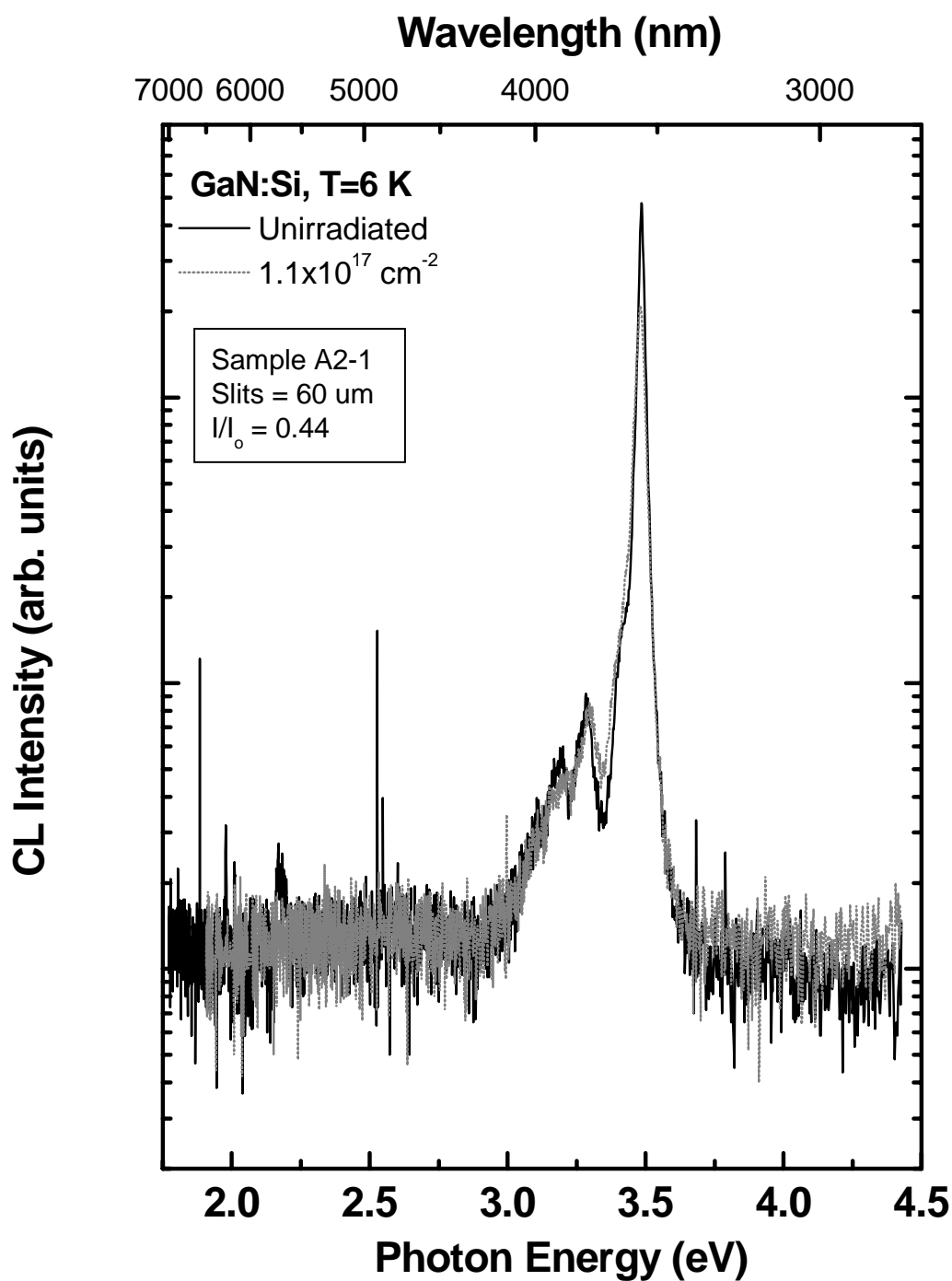


Figure V-51. CL spectrum of GaN (sample A2-1) before and after 1.0 MeV electron irradiation with a fluence of $1.1 \times 10^{17} \text{ cm}^{-2}$.

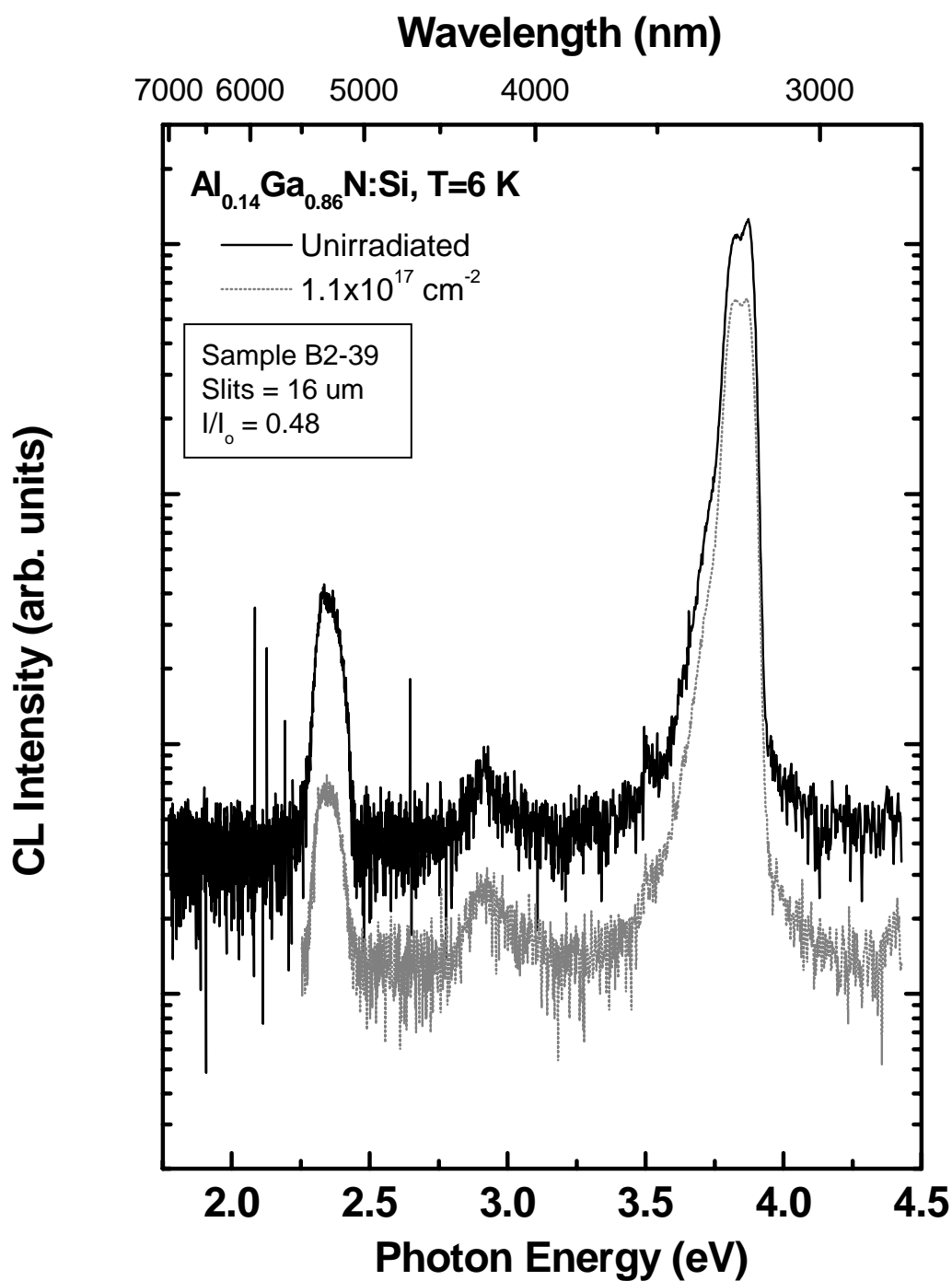


Figure V-52. CL spectrum of Al_{0.14}Ga_{0.86}N (sample B2-39) before and after 1.0 MeV electron irradiation with a fluence of 1.1x10¹⁷ cm⁻².

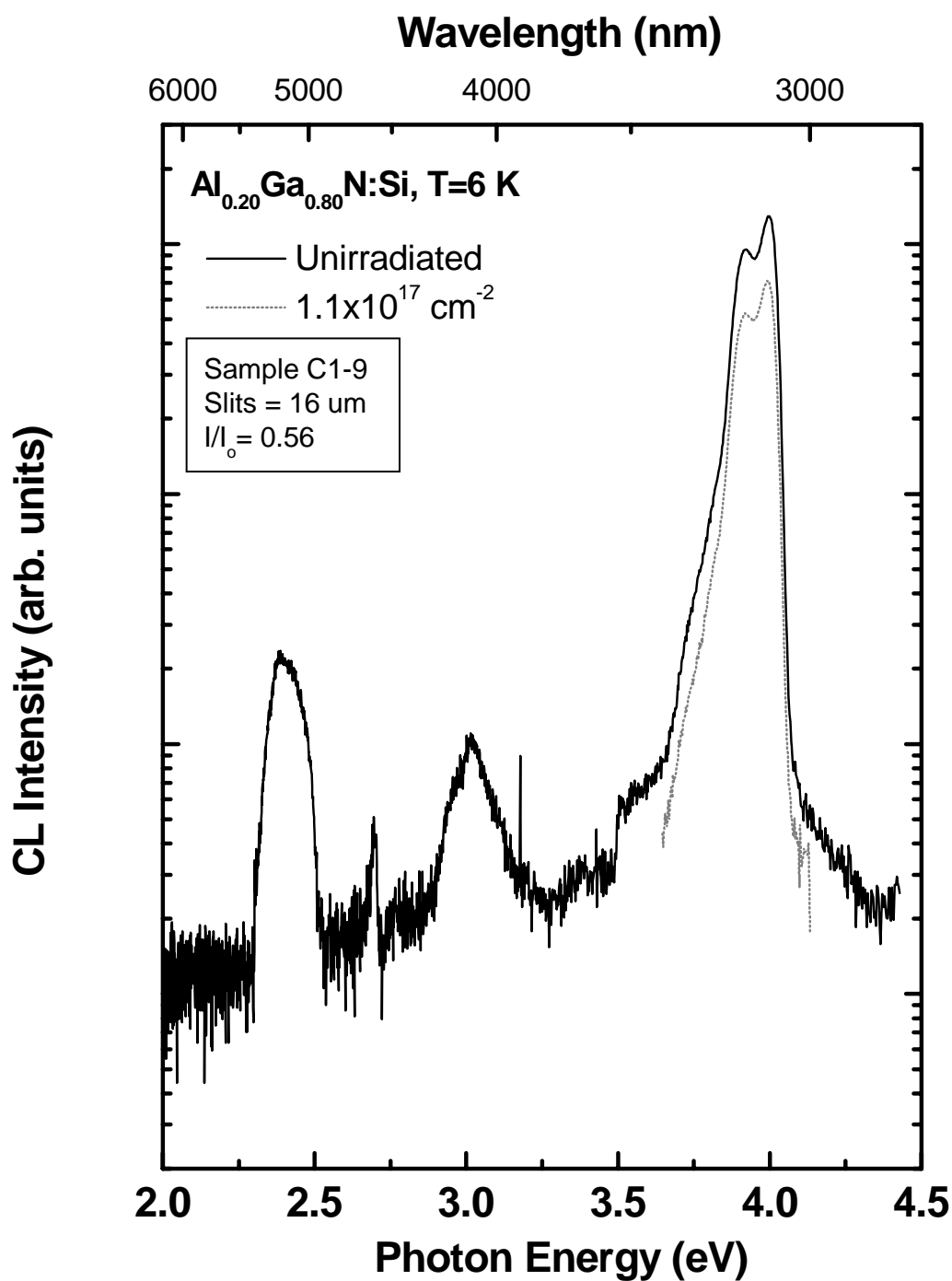


Figure V-53. CL spectrum of Al_{0.20}Ga_{0.80}N (sample C1-9) before and after 1.0 MeV electron irradiation with a fluence of 1.1x10¹⁷ cm⁻².

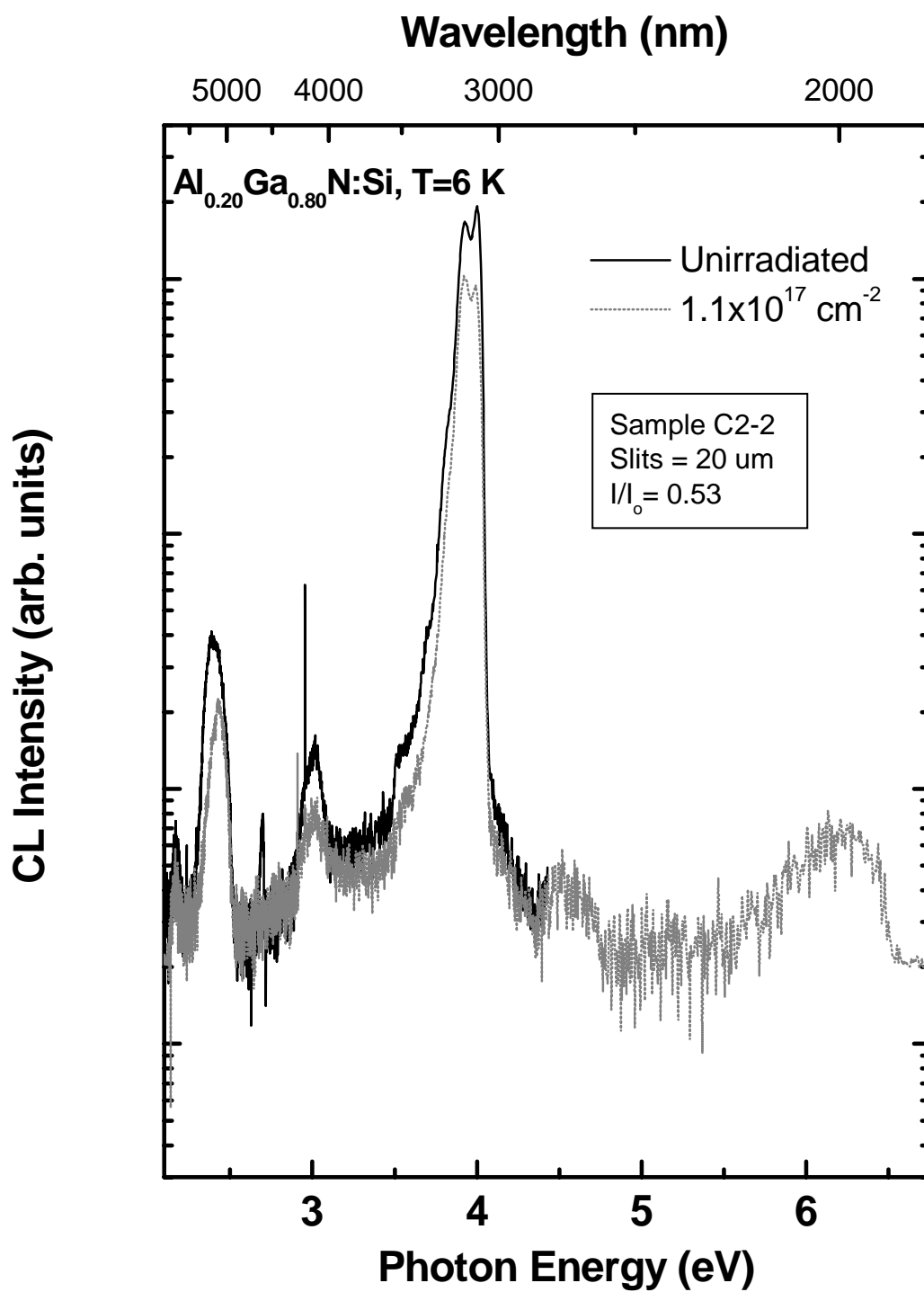


Figure V-54. CL spectrum of Al_{0.20}Ga_{0.80}N (sample C2-2) before and after 1.0 MeV electron irradiation with a fluence of 1.1x10¹⁷ cm⁻².

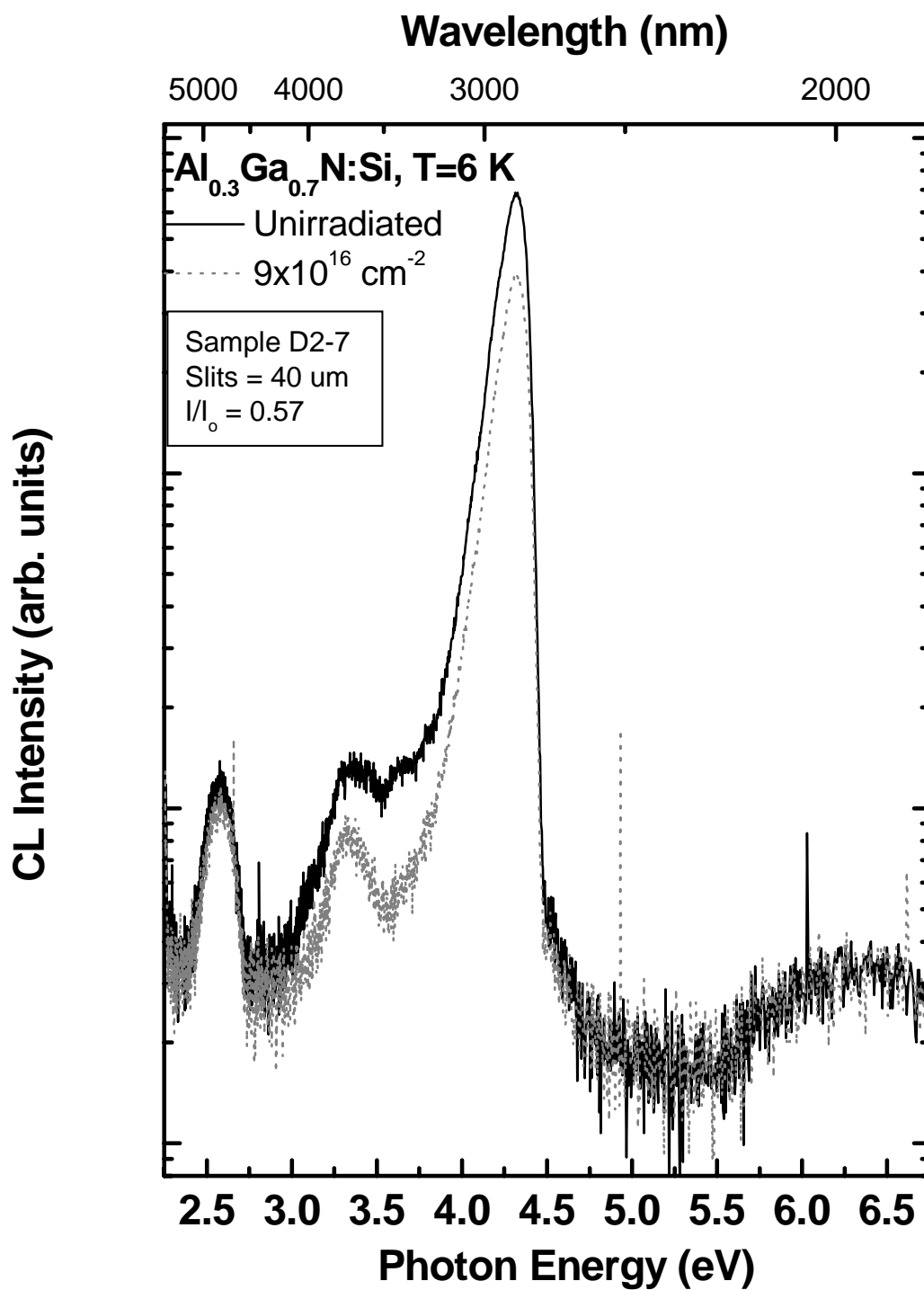


Figure V-55. CL spectrum of Al_{0.20}Ga_{0.80}N (sample D2-7) before and after 1.0 MeV electron irradiation with a fluence of 9x10¹⁶ cm⁻².

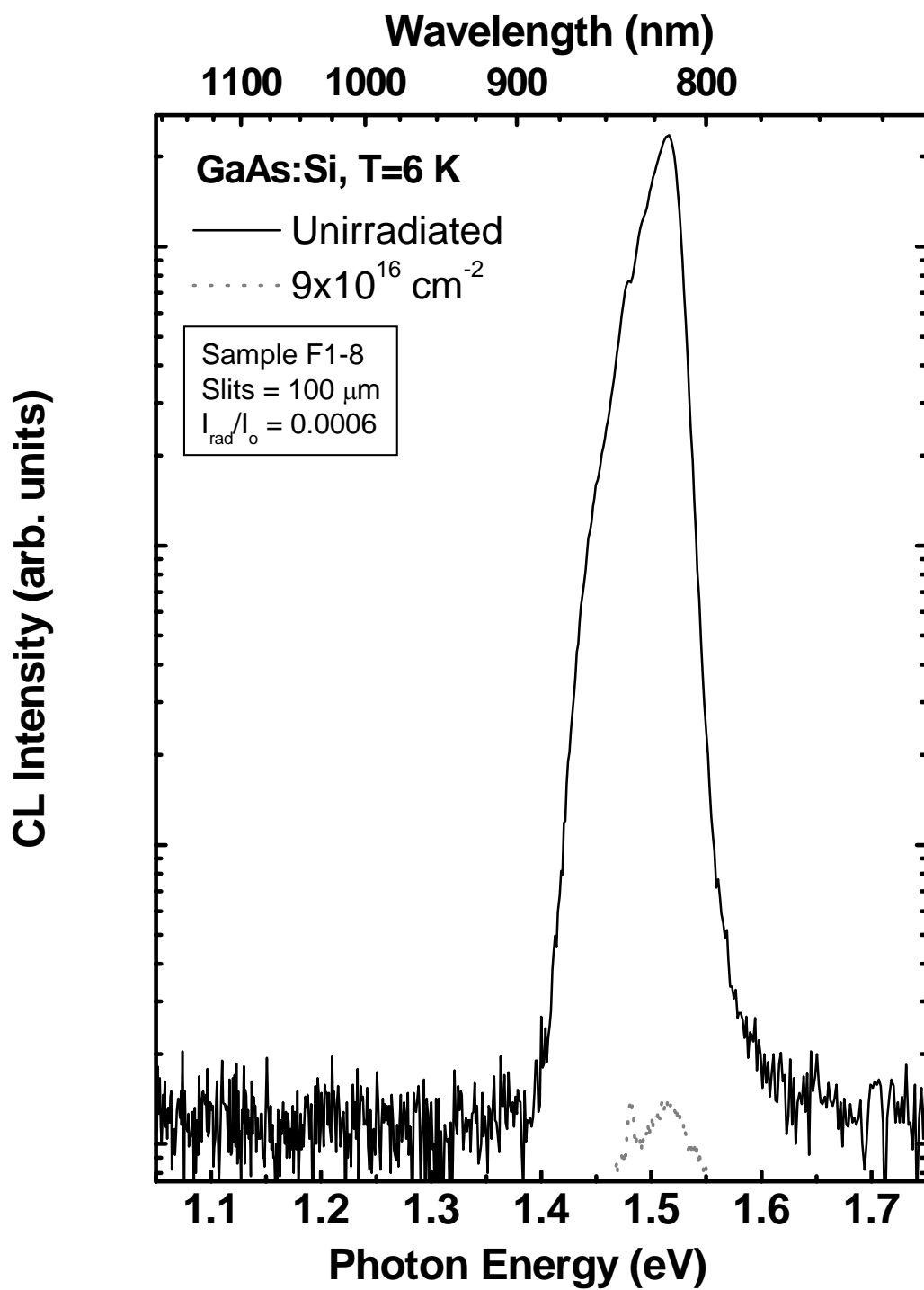


Figure V-56. CL spectrum of GaAs (sample F1-8) before and after 1.0 MeV electron irradiation with a fluence of $9 \times 10^{16} \text{ cm}^{-2}$.

VI. Conclusions and Recommendations

6.1 Conclusions

The primary objective of this study was to quantify the effects of electron radiation upon n-type $\text{Al}_x\text{Ga}_{1-x}\text{N}$ ($x = 0.0$ to 0.3) grown by MBE with regard to carrier removal, mobility reduction, and luminescence degradation, and to electrically characterize radiation-induced defects that may contribute to performance degradation of nitride-based electronic and optoelectronic devices. A secondary objective was to characterize the electrically active defects that exist in the unirradiated $\text{Al}_x\text{Ga}_{1-x}\text{N}$ material, and to compare these defects with those in irradiated material.

The research results from this dissertation research are as follows:

- 1) It has been found that with 1.0 MeV electrons at a fluence of $1 \times 10^{17} \text{ cm}^{-2}$, the carrier removal rate depends foremost on the initial carrier concentration, regardless of aluminum mole fraction. The carrier removal rate, η , was determined to be a linear function of the initial carrier concentration, n_o , as $\eta = (3.96 \times 10^{-18} n_o - 0.15) \text{ cm}^{-1}$. This finding provides a framework for understanding seemingly conflicting reports about carrier removal rates in GaN and AlGaN.
- 2) The result in 1) supports the hypothesis that for 1.0 MeV electron irradiation, a mechanism of carrier removal in Si-doped $\text{Al}_x\text{Ga}_{1-x}\text{N}$ is donor passivation via the formation of Si-N_i complexes. This Si-N_i complex hypothesis is also supported by fitting temperature dependent carrier concentration to a general two-donor model. It was found that following irradiation of GaN, the sum of passivated shallow donors and deep acceptors is approximately equal to an increase in the number of presumed nitrogen vacancies.

- 3) A comparison of carrier removal and luminescence degradation in $\text{Al}_x\text{Ga}_{1-x}\text{N}$ and GaAs was made for irradiated samples, and they were characterized under identical conditions. This comparison study supports the claims that $\text{Al}_x\text{Ga}_{1-x}\text{N}$ is intrinsically more tolerant to electron radiation than conventional semiconductor materials such as GaAs, and especially so with regard to luminescence degradation.
- 4) It was found that three radiation-induced deep defect levels R1 (0.15 eV), R2 (0.21 eV), and R3 (0.26 eV) exist in $\text{Al}_{0.14}\text{Ga}_{0.86}\text{N}$ which correspond to previously reported radiation-induced deep defect levels ER1 (~ 0.11 eV), ER2 (~ 0.16 eV), and ER3 (~ 0.20 eV) in GaN. The corresponding AlGaN levels were shown to deepen significantly with increasing aluminum mole fraction.
- 5) A new radiation-induced defect level R4 (0.33 eV for $x = 0.14$, and 0.38 eV for $x = 0.20$) has been found in AlGaN, and it does not appear to correspond to any known radiation-induced defect level in GaN. The defect was observed to be thermally stable under reverse bias voltage at 450 K, and it did not anneal out completely until after 600 K. Knowledge of this and the other three radiation-induced defect levels enables more complete theoretical modeling of radiation-induced degradation in the gate region of AlGaN/GaN HEMTs, and could help device manufacturers engineer radiation hardened designs.
- 6) Two dominant defect levels, P1 and P2, in unirradiated AlGaN were further characterized. It was demonstrated that P1 is unlikely to be of the same origin as a donor-type electron trap reported in an early AlGaN DLTS study. It was found that for P1, the increase in E_{TOT} with aluminum mole fraction was equal to the increase in band gap energy. Additionally, CL characterization suggests that there exists a radiative

transition from the P2 level to the valence band. The energy of this transition also increases with aluminum mole fraction according to the increase in band gap.

6.2 Recommendations

The observation of dominant radiation-induced electron traps in $\text{Al}_x\text{Ga}_{1-x}\text{N}$ and the discovery of the conditions for which they are well-resolved provides impetus for future DLTS characterization of these traps under different experimental conditions. The logical next step in electrical characterization of these traps is to determine the activation energy capture barrier, E_σ , for each trap, so that the true thermal activation energy, E_{th} , may be extracted from the total activation energy, E_{TOT} , presented here. While there are several ways to attempt such a measurement, the most straightforward and reliable investigation would be to measure the filled trap concentration $N(t_p)$ versus t_p , for $10^{-9} \leq t_p \leq 10^{-6}$ s. From this, the true capture cross section $\sigma_n(T)$ and thus E_σ may be extracted. Another way in which a CV-DLTS system could be extended to better characterize these traps is to incorporate optical excitation. When performed successfully, a direct measurement of the Gibbs free energy (E_T) is obtained, but more importantly, the DX behavior and associated persistent photoconductivity (PPC) could be explored. Additional traps (both electron and hole traps) could be probed throughout the entire band gap. While many additional techniques could be applied to the characterization (and even positive identification) of these new radiation-induced traps, this research can also be extended by determining how the observed traps affect the operation of AlGaN based electronic and optoelectronic devices. Such an investigation should include DC and RF characterization.

Appendix: C-V and I-V Measurements

The greatest technical challenge encountered in this dissertation research was to obtain good quality Schottky and Ohmic contacts that permitted reliable electrical characterization. The Schottky barrier diodes used for DLTS characterization were particularly challenging to obtain because they required both types of contacts and also were subject to other requirements such as the requirement that the depletion region not extend to the substrate and that series resistance be sufficiently small at $T > 100$ K. Adequate SBDs could not be successfully fabricated from the AlGaN wafers B1, C2, and D2. The DLTS results obtained with the good SBDs were presented in chapter V, and representative C-V and I-V plots from these devices are included in this appendix for reference. The $1/C^2$ vs. V plot insets show the calculated carrier concentration versus depth, and these insets also show how the depletion depth increased with applied reverse bias. Aside from carrier concentration determination, C-V and I-V curves were only utilized in this dissertation research as a qualitative diagnostic of problems encountered during DLTS measurements. The I-V vs. T plots give an indication of the reverse bias leakage current and series resistance encountered at various temperatures. Following irradiation, the most noticeable changes in the SBDs resulted from the increase in series resistance. As such, leakage current usually decreased following irradiation and the DLTS peak heights were reduced slightly compared with those seen before irradiation.

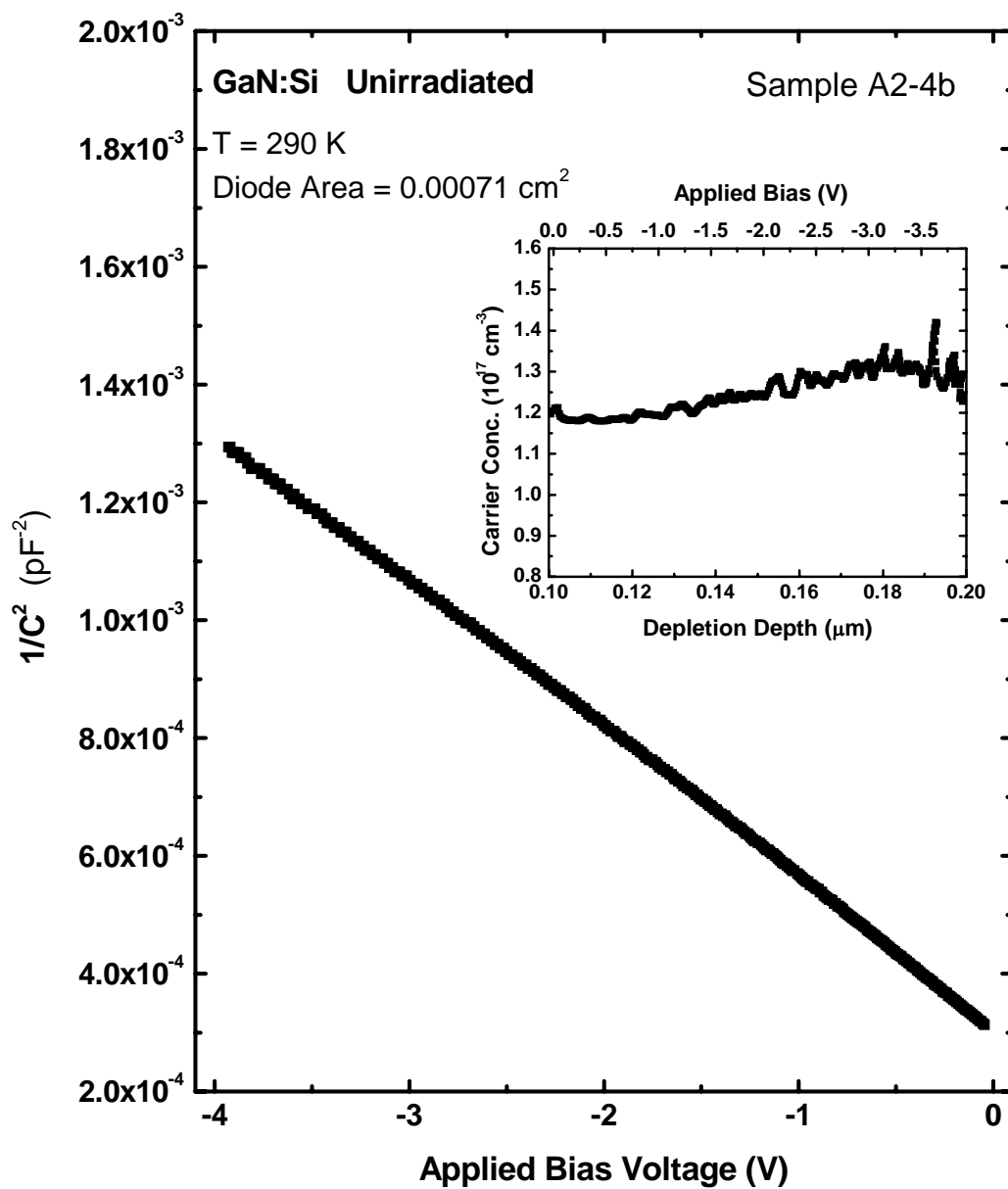


Figure A-1. Plot of $1/C^2$ versus applied bias for unirradiated GaN (sample A2-4b) at $T=290$ K. Inset is the extrapolated carrier concentration versus depletion depth.

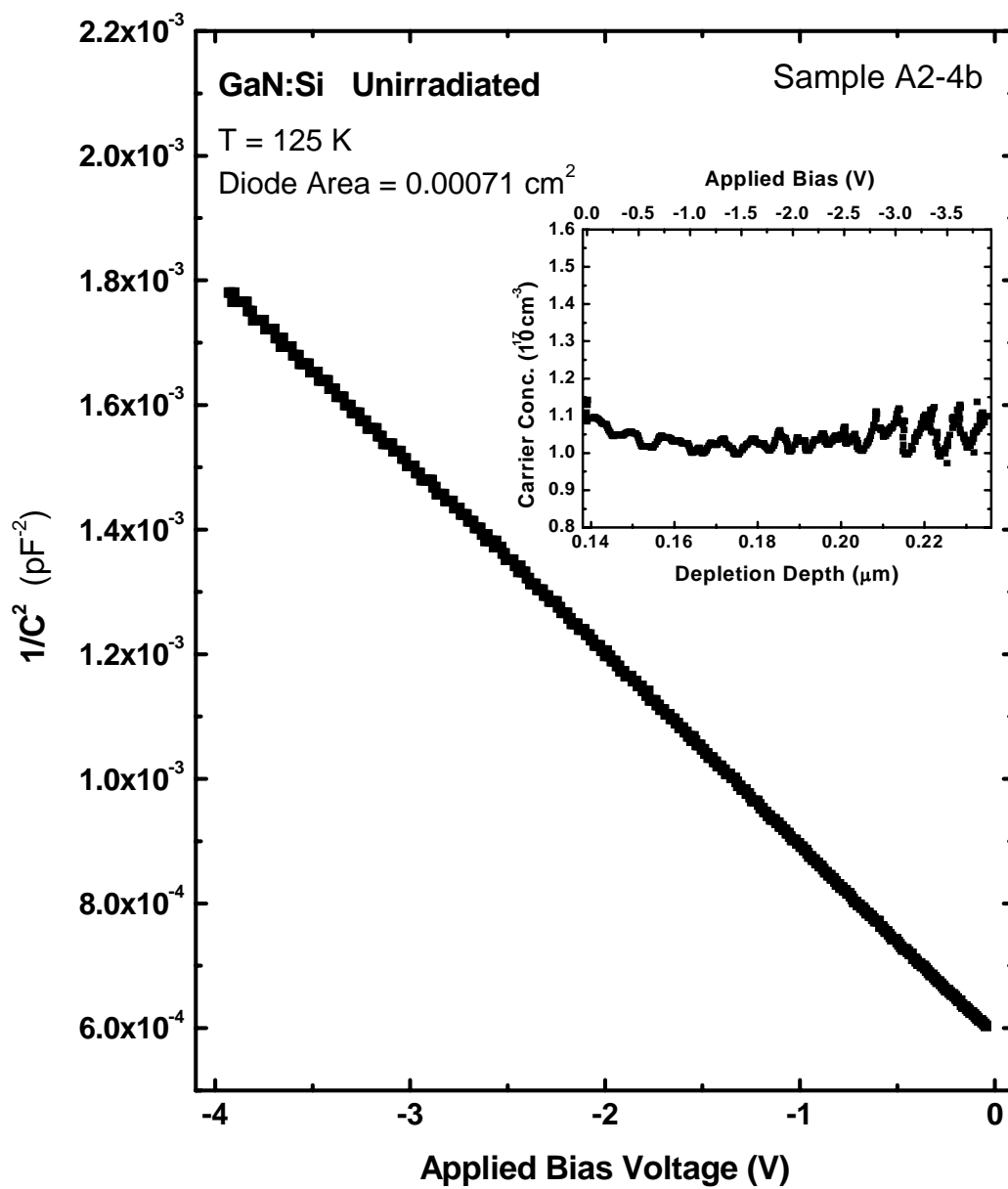


Figure A-2. Plot of $1/C^2$ versus applied bias for unirradiated GaN (sample A2-4b) at $T=150$ K. Inset is the extrapolated carrier concentration versus depletion depth.

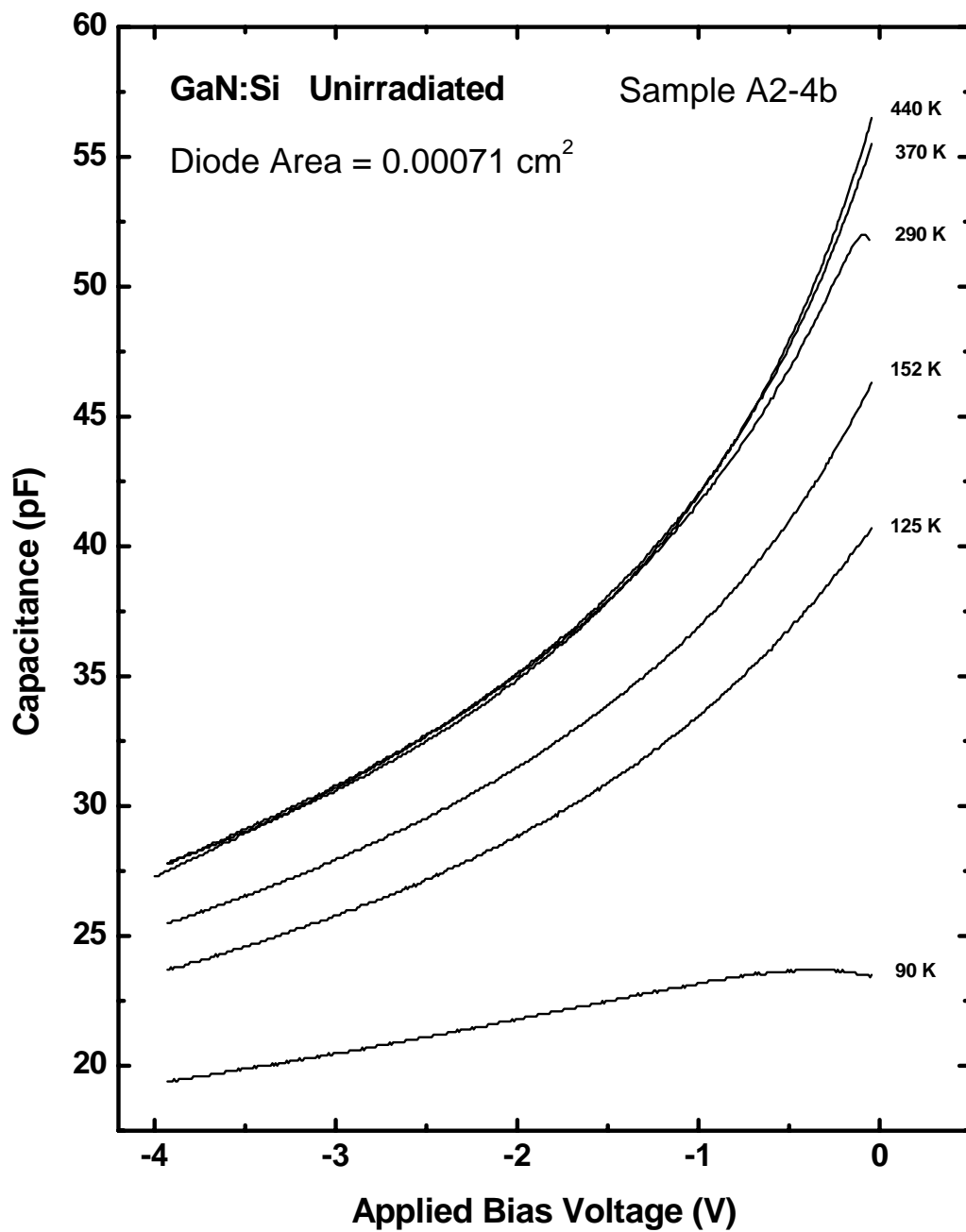


Figure A-3. C-V curves at various temperatures for unirradiated GaN (sample A2-4b).

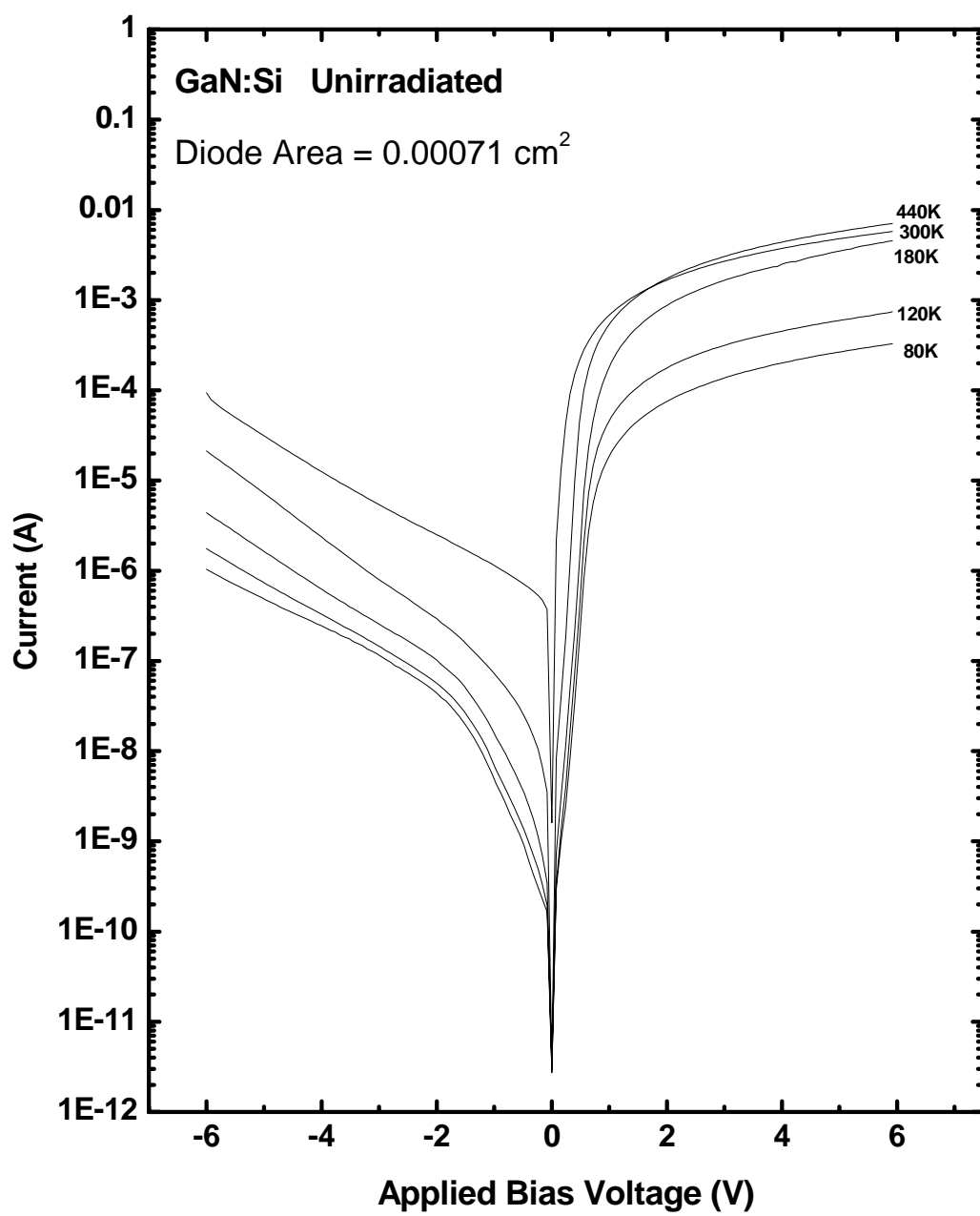


Figure A-4. I-V curves at various temperatures for unirradiated GaN (sample A2-4b).

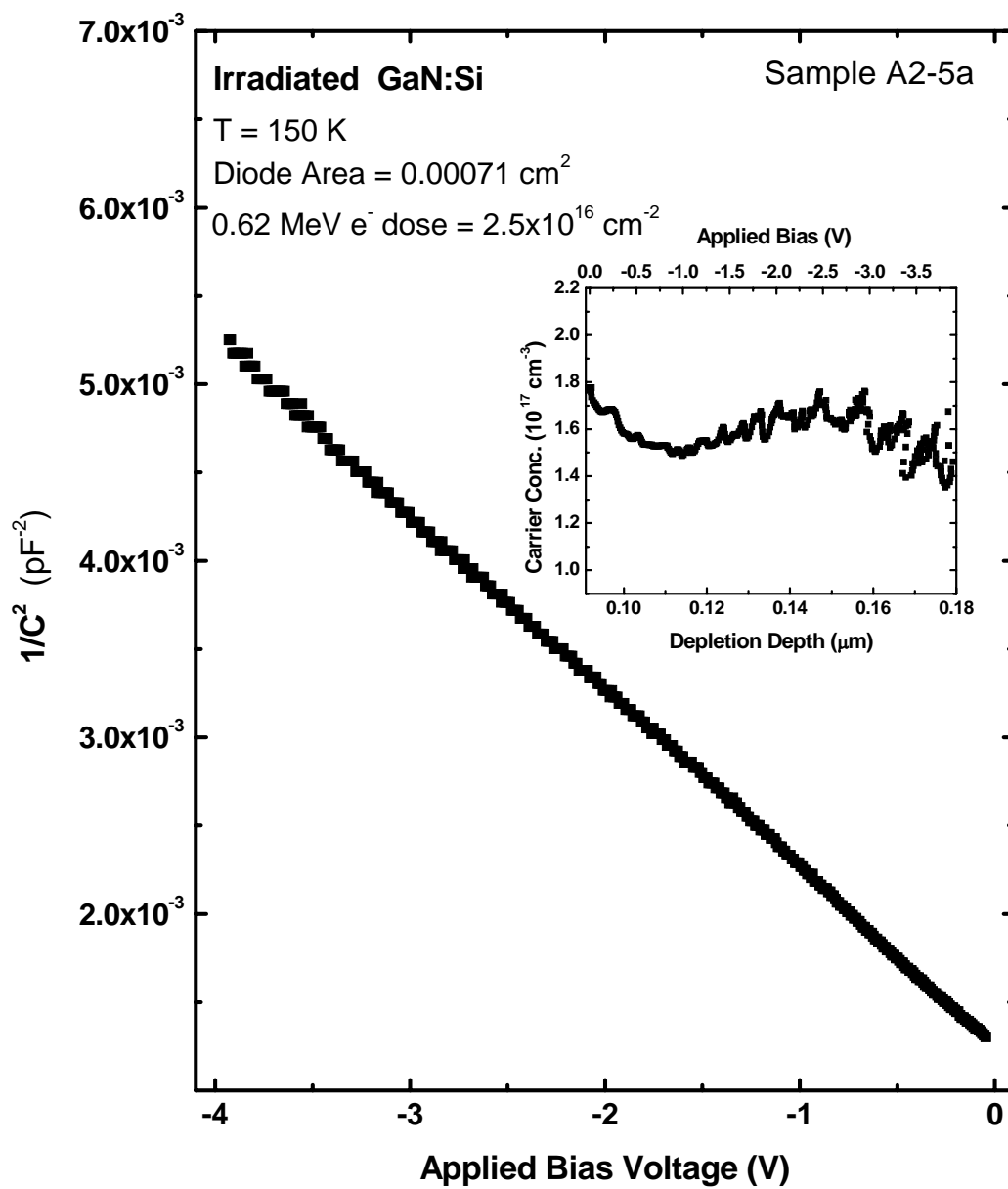


Figure A-5. Plot of $1/C^2$ versus applied bias for irradiated GaN (sample A2-5a) at $T = 150 \text{ K}$. Inset is the extrapolated carrier concentration versus depletion depth.

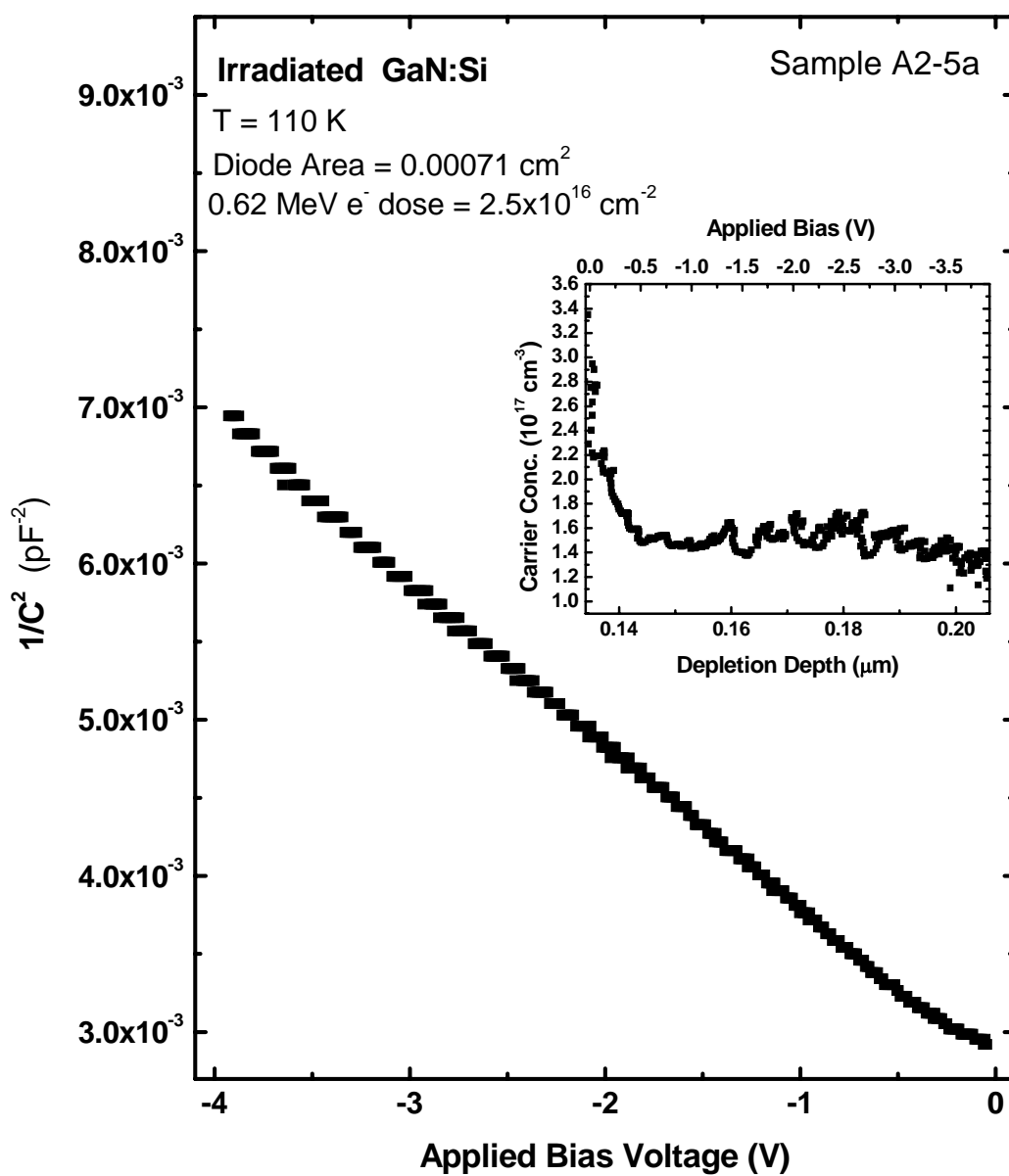


Figure A-6. Plot of $1/C^2$ versus applied bias for irradiated GaN (sample A2-5a) at $T = 110 \text{ K}$. Inset is the extrapolated carrier concentration versus depletion depth.

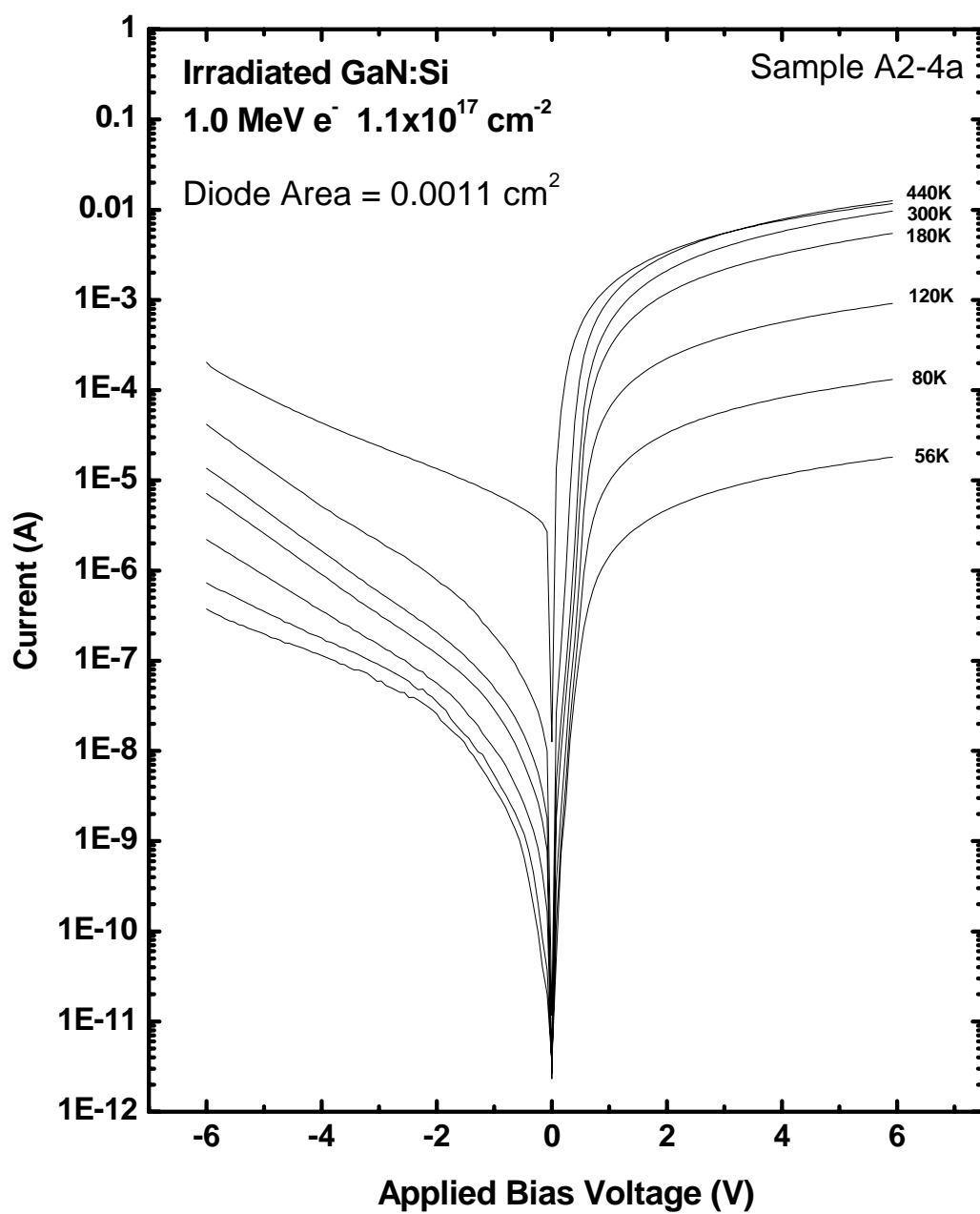


Figure A-7. I-V curves at various temperatures for 1.0 MeV electron irradiated GaN (sample A2-4a).

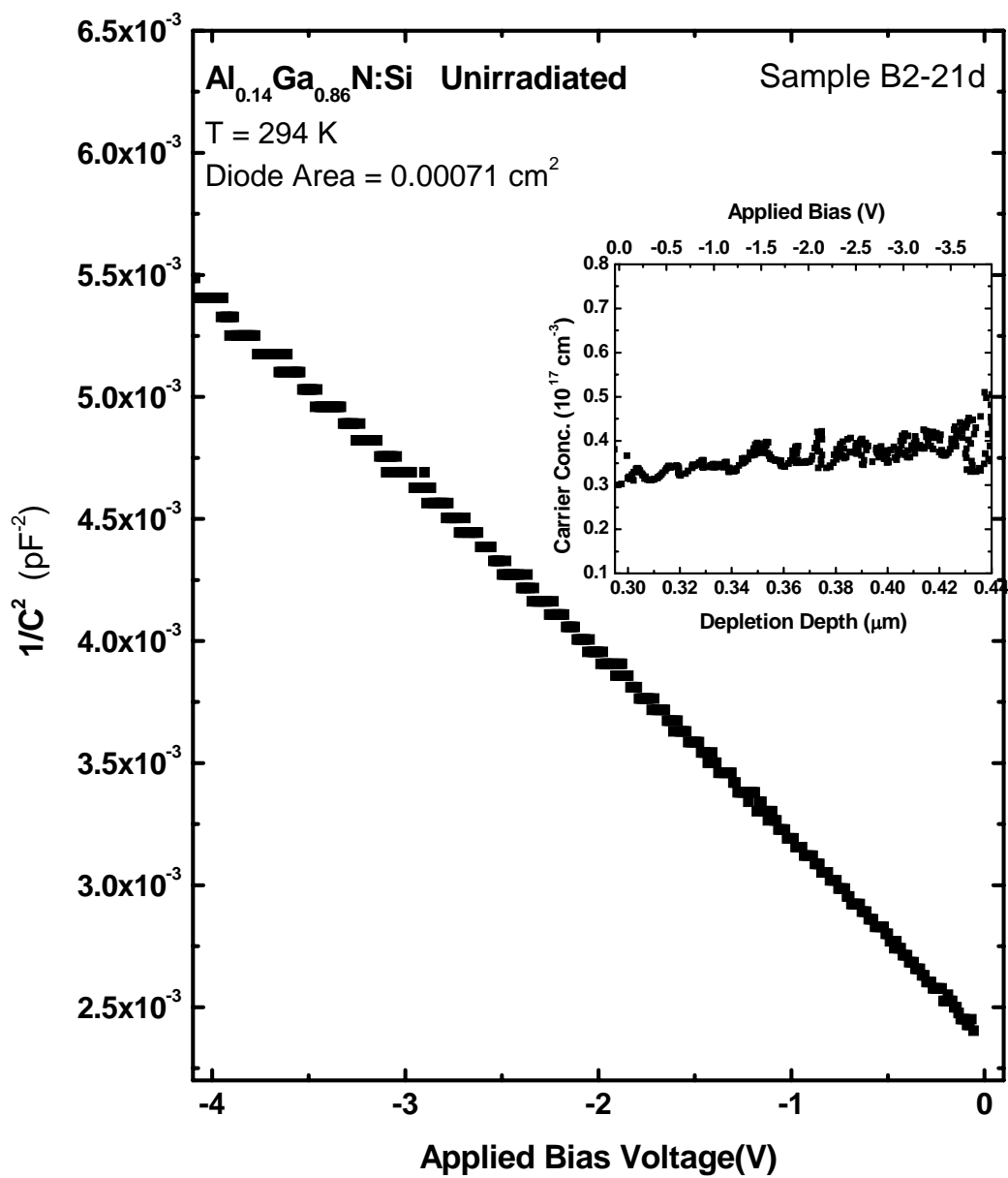


Figure A-8. Plot of $1/C^2$ versus applied bias for unirradiated $\text{Al}_{0.14}\text{Ga}_{0.86}\text{N}$ (sample B2-21d) at $T=294 \text{ K}$. Inset is the extrapolated carrier concentration versus depletion depth.

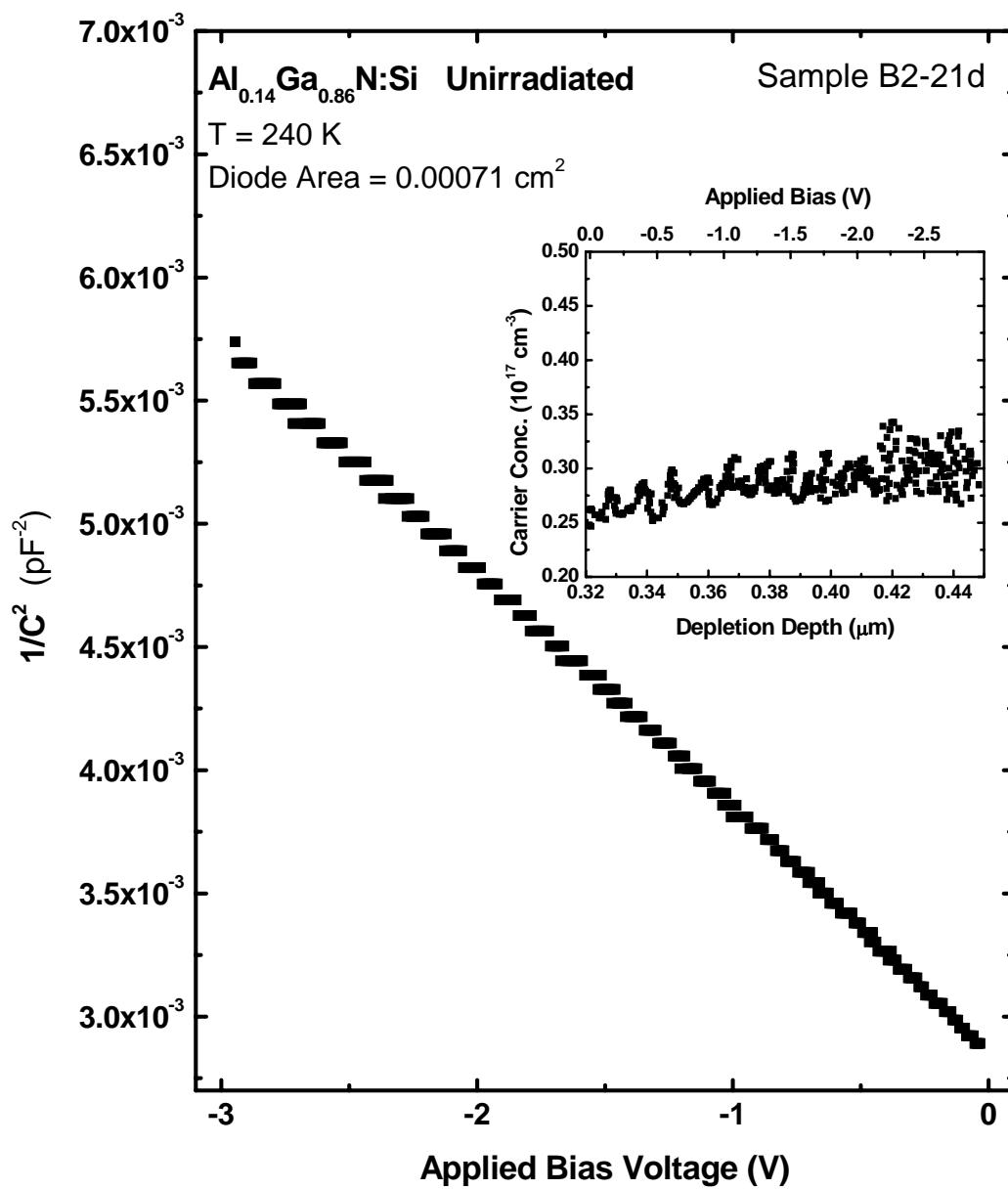


Figure A-9. Plot of $1/C^2$ versus applied bias for unirradiated $\text{Al}_{0.14}\text{Ga}_{0.86}\text{N}$ (sample B2-21d) at $T = 240 \text{ K}$. Inset is the extrapolated carrier concentration versus depletion depth.

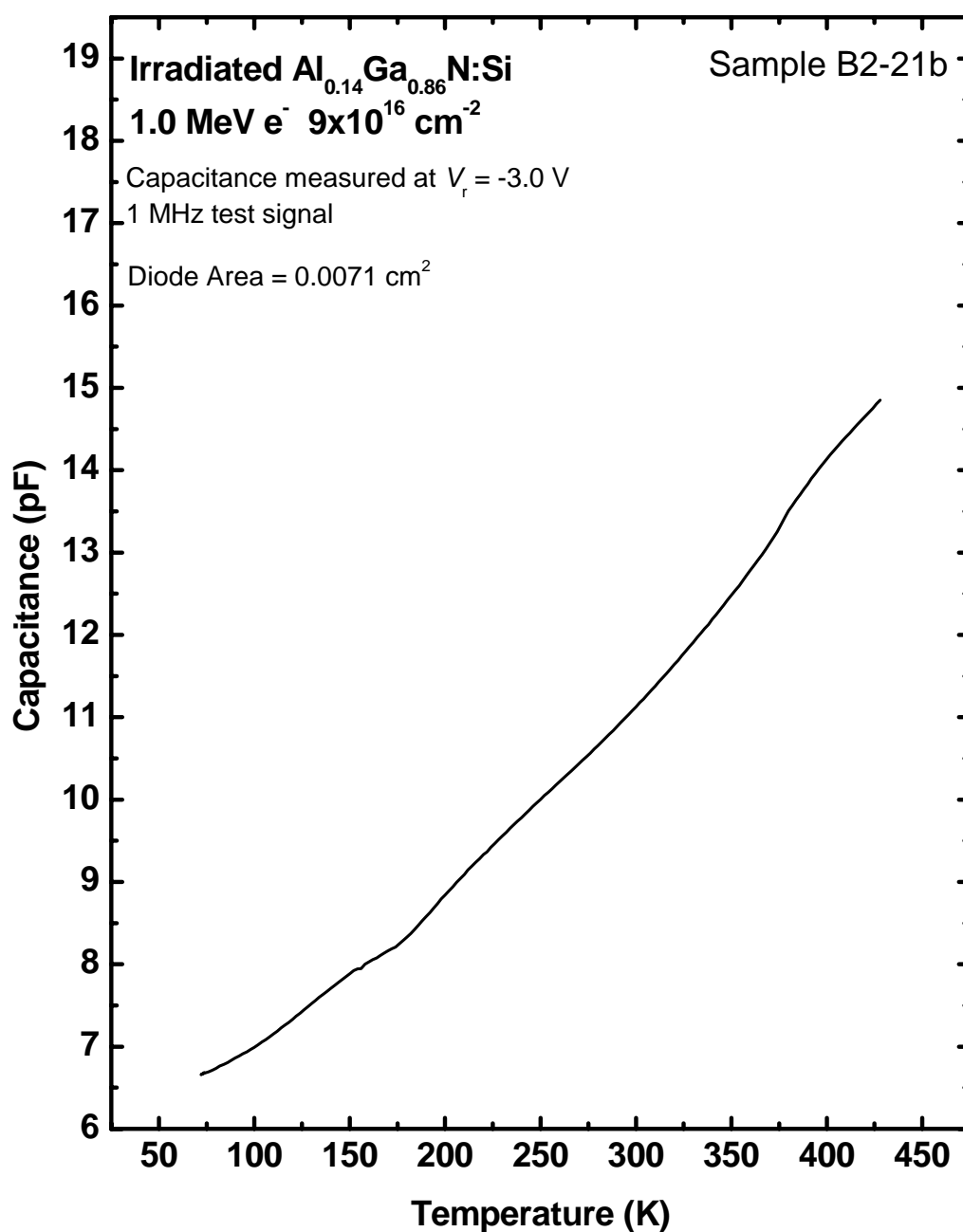


Figure A-10. Capacitance versus temperature in $\text{Al}_{0.14}\text{Ga}_{0.86}\text{N}$ (sample B2-21b) following 1.0 MeV electron irradiation.

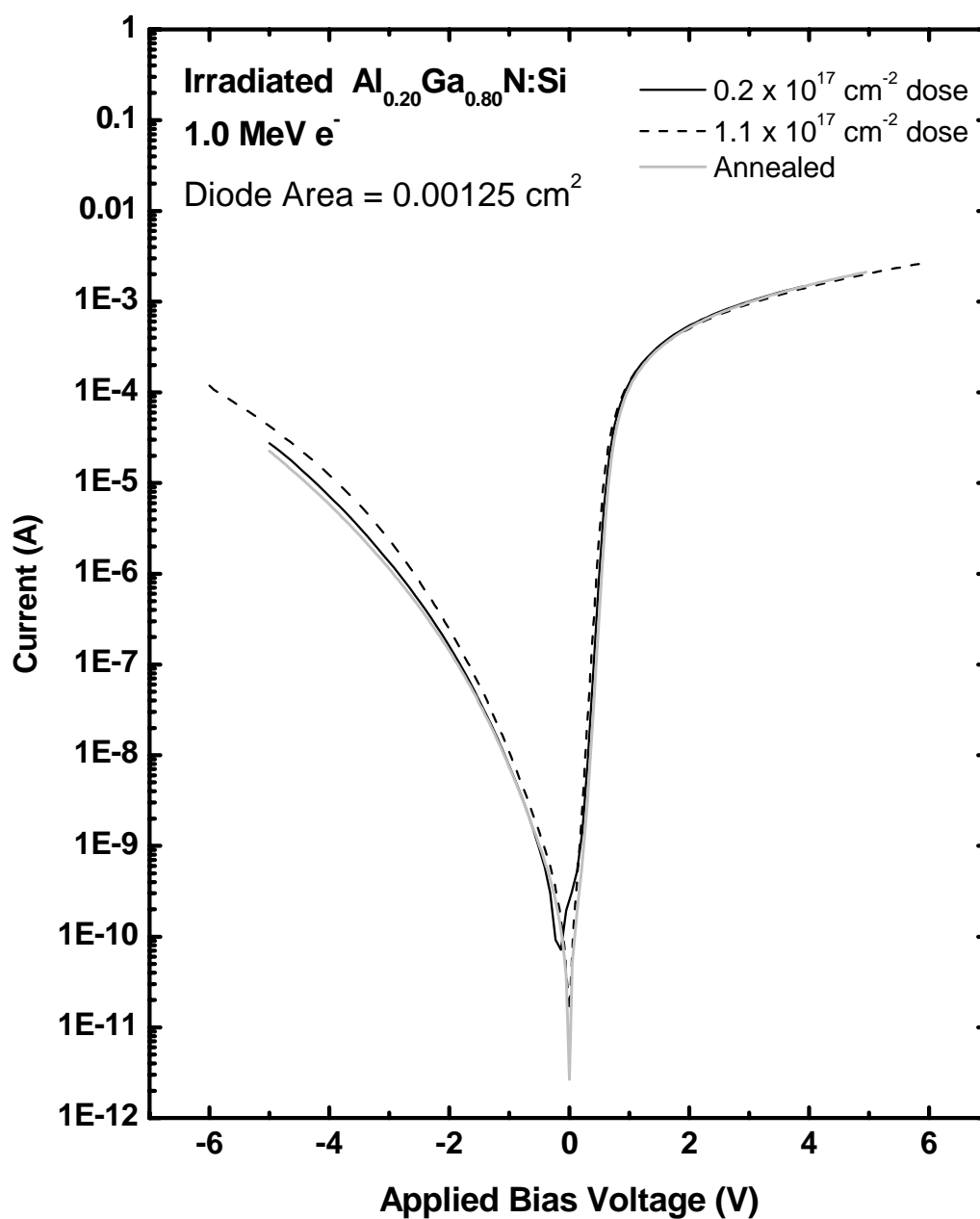


Figure A-11. I-V curves of irradiated $\text{Al}_{0.20}\text{Ga}_{0.80}\text{N}$ (sample C1-38a) before and after annealing at 350°C for 15 min.

Bibliography

-
- [1] B. D. White, M. Bataiev, L. J. Brillson, B. K. Choi, D.M. Fleetwood, R. D. Schrimpf, S. T. Pantelides, R. W. Dettmer, W. J. Schaff, J. G. Champlain, and U. K. Mishra. "Characterization of 1.8-MeV proton-irradiated AlGa_N/Ga_N field-effect transistor structures by nanoscale depth-resolved luminescence spectroscopy," *IEEE Trans. Nucl. Sci.* **49** (6), 2695 (2002).
 - [2] U. Mishra, P. Parikh, and Y-F Wu. "AlGa_N/Ga_N HEMTs - An overview of device operation and applications," *Proc. IEEE* **90** (6), 1022 (2002).
 - [3] D. C. Look, Z. Fang, and L. Polenta, "Electrical measurements in Ga_N: Point defects and dislocations," *Internet J. Nitride Semicond. Res.* **5S1**, W10.5 (2000).
 - [4] H. Boudinov, S. O. Kucheyev, J. S. Williams, C. Jagadish, and G. Li. "Electrical isolation of Ga_N by MeV ion irradiation," *Appl. Phys. Lett.* **78**, 943 (2001).
 - [5] A. I. Titov and S. O. Kucheyev. "Model for electrical isolation of Ga_N by light-ion bombardment," *J. Appl. Phys.* **92**, 5740 (2002).
 - [6] H. Boudinov, A. V. P. Coelho, and J. P. de Souza. "Electrical isolation of p type GaAs layers by ion irradiation," *J. Appl. Phys.* **91**, 6585 (2002).
 - [7] O. Gelhausen, H. N. Klein, M. R. Philips, and E. M. Goldys. "Influence of low-energy electron beam irradiation on defects in activated Mg-doped Ga_N," *Appl. Phys. Lett.* **81** 3747 (2002).
 - [8] D. C. Look. "Defect-related donors, acceptors, and traps in Ga_N," *Phys. Stat. Sol. B* **228**, 293 (2001).
 - [9] C. G. Van de Walle, C. Stampfl, J. Neugebauer, M. D. McCluskey, and N. M. Johnson. "Doping of AlGa_N alloys," *MRS Internet. J. Nitride Semicond. Res.* **4S1**, G10.4 (1999).
 - [10] J. E. Van Nostrand, J. Solomon, A. Saxler, Q.H. Xie, D. C. Reynolds, and D. C. Look. "Dissociation of Al₂O₃(0001) substrates and the roles of silicon and oxygen in n-type Ga_N thin solid films grown by gas-source molecular beam epitaxy," *J. Appl. Phys.* **87** (12), 8766 (2000).
 - [11] Author discussions with D. C. Look, Wright State University (February, 2003).
 - [12] O. Mitrofanov and M. Manfra. "Dynamics of trapped charge in Ga_N/AlGa_N/Ga_N high electron mobility transistors grown by plasma-assisted molecular beam

-
- epitaxy *Appl. Phys. Lett.* **84**, 422 (2004).
- [13] D. C. Look. *Electrical Characterization of GaAs Materials and Devices*, edited by D. V. Morgan and H. L. Grubin. Chichester: Wiley, 1989.
- [14] P. Battacharya. *Semiconductor Optoelectronic Devices*. New Jersey: Prentice Hall, 1997.
- [15] J. A. Fellows. *Electrical Activation Studies of Ion Implanted Gallium Nitride*. Air Force Institute of Technology (AU), Wright-Patterson AFB, OH November 2001 (ADA396548).
- [16] S. M. Sze. *Semiconductor Devices: Physics and Technology*. New York: John Wiley and Sons, 1985.
- [17] K. D. Greene. *Electron Paramagnetic Resonance Spectroscopy and Hall Effect Studies of the Effects of Low Energy Electron Irradiation on Gallium Nitride*. Air Force Institute of Technology (AU), Wright-Patterson AFB, OH September 2003 (ADA420816).
- [18] M. Suzuki, T. Uenoyama, and A. Yanase. "First Principles Calculations of effective-mass parameters of AlN and GaN, " *Phys. Rev. B*, **52** (11), 8132 (1995).
- [19] B. Gill. *Low Dimensional Nitride Semiconductors*. New York: Oxford University Press, 1999.
- [20] M. Shur. *Basic GaN, AlN, and InN Parameters*. January 8, 2005 (last revised February 5, 2002). <http://nina.ecse.rpi.edu/shur/nitride.htm>
- [21] T. J. Ochalski, B. Gil, P. Lefebvre, N. Grandjean, M. Leroux, J. Massies, S. Nakamura, and H. Morkoc. "Photorefectance investigations of the bowing parameter in AlGa_N alloys lattice-matched to GaN," *Appl. Phys. Lett.* **74**, 3353 (1999).
- [22] W. Shan, J. W. Ager III, K. M. Yu, W. Walukiewicz, E. E. Haller, M. C. Martin, W. R. McKinney, and W. Yang. "Dependence of the fundamental band gap of Al_xGa_{1-x}N on alloy composition and pressure," *J. Appl. Phys.* **85**, 8505 (1999).
- [23] R. T. Kemerley, H. B. Wallace, and M. N. Yoder. "Impact of wide bandgap microwave devices on DoD systems," *Proc. IEEE* **90**, 1059 (2002).
- [24] J. Neugbauer C. G. Van de Walle, "Atomic geometry and electronic structure of native defects in GaN." *Phys. Rev. B* **50** (11), 8067 (1994).
- [25] C. Claeys and E. Simoen. *Radiation Effects in Advanced Semiconductor Materials and Devices*. New York: Springer, 2002.

-
- [26] A. E. Belyaev, J. Breza, E. F. Venger, M. Vesely, I.Yu. Il'in, R. V. Konakova, J. Liday, V. G. Lyapin, V. V. Milenin, I. V. Prokopenko, Y. A. Tkhorik *Radiation Resistance of GaAs-Based Microwave Schottky Barrier Devices*. Kiev: Institute of Semiconductor Physics of the National Academy of Sciences of Ukraine, 1998. Available at <http://www.isp.kiev.ua/library/books/books/htm>
- [27] A. Holmes-Siedle and L. Adams. *Handbook of Radiation Effects*. New York: Oxford Press Inc., 2002.
- [28] P. M. Mooney. *Semiconductors and Semimetals*, **51B** 93, M. Stavola (Ed.). Boston: Academic, 1999.
- [29] P. Boguslawski, E. L. Briggs, and J. Bernholc. "Native defects in gallium nitride," *Phys. Rev. B* **51** (23), 17 255 (1995).
- [30] L. E. Ramos, J. Furthmüller, F. Bechstedt, L. M. R. Scolfaro, and F. R. Leite. "*Ab initio* theory of native defects in alloys: application to charged N vacancies in $\text{Al}_x\text{Ga}_{1-x}\text{N}$," *J. Phys: Condens. Matter* **14**, 2577 (2002).
- [31] L. Polenta, Z-Q. Fang, and D. C. Look. "On the main irradiation-induced defect in GaN," *Appl. Phys. Lett.* **76** 2086 (2000).
- [32] Q. Zhou, M. O. Manasreh, M. Pophristic, S. Guo, and I. T. Ferguson. "Observation of nitrogen vacancy in proton-irradiated $\text{Al}_x\text{Ga}_{1-x}\text{N}$," *Appl. Phys. Lett.* **79**, 2901 (2001).
- [33] D. C. Look, D. C. Reynolds, J. W. Hemsky, J. R. Sizelove, R. L. Jones, and R. J. Molnar, "Defect Donor and Acceptor in GaN," *Phys. Rev. Lett.* **79** (12), 2273 (1997).
- [34] S. A. Goodman, F. D. Auret, M. J. Legodi, B. Beaumont, and P. Gibart. "Characterization of electron-irradiated n-GaN," *Appl. Phys. Lett.* **78**, 3815 (2001).
- [35] F. D. Auret, S. A. Goodman, F. K. Koschnick, J.-M. Spaeth, B. Beaumont, and P. Gibart. "Proton bombardment-induced electron traps in epitaxially grown n-GaN," *Appl. Phys. Lett.* **74** 407 (1999).
- [36] F. D. Auret, S. A. Goodman, F. K. Koschnick, J. M. Spaeth, B. Beaumont, and P. Gibart. "Electrical characterization of two deep electron traps introduced in epitaxially grown n-GaN during He-ion irradiation," *Appl. Phys. Lett.* **73**, 3745 (1998).
- [37] A. Castaldini, A. Cavallini, and L. Polenta. "Deep levels and irradiation effects in

-
- n-GaN," *J. Phys.: Condens. Matter* **12** 10161 (2000).
- [38] N. M. Shmidt, D. V. Davydov, V. V. Emtsev, *et al.*. "Mosaic Structure and Si Doping Related Peculiarities of Charge Carrier Transport in III-V Nitrides," *Phys. Stat. Sol. B* **216**, 533 (1999).
 - [39] Z.-Q. Fang, J. W. Hemsky, D. C. Look, and M. P. Mack. "Electron-irradiation-induced deep level in n-type GaN," *Appl. Phys. Lett.* **72**, 448 (1998).
 - [40] A. Y. Polyakov, N. B. Smirnov, A. V. Gorvorkov, Z.-Q. Fang, D. C. Look, S. S. Park, and J. H. Han. "Deep electron and hole traps in freestanding n-GaN grown by hydride vapor phase epitaxy," *Journ. Appl. Phys.* **92**, 5241 (2002).
 - [41] W. Götz, N.M. Johnson, C. Chen, H. Liu, C. Kuo, and W. Imler. "Activation energies of Si donors in GaN," *Appl. Phys. Lett.* **68**, 3144 (1996).
 - [42] M. J. Legodi, S. S. Hullavarad, S. A. Goodman, M. Hayes, and F. D. Auret. "Defect characterization by DLTS of AlGa_N UV Schottky photodetectors," *Physica B* **308-310**, 1189 (2001).
 - [43] K. H. Chow, G. D. Watkins, A. Usui, and M. Mizuta, "Detection of interstitial Ga in GaN," *Phys. Rev. Lett.* **85** (13), 2761 (2000).
 - [44] K. Saarinen, T. Suski, I. Grzegory, and D. C. Look. "Ga vacancies in electron irradiated GaN: introduction, stability and temperature dependence of positron trapping," *Physica B* **308-310**, 77 (2001).
 - [45] D. C. Look, Z. Fang, and L. Polenta. "Electrical measurements in GaN: Point defects and dislocations," *Internet J. Nitride Semicond. Res.* **5S1**, W10.5 (2000).
 - [46] C. Mavroidis, J. J. Harris, M. J. Jappers, C. J. Humphreys, and Z. Bougrioua. "Detailed interpretation of electron transport in n-GaN," *J. Appl. Phys.* **11**, 9095 (2003).
 - [47] D. C. Look and J. R. Sizelove, "Dislocation scattering in GaN," *Phys. Rev. Lett.* **82** (6), 1237 (1999).
 - [48] A. F. Wright and J. Furthmuller. "Theoretical investigation of edge dislocations in AlN," *Appl. Phys. Lett.* **72**, 3467 (1998).
 - [49] Z-Q. Fang, D. C. Look, W. Kim, and H. Morkoc. "Characteristics of deep centers observed in n-GaN grown by reactive molecular beam epitaxy," *MRS Internet J. Nitride Semicond. Res.* **5S1**, W11.84 (2000).
 - [50] J. F. Ziegler, program "Stopping and Range of Ions in Matter" SRIM-2003.10.

-
- [51] J. M. Sattler, *An Analysis of the Effects of Low Energy Electron Radiation on $Al_xGa_{1-x}N/GaN$ Modulation-Doped Field Effect Transistors*. Air Force Institute of Technology (AU), Wright-Patterson AFB, OH March 2004 (ADA423014).
- [52] W. A. McKinley and H. Feshbach. "The coulomb scattering of relativistic electrons by nuclei," *Phys. Rev.* **74** (12), 1759 (1948).
- [53] A. Ionascut-Nedelcescu, C. Carlone, A. Houdayer, H.J. von Bardeleben, J.-L. Cantin, and S. Raymond. "Radiation Hardness of Gallium Nitride," *IEEE Trans. Nucl. Sci.* **49** (6) 2733 (2002).
- [54] J. Nord, K. Nordlund, J. Keinonen, and K. Albe. "Molecular dynamics study of defect formation in GaN cascades," *Nucl. Inst. and Meth. In Phys. Res. B* **202**, 93 (2003).
- [55] D. C. Look and J. W. Farmer. "The type-conversion phenomenon in electron-irradiated GaAs," *J. Phys. Chem. Solids* **49**, 97 (1988).
- [56] H. Boudinov, A. V. P. Coelho, and J. P. de Souza. "Electrical isolation of p type GaAs layers by ion irradiation," *J. Appl. Phys.* **91**, 6585 (2002).
- [57] J. P. de Souza, I. Danilov, and H. Boudinov. "Electrical isolation of n-type GaAs layers by proton bombardment: Effects of the irradiation temperature," *J. Appl. Phys.* **84**, 4757 (1998).
- [58] J. G. Williams, J. U. Patel, A. M. Ougouag, and S. Y. Yang. "Carrier removal and changes in electrical properties of neutron irradiated GaAs," *J. Appl. Phys.* **70**, 4931 (1991).
- [59] G. Dlubek, A. Dlubek, R. Krause, and O. Brümmer. "Point defects in GaAs studied by correlated positron lifetime, optical, and electrical measurements," *Phys. Stat. Sol. A* **107**, 111 (1988).
- [60] G. H. Marcus and H. P. Bruemmer, *IEEE Trans. Nucl. Sci.* **17**, 230 (1970).
- [61] D. C. Look. "High acceptor production rate in electron-irradiated n-type GaAs: Impact on defect models," *Appl. Phys. Lett.* **51**, 843 (1987).
- [62] S. O. Kucheyev, J. S. Williams, C. Jagadish, J. Zou, and G. Li. "Damage buildup in GaN under ion bombardment," *Phys. Rev. B* **62** (11), 7510 (2000).
- [63] F. D. Aurret, S. A. Goodman, M. Hayes, M. J. Legodi, S. S. Hullavarad, E. Friedland, B. Beaumont, and P. Gibart. *Nucl. Instr. and Meth. B* **175-177**, 292 (2001).
- [64] H. Boudinov, S. O. Kucheyev, J. S. Williams, C. Jagadish, and G. Li. "Electrical

-
- isolation of GaN by MeV ion irradiation," *Appl. Phys. Lett.* **78**, 943 (2001).
- [65] A. I. Titov and S. O. Kucheyev. "Model for electrical isolation of GaN by light-ion bombardment," *J. Appl. Phys.* **92**, 5740 (2002).
- [66] S. M. Hearne, D. N. Jaimeson, C. Yang, S. Praver, J. Salzman, and O. Katz. "Electrical characteristics of proton irradiated AlGaIn devices," *Nucl. Instrum. Methods Phys. Res. B* **190**, 873 (2002).
- [67] F. Gaudreau, P. Fournier, C. Carlone, S. M. Khanna, H. Tang, J. Webb, and A. Houdayer, "Spectral properties of proton irradiated gallium nitride blue diodes," *IEEE Trans. Nucl. Sci.* **49** (6), 2702 (2002).
- [68] S. M. Khanna, J. Webb, H. Tang, A. J. Houdayer, and C. Carlone. "2 MeV proton radiation damage studies of gallium nitride films through low temperature photoluminescence spectroscopy measurements," *IEEE Trans. Nucl. Sci.* **47** (6), 2322 (2000).
- [69] R. R. Sumathi, M. Udhayasankar, J. Kumar, P. Magudapathy, and K. G. M. Mair. "Effect of proton irradiation on the characteristics of GaAs Schottky barrier diodes," *Physica B* **308-310**, 1209 (2001).
- [70] M. Hanzaz, A. Bouhdada, P. Gibart, and F. Omnes. "Impact of the defects on the electrical and optical properties of AlGaIn ultraviolet photodetectors," *J. Appl. Phys.* **92**, 13 (2002).
- [71] G. A. Umana-Membreno, J. M. Dell, G. Parish, B. D. Nener, L. Faraone, and U. K. Mishra. "⁶⁰Co gamma irradiation effects on n-GaN Schottky diodes," *IEEE Trans. Nucl. Sci.* **50**, 2326 (2003).
- [72] J. D. Scofield, *Electrical Characterization of Intrinsic and Induced Deep Level Defects in Hexagonal SiC*. Air Force Institute of Technology (AU), Wright-Patterson AFB, OH November 1996 (ADA325121).
- [73] S. T. Bradley, A. P. Young, L. J. Brillson, M. J. Murphy, and W. J. Schaff. "Influence of AlGaIn deep level defects on AlGaIn/GaN 2-DEG carrier confinement," *IEEE Trans. Electron Dev.* **48** (3), 412 (2001).
- [74] S. J. Cai, S. Tang, R. Li, Y. Y. Wei, L. Wong, Y. L. Chen, K. L. Wang, M. Chen, Y. F. Zhao, R. D. Schrimpf, J. C. Keay, and K. F. Galloway. "Annealing behavior of a proton irradiated Al_xGa_{1-x}N/GaN high electron mobility transistor grown by MBE" *IEEE Trans. Electron Dev.* **47**, 304 (2000).
- [75] B. Luo, J. W. Johnson, F. Ren, K.K. Allums, C. R. Abernathy, S. J. Pearton, R. Dwivedi, T. N. Fogarty, R. Wilkins, A. M. Dabiran, A. M. Wowchack, C. J. Polley, P. P. Chow, and A. G. Baca. "High-energy proton irradiation effects on

-
- AlGaIn/GaN high-electron mobility transistors," *Journ. Electron. Mat.* **31**, 437 (2002).
- [76] SVT Associates, Inc.. Eden Prairie, MN. <http://www.svta.com>
- [77] Y. Taniyasu, M. Kasu, and N. Kobayashi. "Intentional control of n-type conduction for Si-doped AlN and $\text{Al}_x\text{Ga}_{1-x}\text{N}$ ($0.42 < x < 1$)," *Appl. Phys. Lett.* **81**, 1255 (2002).
- [78] J.W. Orton and C.T. Foxon. "The electron mobility and compensation in n-type GaN," *Semicond. Sci. Technol.* **13**, 310 (1998).
- [79] S. T. B. Goennenwein, R. Zeisel, S. Baldovino, O. Ambacher, M. S. Brandt, and M. Stutzmann. "Defect-related noise in AlN and AlGaIn alloys," *Physica B* **308-310**, 69-72 (2001).
- [80] B. K. Meyer, D. Volm, A. Graber, H. C. Alt, T. Detchprohm, A. Amano, and I. Akasaki. "Shallow donors in GaN—The binding energy and the electron effective mass," *Solid State Commun.* **95**, 597 (1995).
- [81] G. R. James, A. W. R. Leitch, M. C. Wagener, and F. Omnès. "Investigating the nature of Si doping in $\text{Al}_{0.23}\text{Ga}_{0.77}\text{N}$," *Physica B* **340-342**, 426-429 (2003).
- [82] CREE, Inc. Durham, N.C. <http://www.cree.com>
- [83] D. K. Schroder. *Semiconductor Material and Device Characterization*. New York: Wiley, 1990.
- [84] J. McFall, *Optical Investigation of Molecular Beam Epitaxy $\text{Al}_x\text{Ga}_{1-x}\text{N}$ to determine material quality*. M.S. thesis, AFIT/GMS/ENP/00M-01. Air Force Institute of Technology (AU), Wright-Patterson AFB, OH, March 2000 (ADA384472).
- [85] D. V. Lang. "Deep-level transient spectroscopy: A new method to characterize traps in semiconductors," *J. Appl. Phys.* **45**, 3023 (1974).
- [86] P. Omling, L. Samuelson, and H. G. Grimmeiss. "Deep level transient spectroscopy evaluation of nonexponential transients in semiconductor alloys," *J. Appl. Phys.* **54**, 5117 (1983).
- [87] Y. Zohta and M. O. Watanabe. "On the determination of the spatial distribution of deep centers in semiconducting thin films from capacitance transient spectroscopy," *J. Appl. Phys.* **53**, 1809 (1981).
- [88] P. Omling, E. R. Weber, L. Montelius, H. Alexander, and J. Michel. "Electrical properties of dislocations and point defects in plastically deformed silicon," *Phys.*

-
- Rev. B* **32** (10), 6571 (1985).
- [89] T. Wosinski. "Evidence for the electron traps at dislocations in GaAs crystals," *J. Appl. Phys.* **65**, 1566 (1989).
- [90] Z-Q. Fang, D. C. Look, and L. Polenta. "Dislocation-related electron capture behaviour of traps in n-type GaN," *J. Phys.: Condens. Matter* **14**, 13061 (2002).
- [91] V. V. Kveder, Y. A. Ossipyan, W. Schroter, and G. Zoth, *Phys. Status Solidi A* **72**, 701 (1982).
- [92] S. D. Ganichev, E. Ziemann, and W. Prettl. "Distinction between Poole-Frenkel and tunneling models of electric-field-stimulated carrier emission from deep levels in semiconductors," *Phys. Rev. B* **61** (15), 10361 (2000).
- [93] W. K. Gotz, J. Walker, L. T. Romano, N. M. Johnson, and R. J. Molnar. "Thickness Dependence of Electronic Properties of GaN Epilayers," *Mater. Res. Soc. Symp. Proc.* **449**, 525 (1997).
- [94] P. Hacke, T. Detchprohm, K. Hiramatsu, N. Sawaki, K. Tadatomo, and K. Miyake. "Analysis of deep levels in n-type GaN by transient capacitance methods," *J. Appl. Phys.* **76**, 304 (1994).
- [95] D. Hasse, M. Schmid, W. Kurner, A. Dornen, V. Harle, F. Scholz, M. Burkhard, and H. Schweizer. "Deep-level defects and n-type-carrier concentration in nitrogen implanted GaN," *Appl. Phys. Lett.* **69**, 2525 (1996).
- [96] F. D. Auret and S. A. Goodman, "Radiation and processed induced defects in GaN," *III-Nitride Semiconductors: Electrical, Structural, and Defect Properties*. M.O. Manasreh (Ed.) 251 (2000).
- [97] W. Götz, N. M. Johnson, M. D. Bremser, and R. F. Davis. "A donorlike deep level defect in $\text{Al}_{0.12}\text{Ga}_{0.88}\text{N}$ characterized by capacitance transient spectroscopies," *Appl. Phys. Lett.* **69**, 2379 (1996).
- [98] J. Osaka, M. Nishira, T. Okino, Y. Ohno, S. Kishimoto, K. Maezawa, and T. Mizutani, International Workshop on Nitride Semiconductors (2004).
- [99] D. C. Look, G. C. Farlow, P. J. Drevinsky, D. F. Bliss, and J. R. Sizelove. "On the nitrogen vacancy in GaN," *Appl. Phys. Lett.* **83**, 3525 (2003).
- [100] Author discussions with M-Y. Ryu, University of Dayton Research Center (November 2004).

REPORT DOCUMENTATION PAGE				Form Approved OMB No. 074-0188	
<p>The public reporting burden for this collection of information is estimated to average 1 hour per response, including the time for reviewing instructions, searching existing data sources, gathering and maintaining the data needed, and completing and reviewing the collection of information. Send comments regarding this burden estimate or any other aspect of the collection of information, including suggestions for reducing this burden to Department of Defense, Washington Headquarters Services, Directorate for Information Operations and Reports (0704-0188), 1215 Jefferson Davis Highway, Suite 1204, Arlington, VA 22202-4302. Respondents should be aware that notwithstanding any other provision of law, no person shall be subject to a penalty for failing to comply with a collection of information if it does not display a currently valid OMB control number.</p> <p>PLEASE DO NOT RETURN YOUR FORM TO THE ABOVE ADDRESS.</p>					
1. REPORT DATE (DD-MM-YYYY) 21-03-2005		2. REPORT TYPE Doctoral Dissertation		3. DATES COVERED (From – To) Apr 2003 – Jan 2005	
4. TITLE AND SUBTITLE Deep Level Defects in Electron-Irradiated Aluminum Gallium Nitride Grown by Molecular Beam Epitaxy				5a. CONTRACT NUMBER	
				5b. GRANT NUMBER	
				5c. PROGRAM ELEMENT NUMBER	
6. AUTHOR(S) Hogsed, Michael, R., Captain, USAF				5d. PROJECT NUMBER	
				5e. TASK NUMBER	
				5f. WORK UNIT NUMBER	
7. PERFORMING ORGANIZATION NAMES(S) AND ADDRESS(S) Air Force Institute of Technology Graduate School of Engineering and Management (AFIT/EN) 2950 Hobson Way WPAFB OH 45433-7765				8. PERFORMING ORGANIZATION REPORT NUMBER AFIT/DS/ENP/05-01	
9. SPONSORING/MONITORING AGENCY NAME(S) AND ADDRESS(ES) DTRA/CSNP DTRA HEADQUARTERS ATTN: Mr Gerry Baird/CSNP 8725 John Kingman Road Ft. Belvoir, VA 22060-6201				10. SPONSOR/MONITOR'S ACRONYM(S)	
				11. SPONSOR/MONITOR'S REPORT NUMBER(S)	
12. DISTRIBUTION/AVAILABILITY STATEMENT APPROVED FOR PUBLIC RELEASE; DISTRIBUTION UNLIMITED.					
13. SUPPLEMENTARY NOTES					
14. ABSTRACT <p>Aluminum gallium nitride (AlGa_N)-based devices are attractive candidates for integration into future Air Force communication and sensor platforms, including those that must operate in harsh radiation environments. In this study, the electrical and optical properties of 1.0 MeV electron irradiated n-Al_xGa_{1-x}N are characterized for aluminum mole fraction x = 0.0 to 0.3 using deep level transient spectroscopy (DLTS), temperature-dependent Hall, and cathodoluminescence (CL) measurements.</p> <p>Following irradiation of the AlGa_N, it is found that four different electron traps are created, having energy levels within 0.4 eV below the conduction band edge. Three of these traps correspond to radiation-induced traps previously reported in GaN, and they are found to deepen significantly in the energy band gap with increase in aluminum mole fraction. The room temperature carrier concentration decreases following irradiation, and the carrier removal rate is found to depend foremost on the initial carrier concentration, regardless of the aluminum mole fraction. Also, following 1.0 MeV electron irradiation at a fluence of 1x10¹⁷ cm⁻², the peak CL intensities of the samples are reduced, on average, by 50%. In spite of these findings, it is concluded that n-Al_xGa_{1-x}N is intrinsically more tolerant to radiation than conventional semiconductor materials such as GaAs and Si.</p>					
15. SUBJECT TERMS Gallium Nitrides, Aluminum Gallium Nitrides, Point Defects, Hall Effect, DLTS, Electron Irradiation					
16. SECURITY CLASSIFICATION OF:			17. LIMITATION OF ABSTRACT	18. NUMBER OF PAGES	19a. NAME OF RESPONSIBLE PERSON
REPORT	ABSTRACT	c. THIS PAGE			Yung Kee Yeo (ENP)
U	U	U	UU	204	19b. TELEPHONE NUMBER (Include area code) (937) 255-3636, ext 4532; e-mail: Yung.Yeo@afit.edu

Standard Form 298 (Rev. 8-98)

Prescribed by ANSI Std. Z39-18